

DISS. ETH NO. 19869

**POLY(ALKYL-PHOSPHONATES), A MODULAR APPROACH TO
FUNCTIONALIZATION OF SURFACES**

A dissertation submitted to the

ETH ZURICH

for the degree of
Doctor of Science
Dr. sc. ETH Zürich

presented by
CHRISTOPH KARL KILIAN MAYER
Dipl. chem., University of Regensburg
born September 27th, 1980
citizen of Germany

accepted on the recommendation of

Prof. Dr. N. D. Spencer
Prof. Dr. S. S. Perry
Dr. S. G. P. Tosatti
Dr. S. Zürcher

2011

For my Family

“Science is like sex: sometimes something useful comes out,
but that is not the reason we are doing it. ”

R. P. Feynman

Abstract

The aim of this PhD project was the development of different surface-active, *graft*-copolymers, capable of adsorbing on surfaces, and the subsequent formation of polymer brushes. The synthetic route chosen was based on a modular approach that allows easy modification of the polymer structure during synthesis. Starting from a reactive polymer, the grafting of desired functionalities onto the backbone polymer, namely surface anchor and polymeric side-chains resulting in a *graft*-copolymer, were investigated.

The focus was placed on *graft*-copolymers bearing two different functionalities: a phosphonate surface anchor, capable of binding to a number of different oxide surfaces, and polymer side-chains, assumed to form a polymer brush after adsorption. For synthesis, the nucleophilic ring-opening reaction of maleic anhydride with amines and alcohols was studied. Different polymers were developed, characterized and applied to surfaces in order to study the formation of brush-like adlayers under different conditions.

In a first polymer generation, polyethylene glycol (PEG) side-chains were used to develop a new polymeric system that renders a surface non-fouling, which can be used for biomedical applications, e.g. for implant surfaces. Non-fouling surfaces suppress undesirable, unspecific biomolecular adsorption. This is important for implant materials, where the first step of the so-called foreign-body reaction consists of the adsorption of proteins onto the implant surface. This reaction can be retarded or even suppressed when using PEG-ylated surfaces. Polymers, differing in the grafting density of phosphonate surface anchor, PEG chains and backfiller (to guarantee full reaction of all anhydride rings) were synthesized using the polymer backbone poly(isobutylene-alt-maleic anhydride) and terminal amines as nucleophiles.

The adsorption of these polymers onto titanium dioxide and magnesium oxide/yttrium oxide model surfaces was investigated and the polymers characterized on the surface by X-ray photoelectron spectroscopy (XPS).

For titanium oxide surfaces, a full characterization of the surface adsorption was performed, using *ex situ* and *in situ* measurements, such as variable angle spec-

troscopic ellipsometry (VASE), transmission interference adsorption sensor (TInAS) and XPS. After investigation of the adsorption parameters, the chemical composition of the polymers on the surface was compared with the bulk chemical composition. The same grafting density was derived, being exactly the expected grafting density, as used during polymer synthesis. However, a slight reduction in the effective grafting ratio was observed when reaching higher grafting densities, where steric hindrance gains influence. Additionally the structure of the polymer at the surface was investigated by angle-resolved XPS, confirming the adsorption of the polymer as a monolayer with the phosphonate group responsible for surface-binding and the PEG chains forming the outermost part of the surface-bound polymer. The adsorption mechanism and kinetics of the polymers were investigated by TInAS, VASE and light-scattering methods. It seems to be an adsorption mechanism involving micellar aggregates present in the adsorption solution. The adlayer thickness was investigated *in situ* and *ex situ* with different methods, including VASE, TInAS and AR-XPS to derive a “dry” layer thickness, assuming collapsed side chains. A “swollen” layer thickness was investigated, assuming a swollen brush regime in contact to the solvent. This was performed using a quartz crystal microbalance with dissipation monitoring (QCM-D). The non-fouling properties were investigated by adsorption studies of full human serum onto the polymer brush and the biological performance of the polymers was connected to the findings of the protein adsorption studies by performing preliminary cell tests. Additionally, the stability of the polymer against desorption at different pH values was investigated and compared to other polymers. It was found to be more stable against desorption than the reference polymers.

In a second generation, poly(1,2-butylene glycol) monobutylether (PBG) side chains were used to develop a new polymeric system that can be used as an oil-soluble polymer additive to lower friction, e.g. in motor oils. Surface-active compounds normally act as friction modifiers in the mixed and boundary lubrication regime, where slow sliding speeds and high loads are predominant and thus high friction and wear rates are observed. In order to render the polymer oil soluble, poly(1,2-butylene glycol) PBG side chains were grafted and the backbone poly(octadecene-alt-maleic anhydride), which consists of hexadecane side-chains in every repetition unit, were chosen. This time, the ring-opening of the anhydride ring with the polyether side chain was performed by the free hydroxyl group present at the chain-end of the PBG. Due to the lower reactivity of the alcohol functionality, the reaction was not quantitative, resulting in relatively low grafting densities for the polyether side-chain. The composition at the surface was investigated with XPS on titanium dioxide and 100Cr6 steel surfaces. Furthermore, the “dry” and “swollen” layer thickness was measured on titanium oxide surfaces. The performance of the polymer as a boundary lubricant was studied in poly(alpha-olefin) and diisotridecyl adipate (DITA). Pin-on-

disk measurements were performed under static load/varying speeds and at constant speed/cyclic loads. The polymer additive shows a reduction in the friction coefficient at low speeds and therefore acts as boundary lubricant. Additionally, less wear was observed for the polymer additive after the tribotests. That effect could be explained by a drastic reduction of the adhesion between contacting oxide surfaces that were coated with the polymer. This reduction in adhesion was proven by force-distance measurements using a colloidal probe AFM. Stribeck curves under different loads and slide-roll ratios were acquired using a Mini Traction Machine and PAO and DITA as base oils. The polymer additive showed a reduction of the traction coefficient in both base oils, but was better performing in PAO. In DITA, the polymer additive was compared to stearic acid as a boundary lubricant. Stearic acid showed comparable results in DITA for low loads and low slide-roll ratios. At high loads and higher slide-roll ratios, no visible improvement compared to the base oil could be observed.

Zusammenfassung

Ziel dieser Doktorarbeit war die Entwicklung verschiedener oberflächenaktiver *graft*-Kopolymere, die auf Oberflächen adsorbieren und dadurch Polymerbürsten an der Oberfläche bilden können. Die gewählte Synthesestrategie basiert auf einem modularen Ansatz, um Modifikationen an der Polymerstruktur während der Synthese zu vereinfachen. Die Kopplungsreaktionen einer reaktiven Polymerhauptkette mit Oberflächenanker und Polymerseitenketten wurde untersucht. Im Fokus standen *graft*-Kopolymere mit zwei verschiedenen Funktionalitäten: ein Phosphonat-Oberflächenanker, der die Bindung zu einer Vielzahl von Oxidoberflächen ermöglicht und eine Polymerseitenkette, die eine Polymerbürste nach der Adsorption an der Oberfläche formen soll.

Als Syntheseweg wurde die nukleophile Ringöffnungsreaktion von Maleinsäureanhydriden mit primären Aminen und Alkoholen benutzt. Verschiedene Polymere wurden entwickelt, charakterisiert und auf die Oberfläche aufgebracht, um die Entstehung der büstenartigen Adsorptionsschicht unter verschiedenen Bedingungen zu untersuchen.

In einer ersten Polymergeneration wurden Polyethylenglykol (PEG) Seitenketten verwendet. Diese büstenartigen PEG-Seitenketten bilden eine bio-inerte Oberfläche, welche unspezifische, biomolekulare Adsorption unterbinden kann. Dieses Konzept kann für biomedizinische Anwendungen, z.B. für Implantatoberflächen verwendet werden, die teilweise vom Körper als Fremdstoffe erkannt und abgestossen werden. Die bio-inerten Oberflächen können diese Fremdkörperreaktion verzögern oder gänzlich unterbinden, da sie die Adsorption von Proteinen an die Implantatoberfläche unterbinden.

Basierend auf der Polymerhauptkette poly(Isobutylene-alt-Maleinsäureanhydrid) und primären Aminen als Nukleophil wurden Polymere mit verschiedenen Pfropfdichten an Phosphonatanker, PEG-Kette und Füllmoleküll (um eine vollständige Reaktion aller Anhydridringe sicherzustellen) synthetisiert. Das Adsorptionsverhalten dieser Polymere wurde an Titandioxid und Magnesiumoxid/ Yttriumoxid Modelloberflächen untersucht und die Adsorptionsschicht nachfolgend durch Röntgen-Photoelektronenspektroskopie (XPS) charakterisiert. Eine vollständige Charakterisierung

der Oberflächenadsorption dieser Polymere mittels verschiedener *ex situ* und *in situ* Messungen, wie z.B. Spektrellipsometrie (VASE), Transmissionsinterferenz-Adsorptionssensorik (TInAS) und XPS, an Titandioxidoberflächen durchgeführt. Nach der Untersuchung der Adsorptionsparameter wurde die chemische Zusammensetzung der Polymere an der Oberfläche mit der Zusammensetzung in Lösung verglichen. Beide weisen eine gleiche Zusammensetzung auf, die ebenfalls genau mit der aus der Synthese zu erwartenden Pfropfdichte übereinstimmt. Zusätzlich wurde die Struktur des Polymers an der Oberfläche mittels winkelaufgelöster XPS (AR-XPS) untersucht, welche die Adsorption des Polymers als Monolage mit oberflächengebundenen Phosphonaten und aussenliegenden PEG-Ketten bestätigt. Der Adsorptionsmechanismus und die Adsorptionskinetiken der Polymere wurden mit Hilfe von TInAS, VASE und Lichtstreuungsmethoden untersucht. Es scheint ein Adsorptionsmechanismus unter Beteiligung von mizellartigen Polymeraggregaten aus der Polymerlösung vorzuliegen. Die Dicke der Monolage wurde mittels verschiedener *ex-situ*- und *in-situ*-Methoden untersucht. Sowohl eine "trockene" Schichtdicke, die kollabierete PEG-Ketten annimmt (VASE, TInAS und AR-XPS), als auch eine "geschwollene" Schichtdicke, die eine geschwollene Bürstenanordnung der Polymerketten im Kontakt zum Lösungsmittel annimmt (Quarkristall-Mikrowägung mit Dissipationsmessung) wurde bestimmt. Die proteinresistenten Eigenschaften wurden durch Adsorptionsstudien von menschlichem Serum an die oberflächengebundenen PEG-Bürsten bestimmt. Die Resultate dieser Studien wurden mit der biologische Wirksamkeit dieser Polymere in Zelltests verglichen. Zusätzlich wurde die Stabilität des Polymers gegen Desorption bei verschiedenen pH-Werten untersucht und mit anderen Polymeren verglichen. Es stellte sich heraus, dass die in dieser Arbeit untersuchten *graft*-Kopolymere viel stabiler gegen allmähliche Desorption sind als die Vergleichspolymere.

In einer zweiten Polymergeneration wurden Poly(1,2-Butylenglykol)-Monobutylether (PBG) Seitenketten verwendet um ein neues Polymersystem zu entwickeln, das als Additiv z.B. in Motorenölen eingesetzt werden kann, um die bei Betrieb entstehende Reibung zu vermindern. Oberflächenaktive Verbindungen beeinflussen normalerweise Reibung im Misch- oder Grenzbereich der Schmierung, d.h. in Bereichen niedriger Gleitgeschwindigkeiten und hoher Last, die mit grosser Reibung und hohem Abrieb und Verschleiss einhergehen. Damit das Polymer vollständig in Öl löslich ist, wurden PBG-Seitenketten an die Polymerhauptkette Poly(Oktadezen-alt-Maleinsäureanhydrid) gepfropft. Dieses enthält zusätzlich Hexadekan-Seitenketten an jeder Wiederholungseinheit. Diesmal wurde die Pfropfreaktion durch die terminale Hydroxylgruppe an einem Kettenenden von PBG durchgeführt. Durch die niedrigere Reaktivität der Alkoholfunktion konnte die Reaktion nicht quantitativ durchgeführt werden, weshalb verhältnismässig niedrige Pfropfdichten der Polyether-Seitenkette erhalten wurden. Die Oberflächenzusammensetzung wurde durch XPS an Titandi-

oxid und an Stahl ermittelt. Zusätzlich wurde die Dicke der “trockenen” und “geschwollenen” Monolage an Titandioxidschichten bestimmt. Die Leistungsfähigkeit des Polymers als Schmierstoffadditiv wurde in poly(α -olefin) und in Diisotrizezyladipinat untersucht. Tribologische Versuche mittels Stift-Scheibe Apparatur unter statischer Last / variierender Geschwindigkeit und unter konstanter Geschwindigkeit / zyklischer Last wurden durchgeführt. Die Polymeradditive zeigen eine Reduktion des Reibungskoeffizienten, besonders bei langsamen Geschwindigkeiten und wirken deshalb wie gewollt als Schmierstoff im tribologischen Grenzbereich. Zusätzlich wurde weniger Verschleiss nach den Tribotests mit Polymeradditiv festgestellt. Dieser positive Effekt konnte durch die drastische Reduktion der Adhesion zwischen sich berührenden Oxidschichten erklärt werden, wenn diese mit Polymer beschichtet waren. Diese Adhensionsreduktion wurde durch Kraft-Distanz-Messung mit einem Kolloidproben-Rasterkraftmikroskop bestätigt. Stribeckkurven mit und ohne Polymeradditiv wurden unter verschiedener Last und verschiedenen Gleit-Roll-Verhältnissen (SRR) einer Mini-Traktionsmaschine in PAO und DITA aufgenommen. Das Polymeradditiv zeigt eine signifikante Reduktion im Traktionskoeffizienten in beiden Ölsorten, war jedoch leistungsfähiger in PAO. Das Polymeradditiv konnte mit Stearinsäure als Schmiermitteladditiv für den tribologischen Genzbereich in DITA verglichen werden. Für Bereiche geringer Last und geringer SRR zeigen beide Additive vergleichbare Resultate, In Bereichen hoher Last und hohen SRR zeigte das Polymeradditiv eine signifikante Reduktion des Reibungskoeffizienten, wohingegen für Stearinsäure als Additiv unter diesen Bedingungen keine sichtbare Verbesserung mehr im Vergleich zum Basisöl nachgewiesen werden konnte.

Acknowledgements

During my time at ETH I met many great people, who helped and assisted me and I want to thank all of them for their influence in this part of my life.

Professor Dr. Nicholas Spencer gave me the opportunity to do my PhD in his group. I appreciate all the work and time he invested in my PhD project by supporting me with scientific discussions and professional advice and more generally with his great support, helping to make my scientific work successful.

Dr. Samuele Tosatti and Dr. Stefan Zürcher were my direct supervisors. The combination of their personal deep knowledge in chemistry and materials science was always a great source of input and new ideas for my projects. They always took their times to support and motivate me with personal and scientific advice on my thesis and its organization.

In our research group, there are a lot of members with specific knowledge and experience in instruments and measurements and I appreciate a lot all the interesting discussions and support I got from each member of our group, especially I want to name Filippo (XPS, tribology and profilometry), Maura (XPS and tribology), Tobias (TInAS), Shiva (AFM) and Torben, the best lab mate and friend! Mentioning Torben leads to the other aspect of our group, the social life and the great atmosphere which characterizes it. This great working atmosphere, resulting in a lot of off-science activities (ski-weekends, off-site meetings with social activities, parties, fondue, barbecue, rafting, ...) has been even scientifically approved¹ and I wanted to thank every member of the group for their contribution of the social group life. Special thanks goes to all members of the E-floor office (Doris, Eva, Maura, Filippo, Karthik, Stefan, Fäbu, Torben, Raphi, Pipit, Shiva, Ang, Prathima, Ciccio,), we had a lot of fun together! I want to mention the great administrative work Josephine is doing to keep the group running!

A lot of people were involved in project cooperations and I want to thank them all here for their fruitful help and discussions. Dr. Isabel Gerber for cell testings, Dr.

¹AF Gilbert, "Disciplinary cultures in mechanical engineering and materials science", Equal Opportunities International (2009), 24–35.

Patrik Schmutz and Dr. Alessandra Beni from EMPA for their support with the EIS measurements, Prof. Dr. Peter Uggowitzer and the members of his research group, especially Dr. Anja Hänzi, Dr. Petra Gunde and Michael Schinhammer for all their knowledge and support on magnesium alloys and the preparation of the samples. Prof. Dr. Tomoko Hirayama was supporting me in the measurement, interpretation and analysis of the Neutron Scattering experiments. Dr. Rowena Crockett was kindly giving me access to the MTM present in her labs at EMPA. Dr. Marco Latuada (D-CHAB) was helping me with some specialized field flow fractionation measurements and Sreenath Bolisetti (D-HEST) was giving me access to the static light scattering instrument. The PhD students of the Zenobi-Group, mainly Stefan Fagerer and Dr. Stefanie Mädler were making a lot of efforts in order to characterize my polymers by Maldi-TOF measurements with the research instruments present in their group. Furthermore I want to thank my two master students Henrik and Christoph, as well as my semester student Robert. It was a great pleasure to work with all of you together!

There are many people doing measurement service for special instruments in the chemical and material science department. Especially I want to thank Doris Sutter (NMR), Martin Colussi (GPC) and Thomas Schweizer (TGA) and all the members from the MALDI-TOF service and elemental analysis service.

I want to gratefully thank the Competence Center for Materials Science and Technology (CCMX) for the funding of my research within the interdisciplinary project "Bio-functionalized, bio-degradable, nano-structured magnesium implant for biomedical applications" and BP for the funding of my second PhD project investigating oil lubrication properties of hydrophobic surface brushes.

Last but not least I want to direct my gratitude towards my family. Having moved a lot during my studies, it was great to have the continuous support and motivation of all members of my family, starting by my parents and my brother and sister. They were always with me and just a phonecall away when I felt lonely or I needed somebody to talk to. Luckily I have some cousins - Michael, Thomas and Andreas - living in Zurich. They helped me a lot during my start in Zurich. Especially they allowed me to live in their guest rooms during the really difficult search for a flat, but as well due to their support and motivation during the plenty beers we drank in the evenings or during the regular visits of one of our uncles, my thesis would not have been possible.

Finally I want to thank Soledad and Monika for their understanding and patience they showed during the great times we had together and all the support and balance they gave me! Loads of wonderful memories and the influence of both will always accompany my future life!

Contents

Contents	xi
1 Introduction	3
1.1 Polymers in Solution	3
1.2 Polymer Brushes	5
1.3 Functionalization of Surfaces by Polymer Brushes	9
1.3.1 Grafting-from Approach	9
1.3.2 Grafting-to Approach	10
1.4 Advantages of Graft-Copolymers for the Creation of Polymer brushes	18
1.5 Reference graft-copolymer systems	20
1.5.1 PLL-g-PEG and derivatives	21
1.5.2 Poly(phosphonate)s	23
1.6 Aim and Objective of the Thesis	24
2 Synthesis and bulk Characterization of poly(alkyl phosphonates)	27
2.1 Introduction	27
2.2 The reactive backbone	29
2.3 IR Investigation of the reaction possibilities of maleic anhydride containing polymers	33
2.4 Synthesis strategy	37
2.5 Polymer Nomenclature	41
2.6 Hydrophilic Polymer characterization	42
2.6.1 Characterization of the chemical composition and chemical structure	42
2.6.2 Determination of the molecular weight	49
2.6.3 Determination of the aggregation behavior by DLS and SLS	51
2.7 Acid-base character of the polymers synthesized	54
2.8 Hydrophobic polymer characterization	56
2.8.1 Characterization of the chemical composition and chemical structure	56

2.9	Experimental Synthesis protocols of the polymers synthesized	60
2.9.1	Synthesis of 1,12-aminododecylphosphonic acid diethylester	60
2.9.2	Synthesis of hydrophilic polymers	64
2.9.3	Synthesis of hydrophobic polymers	66
2.9.4	Overview over all polymers synthesized	67
3	Poly(phosphonates) on TiO₂ for biomedical applications	69
3.1	Motivation / Introduction	69
3.1.1	Biomaterials	69
3.1.2	PEG-ylated molecules and protein resistance	71
3.2	Surface Aspects and Applications of Titanium and Titania	72
3.3	TiO ₂ Substrates	75
3.4	Characterization of additional poly(alkyl-phosphonate) adlayers on titanium substrates	78
3.4.1	Adsorption Parameters	78
3.4.2	Chemical Composition of Polymer Adlayers on TiO ₂ based on XPS Results	88
3.4.3	Conformation and Structure of the Polymer Adlayer on TiO ₂ based on AR-XPS results	100
3.4.4	Characterization and Study of Adlayer Thicknesses	105
3.5	Non-fouling properties and biological performance of poly(alkyl-phosphonate) coatings	108
3.6	Stability of poly(alkyl-phosphonate) coatings in aqueous media	112
3.7	Conclusions	116
4	Poly(phosphonates) on MgO for biomedical applications	119
4.1	Motivation/Introduction	119
4.2	Surface Aspects and Applications of Magnesium and Magnesia	121
4.3	WE43 Substrates	125
4.4	Characterization of the Magnesium surfaces	131
4.4.1	Metallurgic characterization	131
4.4.2	XPS surface characterization	135
4.4.3	XPS depth profiling	139
4.4.4	Development of a cleaning protocol	141
4.5	Characterization of additional organic adlayers on magnesium substrates	146
4.5.1	Dodecylphosphate SAMs	146
4.5.2	Surface functionalization by means of poly(alkylphosphonate)s	149
4.6	Corrosion Investigation by Electrochemical Impedance Spectroscopy	152
4.6.1	Conclusions	158

5	Poly(phosphonates) for lubricant applications on Steel	161
5.1	Introduction to Friction and Tribology	161
5.1.1	General	161
5.1.2	Friction	162
5.1.3	Wear	163
5.1.4	Lubrication	164
5.2	Surface Properties and Applications of Steel	169
5.3	Motivation	170
5.4	Steel substrates	171
5.5	Polymer Characterization	173
5.5.1	XPS Characterization of hydrophobic polymer on Titanium oxide	173
5.5.2	XPS Characterization of hydrophobic polymer on steel	177
5.5.3	Dry and swollen layer thickness	178
5.6	Polymer additive for lubrication	180
5.6.1	Calculation of the lubrication regime	180
5.6.2	Pin-on-disk Measurements	182
5.6.3	Mini Traction Machine	188
5.7	Conclusions	196
6	Conclusion and Outlook	199
6.1	Conclusion	199
6.1.1	Synthesis	199
6.1.2	Hydrophilic polymers	200
6.1.3	Hydrophobic polymers	202
6.2	Outlook	202
6.2.1	Synthesis	202
6.2.2	Hydrophilic polymers	203
6.2.3	Hydrophobic polymers	204
7	Materials, Methods and General Protocols	207
7.1	Bulk characterization methods	207
7.1.1	Nuclear Magnetic Resonance (NMR)	207
7.1.2	Elemental Analysis	211
7.1.3	IR Spectroscopy	212
7.1.4	Light scattering	215
7.2	Surface Characterization Techniques	220
7.2.1	Variable-Angle Spectroscopic Ellipsometry	220
7.2.2	X-Ray Photoelectron Spectroscopy (XPS)	223
7.2.3	Transmission Interference Adsorption Sensor (TInAS)	233

7.2.4	Quartz Crystal Microbalance with Dissipation Monitoring (QCM-D)	236
7.2.5	Optical Profilometry	237
7.2.6	Neutron Reflectometry	240
7.2.7	Atomic force microscopy (AFM)	244
7.3	Tribological tests	247
7.3.1	Pin-on-disk Tribometer	247
7.3.2	Mini Traction Machine	253
7.4	Corrosion tests	255
7.4.1	Electrochemical Impedance Spectroscopy (EIS)	255
7.5	Cell tests	260
7.6	Chemicals and Solvents for Surface Modification	261
7.7	Buffers	261
7.7.1	PBS	262
7.7.2	SBF-27	263
7.7.3	HEPES-2	263
7.8	Substrates	264
7.9	General Protocols	265
7.9.1	Glassware and tools cleaning	265
7.9.2	Substrate cleaning before adsorption	265
7.9.3	Adsorption of amphiphilic adlayers	267
7.9.4	Adsorption of serum to metal oxide surfaces	268
Bibliography		271
A Appendix		299
A.1	GPC spectrum of the polymer backbone PIMA	299
A.2	NMR spectra of the polymers synthesized	301
A.3	Concentration dependence of refractive index of the polymer	303
A.4	XPS peak analysis of heat-treated WE43	305
A.4.1	Bare WE43	305
A.4.2	WE43 Surface Cleaning	305
A.4.3	DDPO4 Surface Functionalization	307
Appendices		297
B Curriculum Vitae		309

Introduction

1.1 Polymers in Solution

Polymers, a type of macromolecule, can be synthetic or natural. They can form simple linear chains or more complex structures such as branched polymers, star molecules, dendrimers, hyperbranched polymers or even cross-linked polymer networks. In dilute solution, polymer shape is determined by its molecular or macroconformation, depending on the type, proportion and sequence of the chemical constitution and polymer configuration, as well as the solvent and the environment [1,2]. These effects can be summarized by the term microconformation, which describes the conformation of smaller parts of the polymer. These include free rotation around single bonds, which changes the torsional angle (cis, trans, gauche, anti), as well as steric interactions and therefore chain flexibility. The macroconformation consists of combined arrangements of these microconformations. However, strong interactions, such as hydrogen bonding or π - π interactions between adjacent or neighboring units and an ordering of solvent molecules may impose a certain order on dissolved polymers [1,2].

In biochemistry, when talking about proteins and biopolymers, this effect is defined by the term “secondary structure”. These substructures can be helical structures or crystalline-like structures. Microconformations and thus also the macroconformation are affected by the environment, such as temperature, pressure or the interaction with the solvent. In random distributions of microconformations, environmental changes only induce small changes in the macroconformation. Very large changes can occur upon environmental change in polymers with long, regular sequences of microconformations, as found in helices. The more complex the polymeric structure is, the more difficult the macroconformation can become. The easiest model is for linear chains, which are often described as random coils and correspond to very loose balls of intertwined wires [1, 2]. Short-range interactions are interactions within one segment of the polymer, whereas long-range interactions are interactions between spatially separated segments of the same polymer chain. These interactions can be attractive or repulsive. However, this leads to an internal excluded volume inside the chain, which determines the space required by the atoms of that chain segment, including those set by the interaction forces. These intramolecular interactions determine the shape of the coil. Large amounts of internal excluded volume expand the coil, which therefore becomes perturbed. When attractive and repulsive long-range interactions are equal, the coil is unperturbed. Polymers forming random coils can be characterized by their end-to-end distance and the radius of gyration. The end-to-end distance describes the theoretical spatial distance between two ends of the linear chain, while the radius of gyration provides an experimentally accessible, averaged value for the coil dimensions that is not limited to only linear polymers [1, 2].

This summary of the factors that determine the macroconformation of a polymer in solution is only true in highly diluted solutions, where the interaction of neighboring chains is not present. In concentrated solutions, all intramolecular interactions apply as well as intermolecular interactions, leading to attractive and repulsive forces

between segments of different polymer chains, and therefore contribute to an external excluded volume of each polymer coil. These factors can induce a change in the macroconformation of the polymer, but can also lead to interaction, agglomeration or even self-assembly of the polymers in solution.

1.2 Polymer Brushes

When a surface is in contact to a polymer solution, two different scenarios are possible: the polymer-surface interaction is not favorable and the polymers will stay unaffected in solution, or alternatively in case of strong, attractive interactions between the polymer chain and the surface, the polymer will adsorb to the surface. The same possibilities can occur when attaching the polymer chains with one of their end-groups to a surface. With a strong attractive interaction between the polymer chain and the surface, the polymer will adsorb flat on the surface, resulting in the so called “pancake” conformation. In case of the chain having no affinity to the surface, apart from the end functionality, the polymer chain will display a “mushroom” conformation at the surface. This conformation is basically a random coil with one chain end attached to the surface. Therefore, the conformation of the chain remains close to what it would have been in dilute solution, since only the microconformation at one chain-end is affected.

In the most general way, polymer brushes can be defined as polymer chains, end-grafted to a supporting surface or interface [3,4] and would correspond to the situation as described above. If the polymers attached to the surface have a separation that is larger than their radius of gyration, no polymer-polymer interaction is taking place. As the size of grafted polymer chains approaches the distance between grafting points, the grafted chains start to mutually overlap and the effects presented in Sect.

1.1 for concentrated polymer solutions become predominant. Polymer-polymer interactions take place, yielding in an external excluded volume of the polymer chains. The individual chains are changing their conformations and start to stretch away from the surface, driven by a balance between excluded volume interaction, free energy of the segments, loss of conformational entropy upon stretching and the elastic free energy of the chain. In this way, a so-called “brush” conformation of the polymers is formed. A more specific definition for polymer brushes is tethered polymer chains, which extend unidirectionally, normal to the grafted surface. They can therefore reach a much farther distance from the surface than the typical unconstrained size of a comparable chain. The strong interactions between the polymer chains therefore dominate their behavior and the polymer chains and the properties of the brush. The tethered polymer chains thus correspond to an array of macromolecular chains attached to a surface in such a high density, that the intermolecular interactions are influencing the conformation in a good solvent. Additionally, this close proximity between the chains leads to steric effects of adjacent chains and thus significantly influences the conformation of individual polymer chains by extension of the chains or alteration of the normal radius of gyration in order to avoid unfavorable interactions [3, 4]. This results in much different properties compared to those normally observed in solution. Properties that are significantly different from the properties these chains normally show in solution can be the subsequent result [3–5].

The different states of tethered polymer chains are illustrated in Fig. 1.1. Surface immobilized polymers need well-defined parameters that help to characterize the tethered chains. Normally, the inverse value of the distance D between grafting points is used to characterize the grafting density σ , either by the simple formula $\sigma = 1/D^2$ [6], but also the height of the polymer brush and intrinsic, characteristic parameters of the polymer (M_n, ρ) can be used to calculate the grafting density $\sigma = (h \cdot \rho \cdot N_A) / M_n$ [3]. A quantitative characterization of the transition from mushroom to brush regime

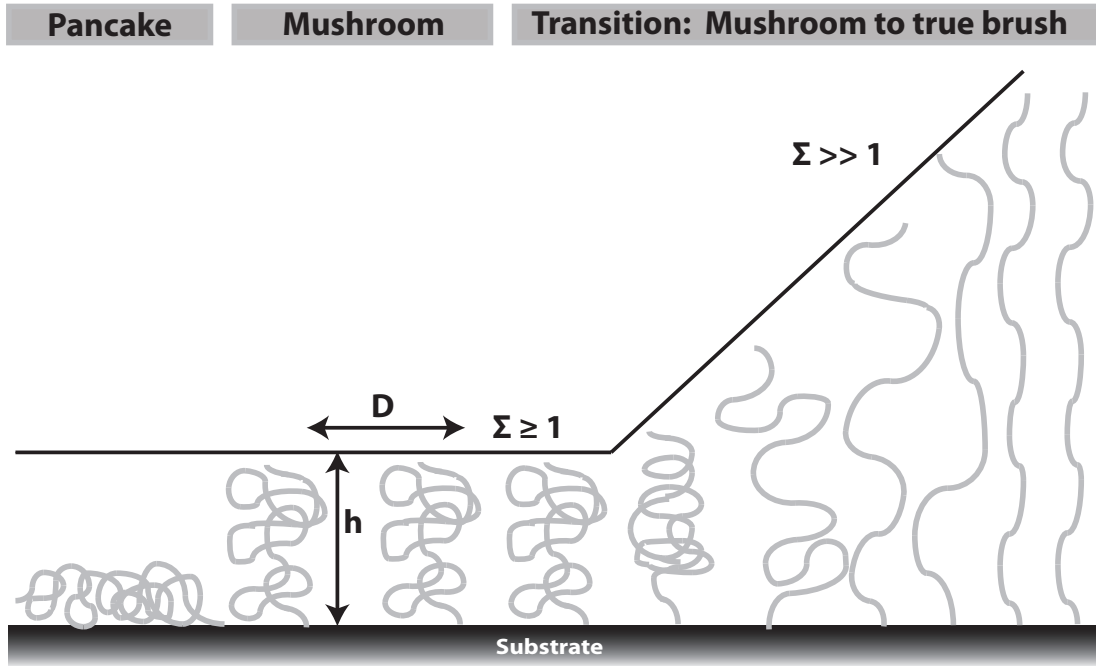


Figure 1.1: Different conformations of polymers at surfaces: pancake conformation of a single adsorbed chain, occurring when there is strong attraction between the surface and the chain monomers and the continuous transition between the mushroom regime and true brush regime. Film thickness h and distance D between grafting points are defined [3].

can be achieved by defining the reduced tethered density $\Sigma = \sigma \cdot \pi \cdot R_g$, where R_g is the radius of gyration of a tethered chain at the specific experimental conditions (solvent, temperature, salt concentration, ...), h the brush thickness, ρ the bulk density of the brush composition and N_A is Avogadro's number. The physical interpretation of Σ is the number of stretched chains that occupy an area at the surface that normally one free, non-overlapping polymer chain would fill under the same experimental conditions. The pancake conformation cannot be described by this model due to the different attachment mechanism driven by strong interactions between chains and surface. However, three different regimes can be defined by different Σ values. $\Sigma < 1$ characterizes the mushroom regime, where the chains do not interact due to their large separation. The transition between mushroom and stretched brush

regime begins at by $\Sigma \gtrsim 1$, where the separated mushrooms start to interact slightly. Nevertheless, the true, highly stretched brush regime is normally characterized by higher numbers of $\Sigma > 5$, but the exact value is strongly affected by the excluded volume of the polymer and varies strongly, depending on the system [3,4].

Polymer brushes began to attract attention in 1950s when it was found that grafting of polymer molecules onto colloidal particles was a very effective way to prevent flocculation and agglomeration of the particles due to the repulsive steric forces between approaching brushes [7]. The novel properties of polymer brushes were mainly depending on the properties (hydrophilic - hydrophobic, ionic - anionic,) introduced by different polymer chains. Subsequently it was found that some of these properties could be as well achieved by interfacial insertion of different terminal groups at the same type of polymer [5, 8, 9]. Polymer brushes can be useful in different applications such as new adhesive materials and polymer compatibilizers [10, 11], cell adhesion, biomaterials and protein resistant surfaces [12–14], lubrication [10, 15, 16], protein analysis and purification [17], molecular recognition and sensors [18], and even nanorobotics [19]. A new field opened with the development of stimuli-responsive polymer chains. Polymer brushes of thermo-responsive polymers possessing a low critical solution temperature (LCST) and thus showing different wetting properties above and below the LCS temperature have been extensively investigated [20, 21]. This field was further highly exploited with polymer brushes having pH sensitivity, photosensitivity or oxireductive sensitivity [22–28]. Patterned polymer brushes already attracted attention for application in microelectronics, cell growth, biomimetic

material fabrication and drug delivery [29,30].

1.3 Functionalization of Surfaces by Polymer Brushes

There exist a huge variety of different approaches to attaching polymers or molecules to surfaces, taking advantage of different physico-chemical or chemical possibilities of surface attachment. A simplified overview over these possibilities is presented in Fig. 1.2. There are two different general methods for covering a surface with polymers :

grafting-to: Molecules and polymers can adsorb actively to surfaces via physisorption, chemisorption or covalent interaction.

grafting-from: a surface either covered with an initiator or by direct activation acts as a template for surface-initiated polymerization reactions

1.3.1 Grafting-from Approach

The grafting-from procedure involves surface-bound initiators for polymerization reactions with the monomers present in the solution [31]. Most of the standard polymerization reactions are compatible with the grafting-from concept, including free radical, ionic and living/controlled polymerization, such as Atom Transfer Radical Polymerization (ATRP) or Reversible Addition Fragmentation Chain Transfer Polymerization (RAFT) [32]. Nevertheless, the polymerization procedure can lead to relatively thick polymer layers in the micrometer range. Normally the polydispersity is slightly higher than under comparable bulk polymerization reactions [32]. This can be attributed to the increasing density of the surface brush with raising chain lengths. Polymer chains, which entangle within other chains are trapped inside the growing

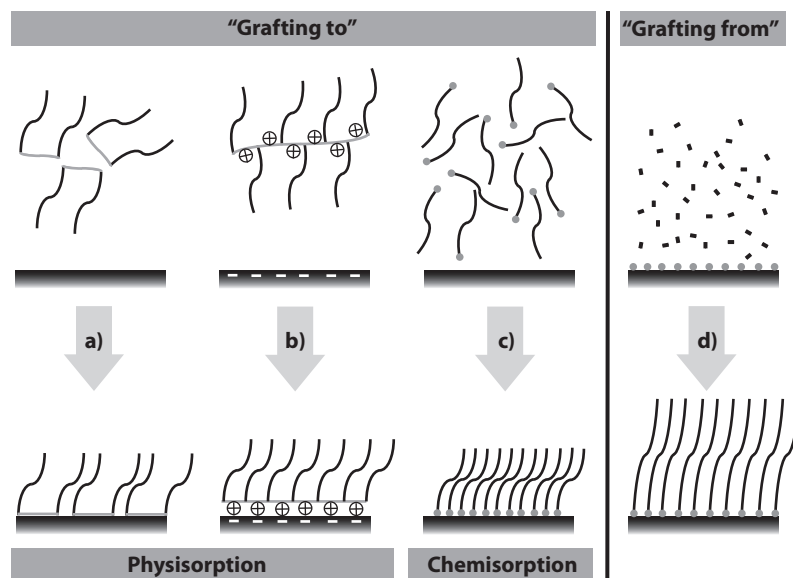


Figure 1.2: Different ways of immobilizing polymers on a surface via “grafting-to” by physisorption via a) hydrophobic or b) electrostatic interactions, c) chemisorption and d) “grafting-from”

surface brush. There, the reaction rate may be lower due to steric interactions, but also due to a limited diffusion of monomers inside the polymer brush. Another approach to grafting from, is via plasma activation of the surface [33,34]. Because of the surface-bound nature of the polymer chains in a brush, they are substantially more difficult to characterize than polymers synthesized in bulk.

1.3.2 Grafting-to Approach

The grafting-to approach can be further classified into several different adsorption mechanisms, which are illustrated in Fig. 1.2.

Physisorption

All systems based on a rather weak polymer-surface interaction are summarized under the term physisorption. These systems often consist of an amphiphilic, surfactant-type structure, containing a hydrophilic part and a hydrophobic tail. The hydrophobic interactions are thus the main driving force for surface adsorption for some of these adsorption mechanisms:

Block polymers with at least 2 different block types physisorb to a surface especially by solvent effects. A selective solvent is only a good solvent for one of the blocks, whereas it is a bad solvent or even a precipitant for the other block. This is the main driving force for surface adsorption: it is energetically more favorable for the poorly dissolved block to interact with the surface and minimize therefore the contact with the solvent. This situation is comparable to the “pancake” conformation explained above. The fraction of the polymer which is well soluble stays in solution and thus points out into the solution [35]. The most prominent example in this category is certainly the triblock polymer poly(ethylene oxide)-poly(propylene oxide)-poly(ethylene oxide) (PEO-PPO-PEO, Pluronic[™]) [36]. In aqueous solutions, the hydrophobic PPO block adsorbs to the surface, while the well-soluble PEO chain points out into the solution.

Another well-established grafting-to approach is the pre-assembly of surfactants at a liquid-air interphase (Langmuir-film), e.g. with a Langmuir-trough, and subsequent deposition of the well-assembled monolayer film onto a substrate, either as a homogeneous monolayer (crossing the interphase once with the substrate by immersion or emersion) or as a multilayer by crossing the interphase multiple times with the substrate (Langmuir-Blodgett) [7, 37–39].

Another adsorption mechanism can be found for polyelectrolytes, charged polymers, that can spontaneously adsorb from solutions to oppositely charged surfaces by mul-

multiple electrostatic interactions. The stability of these spontaneously adsorbing thin films is (due to the electrostatic interaction) much higher than for the previously described physisorption methods, but is limited and depends strongly on the environmental conditions.

Polyelectrolytes

Polyelectrolytes are macromolecules carrying covalently bound anionic or cationic groups, and low-molecular-weight “counterions” ensuring electroneutrality [40]. There are many different classes and types of polyelectrolytes, including natural polymers, such as anionic and cationic polysaccharides (e.g. starch), nucleic acids and gelatin, but also many kinds of non-natural polymers, such as poly(meth)acrylic acid and its derivatives as well as polyethylene imines among others [40]. The most frequently used structures of polyelectrolytes are shown in Table 1.1.

Table 1.1: Structures of ionic sites of polyelectrolytes

negative charges	Example
carboxylic acids	poly(acrylic acid)
sulfates	poly(vinyl sulfate)
sulfonates	poly(styrene sulfonic acid)
phosphates	neutralized desoxyribonucleic acid
positive charges	Example
primary amines	poly(L-lysine)
Amides	Poly(acrylamide)
quarternary ammonium	poly(diallyl-dimethyl ammonium) chloride
heterocycles	poly(N-butyl pyridinium hydroxide)

Polyelectrolyte brushes or layers of polyelectrolytes tethered at solid-liquid interfaces due to the electrostatic attractions with countercharged surfaces, have attracted

considerable attention in many different applications such as flocculation of colloids, protection and modification of natural and artificial membranes, biological cells, vesicles and drug-delivery systems, etc. [40–45].

The polyelectrolyte adsorption mechanism can be thought of as a three-step process [43]:

1. transport from the bulk to the surface
2. attachment to the surface and
3. rearrangement

During all initial stages of adsorption, only steps 1 and 2 can generally be observed, whereas the rearrangement process is often rather slow. When all polymer chains arriving at the surface adsorb immediately, the adsorption rate is transport limited. As adsorption proceeds, the surface becomes increasingly covered with polymer and therefore the adsorption becomes hindered at a certain point. At this stage, the rate of adsorption depends mainly on the attachment process. This influence increases at even higher coverages, reaching a rate-limiting plateau value [42–45].

At an oppositely charged surface, these interactions favor a flat conformation [46], in which the segments are mainly situated in trains in such a way that the interaction between the segments and the surface is maximized and balanced by the chain entropy. When the surface charge is compensated by the polymer, the electrostatic attraction of the segments with the surface is additionally balanced by the repulsion in the adsorbed layer [42, 43]. This provides a flat deposition on oppositely charged surfaces and ensures both a full coverage of the surface and a high stability due to multiple electrostatic anchoring points [40–42]. Moreover the pH [47–51] and other environmental conditions such as the ionic strength [52–56], temperature, solvent, deposition time and polymer concentration [53, 57–59] have influence on both the

charge state and conformation of the polymer prior to physisorption and on the apparent surface charges [60]. Additionally, complete and uniform coverage also depends on a low surface roughness in comparison to the molecular dimensions of the assembly system [61]. All these parameters contribute to the resulting total amount of polymer adsorbed at the surface [40, 53, 57, 58, 62], and that variations of these parameters may result in modification or desorption of the adsorbed polymers.

Polyelectrolytes can be chemically modified prior to their adsorption with the aim of immobilizing some specific functions onto a surface (c.f. Fig. 1.3), but an optimization of the architecture, especially between the charge density and functionalization must be developed to obtain an efficient adlayer formation [52, 63, 64]. Indeed all named factors influencing physisorption properties and adsorption density, also influence the polymer conformation after attachment, as well as the polymer adlayer stability, quality and properties.

Generally speaking, especially in comparison to Self Assembled Monolayers (SAMs) described in the following paragraph, the polyelectrolyte system shows several advantages [40, 45, 62]:

- multipoint attachment provides higher stability against desorption
- multipoint attachment provides easy modification of the surface properties via different or even functional side-chains

The main disadvantage is the lower binding energy of electrostatic binding (single-charge interaction of the order of kT) [57, 59, 65] in comparison with chemisorption, resulting in more labile anchoring points, which are more susceptible to displacement, desorption and exchange with other surface-active compounds in comparison to the mostly irreversible chemical bonding in the case of SAMs [42, 43]. Additionally to the limited stability of polyelectrolyte-based assembly systems, the strong need for opti-

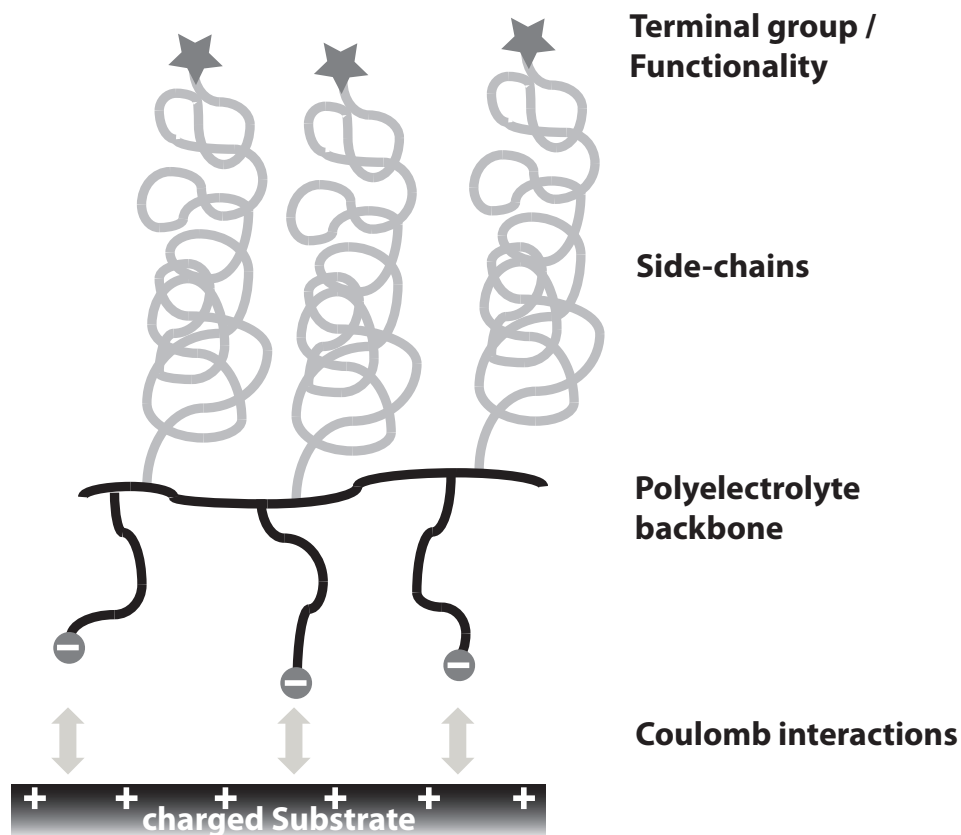


Figure 1.3: Adsorption of polyelectrolyte grafted with neutral side-chains

mization of such a great variety of parameters towards the maximum of adsorption density is a major drawback of this kind of adlayer system.

Self Assembled Monolayer (SAM)

SAMs are the most studied monomolecular adlayer systems for surface functionalization, due to their ease of synthesis and ability to be end-functionalized by different terminal groups. There exist many potential applications in various domains, such as corrosion science, catalysis, sensors and electronics [66–69]. A well defined and flexible model system is required for the investigation of the *in vitro* molecular behavior of biomolecules such as proteins and enzymes at biological interfaces, as well

as for the development of biocompatible surfaces. SAMs provide a powerful tool to generate monomolecular films on a huge variety of substrates [70–73] and also allow reliable control over the packing density [74, 75]. SAMs show advantages due to higher adhesion strength [73, 76–78], thermal [78, 79], chemical [78, 80] and mechanical stability [77, 78] in comparison with more traditional, physisorbed thin-films systems or organic films prepared by evaporation techniques, e.g. by organic molecular beam deposition [81]. Molecular order and stability of SAMs also arise from the inherent chemical structure [82], orientation and dense packing of molecules [75, 78]. The broad flexibility of SAMs, because of the wide choice of possible endgroups and surface anchors, has substantially influenced the field of surface chemistry and opened a new area for organic functionalization of well defined inorganic surfaces [83].

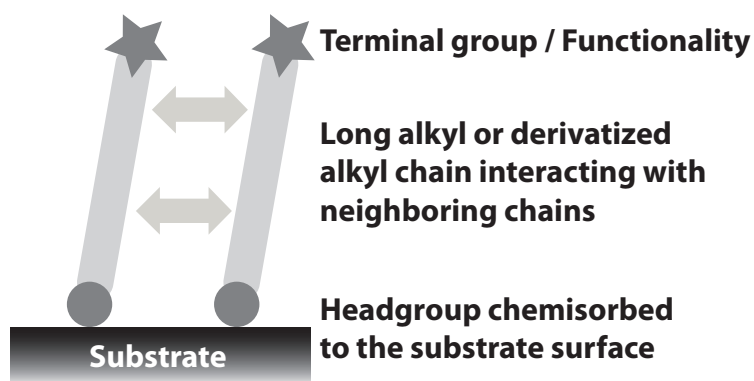


Figure 1.4: A self-assembling molecule consisting of a headgroup, a long alkyl spacer and a terminal group

Molecules, capable of forming such SAMs have special characteristics [75, 83] as shown in Fig. 1.4:

- a headgroup, capable of binding to the surface material (phosph(on)ates, thiols, silanes,) [73, 76]
- a spacer, often a long alkyl chain, that stabilizes the whole system during and after formation via intermolecular interactions [71, 84, 85]

- a terminal functional endgroup (amines, alcohols, polymeric chains,) [86–89]

Self-assembly in general might be defined as the spontaneous formation of complex and hierarchical structures from pre-designed building blocks, typically involving multiple energy scales and multiple degrees of freedom [75]. Self assembled monolayers are ordered molecular assemblies created from a spontaneous adsorption of a surfactant (with a specific chemical affinity of its headgroup) to a substrate. There are competing interactions that work in favor of adsorption (binding energy of the anchoring group with the surface, van der Waals energy stemming from the spacer interaction) or against it (loss of entropy, thermal effects, molecule and solvent displacements, solvent solution structuring) leading to the minimization of the free energy [75, 78, 83].

The SAM approach has the important advantage of making surface engineering at the molecular scale possible, since a specific reactive endgroup can be used to modify the molecules with functionalities after the adsorption process [90–92] or by coadsorption of two or more different SAM species [93]. These techniques facilitate the quantitative tailoring of the density of functional groups at the interface [94, 95] or can be used even for linear [96] or orthogonal functional gradients [97].

Nevertheless, the terminal endgroups and the grafted functionalities have a direct influence on both the stability of the molecular assembly and on its initial formation. A dense adsorption or coadsorption of molecules with an active chain end, resulting in a homogeneously ordered and closely packed SAM, is not always achieved. Preferential adsorption of one species, steric hindrances and repulsion might counteract an ordered assembly and require more control over the adsorption parameters or more complex adsorption protocols, involving e.g. multiple adsorption steps [86, 98, 99]. Additionally, single chains, with only one single anchorage foot may not always provide sufficient thermodynamic and/or kinetic stability [100].

1.4 Advantages of Graft-Copolymers for the Creation of Polymer brushes

Going away from the weak binding energy of physisorbed adlayers, a higher binding energy, but still combined with a mostly reversible binding mechanisms, can be achieved by chemisorption. SAMs offer an extremely flexible route to modify and tailor the surface chemistry of a wide range of metals, metal oxides and semiconductors, but a number of limitations have come apparent. Due to the self-assembly mechanism and the mostly reversible binding of many surface anchors, it is practically impossible to obtain defect-free monolayers over larger areas and, furthermore, the stability of these SAMs at the surfaces is limited due to the single-foot adsorption.

Multi-foot adsorption is mainly possible with polymeric systems carrying chemisorptive groups. The use of copolymers to create polymer brushes has several advantages in comparison to competing approaches. First of all, copolymers with multiple chemisorptive groups, normally adsorb to surfaces via multi-anchor binding. This renders the polymer much more stable at the surface, since upon the desorption of one anchor point of the polymer, the latter does not lose its entire surface attachment. Therefore the probability for that surface anchor to re-adsorb to the surface in proximity is much higher than for a SAM molecule, which risks diffusing away from the surface after having lost surface binding. Nevertheless, this multibinding approach can disturb the self-assembly process and is therefore normally compensated by a lower degree of ordering at the surface.

There exist different approaches to copolymer design for surface adsorption. On the one hand, block copolymers could be used, where one of the polymeric blocks is providing multiple chemisorption anchors. The other blocks, normally situated at the ends of the block copolymer act as end-grafted chains, pointing towards the solvent.

On the other hand, *graft*-copolymers, with grafted side chains and chemisorption groups present all along the polymeric backbone are possible. In Fig. 1.3 on page 15, an exemplary structure of a *graft*-copolymer for the polyelectrolyte case is shown. Substitution of the polyelectrolyte charges with chemisorptive groups would result in a polymer as discussed here. The *graft*-copolymer approach contains some advantages. The main advantage is that the side chains are grafted all along the backbone, which carries the chemisorption groups. Since the resulting tethered chain density is depending on the self-assembly of the polymers, a higher density could be easily achieved with the *graft*-copolymer approach easily. In comparison, the longer the surface-active block of di- or triblock polymers, the higher is the average separation D at the surface. A variation in chain density at the surface is therefore only achievable, when varying the length of the middle, surface-active block. This could have effects on the self-assembly behavior, but especially it influences the stability of the polymer at the surface. Therefore, high chain densities at the surface have to be balanced by a reduced stability against desorption for di- and triblock polymers. However, with the *graft*-copolymer approach, the chain density at the surface can be influenced easily in varying the grafting ratio of the side chains at the backbone. The stability after surface attachment can be varied independently of the grafting density in choosing an appropriate molecular weight of the backbone bearing the chemisorption functionalities. However, while di- or triblock polymers normally have relatively low molecular weights, *graft*-copolymers have comparably much higher molecular weights and thus the kinetics and mobility of those polymers is lowered compared to the lower molecular weight alternatives. Especially the diffusion coefficient is depending on the molecular mass, but as well the lateral mobility at the surface. Both factors can influence the adsorption kinetics, but also prolong the rearrangement process at the surface after adsorption.

In comparison with grafting-from approaches, the use of *graft*-copolymers offers a

synthetic advantage. The high grafting density can already be obtained during synthesis of the polymer prior to adsorption. If grafting occurs on a 2-dimensional surface, spatial, steric and conformational constraints may get easily predominant, limiting the maximum grafting density much earlier than for grafting-reactions to a backbone in solution. Furthermore, polymer characterization is more straight forward for bulk polymerized *graft* polymers in comparison to polymers grafted from the surface. Additionally, the adsorption processes for *graft*-copolymers are usually rather straight forward and comparable with the techniques developed for SAM formation. Mostly, a simple dip-and-rinse procedure (i.e. immersion of the surface in a polymer solution for some time, followed by rinsing with an appropriate solvent) is in most cases sufficient to reach full coverage of the surface. A big advantage is the fact that the coating process does not involve complicated chemistry and is thus quite easy to handle for possible applications, especially in terms of batch-to-batch reproducibility and cost efficiency.

1.5 Reference graft-copolymer systems

There are many grafting-to approaches. The present thesis is closely linked to the work performed on poly(L-lysine) backbone, grafted with different polymeric chains, such as PEG and dextran and the poly(phosphonate)s approach, both widely used and investigated deeply in a number of PhD theses in our research group.

Both approaches yield grafted polymers, showing a molecular bottle brush of, in most cases, PEG chains grafted to a polymeric chain, further denoted as polymeric backbone. However synthesis and surface-attachment mechanisms are different for both systems.

1.5.1 PLL-g-PEG and derivatives

Poly(L-lysine)-*graft*-poly(ethylene glycol) (PLL-g-PEG) is a widely used, characterized and investigated *graft*-copolymer systems. It was designed to attach via the polyelectrolyte backbone, using the (at neutral pH) positively charged amine groups from the lysine groups as electrostatic attachment sites to oxidic surfaces showing negative charges at neutral pH, such as titania and niobia [101–108]. The surface charging is strongly dependent on the substrate material, characterized by the isoelectric point (IEP) of the surface. This is the pH, at which the same number of positively and negatively charged hydroxyl groups are present at the surface, thus no overall surface charge is observed. For oxidic surfaces, at pH values lower than the isoelectric point, protonation of the hydroxyl groups is predominant, yielding an overall positively charged surface, for pH values higher than the IEP, the surface is charged negatively by predominant deprotonation of the hydroxyl groups [109].

PLL-g-PEG shows a good performance in a number of biological research areas, such as resistance to protein adsorption [105, 106, 108]. End-functionalization of PEG-chains was investigated to enable the polymer-coated surface to undergo specific interactions with molecules in the adjacent medium, e.g. by attachment of biotin to the PEG chain [104, 110], enabling the interaction with streptavidin or by attachment of peptide sequences, promoting cell adhesion while reducing bacterial adhesion [111–113]. Furthermore PLL-g-PEG coatings were used to facilitate the micro-3D-culturing of single cells using microwells [114, 115]. PLL-g-PEG gradients of end-functionalized PEG chains have been successfully prepared [96, 116, 117]. Different patterning techniques, i.e. containing regions that interact specifically with biomolecules, while other areas would be inert, have been developed for biosensor applications [118–122] or microfluidics [123]. The non-fouling behavior of the surface brush was not only investigated for PLL-g-PEG. A variation of the grafted

side chains lead to the development of dextrane [124] and poly-2-methyl-2-oxazoline (PMOXA) [125, 126] *graft*-copolymers using PLL as backbone. In parallel to the bio-applications, the influence of PLL-g-PEG surface brushes on aqueous lubrication was studied, showing a strong decrease of the coefficient of friction, depending on the polymer composition [103, 127–131]. Cloud-point conditions during adsorption (high ionic strength, elevated temperature due to the LCST lead to partially collapsed PEG chains) were found to be advantageous for producing high grafting densities [106].

The functionality of the coated surfaces remains intact over ten days of storage in biological, serum-containing medium. As usual for polyelectrolytes, a change in ionic strength or pH can trigger possible desorption mechanisms, as explained in Sect. 1.3.2.

After first steps attaching PLL-g-PEG under cloud-point conditions to increase surface coverage, another approach was tested to use the amine groups present on the PLL backbone not only to attach the PEG chains, but also to attach the polymer to the surface covalently, especially to aldehyde covered, plasma-modified substrates [107]. Recently, significant steps away from polyelectrolyte binding towards covalent binding of PLL-g-PEG and therefore a higher stability at the surface were achieved by coupling catechol surface anchors onto the amine groups of the PLL backbone, which can undergo chemisorption to metal oxide surfaces [132]. This approach yields a mixed electrostatic and chemical binding with highly improved stability as compared to PLL-g-PEG and a high compatibility with different substrate compositions [132].

1.5.2 Poly(phosphonate)s

The poly(phosphonate)s approach was developed within the thesis of Dr. V. Zoulalian [133] and Dr. F. Durmaz [134] to extend grafting of PLL-g-PEG with surface anchors which undergo chemisorption [132]. The approach was based on different techniques: different monomers, already carrying a specific functionality, such as PEG chains or phosphonate surface anchors were synthesized first. With the aid of a spacer monomer (with no specific functional group), different polymer compositions could be prepared. The approach in polymerizing already functionalized monomers has the advantage of being a highly flexible synthetic route towards functional polymers including direct influence on the polydispersity of the system by the right choice of an appropriate (living/controlled) radical polymerization method and the possibility of a high and flexible grafting density [135, 136].

Nevertheless, there are several drawbacks to this synthetic route: possible functionalities for end-functionalization of the PEG chains have to withstand the harsher polymerization conditions or have to be reacted onto the polymer after polymerization. Additionally, a high chemical expertise is needed for polymerization of the polymer. All functional monomers have to be synthesized and, additionally, chemical reactivities for polymerization strongly depend on the chemical structure - this could lead to drastic changes of the chemical reactivity in just changing small parts of the monomer. Thus control, modification and reassessment of the polymerization conditions is always needed when changing the monomer. Additionally, different reactivities of the monomer can lead to a gradient polymerization, meaning that monomers with a high reactivity are preferentially polymerized first and upon depletion of that monomer, the other monomers are reacted at a higher rate. The advantage of having random polymerization with an equal distribution of the functional groups along the polymer backbone is no longer assured, yielding unfavorable behavior of the polymer,

e.g. tadpole formation [137].

Nevertheless, poly(phosphonates) showed a remarkably high stability at the surface and within the investigated applications, especially towards non-fouling, protein-resistant surfaces, a very good performance [135, 136].

1.6 Aim and Objective of the Thesis

The main objective of my thesis is the development of a novel polymeric system using phosphonate anchor groups and a reactive backbone copolymer onto which the desired grafting functionalities could be reacted at low temperatures and without any further chemical reaction partners, and then the utilization of that new general polymeric system for different applications. Generally speaking, each application can be assigned to a certain material, namely:

Titanium dioxide is the surface of a widely used and important implant material.

WE43 magnesium alloy is a newly developed implant alloy. The material degrades within months after implantation due to corrosion in contact with the aqueous body fluid.

100Cr6 Steel is a model alloy for all applications using steel as construction material. In this thesis the main focus for this materials is for tribological applications.

Therefore the chapters of my thesis are organized as follows:

Chapter 1 The present chapter gives a rather general introduction to polymer brushes. All further chapters will start with a more focused and detailed introduction to the specific topic discussed there.

Chapter 2 deals with the polymer development, it covers the general presentation, synthesis route of the chosen polymeric system and describes the synthesis and chemical characterization of all polymers used within this thesis. At the end of the chapter there is a summarizing table, linking the different polymers presented in this chapter to the different applications presented in the following chapters.

Chapter 3 gives an introduction to titania and PEGylated polymers and shows a detailed study on functionalization of TiO_2 substrates with PEG-ylated polyphosphonates for biomedical applications

Chapter 4 gives an introduction to magnesium, explains the aims of the project on biomedical applications, shows a full surface characterization of the magnesium surfaces used within this study and a summary of opportunities for polymer monolayers for biomedical applications of that surface.

Chapter 5 introduces friction, tribology and lubrication and describes the application of polymers bearing poly(1,2-butylene glycol) grafted chains as additives for oil lubrication

Chapter 6 summarizes the main findings of this work

Chapter 7 summarizes materials and general protocols used throughout the chapters. Since the materials science community is rather heterogeneous, ranging from experimental chemistry, physics and biology to theoretical studies, basic introductory aspects of all measurement techniques are added, to give hopefully a short, but clear and comprehensive overview of these techniques for those readers who are not familiar with some of these methods.

Synthesis and bulk Characterization of poly(alkyl phosphonates)

2.1 Introduction

Reactive polymers bear reactive functionalities and can therefore readily undergo further reactions with other, appropriate polymers or molecules. They have attracted a lot of interest in different applications, ranging from polymer-blend compatibilization [138] to reactive HPLC column packages [139], antibody and enzyme resins [140] and all kind of surface coatings for different applications, from microfluidic devices [141], patterning of structures onto a broad range of materials [142], or immobilization of functional molecules onto nanoparticles [143] or surfaces [144–146]. A normal assumption in polymer chemistry is that the reactivity of the functional group does not depend upon the size of the molecule to which it is attached. However, the polymer backbone and the density of the functionalities can lead to a steric hindrance, which reduces the reaction rate drastically. Additionally, the reaction rate can be reduced by a restricted diffusion mobility of the functional groups. There-

fore, to achieve successful, complete and fast reactions, the polymers must consist of enough reactive functional groups and additionally, the reaction should be fast, selective and preferably irreversible [138, 147].

It is difficult to distinguish between the terms functional polymers and reactive polymers. “Functional polymers” is a wide term used for polymers, possessing special properties (e.g. electric, optic, biomimetic, stimuli-responsive). The term “reactive polymers” groups all polymers that can be further reacted due to the functional groups present on the polymer. Therefore, these polymers can act as precursors for the synthesis of more complex, functional polymers. Such a polymer is the polymer poly(L-lysine), which can be used for the synthesis of the functional polymer PLL-g-PEG, as described above in Sect. 1.5.1. Other prominent functionalities apart from amines are carboxylic acids or hydroxyl groups. Normally, these groups are not reactive enough to assure quantitative and fast reactions, and therefore, normally an *in-situ* activation for one of the reactants is necessary. Another group of reactive polymers are those bearing functionalities that are already activated and capable of reacting with appropriate reactants quantitatively. This property is normally introduced by an appropriate leaving group, to facilitate nucleophilic attack or substitution at the reactive functionality. This could be done *in situ*, yielding a less stable, reactive intermediate. More ideally, the activation creates a new and stable intermediate, which can be isolated, characterized and stored prior to further reaction. Among other derivatives of the functionalities mentioned above, mostly hydroxyl groups and carboxylic acids yield stable intermediates. Active esters in case of the carboxylic acids are susceptible to transesterification or aminolysis. Halogen substitution of the hydroxyl groups is the most commonly used activation pathway for further substitution reactions. Another approach towards higher reactivity is the use of reactive rings. The main forms are anhydride rings, epoxy rings, oxazoline rings and lactam rings. Other reactions, such as click chemistry are also used. A

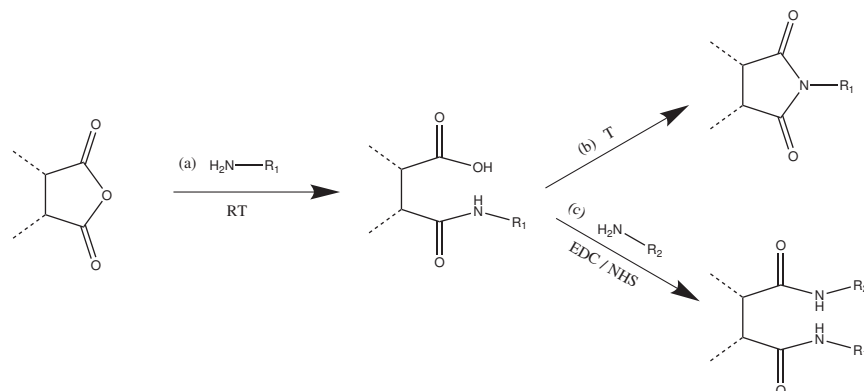


Figure 2.1: Reaction possibilities of maleic anhydride: (a) ring-opening of a maleic anhydride functionality with a primary amine, yielding an amide and a free carboxylic acid. Recyclization by imidation (b) is possible at higher temperatures and further functionalization of the polymer (c) is possible by using the free carboxylic acid for further coupling reactions, e.g. with further primary amines using *in situ* activation of the carboxylic acid by EDC/NHS. *in-situ*

summary of the mentioned reactions is found in Tab. 2.1.

2.2 The reactive backbone

Activated carboxylic acids, either in the form of active esters or anhydride rings are the most commonly used reactive polymers, mainly due to their fast and reliable reaction with nucleophiles, especially with primary amines. Maleic anhydride is the cyclic anhydride of maleic acid, which cannot be readily homopolymerized by radical polymerization [160]. The monomer is strongly electron accepting, thus electron donating co-monomers are necessary, which increase the tendency towards alternation [160]. However, copolymerization with free radical and even living/controlled radical polymerization has been well established with most common monomers [160–163]. Active esters of carboxylic-acid-containing polymers can be synthesized according to the protocols published by the Theato group [146, 149–151].

Table 2.1: Examples of different functionalities and reaction types possible for reactive polymers.

Reaction	Reactant	Co-reactant	Product	Reference
Amidation / Esterification	Carboxylic acid	Amine / Alcohol / Thiol	Amide / Ester / Thioester	[148]
Transesterification / Aminolysis	Active-ester	Amine / Alcohol	Amide / Ester	[143, 144, 146, 149-151]
Esterification / Substitution	Alcohol	Carboxylic acid / Amine	Ester / secondary Amine	[138, 139]
Substitution	Halogenide	primary Amine	secondary Amine	[138, 139]
Anhydride ring	Anhydride	Amine, Alcohol, Thiol	Carboxylic acid, Amide / Ester / Thioester	[142, 145]
Epoxide ring	Epoxide	Hydroxyl primary Amine Carboxylic acid	Hydroxyl, Ether Hydroxyl, secondary Amine Hydroxyl, Ester	[152]
Oxazoline ring	Oxazoline	Carboxylic acid Phenol	Amide, Ester Amide, Phenolether	[153]
Azlactone ring	Azlactone	Amine	Amide, Amide	[154-156]
Lactam ring	Lactam	Amine	Amide, secondary Amine	[157]
click chemistry	Azide	Alkyne	1,2,3-triazole	[158, 159]

Apart from their reactive performance, maleic-anhydride-containing polymers were chosen due to the fact that these polymers are commercially available. Furthermore, these polymers have different advantages in comparison to polymers bearing active esters. Both active esters and anhydrides are prone to hydrolysis during storage. This hydrolysis reaction is reversible upon heating for the anhydride rings, whereas for the active ester a less reactive carboxylic acid is formed non-reversibly. Therefore, activation towards a well-defined state for reactions is possible when using the anhydride polymers. Generally, both architectures can be reacted with a variety of nucleophiles, with primary amines reacting faster than alcohols or thiols. Since amide bonds are less prone to hydrolysis in comparison to esters, the reaction with primary amines is of further advantage. Additional reactions, i.e. cyclic imidation or further reaction with the formed free carboxylic acid are possible by using maleic anhydride containing polymers, as shown in Fig. 2.1. However the disadvantage of this polymer is the high reaction temperature necessary for further recyclization after functionalization. As for biomedical devices and implant research, drug-eluting systems and other bioactive molecules have to be attached on the surface without further degradation or denaturation, the relatively high recyclization temperature of 120°C is the limiting factor. If possible, another system with lower reaction temperatures would be preferable. On the other hand, the recyclization of the five-membered ring is not necessary for the grafting. The additional introduction of another, second functional group (via the carboxylic acid group) could be favorable for further functionalization. That is the reason why the reaction pathways (b) and (c) were considered to be advantageous for further development of polymers, but these reactions were not studied in detail and only the reaction (a) was used for the synthesis of the polymers used within this thesis.

Functionalization of maleic anhydride copolymers with primary amines for surface functionalization and furthermore for covalent protein immobilization and with PEG



Figure 2.2: Schematic drawings of both reactive backbone polymers used in this thesis, (a) Poly(maleic anhydride-alt-1-octadecene) and (b) Poly(isobutylene-alt-maleic anhydride)

functionalities for protein repelling, non-fouling surfaces has been already shown to be possible [164].

Two different maleic anhydride backbone polymers were chosen for the preparation of surface-active polymers bearing hydrophilic and hydrophobic polymer chains. These backbone polymers are

- Poly(1-octadecene-alt-maleic anhydride) (POMA) with a molecular weight of $M_n = 30\text{-}50$ kDa, or an average degree of polymerization of 85-140.
- Poly(isobutylene-alt-maleic anhydride) (PIMA) with a molecular weight of $M_n = 6$ kDa, or an average degree of polymerization of 39.

The polymer structures are shown in Fig. 2.2. Both polymers are alternating polymers with maleic anhydride as one monomer and either isobutylene as rather small comonomer or 1-octadecene as long and hydrophobic co-monomer. This polymer will then be used for hydrophobic polymer structures due to the C₁₆- side chains, whereas the polymer poly(isobutylene-alt-maleic anhydride) will be the base for hydrophilic polymer structures.

Group	band 1	band 2
5-membered anhydride	1870-1820	1800-1750
carboxylic acid	1725-1700	
ester	1750-1735	
amide	1680-1630	1570-1515
5-membered imide	1770	1700

Table 2.2: expected IR absorption bands in cm^{-1} for carbonyl bands from [165]

2.3 IR Investigation of the reaction possibilities of maleic anhydride containing polymers

In order to check the feasibility of the reaction pathways shown in Fig. 2.1, an investigation of different reactions was performed by infrared (IR) spectroscopy. In IR spectroscopy, different carbonyl bands can be distinguished by the appropriate absorption band around $1600\text{-}1800\text{ cm}^{-1}$ [165]. Carboxylic acids have a narrow and strong absorption band in the range of $1725\text{-}1700\text{cm}^{-1}$. Carboxylic anhydrides have normally two different absorption bands at approximately $1850\text{-}1800\text{cm}^{-1}$ and at around $1790\text{-}1740\text{cm}^{-1}$, shifted towards higher wavenumbers for 5-membered anhydride rings. During ring-opening, a free carboxylic acid group ($1725\text{-}1700\text{cm}^{-1}$) and an amide bond ($1700\text{-}1500\text{ cm}^{-1}$) are formed [165]. After ring-closing, a five-membered imide ring ($1770\text{-}1700\text{ cm}^{-1}$) is formed.

Due to the shift in the absorption bands, as summarized in the Table 2.2, cyclic anhydride groups can be distinguished from carboxylic acid and amide peaks and after treatment the imide group can be observed.

To investigate the behavior of the reactivity of the anhydride rings, the reaction with test reactants was investigated. In a first step, the IR spectra of the polymer backbone as received was measured and compared to a spectrum of the same polymer, but heated in dry state to 110°C under vacuum for 20h. In Fig. 2.3, the appropriate

spectra are summarized. It can be clearly seen that the hydrophobic POMA backbone seems to be more prone to hydrolysis than the PIMA polymer. The PIMA polymer shows before and after the heat-treatment the same carbonyl absorption spectrum, with two main peaks deriving from the anhydride ring, namely at 1775 and 1850 cm^{-1} . For the POMA polymer, a third absorption band at lower wavenumbers can be clearly seen, indicating a certain amount of hydrolyzed anhydride rings, yielding free carboxylic acid functionalities at 1710 cm^{-1} . These carboxylic acids can be recovered to the anhydride structure after the heat-treatment is performed.

In a next step, the reaction pathways were tested. Full ring-opening of the anhydride rings was performed by dissolving the polymer backbone in butylamine and stirring overnight at RT (Reaction (a) in Fig. 2.1). The butylamine was removed by distillation, followed by drying of the polymer under vacuum. The IR-spectra are shown in Fig. 2.4.

It can be observed that the carbonyl absorption bands are shifted towards lower wavenumbers and three main bands can be detected. These are at 1570, 1640 and 1705 cm^{-1} and correspond well to the absorption bands of the free carboxylic acid (1705 cm^{-1}) and the two amide bands, namely amide I (1640 cm^{-1}) and amide II (1570 cm^{-1}) absorption band. The band visible below 1500 cm^{-1} corresponds to both ring-opened and anhydride monomer units and belongs to the fingerprint region of the IR spectrum.

The subsequent ring-closing to the cyclic imide (according to pathway (b) in Fig. 2.1) was tested in analogy to the heat-treatment performed before ring-opening, in order to avoid already ring-opened anhydride rings due to hydrolysis. The polymers ring-opened with butylamine, as discussed in Fig. 2.4, were heat-treated at 150°C in a dry state under vacuum overnight. The resulting IR spectra are shown in Fig. 2.5. In the case of the PIMA backbone, a clear formation of the cyclic imide is visible. Two new

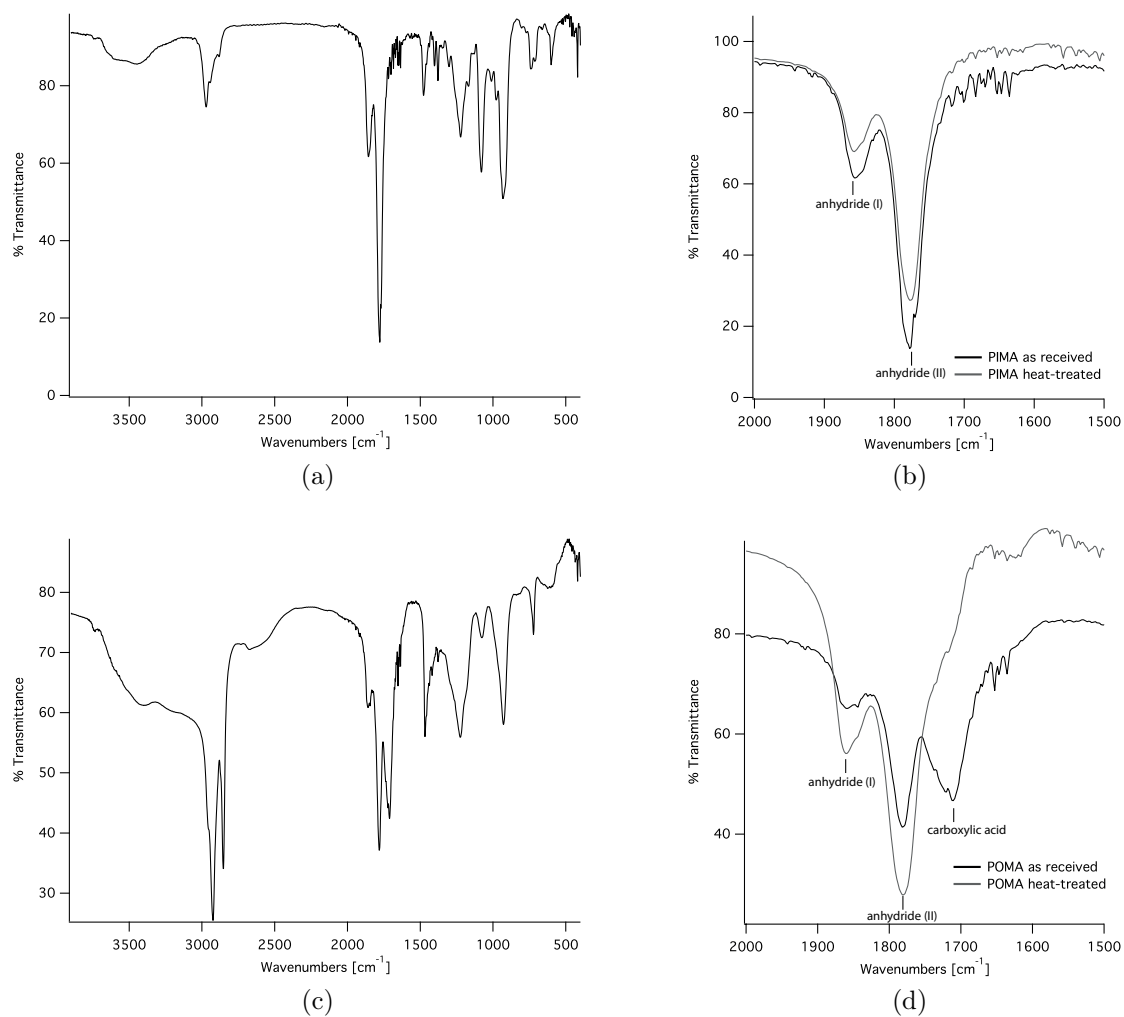


Figure 2.3: IR spectra of PIMA and POMA as received and after heat-treatment. (a) full IR-spectra of PIMA as received, (b) overlay of the carbonyl region of PIMA as received and heat-treated, (c) full IR spectrum of POMA as received and (d) overlay of the carbonyl region of POMA as received and heat-treated.

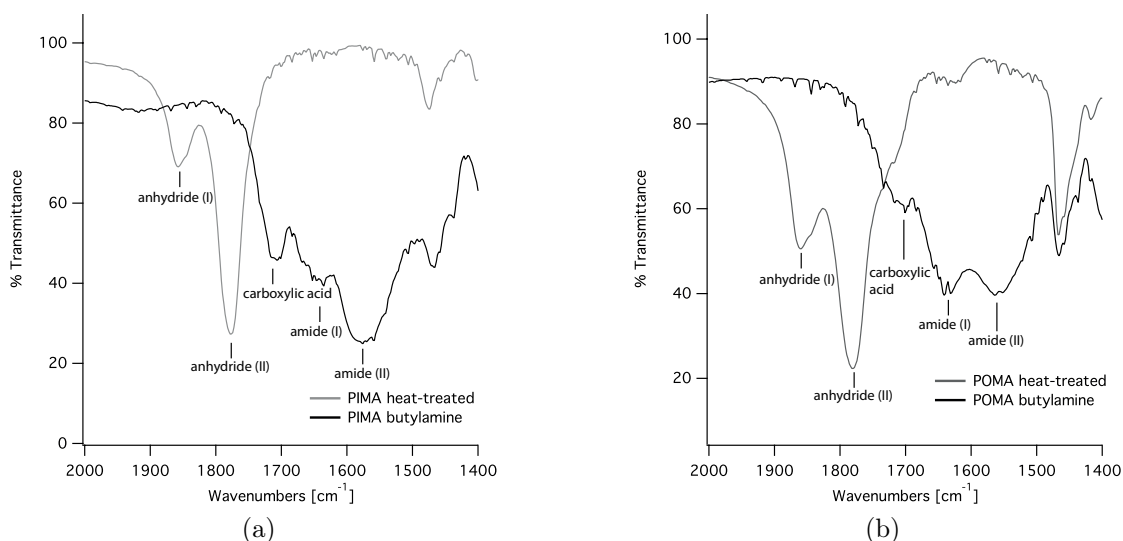


Figure 2.4: Ring-opening of PIMA and POMA by butylamine. The spectra show the overlay of the carbonyl region of the IR spectra of the heat-treated, pure and the ring-opened polymer (a) for the PIMA backbone and (b) for the POMA backbone.

absorption bands are visible, lying between the absorption bands of the anhydride ring and the free carboxylic acid. The bands are at 1690 cm^{-1} and at 1770 cm^{-1} , which correspond well with the theoretic absorption bands for cyclic, 5-membered imides. There is no band above 1800 cm^{-1} visible, which would indicate a partial anhydride formation (due to possible, prior hydrolysis), and no amide peaks noticeable, which would indicate only a partial imide formation. The interpretation of the results for the POMA backbone becomes slightly more difficult, because a mixed state of amide and imide is obtained. It seems that the cyclic imidation has not been carried out quantitatively. Nevertheless, the imide bands (1700 and 1770 cm^{-1}) are more intense than the amide bands. Those are still visible, but with highly decreased intensity.

Additionally, the ring-opening of the anhydride rings with alcohols was investigated for the POMA backbone. Since the reactivity is expected to be decreased compared to the reaction with primary amines, the feasibility of that reaction was tested. The POMA polymer was dissolved in 1-butanol and stirred overnight at RT. It can be

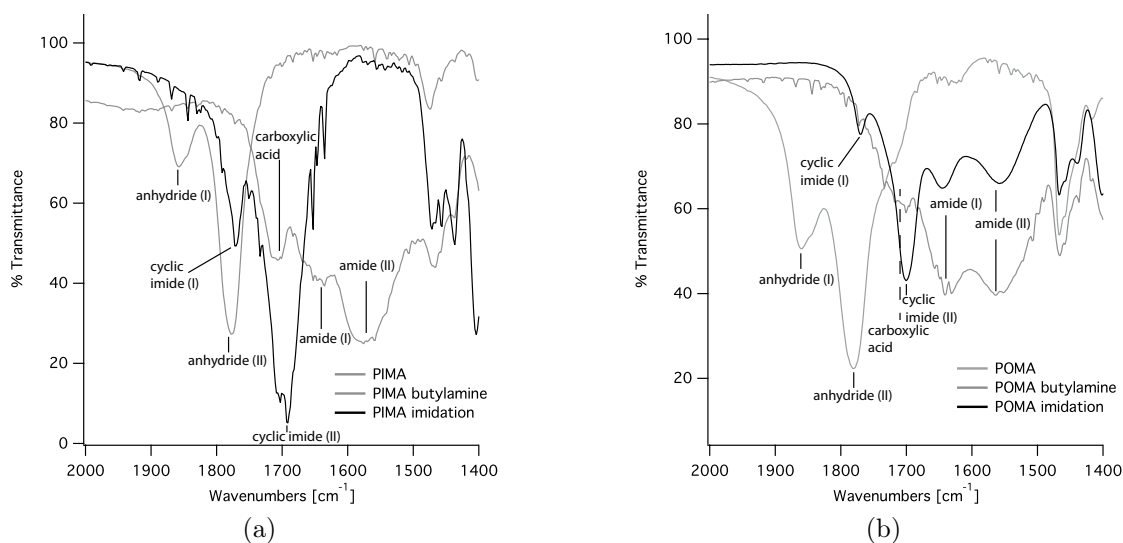


Figure 2.5: Cyclic imidation of both polymers after ring-opening with butylamine: (a) for the PIMA backbone and (b) for the POMA backbone

clearly seen in Fig. 2.6, that the majority of the anhydride rings is still unreacted, whereas the two lower, overlapping bands at 1710 and 1740 cm^{-1} represent the ring-opened functionalities, namely the free carboxylic acid at lower wavenumbers and the ester at slightly higher wavenumbers. For a more quantitative reaction, a much higher reaction temperature would be more favorable.

2.4 Synthesis strategy

The synthesis target envisaged is a series of polymers bearing phosphonate anchor groups, in order to attach to surfaces, such as titanium oxide or magnesium oxide. Furthermore, to form a brush structure at the surface, grafted side chains of polyalkylene oxide chains are used. The maleic anhydride backbones presented in Fig. 2.2 were chosen due to the anhydride functionalities readily present at the back-

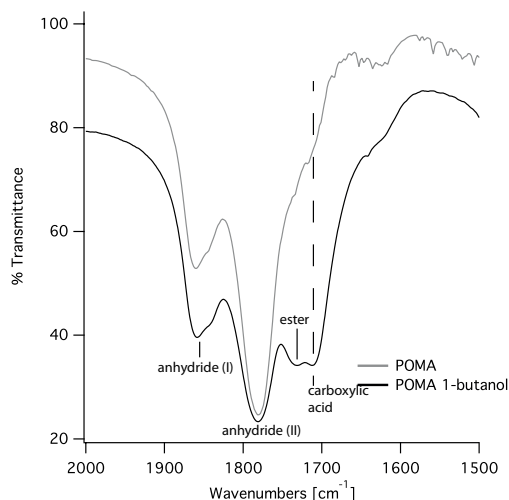


Figure 2.6: Ring-opening of POMA with 1-butanol at room temperature

bone. For hydrophobic polymers, the backbone with the C_{16} - side chains was selected. In order to allow low synthesis temperatures, which would facilitate further modifications, e.g. attachment of bioactive compounds at the end-groups of the surface brush, only reaction pathway (a) shown in Fig. 2.1 is used. Therefore, a multi-step reaction was chosen as a synthesis approach, in which the functionalities are reacted to the polymer backbone mainly via terminal, free amine functionalities. In Fig. 2.7, a generalized synthesis strategy is shown. In order to achieve a well-defined polymer backbone before synthesis and to ensure that all anhydride rings are closed and not partially ring-opened by water, the backbone polymers were heat-treated in a dry state at 150°C under vacuum before each synthesis. To keep possible hydrolysis of the anhydride rings by water to a minimum, dry solvents over molecular sieves were used. In a first step (a), the polymer side-chains were reacted with the backbone. In a second step (b), the phosphonate surface anchors were reacted. In order to be able to synthesize different grafting densities, a certain amount of all maleic anhydride rings could be left unreacted after both reaction steps and therefore those unreacted anhydride rings need to be opened by a third reaction step (c) with a

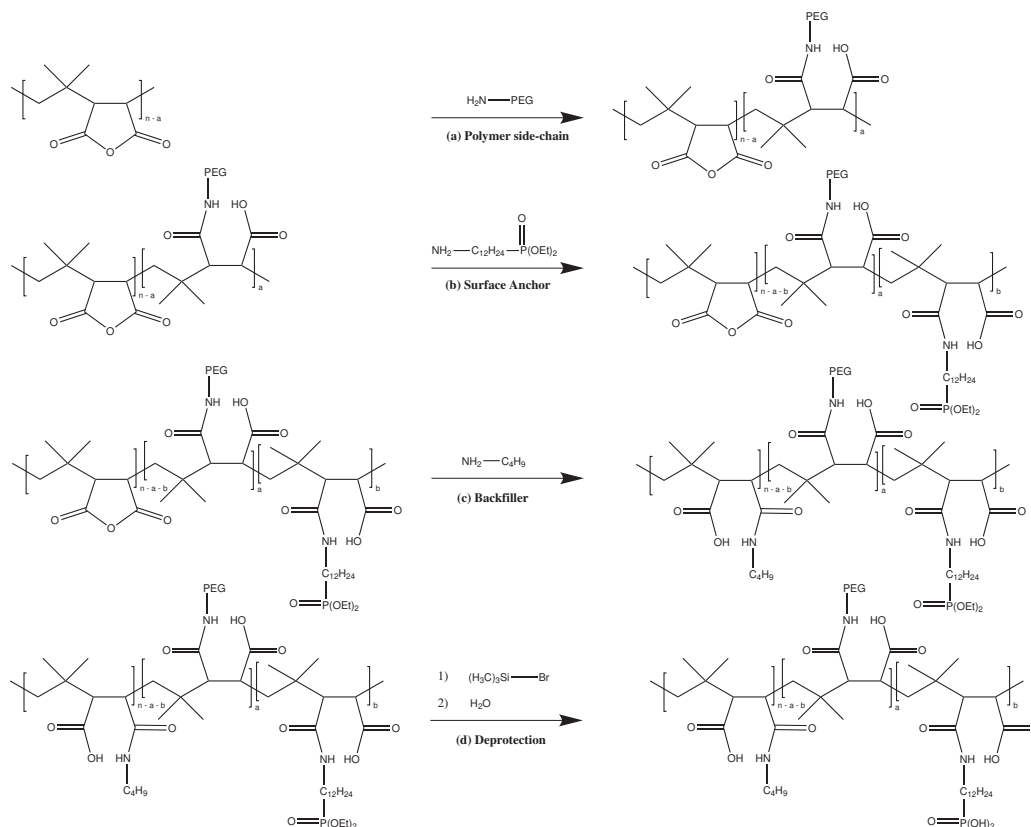


Figure 2.7: Schematic reaction scheme of a typical polymer synthesis, exemplarily shown on the hydrophilic polymer. In the first step (a), the polymer side-chains are grafted to the backbone, followed by (b) reaction with the surface anchor and (c) subsequent quenching of all unreacted anhydride rings with the backfiller. Step (d) is the deprotection of the phosphonate group by hydrolysis.

small primary amine. This reaction ensures that all reactive maleic anhydride rings have been opened quantitatively after functionalization and that there is no further reactivity present at the backbone. In the following, this reaction is referred to as quenching or backfilling.

The surface anchor was chosen to be 1,12-aminododecylphosphonate, during the reaction present in protected form as the corresponding diethylester. The synthesis of the surface anchor is described at the end of the chapter in Sect. 2.9.1. Due to the protection of the surface anchor during synthesis, the polymer is not supposed to be

surface active upon deprotection as forth step. A C₁₂-hydrocarbon spacer between amine and phosphonate anchor group was chosen in analogy to the SAMs structure. The longer the hydrocarbon chain, the more favorable the Van-der-Waals interaction forces become and the better is the ordering. Therefore, a sufficiently long hydrocarbon chain was chosen for the surface anchor to achieve a better or faster self-assembly. Therefore, the surface anchor itself could be used as surface-active molecule, forming self-assembled monolayers, which then can be further used to couple maleic anhydride containing polymers onto the SAMs via its terminal amine groups. Within this thesis, that approach was not further investigated. However, the fourth reaction step (d) shown in Fig. 2.7 after workup of the polymer consists of the deprotection of the phosphonic acid diethylester to the free phosphonic acid or its corresponding monosalt.

In Tab. 2.3, the reactants used for the synthesis of the hydrophilic and hydrophobic polymers are summarized. For both types of polymers - hydrophobic and hydrophilic - the same surface anchor 1,12-aminododecylphosphonate was used. The polymer used for the grafting reaction is in both cases a poly(alkylene oxide) derived polymer, namely O-(2-aminoethyl)-O'-methylpolyethylene glycol (mPEG-amine) with a molecular weight (M_n) of 2 kDa and poly(1,2-butylene glycol) monobutylether (PBG-monobutylether) with a molecular weight (M_n) of 1.5 kDa. It has to be emphasized, that the polymer PBG-monobutylether does not contain an amine group and therefore a coupling reaction in using the terminal alcohol functionality is tried. As already seen in the IR investigation of the reaction possibilities, c.f. Fig. 2.6, the reaction with alcohols is not complete at room temperature. Since the hydrophobic polymers will not be used for biomedical applications, where the attachment of additional, bioactive compounds onto the polymeric system is always of advantage, the synthesis temperature is set to much higher values in order to achieve a sufficiently high coupling rate. A detailed description of the synthesis of the polymer is shown at the

Table 2.3: Summary of the reactants used for the polymer synthesis

	Surface Anchor	Graft Polymer	Backfilling
hydrophilic polymer	1,12-aminododecylphosphonate	mPEG-amine ($M_n=2$ kDa)	1,6-Diaminohexane Ethanolamine Butylamine
hydrophobic polymers	1,12-aminododecylphosphonate	PBG-monobutylether ($M_n=1.5$ kDa)	Butanol

end of the chapter in Sect. 2.9.2.

2.5 Polymer Nomenclature

In the following, the polymers will be named according to their grafting composition and the backbone used. A systematic naming, starting with the abbreviation of the backbone polymer, i.e. PIMA for poly(isobutylene-alt-maleic anhydride) or POMA for poly(1-octadecene-alt-maleic anhydride) has been developed. Since the grafting consists of 3 steps, those are named in the order of reaction: polymer side chain, surface anchor, backfiller, followed by the corresponding molecular weights and grafting densities (corresponding to the number of that grafted functionality divided by the total number of initial anhydride rings). For example, the full name of the hydrophilic polymers would be PIMA-graft-(PEG, ADP, backfiller) ($[a]:[b]:[c], d$), where $[a]$, $[b]$ and $[c]$ are the respective grafting densities of PEG, ADP and backfiller. In the case of different chain lengths of the backbone and/or the polymeric side chain, this would be necessary to be included in the naming, but this is not the case within this thesis. Still this naming system yields relatively long names, therefore a shorter abbreviation was developed. The backbone indicates already the grafting either of PEG or PBG, therefore those are no longer named. Since the grafting densities ideally all add up to one, two out of three grafting densities are sufficient to characterize the polymer

Table 2.4: Abbreviations used in the naming of the polymer

Abbreviations	Full chemical name
PIMA	poly(isobutylene-alt-maleic anhydride)
POMA	poly(1-octadecene-alt-maleic anhydride)
PEG	mPEG-amine
PBG	PBG-monobutylether
ADP	1,12-aminododecylphosphonate
DAH	1,6-Diaminohexane
EA	Ethanolamine
BA	Butylamine

entirely. For all polymers of one family, the type of surface anchor (ADP) and polymeric side-chain are the same, thus those do not need to be named explicitly. The backfiller, however still can vary between different polymers and thus it has to be named. This leads to the short name of the example above: PIMA([a]: [b], backfiller).

In Table 2.4, all characteristic abbreviations are summarized, as used for the polymer naming system.

An overview shown in Tab. 2.5 list of the polymers synthesized within this thesis, including the theoretical grafting densities, as used during chemical synthesis, assuming 100% reaction efficiency.

2.6 Hydrophilic Polymer characterization

2.6.1 Characterization of the chemical composition and chemical structure

The chemical composition and the polymer structure was characterized by 1H - and ^{31}P -NMR and elemental analysis (EA). For the NMR measurements, the polymers

Table 2.5: Overview over the synthesized polymers, including theoretic grafting densities of the polymer as used during the synthesis and the theoretic short name of the polymers.

(*) The value 0 means that quenching with the backfiller was applied, but that theoretically, all anhydride rings should be ring-opened by either the respective ether or ADP.

Polymer	d_{ether}	d_{ADP}	$d_{\text{backfiller}}$	Backfiller
PIMA-(0.3:0.3, DAH)	0.3	0.3	0.4	Diaminohexane (DAH)
PIMA-(0.3:0.3, EA)	0.3	0.3	0.4	Ethanolamine (EA)
PIMA-(0.5:0.5, DAH)	0.5	0.5	0 ^(*)	Diaminohexane (DAH)
PIMA-(0.5:0.5, EA)	0.5	0.5	0 ^(*)	Ethanolamine (EA)
PIMA-(0.5:0.5, BA)	0.5	0.5	0 ^(*)	Butylamine (BA)
POMA-(0.3:0.7, Butanol)	0.6	0.4	0 ^(*)	Butanol

were first characterized in deuterated water, resulting in very broad peaks, indicating that the internal flexibility of the polymer is not very high in this solvent. After a screening of different deuterated solvents, methanol-d4 was chosen because of the much reduced peak broadening. Still, the peaks are not as well resolved as it is the case for other, comparable polymers, such as PLL-g-PEG [166]. There could be different reasons for that behavior. As already mentioned, the polymer is amphiphilic and thus the conformation in a polar solvent could induce an internal conformational change with the hydrophobic parts trapped inside the polymer and the hydrophilic parts pointing out, towards the solvent. This could already decrease the flexibility of the internal parts, rendering them broader in their NMR response. Another possibility is the formation of polymeric micelles by agglomeration. This aspect is described in Section 2.6.3 on page 51 using lightscattering methods.

Deprotection of the phosphonate group

The deprotection step was followed by ³¹P-NMR, where a shift in the phosphorus peak was clearly observed. This shift of the phosphorus peak before and after depro-

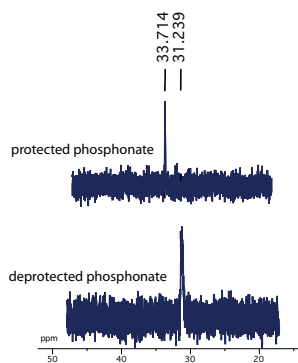


Figure 2.8: Shift of the phosphorus peak in the ^{31}P -NMR before and after deprotection of the phosphonate ester

tection is shown in Fig. 2.8. The peak shifts from 33 ppm to 31 ppm after hydrolysis.

NMR characterization of the polymers

The polymers were characterized by means of ^{31}P - and ^1H -NMR measurements. In Fig. 2.9 on the facing page, a representative ^1H -NMR spectrum is discussed in detail, assigning the main peaks of the NMR spectra to the polymeric structure. Generally, the spectrum can be divided in two parts - between 0-2 ppm and between 2.7 and 3.7 ppm. In the first part at higher fields, mainly the hydrocarbon contributions can be found. These are the $-\text{CH}_3$ groups at the backbone at approximately 1 ppm and other $-\text{CH}_2$ groups, mainly deriving from the hydrocarbon spacer of the surface anchor at 1.2 ppm. The two peaks between 1.4 and 1.5 ppm are originating from the backbone, namely the hydrocarbon connected to the carbonyl groups of either the free carboxylic acid (1.4 ppm) or the corresponding amide (1.5 ppm). Both peaks are supposed to have the same integral, since they are created simultaneously during the ring-opening reaction of the prior anhydride ring at the backbone. The peak at 1.7 ppm is deriving from the hydrocarbon in vicinity of the phosphorus. The second part between 2.7 and 3.7 ppm contains the peak of the hydrocarbons connected to free amines (in case of the DAH backfiller) at 2.8 ppm, followed by the hydrocarbon

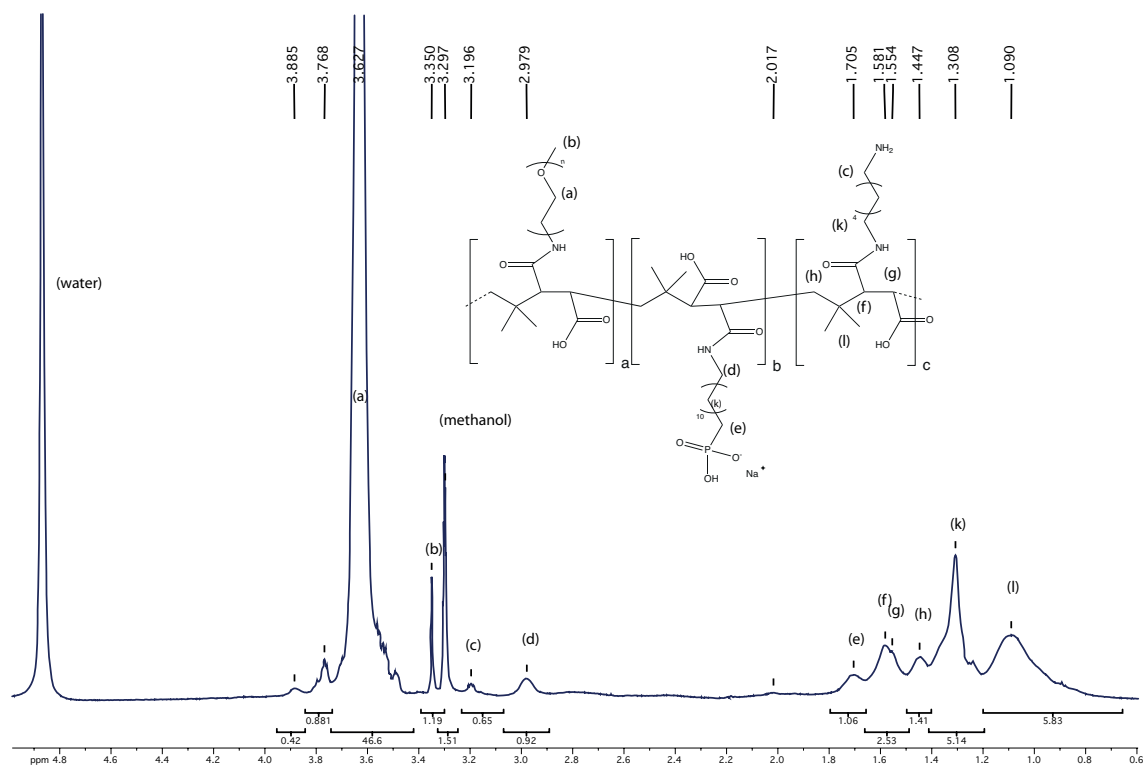


Figure 2.9: Representative NMR of a polymer synthesized and assignment of the peaks to different groups. The NMR spectra shows the polymer PIMA-(0.3:0.3, DAH).

directly connected to an amide bonding ($-\text{CH}_2-\text{C}(\text{O})-\text{NH}-$) at slightly higher chemical shifts of 3.0 ppm. The peak at 3.3 ppm in close neighborhood to the methanol solvent trace at 3.2 ppm derives from the terminal methoxylated end-group of the PEG chains. The repetition unit of the PEG chains contains only equivalent CH_2 - groups, all summing up to a peak at 3.5 ppm. Additionally, a huge water impurity deriving from the PEG chains and from the deuterated methanol is detected at 4.8 ppm. The ^1H - and ^{31}P -NMR spectra of all polymers synthesized are shown in Appendix A.2 as a summary.

Determination of the grafting Ratio by NMR

Interestingly, the broadening of the peaks is much more enhanced for the hydrophobic parts of the polymer, especially the hydrocarbon contributions. This indicates a polymer conformation, in which the hydrophobic parts are not well dissolved and trapped inside the polymer, whereas the PEG chains point outwards, providing good solubility. For the calculation of the grafting density the following peaks were chosen: the methoxy peak of the PEG chain (b). For the surface anchor, the relatively broad, but unfortunately overlapping peak (e) at 1.6 ppm was chosen. Since different backfilling reagents were chosen, it is impossible to find corresponding peaks from ethanolamine or butylamine within the hydrocarbon peaks. Two rather well resolved peaks (f) and (g) are situated between 1.4 and 1.6 ppm, indicating the hydrogen signal deriving from the backbone carbons directly connected to a carbonyl group. Both peaks together give a good signal deriving from the amide groups. Therefore, the grafting densities can be calculated as followed:

$$d_{PEG} = \frac{2}{3} \cdot \frac{I_{(b)}}{(I_{(f)} + I_{(g)})}$$

$$d_{phosphonate} = \frac{I_{(e)}}{(I_{(f)} + I_{(g)})}$$

The resulting grafting density $d_{backfiller}$ is then calculated to be the missing summand of all three grafting densities to sum up to one. Due to the fact that peaks (e), (f) and (g) are not well resolved and rather broad due to the micellation of the polymer and, additionally, the peaks are overlapping, this all contributes to quite a high error. The calculated grafting densities are displayed in the Tab. 2.7 on the next page, together with the grafting densities obtained by elemental analysis, which is explained and discussed in comparison to the values obtained from NMR in the following section.

Table 2.6: Summary of the EA of all polymers. The grafting densities stated are the theoretical, as used during synthesis

theoretical name	weight percentage				
	C	H	N	O	P
PIMA-(0.3:0.3, EA)	54.68	9.07	1.55	33.01	0.95
PIMA-(0.3:0.3, DAH)	55.08	9.02	2.08	31.59	0.94
PIMA-(0.5:0.5, EA)	54.17	9.11	1.28	31.71	1.26
PIMA-(0.5:0.5, BA)	54.32	8.74	1.3	32.46	1.31
PIMA-(0.5:0.5, DAH)	53.75	9.05	1.65	34.25	1.30

Table 2.7: Comparison of grafting densities calculated by EA and NMR. The theoretical name contains the grafting densities as calculated from the synthesis

theoretic name	method	Grafting densities		
		d_{PEG}	$d_{phosphonate}$	$d_{backfiller}$
PIMA-(0.3:0.3, EA)	EA	0.31	0.28	0.41
	NMR	0.28	0.45	0.27
PIMA-(0.3:0.3, DAH)	EA	0.32	0.28	0.40
	NMR	0.31	0.40	0.29
PIMA-(0.5:0.5, EA)	EA	0.40	0.45	0.15
	NMR	0.37	0.43	0.2
PIMA-(0.5:0.5, BA)	EA	0.39	0.45	0.16
	NMR	0.35	0.35	0.3
PIMA-(0.5:0.5, DAH)	EA	0.38	0.46	0.16
	NMR	0.32	0.37	0.43

EA characterization of the polymers

In Tab. 2.6 the findings of the EA for all synthesized polymers are summarized. The weight percentages of the EA were used to calculate a grafting ratio of the polymers. If possible the weight percentages of the heteroatoms of the polymers were taken into account for the calculations, e.g. phosphorus content to indicate the surface anchor. Additionally, the calculated grafting ratios of the NMR analysis are included into the Tab. 2.7.

In looking only to the values obtained from EA, it can be seen that for the polymers synthesized with a lower grafting density, the theoretical grafting density perfectly matches the grafting density found during polymer characterization. This shows the high reactivity of the anhydride rings and that stoichiometric reactions are possible with terminal amines. However, the polymers with higher grafting densities differ more between the theoretical grafting density, calculated from the stoichiometry of the reaction solution and the characterized polymer composition. This, however is contributed to the fact, that a theoretical grafting density of 0.5 is difficult to achieve for the PEG chains. Since the PEG chains are polymers itself, carrying only one terminal amine group, steric hindrance and thus a lower reaction probability is starting to inhibit further reaction of the PEG chains onto the backbone. Since both surface anchor and backfiller are much smaller in size, the steric hindrance for them is less pronounced. The surface anchor reacts as expected, up to a grafting density of 0.5. The slightly smaller values achieved could be attributed to the steric hindrance that is more and more present in the backbone and which is shielding the remaining, still unreacted anhydride groups from further nucleophilic attack. Nevertheless, the backfiller is clearly opening all unreacted anhydride rings. This can be explained mainly due to its higher concentration present in synthesis and its small size, which raises the probability for a reaction with the unreacted anhydride groups, even despite the relatively high steric hindrance around the anhydride groups.

The values obtained from NMR seem to have bigger deviations from the expected stoichiometry. The polymers with lower expected grafting densities show a trend to higher phosphonate contents, whereas the PEG content is close to the theoretical content. The polymers with a theoretical higher grafting density, generally a lower grafting density is observed for both, PEG and phosphonate grafted moieties, when compared to the theoretical values. However the grafting densities obtained for polymers of one family, i.e. high or low theoretical grafting density in terms of

phosphonates and PEG, is much more varying than in case of the calculations based on the EA. It has to be taken into account that the grafting with PEG and surface anchor was performed in one synthesis prior to the split-up of the reaction in order to quench with different backfiller. Therefore, the grafting density of PEG and surface anchor is supposed to be similar for the polymers only differing in the backfiller. This is true for the results obtained from the EA calculations, but not for the calculated grafting densities derived from the NMR measurements. Therefore, in the following the grafting densities of the elemental analysis are used for further discussion of the polymers.

2.6.2 Determination of the molecular weight

The molecular weight and the polydispersity of the synthesized polymers are important properties, usually measured by standard polymer characterization techniques, such as gel permeation chromatography (GPC) or matrix assisted laser desorption ionization - time of flight (MALDI-ToF). GPC measurements were performed in different solvents (DMF, CHCl_3), but no polymer was eluted after the column, even for the still protected polymers. The same situation was found for the MALDI-TOF analysis of the polymers. No matrix (DCTB, dithranol, DHB) was found to ionize and thus desorb the polymer for detection. Only flat baselines with matrix clusters were obtained in both positive and negative mode of the detector for different concentrations. Additionally, it was tried to include Na^+ ions inside the matrix (Na Mix 1:10:1), in order to transfer the charges more easily. It seems that the polymer, despite being protected, is adsorbing onto the matrix of the GPC column and for the same reason is, due to its molecular weight, unable to ionize in the MALDI matrix. Field flow fractionation (FFF) was tried to get the molar mass and the polydispersity. Since the system of separation is different from GPC and MALDI-ToF, the apparent

surface active properties of the polymer seem to be less influencing the result. FFF is a separation technique, where a flow vector is applied perpendicular to the polymer solution pumped through a narrow channel. This causes a separation of the particles present in the solution, depending on their different mobility (which is proportional to the polymer size and molecular weight) under the force exerted by the external vector. The different fractions are then detected by a light scattering detector. Since the polymer stays in bulk solution and there is no high surface area close to the polymers, the surface active character of the polymers is less important for the successful separation and detection of the polymers. The light scattering detector, however, showed unreasonably high values of $10^3 - 10^4$ kDa in water and methanol. These high values cannot be explained by a single polymer, but by micelles formed by aggregation of polymer chains. The determination of the aggregation behavior of the polymers in different solvents is discussed in Sect. 2.6.3. Despite these measurements, unfortunately the exact molar mass of the single polymer chains and the polydispersity could not be measured.

However, since the polydispersity of the polymer chains influences highly the molecular weight of the polymer significantly, GPC of the PIMA backbone was measured, resulting in a polydispersity of 2.4 and a molecular weight of $M_n=11500$ and $M_w=27500$ Da and is shown in Sect. A.1. Assuming the polymer chains ranging between the values of M_n and M_w , the degree of polymerization ranges between 74 and 177. Taking into account that the backbone polymer is then grafted by PEG chains of 2kDa, the differences in molecular weight get more pronounced. Assuming a polymer with a grafting density of 0.4 in terms of PEG chains, the maximum and minimum molecular weights for the polymer PIMA(0.40:0.45,BA) then add up to 70 kDa and 167 kDa. However, this still would result in a polydispersity index of 2.4, as for the backbone. Additionally, a polydispersity of the PEG chains has to be taken into account, as well as the fact that the polymer is a statistical *graft*-copolymer. This statisti-

cal effect induces an additional factor that contributes to the polydispersity. Since the calculated grafting density is a statistical and averaged value, polymers with a higher grafting density in PEG chains, and others with lower grafting density coexist in bulk. Assuming a relatively low fluctuation of the grafting density of PEG to be in the order of 0.35 - 0.45, still, the differences in molecular weight range from 63 kDa to 185 kDa, reaching a polydispersity of 3. Therefore, the overall polydispersity of the polymers is assumed to be relatively higher than the measured polydispersity of the backbone itself.

2.6.3 Determination of the aggregation behavior by DLS and SLS

The workup of the polymers indicated already a highly amphiphilic character of the polymers synthesized. A probable self assembly to micelles was already supposed due to the results of the field flow fractionation system (FFF). Light scattering, especially dynamic light scattering (DLS) and static light scattering (SLS) (c.f. Sect. 7.1.4) were used to investigate the aggregation behavior of the hydrophilic polymers at different concentrations in aqueous solution and different organic solvents. Especially the R_g , R_h , the translational diffusion coefficient D and the molecular weight in M_w were in the focus of interest. Dynamic light scattering were acquired at a polymer concentration of 0.5 mg/ml, resulting in the hydrodynamic radius R_h . The radius of gyration R_g was determined in using the Guinier approximation from SLS data at a concentration of 0.5 mg/ml. A Zimm plot analysis over 4 different concentrations using SLS was performed to determine M_w . More detailed explanations are presented in Sect. The polymers showed similar behavior, not dependent on the backfilling or on the grafting ratio.

A wide range of solvents (water, methanol, chloroform, DMSO, DMF and THF) were

Table 2.8: Summary of the findings by SLS and DLS for the polymer solutions in water and methanol. Dynamic light scattering values were acquired at a polymer concentration of 0.5 mg/ml. The radius of gyration R_g and the molar weight M_w was determined in using the Guinier plot from SLS data at a concentration of 0.5 mg/ml.

Solvents	Water			Methanol		
	minor 1	minor 2	mayor	minor 1	minor 2	major
R_h [nm]	2.4	10.5	80.0	2.2	9.1	85.5
R_g [nm]			90 ± 5			89 ± 5
M_w [kDa]			$1.5 \cdot 10^3$			$0.3 \cdot 10^3$
D [mm^2/s]	$1.0 \cdot 10^8$	$2.4 \cdot 10^7$	$2.8 \cdot 10^6$	$1.8 \cdot 10^8$	$4.5 \cdot 10^7$	$4.8 \cdot 10^6$

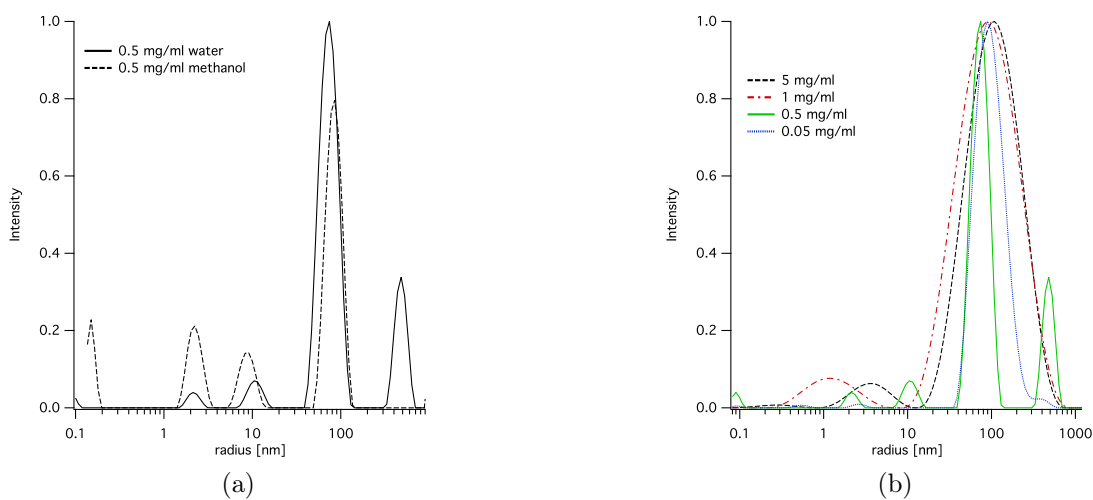


Figure 2.10: DLS size distribution for (a) a polymer concentration of 0.5 mg/ml in water and methanol and (b) concentration dependence of the size distribution for water as solvent

checked for the aggregation behavior by DLS, but no noticeable difference was found for those solvents in terms of R_h . The major species was found at very high radii of 90 ± 10 nm, whereas one or two minor species at much lower intensity at 3 ± 1 nm and 10 ± 2 nm were present. A full investigation by SLS and DLS was performed in water and methanol, where the molar mass (M_w) and the radius of gyration (R_g) was derived from the Guinier approximation at different polymer concentrations, as described in Sect. 7.1.4. The determination of the molar mass resulted in unusual high molecular masses in the range of 10^3 kDa. The exact values derived from the light-scattering experiments are shown in Tab. 2.8. This high molecular mass obtained in both solvents is indicating an agglomeration of the polymer, especially when taking into account the much smaller, minor peak at much lower sizes, which could indicate the unassociated polymer species. The concentration was lowered stepwise down to a concentration of 0.05 mg/ml, which was close to the detection limit of the light scattering instrument, but no difference in the aggregation behavior was found in comparison to higher concentrations, indicating a high stability of the polymer aggregates. The critical micelle concentration is therefore assumed to be lower than the lowest concentration investigated. In Fig. 2.10 (a), the size distributions from DLS are shown for a polymer concentration of 0.5 mg/ml in water and methanol. It can be clearly seen that the polymer aggregation is different in both solvents. It seems that a higher percentage of the polymers is dissolved unassociated in methanol, explaining the better NMR spectra recorded in deuterated methanol compared to deuterium oxide. Additionally, the molecular weight of the polymer assemblies is found to be lower for methanol as solvent, indicating a lower aggregation number. The lateral diffusion coefficient was calculated for the 0.5 mg/ml polymer solution of water and methanol for all agglomeration sizes. A summary of the findings for water and methanol are given in Tab. 2.8.

Comparing the values of R_g and R_h at 0.5 mg /ml solution, it can be seen that those

are in the same order of magnitude. The ratio R_g/R_h can be used to indicate changes in the polymer conformation or in the shape of the aggregates. A consistent effect was found in water, where the ratio R_g/R_h was rising from 0.8 at concentration of 5 mg/ml to values slightly higher than 1 at the lowest concentrations, whereas for the polymer solutions in methanol, a value slightly higher than one was always found. As can be seen at the Fig. 2.10 (b), the polydispersity of the micellar structures is shrinking with lower concentrations, resulting in more defined species. Starting at concentrations of below 0.5 mg/ml, as shown in Fig. 2.10 (a), a more discrete agglomeration in different species is found and is thus influencing the calculations of the corresponding radii. Furthermore, due to the relatively high deviation of the R_g value derived from the Guinier approximation, the resulting differences in the ratio R_g/R_h could be mainly within the deviations induced by the radius of gyration.

2.7 Acid-base character of the polymers synthesized

The pH of the aqueous polymer solution with a concentration of 0.5 mg/ml was measured and found to be at pH 5.0. With the structural information of the polymers, acid-base equilibria could be calculated, in order to determine the number of positive and negative charges present at the backbone and in checking the chemical state of each functionality present at the polymer. The functionalities present at the polymer, susceptible for acid-base reactions are mainly:

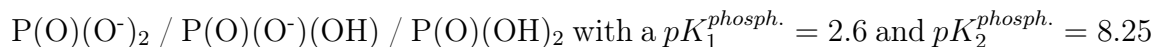
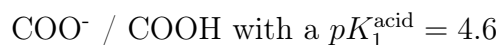
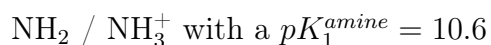


Table 2.9: Acid base calculation of the functionalities at a pH of 5. 39 initial anhydride functionalities are assumed per polymer backbone, and the polymer composition is calculated according to the grafting density. From this basis, the acid-base equilibrium at the polymer was calculated based on a pH of 5 of the bulk solution.

Functionality	PIMA(0.38:0.46, DAH)	PIMA(0.38:0.46, EA)	PIMA(0.30:0.30, DAH)	PIMA(0.30:0.30, EA)
NH ₂	0	0	0	0
NH ₃ ⁺	7	0	16	0
COO ⁻	28	28	28	28
COOH	11	11	11	11
P(O)(O ⁻) ₂	0	0	0	0
P(O)(O ⁻)(OH)	18	18	12	12
P(O)(OH) ₂	0	0	0	0
Sum positive charges	7	0	16	0
Sum negative charges	46	46	40	40

Therefore, the protonated and deprotonated state of all functionalities were calculated for the different polymers. In Tab. 2.9, the findings of the calculations are summarized, assuming a polymer with 39 initial anhydride functionalities (corresponding to the polymer backbone of 6 kDa) and the polymer structure according to the grafting densities as derived from EA. Since polymers backfilled with ethanolamine and butylamine behave the same for acid-base calculations, only one of both polymers is considered in the table.

The effect of the 1,6-diaminohexane is clearly visible in the calculations. All free amine functionalities are positively charged at a pH of 5. The phosphonate moieties are all in the monoacid state, whereas the carboxylic acid groups are charged negatively to approximately 75%. In looking at the overall charges, it can be clearly seen,

that all polymers are highly negatively charged, while the diamino-hexane backfiller is counterbalancing slightly by introducing positive charges. Nevertheless, a high excess of negative charges can be found for all polymers at the pH of 5, mainly because of the free carboxylic acids.

2.8 Hydrophobic polymer characterization

2.8.1 Characterization of the chemical composition and chemical structure

The workup of the hydrophobic polymer turned out to be challenging due to its highly amphiphilic character. Precipitation or extraction was not possible with the polymer since it always stayed in solution or triggered emulsification of the system. Dialysis in organic solvents and size exclusion chromatography were not successful in separating the reacted polymer from unreacted side-chains. A high peak at 3-4 ppm showed a relatively high content of poly(1,2-butylene glycol) present in the polymer mixture, but the assays in purification showed no decrease of those peaks in respect to the hydrocarbon peaks present between 1 and 2 ppm and not deriving from contributions of the PBG. Since the PBG has 2 major contributions in that area, too, it is however difficult to determine a grafting ratio or to perform a structural analysis based on NMR. Due to the high amount of PBG present, the peaks are relatively intense and broad and overlap with the peaks deriving from the other parts of the polymer. In parallel to the findings of the hydrophilic polymers a possible micellation and association of the polymer chains in the solution can be suggested to explain the relatively broad peaks. As for the hydrophilic polymers a solvent dependence in the peak broadening could be observed. The NMR spectra generally seemed to be better

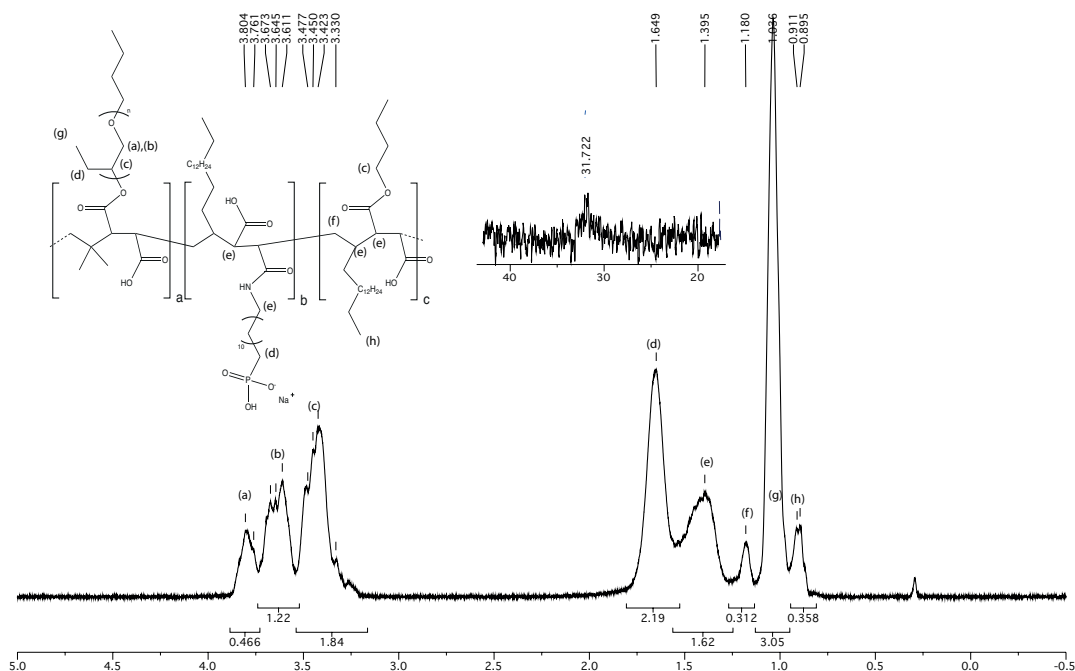


Figure 2.11: Representative NMR spectrum of the hydrophobic polymer.

resolved in deuterated benzene than in deuterated chloroform. The NMR spectrum is shown in Fig. 2.11.

The main contributions of the PBG chains are the peaks labelled (a), (b), (c) in the range of 3-4 ppm. Here, mainly the protons in the neighborhood of the ether oxygen contribute to the signal. Three different peaks are obtained, because apparently the chemical shift of the two protons of the $-O-CH_2-$ group splits in two peaks because of different chemical environments, mainly due to the ethylene side-chain. The contribution of the hydrocarbon $-O-CH(C_2H_5)-$ is shifted towards higher fields (lower ppm). There, contributions from the ester bonds, deriving from the backfilling with butanol are present and explain the higher integral compared to the other two peaks. The contribution of the C_2H_5 side-chains present in every repetition unit of the poly(1,2-butylene glycol) is visible in peak (d) and (g). Peaks (e), (f) and (h) derive from the other polymer functionalities and mainly derive from the polymer

backbone. Peak (e) originates mainly from the hydrocarbons in the vicinity of the carbonyl group of ester, amide or carboxylic acid. Peak (h) could be the CH₃-groups of the octadecene side-chains and/or the butanol backfiller, whereas peak (f) shows the contribution of the -CH₂- group present at the backbone. However, each of the big peaks deriving from the polyether chains contains contributions from the polymer backbone, namely hydrocarbon contributions of the octadecene side-chain and the butanol backfiller in peak (g), the CH₂-group in the neighborhood of the phosphonate contributes to peak (d) and in peak (c) contributions of the hydrocarbon connected to the ester is found. Therefore, it is nearly impossible to derive a grafting ratio from the NMR spectrum.

Additionally, due to the non-sufficient purification, it is supposed that there are unreacted polyether chains present in the polymer. That is due to the fact that alcohols are less efficient nucleophiles than amines and because of the already sterically hindered POMA backbone with C₁₆-side chains present at every repetition unit. This renders the backbone relatively challenging for nucleophilic attack of bulky polymers. Therefore, a non-stoichiometric reaction is assumed for the polyether side-chain and a relatively low grafting ratio is expected.

Therefore, MALDI-TOF analysis was carried out. The spectrum is shown in Fig. 2.12. Only the relatively sharp spectra with low polydispersity deriving from the PBG chains is visible and no polymer peak at higher m/z . This is another indication that unreacted PBG chains are still present inside the polymer.

The necessity to calculate the grafting density of the polymers, even though there are still unreacted side-chains present is still an unsolved issue for these polymers taking into account that the standard purification methods, such as precipitation, extraction and chromatographic approaches only show limited efficiency for this highly amphiphilic polymer. Additionally, due to the mainly hydrophobic character of the

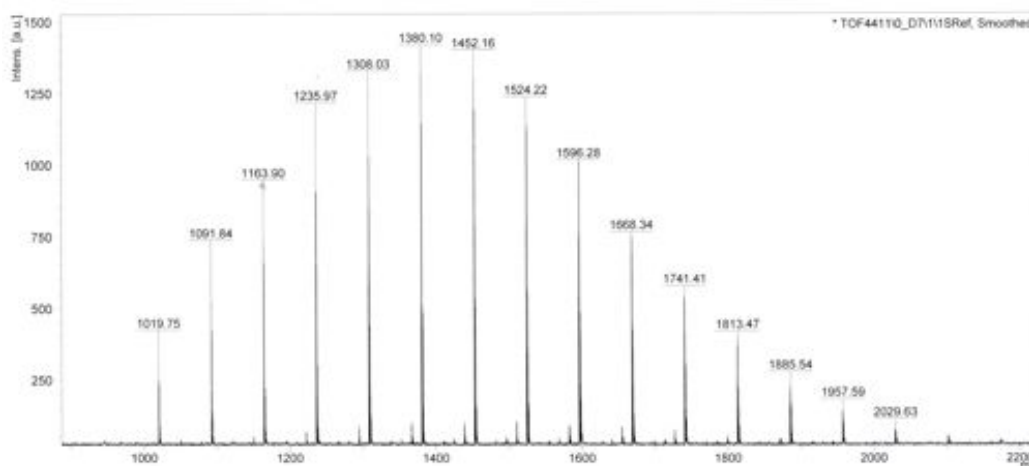


Figure 2.12: MALDI-TOF spectrum of the polymer in DCTB+Na Mix 1:10:1

polymer, apolar and especially aprotic solvents have to be used. Dialysis in those organic solvents was not successful, since aprotic solvents do not swell the dialysis membrane properly. Therefore, the grafting density could not be derived. Nevertheless, active species are present in the mixture of unreacted PBG and the POMA polymer with grafted side-chains. Still, the structure remains unknown. Because of the assumed, much higher surface-activity of the polymer species of interest - the POMA backbone, grafted with phosphonate anchor and PBG side-chain, it was decided to characterize the species adsorbed onto a surface. The further structural investigation is presented in Chapter 5, Sect. 5.5 on page 173.

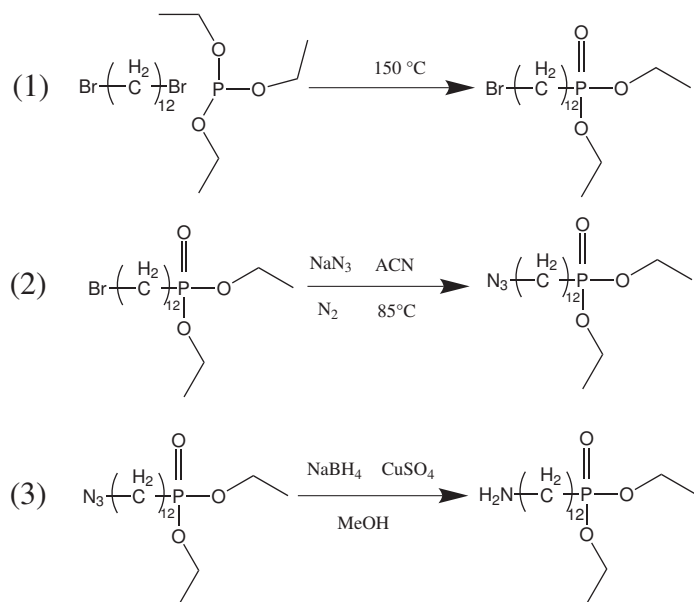


Figure 2.13: Synthesis of 1,12-Aminododecylphosphonic acid diethylester from 1,12-Dibromododecane in 3 steps

2.9 Experimental Synthesis protocols of the polymers synthesized

2.9.1 Synthesis of 1,12-aminododecylphosphonic acid diethylester

1,12-aminododecylphosphonate diethylester was synthesized based on the work of Dr. F. Durmaz [134] in 3 steps by (1) Michaelis-Arbusow Reaction [167, 168] of 1,12-Dibromododecane with 1 eq Triethyl phosphite (Fluka), (2) Finkelstein type Reaction of 1,12-Aminododecanephosphonate diethylester with Sodium azide in Acetonitril for 48h under reflux, (3) Reduction of the obtained azide with sodium borohydrate/Copper(II) sulfate [169]. The reaction scheme is shown in Fig. 2.13. The experimental synthesis protocol can be found at the end of the chapter in Sect. 2.8.

Synthesis of 1,12-aminododecylphosphonic acid diethylester (ADP) was synthesized in 3 steps by:

1,12-Bromododecylphosphonic acid diethylester: 1,12-Dibromododecane (5 g, 15.24 mmol) was heated to reflux and triethyl phosphite (2.53 g, 15.24 mmol) was added drop-wise for 30 min. The yellow solution was stirred at 150 °C for 4 h. The byproduct ethylbromide was distilled into a cold trap and the crude product was purified by column chromatography on silica gel with petroleum ether / acetone (2:1) (2.11 g, 36 %). The corresponding 1H - and ^{31}P - NMR spectra are shown in Fig. 2.14.

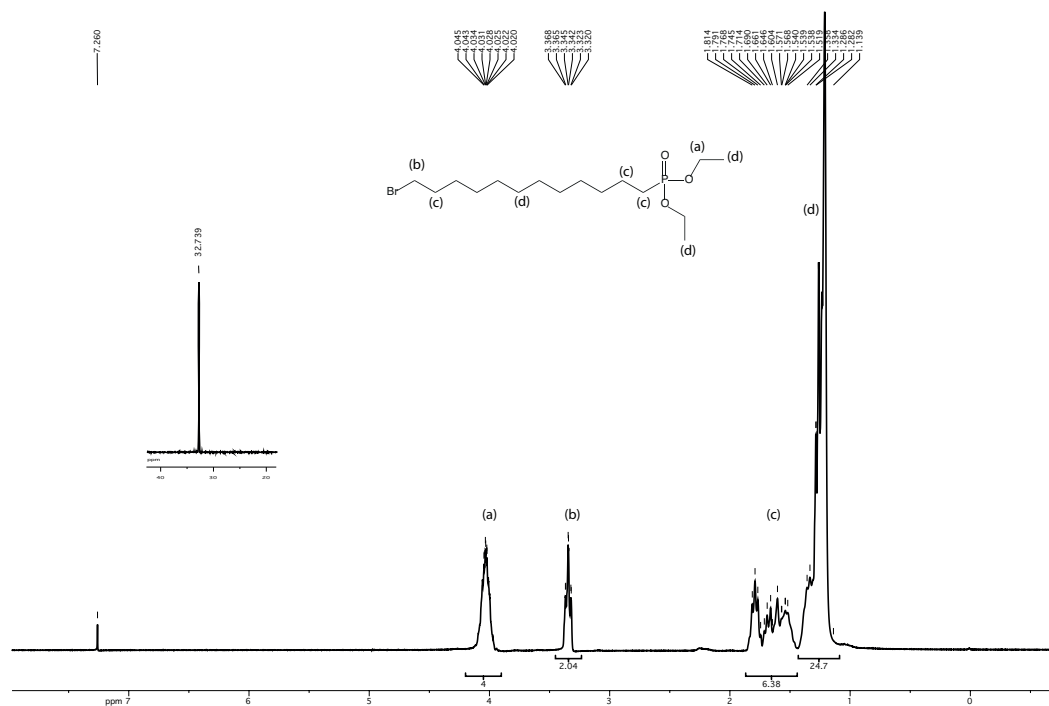


Figure 2.14: The 1H - and ^{31}P -NMR of 1,12-Bromododecylphosphonic acid diethylester

1,12-Azidododecylphosphonic acid diethylester: 12-Bromododecylphosphonic acid diethylester (2.3 g, 6 mmol) was dissolved in acetonitrile and sodium azide (1.2g, 18 mmol) was added under nitrogen gas flow. The reaction mixture was stirred at reflux for 48 h. The mixture was filtered over cellite and the solvent evaporated under reduced pressure. The resulting yellow oil dried under vacuum (2.1 g, 96 %). The corresponding 1H - and ^{31}P - NMR spectra are shown in Fig. 2.15.

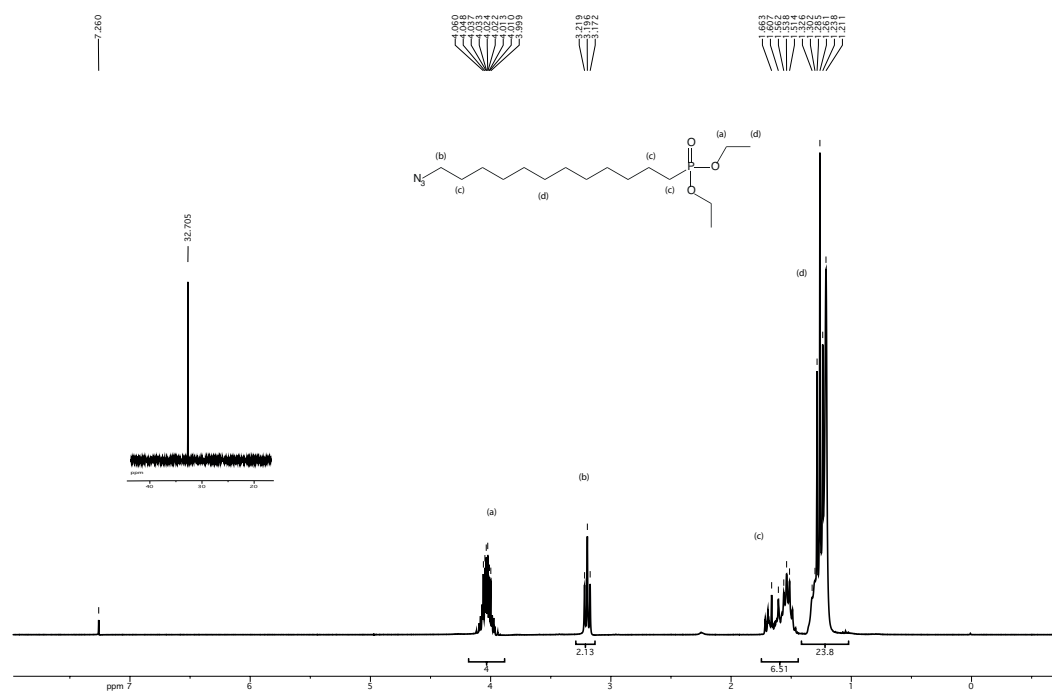


Figure 2.15: The 1H - and ^{31}P -NMR of 1,12-Azidododecylphosphonic acid diethylester

1,12-Aminododecylphosphonic acid diethylester: $CuSO_4$ (8.5 mg, 0.03 mmol) was dissolved in 10 mL methanol and 35 mg (0.9 mmol) $NaBH_4$ was added to the solution under stirring. 1,12-azidododecylphosphonic acid diethylester (1.2 g, 3.45 mmol) in MeOH (10 ml) was added to the black solution and additional

NaBH_4 (0.131 g, 3.45 mmol) was added slowly at 0°C over 1h under gas evolution. The black reaction mixture was stirred at RT for 12h. The resulting dark blue solution was made basic with 1N NaOH (pH 12-13) and filtered over cellite. The solvent was evaporated under reduced pressure. 100 ml dichloromethane was added and the mixture was extracted first with H_2O (3x50 ml) then with acidic brine (3x50 ml). The combined organic layers were dried over anhydrous MgSO_4 and concentrated under reduced pressure, resulting in a yellow gel (1.06 g, 96%). The appropriate ^1H - and ^{31}P - NMR spectra are shown in Fig. 2.16.

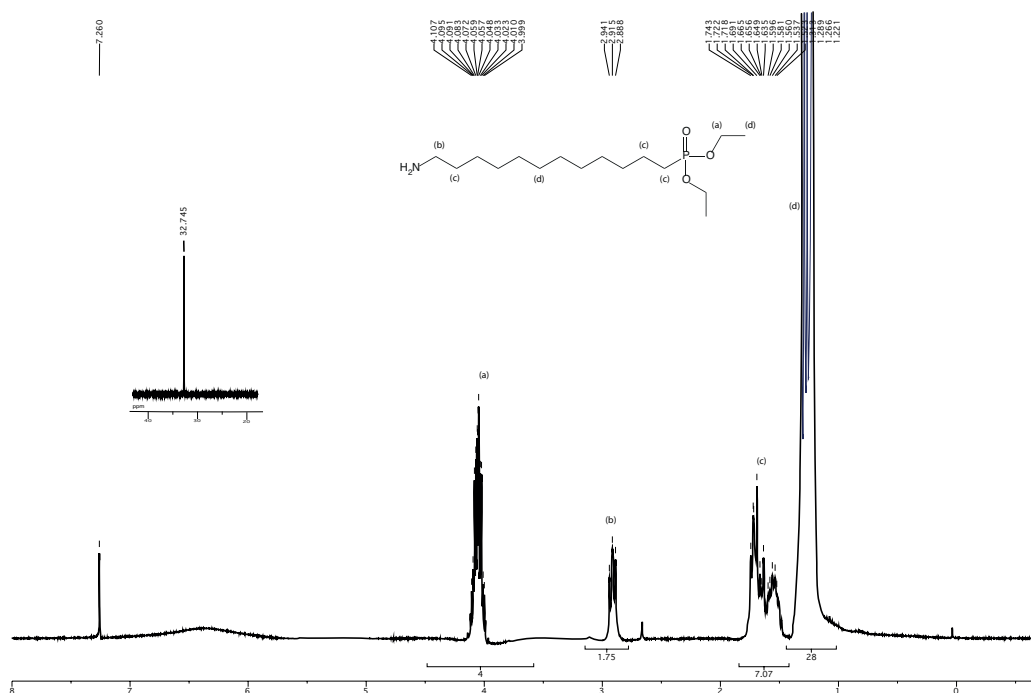


Figure 2.16: The ^1H - and ^{31}P -NMR of 1,12-Aminododecylphosphonic acid diethylester

The predominant peaks in the ^1H -NMR are the hydrocarbon groups in proximity to the phosphorus, either bound as ester or via the C-P bond and the $-\text{CH}_2$ group in

vicinity to the bromide. When reacting from the bromide to the azide, a slight shift of about 0.15 ppm towards higher fields of the corresponding peak of the neighboring $-\text{CH}_2$ group is observed. This peak is further shifted about 0.2 ppm in reducing the azide towards the amine. The main peaks at high ppm values correspond all well to the theoretic integral ratio of 2:1, whereas in the region of higher field, the integrals are slightly overestimating the theoretic hydrogen number, which is presumably an effect of incomplete drying of the product from solvent traces.

2.9.2 Synthesis of hydrophilic polymers

A general protocol of the hydrophilic polymers is given in the following:

The hydrophilic polymers were synthesized using poly(isobutylene-alt-maleic anhydride) (Sigma Aldrich) as reactive backbone polymer, which was heat-treated overnight in dry state at 150°C under vacuum. After dissolution in dry DMF (Sigma Aldrich), the polymer O-(2-aminoethyl)-O'-methylpolyethylene glycol (mPEG-amine) was added in terms of the calculated substoichiometric weight relative to the maleic anhydride functionalities present at the PIMA and stirred overnight at room temperature and argon atmosphere. After 20 hours reaction time, the surface anchor 1,12-amino-dodecyl-phosphonate diethylester was added in the calculated substoichiometric weight relative to the maleic anhydride functionalities at the PIMA and stirred at RT for another 20h under argon atmosphere. In order to achieve the same polymer composition for different backfilling reagents, the solution was separated in different parts and each reacted with a high excess (20 fold excess relative to the initial anhydride rings) of the backfilling reagent under stirring for 20h under argon atmosphere. The protected polymer was precipitated three times in cold n-pentane and dried under vacuum. The purified, protected polymer was then dissolved in dichloromethane and the reaction mixture was carefully degassed and saturated un-

der argon atmosphere. After having protected the solution from light by means of aluminum foil, a 10 fold excess of bromotrimethylsilane (Sigma Aldrich) was added at room temperature [170]. The hydrolysis of the formed intermediate was performed in a diluted methanol solution of NaOH (0.05 mol/l) and stirred overnight at RT. After precipitation of the polymer in cold n-pentan, the polymer was dissolved in a 0.05 mol/l, aqueous NaOH solution and dialyzed against water 3 times (Spectra/Por[®] 1 Dialysis Membrane, MWCO: 6-8 kDa). The resulting polymer solution was then lyophilized (for 48h at -60°C and 0.2 mbar), yielding in white powder which was then stored under exclusion of light at -20°C. The final products were analyzed at the end using ¹H- and ³¹P-NMR and elemental analysis.

Synthesis of the polymer generation PIMA(0.3:0.3, X)

The polymers were synthesized using 50 mg (0.32 mmol in terms of repetition units) PIMA and were reacted with 0.194 g (0.097 mmol) mPEG-amine and 31 mg (0.097 mmol) 1,12-amino-dodecyl-phosphonate diethylester according to the general protocol stated above. The reaction mixture was aliquoted in 2 different vials and backfilled each with either 0.1 ml (1.6 mmol) ethanolamine or 0.2 g (0.17 mmol) diaminohexane. After precipitation and drying, the polymers were deprotected by 0.45 ml (3.4 mmol) of bromotrimethylsilane each. After workup and purification, 100 - 110 mg of each polymer was obtained, corresponding to a yield of 70-80%.

Synthesis of the polymer generation PIMA(0.5:0.5, X)

The polymers were synthesized using 88 mg (0.75 mmol in terms of repetition units) PIMA and were reacted with 0.57 g (0.29 mmol) mPEG-amine and 92 mg (0.29 mmol) 1,12-amino-dodecyl-phosphonate diethylester according to the general protocol stated above. The reaction mixture was aliquoted in 3 different vials and backfilled

each with either 0.1 ml (1.6 mmol) ethanolamine , 0.15 ml (1.5 mmol) butylamine or 0.2 g (0.17 mmol) diaminoethane. After precipitation and drying, the polymers were deprotected by 0.45 ml (3.4 mmol) of bromotrimethylsilane each. After workup and purification, 0.15 - 0.2 g of each polymer was obtained, corresponding to a yield of 60-80%.

2.9.3 Synthesis of hydrophobic polymers

The hydrophobic polymer was synthesized using 0.3g (0.86 mmol in terms of repetition units) poly(1-octadecene-alt-maleic anhydride) (Sigma Aldrich) as reactive backbone, which was heat-treated over night in dry state at 150°C under vacuum. After dissolution in dry toluene (Sigma Aldrich), 0.77g (0.51 mmol) poly(1,2-butylene glycol) monobutylether (PBG-monobutylether) with 1.5 kDa molecular weight (Sigma Aldrich) was added. After 20h reaction time at 120°C, 0.11g (0.34 mmol) of the surface anchor 1,12-aminododecylphosphonate diethylester was added and stirred at 120°C for another 20h under argon atmosphere. As backfilling reagent, 0.5 ml (5.5 mmol) butanol at 120°C for 20h was used. The resulting polymer was dried under vacuum, resulting in a yellow, viscous oil. The deprotection of the polymer was performed in dissolving the polymer in a mixture of dichloromethane and pentane (1:1 v/v). The reaction mixture was carefully degassed and saturated under argon atmosphere. After having protected the solution from light by means of aluminum foil, 1.2 ml (10 mmol) of bromotrimethylsilane (Sigma Aldrich) was added at room temperature [170] . The hydrolysis of the formed intermediate was done by dissolving the polymer in pentane and adding a diluted methanol solution of NaOH (0.05 mol/l). An emulsion was formed, which was stirred overnight at RTT and the solvents were evaporated afterwards. The workup of the polymer was practically impossible because of the highly amphiphilic character of the polymer. Even

before deprotection, neither precipitation nor extraction was possible to separate unreacted PBG-monobutylether chains from the polymer. The polymer always stayed in solution or initiated emulsification. Gel permeation chromatography (Sephadex®) showed no effective separation of the polymer and unreacted PBG side-chains. The final products were analyzed at the end with ^1H - and ^{31}P -NMR.

2.9.4 Overview over all polymers synthesized

In Tab. 2.10, an overview list of the polymers synthesized within this thesis and including the naming based on the actual grafting densities found during bulk characterization of the hydrophilic, PEG-ylated polymers. Unfortunately, no grafting density could be derived yet for the hydrophobic, PBG-ylated polymer and therefore, the calculated grafting densities, as used in synthesis and assuming a 100% reaction efficiency are assumed. However, the actual grafting density, especially of the PBG side-chain is much lower due to steric hindrance during reaction and due to the not very reactive alcohol group used for coupling. This was confirmed by XPS analysis of the adsorbed polymers on TiO_2 (c.f. Chapter 5, Sect. 5.5 on page 173).

Table 2.10: list of polymers synthesized, including the naming used further in that thesis. Overview over the synthesized polymers, including the naming on the actual grafting densities

(*) The value 0 means that quenching with the backfiller was applied, but that theoretically, all anhydride rings should be ring-opened by either the respective ether or ADP. Due to the fact that no grafting density of the hydrophobic polymer could be derived, the synthesis composition is stated. The actual grafting density may be much lower for the PBG-ylated polymer .

Polymer	d_{ether}	d_{ADP}	d_{backfiller}	Backfiller
PIMA-(0.30:0.30, DAH)	0.30	0.30	0.4	Diaminohexane (DAH)
PIMA-(0.30:0.30, EA)	0.3	0.3	0.4	Ethanolamine (EA)
PIMA-(0.40:0.45, DAH)	0.40	0.45	0.15	Diaminohexane (DAH)
PIMA-(0.40:0.45, EA)	0.40	0.45	0.15	Ethanolamine (EA)
PIMA-(0.40:0.45, BA)	0.40	0.45	0.15	Butylamine (BA)
POMA-(0.3:0.7, Butanol)	0.6	0.4	0 ^(*)	Butanol

Poly(phosphonates) on TiO_2 for biomedical applications

3.1 Motivation / Introduction

3.1.1 Biomaterials

Upon inserting a foreign material into the human body, non-specific protein adsorption will immediately occur and can evoke diverse biological reactions, potentially interfering with the function of the medical device [171, 172]. Possible consequences can be inflammatory reactions, foreign-body responses and even failure or rejection of the implant. Therefore, surfaces of biomaterials require additional design to present the same signaling groups to the body as the surface of a clean, fresh wound, for example by attaching pharmacological active or bioactive agents on the surface to prevent adverse events during wound healing [171, 173]. Alternatively, surface coatings that minimize reactions due to their non-adhesive character may be considered [173, 174]. These devices can be used in medicine *in vivo* as blood-contacting devices, where

they have to resist fibrinogen and platelet adsorption, as implanted devices or urinary catheters, but also for *in vitro* diagnostic assays, biosensors and microchannel flow devices [171]. Also, similar considerations regarding biointeractions apply in non-medical uses, such as biofouling-resistant heat-exchangers [171] or ship-bottom paints improving marine biofouling resistance [175].

Table 3.1: Different strategies to achieve non-fouling surfaces, and different attachment strategies compared for PEG [173].

Surface strategy	Comments	Reference
PEG	Effective, but dependent on chain density; degradation by oxidants	[176]
PEG oligomers in SAMs	Highly effective, SAMs approach applicable for high variety of surfaces; low durability to elevated T	[177]
PEG containing surfactants adsorbed to the surface	Simple method, low durability, normally low surface densities	[178]
surface coating of polymers containing PEG blocks	Effective, may provide a relatively low density of surface PEG groups	[63]
Saccharides	Nature's route to non-fouling surfaces, some success, high degradation rate by bacteria and autoxidation	[124, 179, 180]
phosphatidyl choline	Has shown great success in many applications	[181]
poly(2-methyl-2-oxazoline)	Effective, more stable against autoxidation than PEG	[125, 126]
(Pre-) adsorbed protein layer	easy to implement but of low durability	[182]
Hydrogels	PEG and many other hydrogels have shown non-fouling behavior	[183]

There are many strategies to inhibit non-specific protein adsorption and non-fouling surfaces - an overview is given in Table 3.1. The majority of the literature on non-fouling surfaces focuses on surfaces containing the relatively simple polymer PEG, poly(ethylene glycol), also known as poly(ethylene oxide).

3.1.2 PEG-ylated molecules and protein resistance

PEG

PEG with the chemical structure $\text{OH-CH}_2\text{-[CH}_2\text{-O-CH}_2\text{]}_n\text{-CH}_2\text{-OH}$ is one of the best studied molecules for a great variety of chemical, biological, biomedical and biotechnological applications, because of its solubility in water and many organic solvents, its insolubility in water at elevated temperatures (cloud point), its capability to form complexes with metal cations, its high mobility combined with a large exclusion volume in water, its non-toxicity and weak immunogenicity [175]. Preventing protein adsorption [184] is, together with the control and/or reduction of electro-osmosis [185], one of the most studied properties of PEG for biotechnological applications.

Non-fouling surfaces with PEG layers

Various methods for covalent attachment of PEG to surfaces have been proposed [175, 176]. They usually require chemical derivatization of the terminal groups of PEG prior to reaction with a functionalized surface [186], but also other techniques have been applied, such as grafting to surfaces via a backbone polymer [187], incorporation as block segments in a variety of polymers [183, 188], cross-linking PEO homopolymers [175, 176], or PEG deposition on a rf-plasma activated surface [189, 190].

A very important aspect for the non-fouling properties of PEG surfaces is the necessary minimum molecular weight of the PEG chains, which depends highly on the packing density achieved [191–194]. The protein-resistance mechanism by the PEG surfaces may be due to a combination of factors, including the resistance of a polymer coil to compression due to entropic repulsion plus the resistance of the PEG molecule to release both bound and free water within the hydrated coil (osmotic repulsion) [171, 195, 196]. These factors, but also the protein size [197] and

the thermodynamic principles of protein adsorption, involving a number of enthalpic and entropic terms favoring (entropic gain of water-release, enthalpy loss caused by attractive coulomb interactions between surface and protein charges) or resisting (retention of bound water, entropic and osmotic repulsion of the polymer coils) adsorption [171, 193, 197] play an important role in determining protein-adsorption resistance.

It has been pointed out that the main disadvantage, which may reduce the utility of PEG chains for non-fouling surfaces in real-world situations, is their susceptibility to oxidative damage [196].

3.2 Surface Aspects and Applications of Titanium and Titania

Titanium and its alloys are widely used metallic biomaterials, especially for implants in bone or dental-related applications, due to their outstanding low specific weight combined with favorable mechanical properties, which are found to be close to those of bone [198]. The Young's modulus of titanium alloys is much closer to the values of osseous structures in comparison to other metals, thus rendering them a perfect choice for the design of load-carrying implants [198, 199]. Additionally, favorable physical and biological properties, including corrosion resistance due to the stable and dense protective oxide layer and biocompatibility [200, 201] and their high ductility, which facilitates processing make them important implant materials. Furthermore, it is found that titanium is capable of adsorbing proteins on the surface and inducing differentiation of bone cells. Despite all these beneficial properties, improved healing response and an increased speed of osseointegration are still active research topics,

especially for dental implants. Biologically inspired surfaces, bearing functionalities, transform titanium oxide into biologically more compatible surfaces [171, 198]. This could be a PEG-ylated surface as presented above (c.f. Sect. 3.1.1 on page 69), which is non-fouling, preventing the first step (protein adsorption) of the foreign body reaction cascade. More advanced and innovative bio-interfaces provide specific cell attachment points and tailor the selective attachment, proliferation, differentiation or mobility of the cells in order to increase the healing potential of the implant [171].

Due to the excellent behavior of the natural oxide layer to regenerate instantly after damage, that natural passivation of the surface renders titanium metal extremely stable against corrosion in air or aqueous solutions [202]. The driving force for this unusual behavior is that titanium has the highest affinity among all metals to oxygen and reacts spontaneously to titanium oxide, mainly of TiO_2 stoichiometry. The natural oxide film is quite dense, but mostly amorphous, and kinetically prevents the further oxidation of the underlying titanium metal. The oxide film growth is quite fast in the initial stage within hours to days, slowing down to much lower rates over months and years, reaching a steady state at a final thickness between 3-7 nm. Due to the limited oxygen diffusion, there is a gradient in the O/Ti ratio and thus a gradient in oxide stoichiometry and oxidation state of the titanium. The oxidation state of titanium thus varies with increasing depth from $\text{Ti}^{(\text{IV})}\text{O}_2$ through $\text{Ti}_2^{(\text{III})}\text{O}_3$ and $\text{Ti}^{(\text{II})}\text{O}$ to $\text{Ti}^{(0)}$ [198, 199].

Three different crystalline structures of TiO_2 (and some additional metastable or high-temperature forms), different in their coordination structure, exist: rutile (prismatic coordination), anatase (bipyramidal coordination) and brookite (orthorhombic coordination). Rutile is the most stable form, to which the two other forms convert upon heating. However, the native oxide films grown at ambient temperatures and atmospheric pressures on titanium normally show amorphous structure with a small degree in short-range order at the nanoscale [203]. At higher temperatures, crys-

talline structures of rutile and anatase can be observed. Interesting for all TiO₂ structures is their unusual high refractive index (above $n=2$), which makes titania an interesting material for optical applications, such as sensors [198].

The surface of titania exposed to ambient atmosphere or aqueous media has equivalent properties to all oxidic surfaces with different oxygen species found at the surface [204, 205]:

- oxide groups
- bridging oxygen groups
- hydroxide groups
- chemisorbed water molecules strongly bound to the Ti^(IV) cations

These different oxygen groups show different K_a values, depending on their coordination to the Ti cation. Basic hydroxides are bound to one Ti cation, whereas more acidic hydroxides derive from protonated bridging oxygen groups, simultaneously coordinated to two Ti cations [204–206]. Since these groups are amphoteric in contact to water, a net surface charge is created, depending on the pH of the solution. Therefore, the isoelectric point of a surface characterizes the pH, at which the overall positive and negative charges at the surface are equal and thus compensate, leading to a macroscopically uncharged surface. Positive or negative charges are thus created at the solid-liquid interface at a pH below or above the IEP, respectively. The isoelectric point of TiO₂ is between 5.2–6.2, depending on the type of titania. Therefore, at physiological pH, the titania surface consists of a slight negative net surface charge [109].

An interesting property is the band gap of TiO₂ of around 3 eV, displaying an absorption maximum in the UV, which is responsible for its photocatalytic activity. Upon absorption of UV light in the range of the band gap, electron-hole pairs

($e^- - h^+$) are generated. These can interact with molecules such as O₂ and create radicals, i.e. superoxide O₂⁻ or OH[·] from the reaction of water with h^+ . These radicals in return oxidize or reduce organic adsorbates, thus leading to their degradation to volatile species, mainly consisting of water, CO₂ and volatile hydrocarbons [207–209]. Therefore, UV-Ozone cleaning of the surface is especially appropriate for titanium dioxide surfaces, due to the combination of the ozone and the photocatalytic effect. In this thesis, the titanium metal oxide surface was considered as a stable system, the adsorbed hydrocarbon contaminants being carefully removed by an appropriate cleaning protocol involving ultrasonication and UV-Ozone [210], according to the cleaning protocol presented in 7.9.2. However, a certain amount of recontamination from air (in order to lower the surface energy) had to be taken into account even by minimizing the duration of the exposure of the cleaned samples to ambient atmosphere [211]. Consequently, in this work, adsorbed contaminants on titania were always carefully removed and the efficiency was checked regularly by surface-analytical techniques. All samples were handled, whenever possible in a laminar flow-box.

3.3 TiO₂ Substrates

For a defined preparation of titanium oxide surfaces, a magnetron sputter coating process (PSI, Villingen, CH) on silicon wafers (Si-Mat Silicon Materials, D) was used to deposit 15nm or 20nm ±3 nm (variation determined by ellipsometry) of TiO₂. This technique ensures a fast and reproducible production of titanium oxide layers over large areas with low amounts of defects and impurities and a very good homogeneity combined with a low roughness (close to atomically flat). The principle consists of sputtering a metal target of source material under plasma conditions - normally low pressures of argon gas including a specific fraction of oxygen, in order to generate oxide surfaces. The neutral charged species are then deposited at the surface of

interest by an argon gas vector. Normally the deposited oxide layer is of amorphous structure, even when some crystallized regions can be found, mostly consisting of rutile or anatase structure, but however within studies in our research group, no XRD pattern of the crystalline forms could be found [212]. Oxygen vacancies are produced within the material due to the fact that the deposition was performed under oxygen deficiency. This oxygen deficiency is supposed to favor higher surface concentrations of hydroxide groups at the TiO₂ surface once exposed to ambient atmosphere.

After sputter coating, the wafers were mounted on a polymeric foil used to support cutting of the wafer to 1x1 cm² pieces (Powatec GmbH, CH). The foil was removed and the cut samples cleaned by ultrasonication in toluene and isopropanol for 3x10min each to remove

- Dust from cutting, handling and removing of the polymeric foil
- Glue residues from the polymeric foil
- Hydrocarbon contamination, adsorbed from the ambient atmosphere

After cleaning, the samples were placed in 24-well plates for long-term storage and cleaned according to the protocol described in 7.9.2 before further use. This cleaning protocol was already well established [213], there was no need for a deeper reinvestigation of the surface cleaning. Due to the relatively fast growth of an airborne contamination adlayer on freshly cleaned TiO₂ surfaces, as described within the PhD thesis of Dr. M. Rodenstein [212], cleaned samples were used immediately after the cleaning process. Fig. 3.2 shows the XPS detail spectra for a clean TiO₂ surface and the chemical composition in at-% is summarized in Table 3.2.

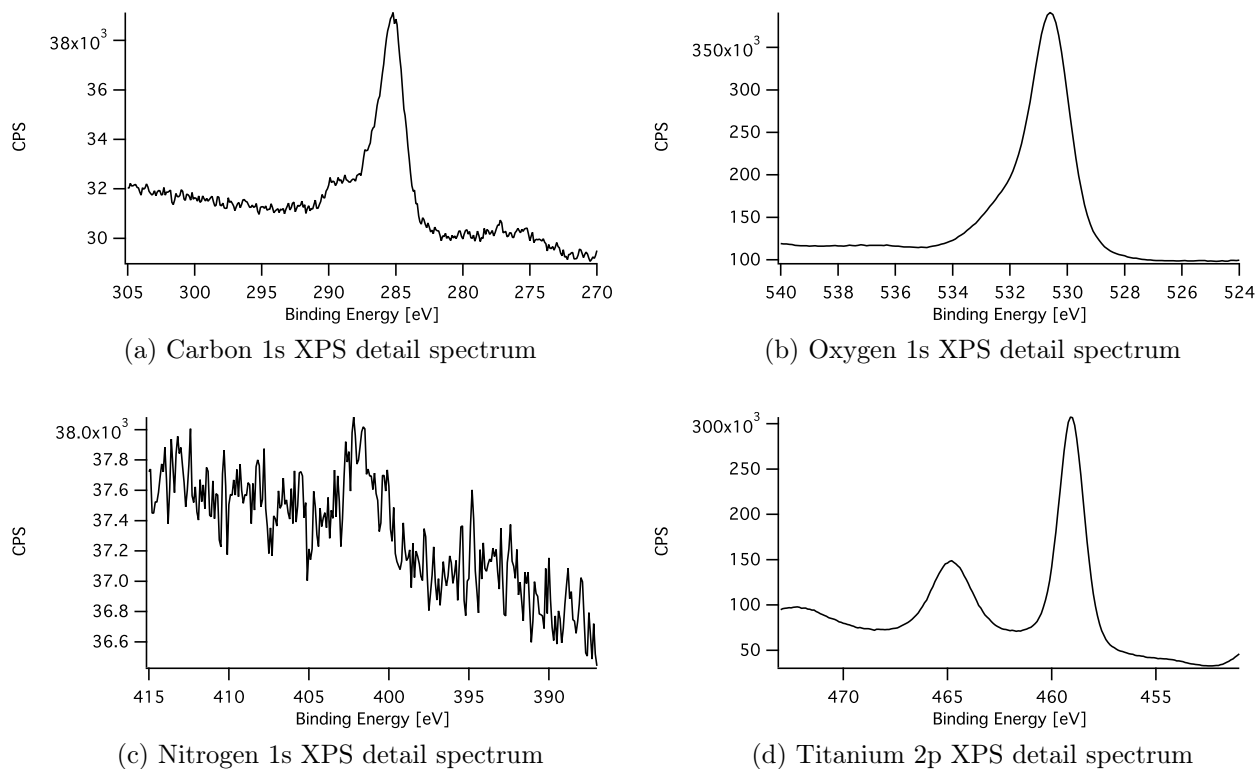


Figure 3.1: XPS (Sigma2) detail spectra of clean TiO₂ (≈ 20 nm on SiO₂ wafers) substrates. For TiO₂ layers with a thickness of less than 20 nm, an additional silicon peak arising from the underlying silicon wafer can be observed: (a) carbon spectrum, (b) oxygen spectrum, (c) nitrogen spectrum, (d) titanium spectrum.

Table 3.2: Atomic % for clean TiO₂ (on Si-wafers) as determined by XPS

Element	at-%
Carbon (C1s)	5 \pm 1
Oxygen (O1s)	66 \pm 2
Nitrogen (N1s)	0.5 \pm 0.2
Titanium (Ti2p)	27 \pm 2
Silicon (Si2p)	< 0.2 \pm 0.1 ¹

The IEP of 5.5 and a surface roughness of approximately 3.2 nm (RMS) were determined within the PhD thesis of Dr. W. Hartung [214] for similar TiO₂ coated Si wafers.

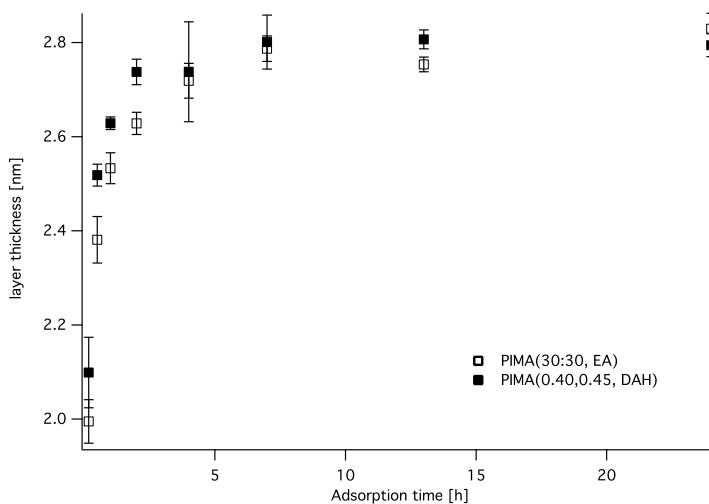
3.4 Characterization of additional poly(alkyl-phosphonate) adlayers on titania substrates

3.4.1 Adsorption Parameters

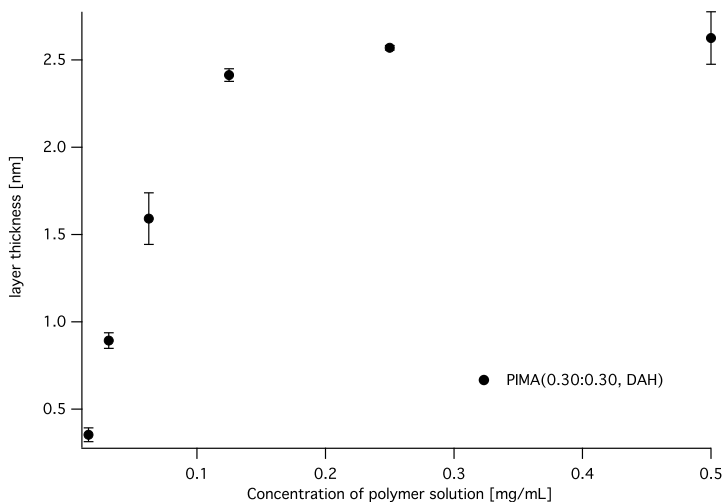
Development of a Standard Adsorption Protocol

Poly(phosphonate) polymers are conceptually a combination of alkanephosphonate SAMs [71, 84, 99, 213, 215] and polyelectrolyte graft copolymers such as PLL-g-PEG [28, 53, 63, 106, 216, 217]. Since the chemical structure of the polymers developed in this thesis have many structural similarities to the polymers developed by Dr. V. Zoulalian, especially due to grafted PEG chains and phosphonate anchor groups, many parameters and conditions have been chosen based on the experience with that system, e.g. solubility in water, polymer concentration during adsorption, adsorption time, protection of the samples to light during the adsorption process, temperature of adsorption, pH of the adsorption solution (important for the state of acidic/basic functional groups, hydrogen bondings, ...), ionic strength of the polymer solution (screening electrostatic charges).

The adsorption parameters of typical adsorbates used in our group are around



(a) Adsorption kinetics of polymers PIMA(0.30:0.30, EA) and PIMA(0.40:0.45, DAH) with a polymer concentration of 0.5 mg/mL



(b) Adsorption of polymer PIMA(0.30:0.30, DAH): concentration dependence with 24h adsorption time

Figure 3.2: Determination of adsorption kinetics and concentration dependence of poly(phosphonate) polymers by ellipsometry.

100 mg/ml solution of alkanephosphate SAMs with adsorption times between 24-48h [84,99,215], 0.1 mg/mL solution of PLL-g-PEG in HEPES2 for 20min adsorption time [63,105] and adsorption from an aqueous 0.5 mg/mL polymer solution overnight for the polymers developed within the PhD thesis of Dr. V. Zoulalian [135,136,218]. Phosphonate anchor groups adsorb much more slowly to a surface than polyelectrolytes, which are driven by electrostatic interactions. This is due to the different adsorption mechanism of the phosphonate anchor groups, which bind chemically to the surface and need much more time for the rearrangement of the chains, in order to obtain a dense packing [215,219]. Because of the negative charges present at the polymer backbone and additionally those of the phosphonate groups, the adsorption of the polymers to a negatively charged surface (at neutral pH) could possibly induce a repulsive retardation of the adsorption onto negatively charged surfaces, resulting in comparably slower adsorption kinetics.

In order to find the right parameter window to adsorb the maximum amount of polymers onto the titanium oxide surface, initial adsorption tests were performed. In Fig. 3.2a, the adsorption kinetics using the adsorption parameters developed from Dr. V. Zoulalian [133] was studied for two different polymers, which have the major structural differences (in terms of phosphonate and PEG grafting ratio and backfiller type) within the polymers investigated: polymer PIMA(0.30:0.30, EA) and PIMA(0.40:0.45, DAH). The VASE technique was used to measure the layer thickness of the polymers in a dry state after different adsorption times. The adsorption kinetics of the polymer PIMA(0.40:0.45, DAH) seems to be slightly faster, due to the higher content of phosphonates present in the backbone, but taking into account the experimental error represented by the standard deviations, the two polymers show similar adsorption kinetics. A more detailed study of the adsorption kinetics is shown further below in Fig. 3.3 on page 84. This shows that the adsorption plateau is reached after 2-3 h adsorption time at the chosen polymer concentration of 0.5

mg/mL. In order to check the concentration dependence of the adsorption, different polymer concentrations were used for adsorption on titania after a fixed adsorption time of 24h. This shows the relative differences in adsorption kinetics for different adsorption concentrations of the polymer for a fixed time. Since the adsorption time was fixed, the small layer thicknesses achieved with low polymer concentrations could have two different origins: a) with longer adsorption times the maximum layer thickness could have been achieved or b) even with longer adsorption times, the layer thickness would not have been reached the maximum possible layer thickness under the chosen experimental conditions. The concentration of the polymer in solution acts as a driving force for adsorption of the polymers to the surface, thus when the concentration of the polymer in solution becomes too low, the adsorption-desorption equilibrium is shifted, resulting in an incomplete polymer layer on the surface. Fig. 3.2a clearly shows that under the chosen adsorption parameters, the minimum polymer concentration necessary to reach the maximum polymer layer thickness is close to 0.2 mg/mL. Since there are structural differences between all polymers and a unified adsorption protocol would be of advantage, the polymer concentration was fixed at 0.5 mg/mL in order to be definitely at the adsorption plateau for all polymers. To give the polymers time for a possible slow rearrangement, which does not necessarily raise the layer thickness significantly, the adsorption time was set to overnight meaning 20h of adsorption time.

Investigation of the Adsorption Kinetics by TInAS

Adsorption kinetics and protein resistance were measured by the transmission interference adsorption sensor (TInAS), its measurement principle being presented in Sec. 7.2.3 on page 233. The instrument was still in an early stage of development, and therefore some features were missing during measurement, especially pumps to keep a constant flow in the flow cell and a thermostated environment in order to

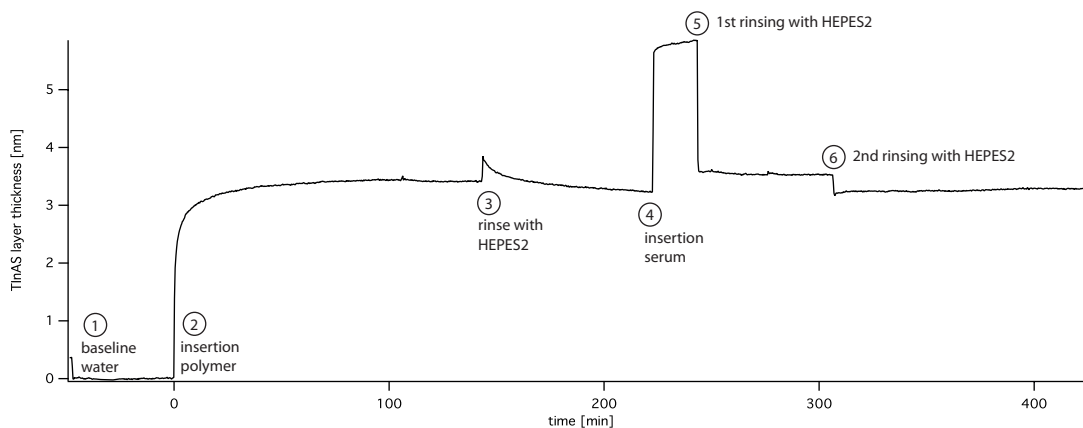
avoid temperature drifts. A cleaning protocol for the sensors was developed, yielding a clean TiO₂ surface, determined by XPS, allowing reuse of a specific sensor. The cleaning protocol consisted of rinsing the flow cell with Roche cleaning reagent, UV-irradiation of the sensor for 30min, ultrasonication in 0.1M NaOH, water and ethanol 2x10 min each, followed by UV-Ozone cleaning before storage, as described in Sect. 7.2.3. The cleaning protocol, especially the NaOH treatment leads to a reduction of the TiO₂ layer thickness, but the sensor could be used for a maximum of three times before a significant reduction in the adsorbed polymer layer was observed. The normal cleaning procedure for all kinds of samples (c.f. Sect. 7.9.2) was used just before the measurements.

A big drawback of the chosen adsorption parameters was the adsorption from water. A stable and horizontal baseline in ultra-pure water was never achieved during the experiments, even with immersion of the sensor overnight in water or really long baseline tests for several days. These problems are highly reduced when working in a salt-containing environment, e.g. HEPES2. This seems to be a salt-effect, which is not yet clearly understood. Apparently the electrostatic double-layer formed at the TiO₂ surface plays a quite important role to stabilize the signal drift. In order to have an idea about the real adsorption kinetics within the parameters chosen in Sec. 3.3 on page 78, the adsorption from water was performed until the drift of the signal after the adsorption kinetics was smaller or equal to the initial baseline drift before adsorption. This baseline drift was then subtracted as a linear function of time from the starting baseline drift to the drift observed at the end of the adsorption kinetics, resulting in two horizontal plateaus - the baseline and the end of the adsorption measurement. A combined TInAS experiment is shown in Fig. 3.3, which shows the baseline, adsorption kinetics and a subsequent serum test, in order to test the protein adsorption and thus the non-fouling behavior of the polymer brushes. Due to the length of the experiment, usually problems were frequently encountered, including

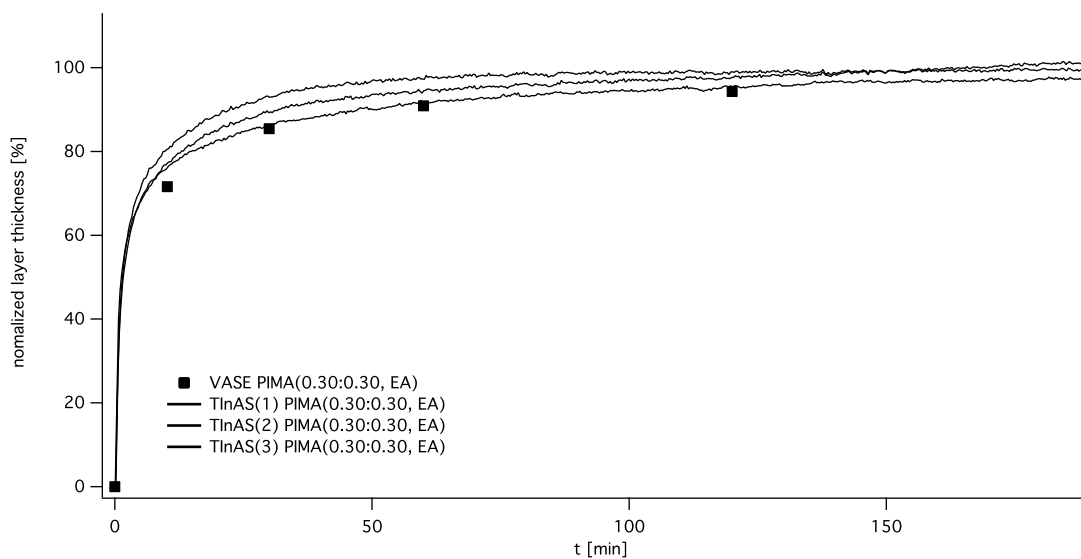
bubbles formation, slightly visible effects between day and night (probably a temperature effect). For these reasons and in order to have a defined polymer rearrangement time before the serum test, it was furthermore decided to separate both parts – kinetics and serum test – into two different experiments. In a first experiment, the adsorption kinetics were measured by TInAS. In parallel, sensors were coated with polymers according to the standard protocol described in Sect. on page 78 in order to have a fully reorganized and dense polymer brush at the surface, which is then comparable with the ex-situ tests performed, e.g. with VASE. These polymer-coated sensors were then introduced in the TInAS sensor and only the serum adsorption was measured. Due to the early stage of development of the instrument, a rather high deviation of the measurements was observed, namely up to 15% variation in the obtained layer thickness for the same polymer adsorption under standard conditions. This is therefore a bit higher than with the OWLS technique, which typically shows deviations of around 10% for standard polymers, such as PLL-g-PEG adsorption. The deviations stated here are not only due to instrumental factors, but also depend highly on the polymer system investigated and on the sensor batch.

In Fig. 3.3b, normalized adsorption kinetics of several TInAS measurements and one VASE measurement are shown. These differences in adsorption behavior are partially induced by instrument factors (no temperature control, manual injection by syringes inducing a pressurized environment inside the flow cell, sensors with a quite high surface roughness, etc.) and random errors, such as in the polymer concentration. Qualitatively, it is found that the kinetics obtained by VASE are always slower than those measured by TInAS. This can be explained by the *ex-situ* procedure of VASE, where loosely bound polymers are removed during the washing step.

The kinetics obtained from TInAS and those from VASE (c.f. Fig. 3.2a) were fitted with the help of different Langmuir-type adsorption isotherms, already used to investigate the adsorption kinetics of SAMs. A Langmuir-type adsorption considers



(a) Exemplary TInAS experiment, describing polymer kinetics and serum testing starting from a baseline in water, polymer adsorption, subsequent rinsing and change to HEPES2 as biological buffer, serum test and heavy rinsing steps.



(b) Normalized kinetics of different TInAS measurements and one VASE kinetics of polymer PIMA(0.30:0.30, EA). The different TInAS measurements give a better indication of the differences in the kinetics observed for the same polymer

Figure 3.3: TInAS measurements of (a) an exemplary TInAS experiment including Serum test and (b) a normalized TInAS and VASE kinetics

important assumptions about the adsorption process, namely that

1. only monolayer coverage is possible
2. all surface sites are similar
3. there is no interaction taking place between already adsorbed molecules

The classical Langmuir isotherm is

$$\theta(t) = 1 - e^{-k_a \cdot t^a} \quad (3.1)$$

where $\theta(t)$ describes the surface coverage as function of time, k_a , the constant, effective adsorption rate, which is highly sensitive to all changes of the system, including solvent, substrate, temperature and concentration. The exponent a takes only 2 different values for the classical Langmuir theory, namely $a = 1$, when there is no diffusion limit and $a = 0.5$ for a fully diffusion-limited model. Eq. 3.1 can be rewritten to the following scheme in order to investigate not the surface coverage, but the film thickness in function of time $D(t)$, with D_{max} being the maximum layer thickness at the adsorption plateau.

$$D(t) = D_{max} \cdot (1 - e^{-k_a \cdot t^a}) \quad (3.2)$$

An exponent a differing from 1 is forcing k_a to have physically unrealistic units ($M^{-1}s^{-a}$), since the exponent must not have any unit. Therefore, the equations can be rewritten to the following

$$D(t) = D_{max} \cdot (1 - e^{-(k_b \cdot t)^a}) \quad (3.3)$$

Table 3.3: Fit parameters of the adsorption kinetics from TInAS and VASE (polymer concentration 0.5 mg/ml)

Measurement	Polymer	D_{max} [nm]	k_a [min ^{-a}]	k_b [min ⁻¹]	a
TInAS	PIMA(0.30:0.30)	3.2 ± 0.5	0.6 ± 0.1	0.3 ± 0.1	0.4 ± 0.1
	PIMA(0.40:0.45)	3.5 ± 0.2	0.7 ± 0.2	0.4 ± 0.2	0.42 ± 0.05
VASE	PIMA(0.30:0.30,EA)	2.80 ± 0.02	0.57 ± 0.05	0.19 ± 0.02	0.35 ± 0.03
	PIMA(0.40:0.45:DAH)	2.79 ± 0.02	0.53 ± 0.05	0.22 ± 0.02	0.42 ± 0.03

Generally, the best fit was obtained when fitting all parameters, including the exponent a . This unusual fit gives an indication, how well the adsorption curves can be described via the classical or diffusion-limited Langmuir models. Interestingly, neither the classical ($a = 1$) nor the diffusion-limited ($a = 0.5$) Langmuir model represent the actual adsorption kinetics, since a is fitted to be ~ 0.4 . The results are summarized in Tab. 3.3, where the fitted adsorption constants for eq. 3.2 (k_a) and eq. 3.3 (k_b) and the other fit parameter a are summarized for a polymer concentration of 0.5 mg/ml in the adsorption solution. For polymer concentrations of 1 mg/ml, consistent values of D_{max} and a were measured, but the adsorption constant was higher, at $k_a = 1.0 \pm 0.1$ and $k_b = 0.9 \pm 0.1$, respectively. Nevertheless, due to the high standard deviations, it was not possible to find relevant differences in the adsorption kinetics between polymers having a similar structure and only differing in the backfilling moiety. That is why for this study, these polymers are taken together and only the amount of phosphonate content is taken as distinction parameter. Even the adsorption behavior of these two polymer groups is comparable and not differing much within the standard deviation. The slightly slower kinetics determined by VASE measurements fits well with the kinetics investigated by TInAS, indicating that the adsorption investigation ex-situ and in-situ results in comparable values within the standard deviations and taking into account the differences of *ex-situ* and *in-situ* measurements. Still, the exponent a is fitted close to 0.4, indicating the even

slower reaction kinetics than it would be observed with a diffusion-limited Langmuir-type adsorption model. This means that the adsorption rate at low surface coverages is slightly faster than the rate predicted by the standard models, but with higher surface coverages, the rate is slowing down even below the adsorption rate obtained for the diffusion-limited case, yielding in a longer absolute adsorption time. Other, modified models based on the Langmuir model [220], e.g. the second harmonic generation model proposed by Dannenberg et al. [221] for thiol SAMs on gold or a second order Langmuir kinetics as used by Koutsioubas et al. [222] for phosphonic acid SAMs do not hold for the present adsorption behavior. Comparable results have been observed for different SAMs using the same fitting model [212]. These results indicate that the three assumptions presented on page 85 are not holding for the studied adsorption kinetics. Especially the last two points cannot be given and are ideal assumptions. Amorphous TiO_2 as used within this study could provide different surface sites for adsorption. Additionally, TiO_2 always shows a quite intense hydrocarbon contamination layer at the surface, which is (partially) replaced during the adsorption process and could lower the adsorption kinetics by limiting the accessible binding sites, especially at high surface coverages. Furthermore, the polymeric structure of the polymer favors different adsorption possibilities. Two (phosphonate and carboxylic acid groups) or for some polymers three (additionally amine groups) different functionalities can bind to the surface either by a more (phosphonates) or less (carboxylic acids) stable chemical binding or due to electrostatic interaction (amines). Therefore, more than one adsorption/desorption rate and binding strength are present at the polymer by taking into account all possible attachment points. Only looking at the phosphonate binding sites, mono- and bidentate binding can occur [72, 84, 223–225], rendering the system more complicated than it is for standard SAMs systems, such as thiols. The best interpretation for the adsorption kinetics being different from the standard, Langmuir-type model is a different adsorption mechanism. As already

shown in Sect. 2.6.3, DLS and SLS measurements are indicating agglomeration of the polymers, yielding extremely high molecular-weight values in the range of 10⁷ Da for the polymers dissolved in water at the concentrations used for the adsorption studies. This can be explained by the amphiphilic character of the polymers having a rather hydrophobic backbone including the C₁₂-hydrocarbon spacer to the phosphonate anchor and the highly hydrophilic moieties, especially the PEG chains and the free carboxylic acid groups. The highly amphiphilic character of the polymers was already complicating the workup and purification of the polymers, except for dialysis. The polymer tends to form micelles when dissolved in water, with the PEG chains pointing outside and the surface anchors trapped towards the core of the micelles. The adsorption still takes place due to the high chemical affinity of the phosphonates to titania surfaces, but the kinetics is hindered due to the micellation effect. There are more than one adsorption/desorption equilibria to consider with the surface, especially association/dissociation constants for the micelles. Additionally, for heavy and bulky aggregates such as micelles, the diffusion is slower than for the polymers itself, leading to slower adsorption kinetics, even when taking into account the diffusion-limited Langmuir model.

3.4.2 Chemical Composition of Polymer Adlayers on TiO₂ based on XPS Results

Species analysis and component composition of the adsorbed layer

With the XPS technique, all elements of the polymer and of the titania surface (except for hydrogen) can be analyzed, i.e. carbon (C), oxygen (O), phosphorus (P), nitrogen (N) and titanium (Ti). Since most of the XPS peaks contain contributions from several different chemical species, a systematic scheme was developed to derive the real component composition from the peaks by peak fitting. Especially the

C1s and O1s peaks are of interest for component analysis. The carbon peak contains only information of the chemical structure of the polymer (apart from possible hydrocarbon contamination), whereas the oxygen peak contains both contributions from the polymer and from the titanium oxide surface. The curve resolution started with an iterative peak fitting from values of binding energies (BE) obtained from literature [226]. During this process, some ratios between components were constrained according to the known bulk structure of the polymer, in order to get a reproducible and universal fit scheme for all XPS spectra. The fitted spectra are displayed in Fig. 3.4.

The phosphorus signal (P 2p) was fitted as a single doublet with the P 2p_{3/2} at 133 ± 0.1 eV and P 2p_{1/2} with a binding energy difference of +0.84 eV and a fixed-area ratio of 2:1. The titanium peak (Ti 2p) was fitted with a single doublet with a BE of 458.5 ± 0.1 eV for the Ti 2p_{3/2}, which corresponds well to the binding energy (BE) of titanium oxide. The Ti 2p_{3/2} and Ti 2p_{1/2} were fitted with and a fixed-area ratio of 2:1. The nitrogen signal (N1s) was fitted with two peaks, the main peak being at lower BE of 400.3 ± 0.1 eV and the second peak fitting a shoulder at higher BE of 401.9 ± 0.1 eV. This second peak cannot be explained by the polymer structure. There are several possible explanations for this peak. Since the polymers not backfilled with hexanediamine consist of only nitrogen bound within the amide groups, only one peak would be expected, whereas for those polymers backfilled with hexanediamine free amine groups would be expected. The second, smaller peak at higher BE can be assigned to the amine group or to a more electron-deficient state of the nitrogen, which could be explained by some oxidative degradation of the amide groups. Another explanation could be amine groups still present in the polymer structure, even for the polymers not backfilled with hexanediamine. In general, hydrogen-bonding effects between the neighboring carboxylic acid group and the amide group could explain well the second peak. Acid-base calculations indicate

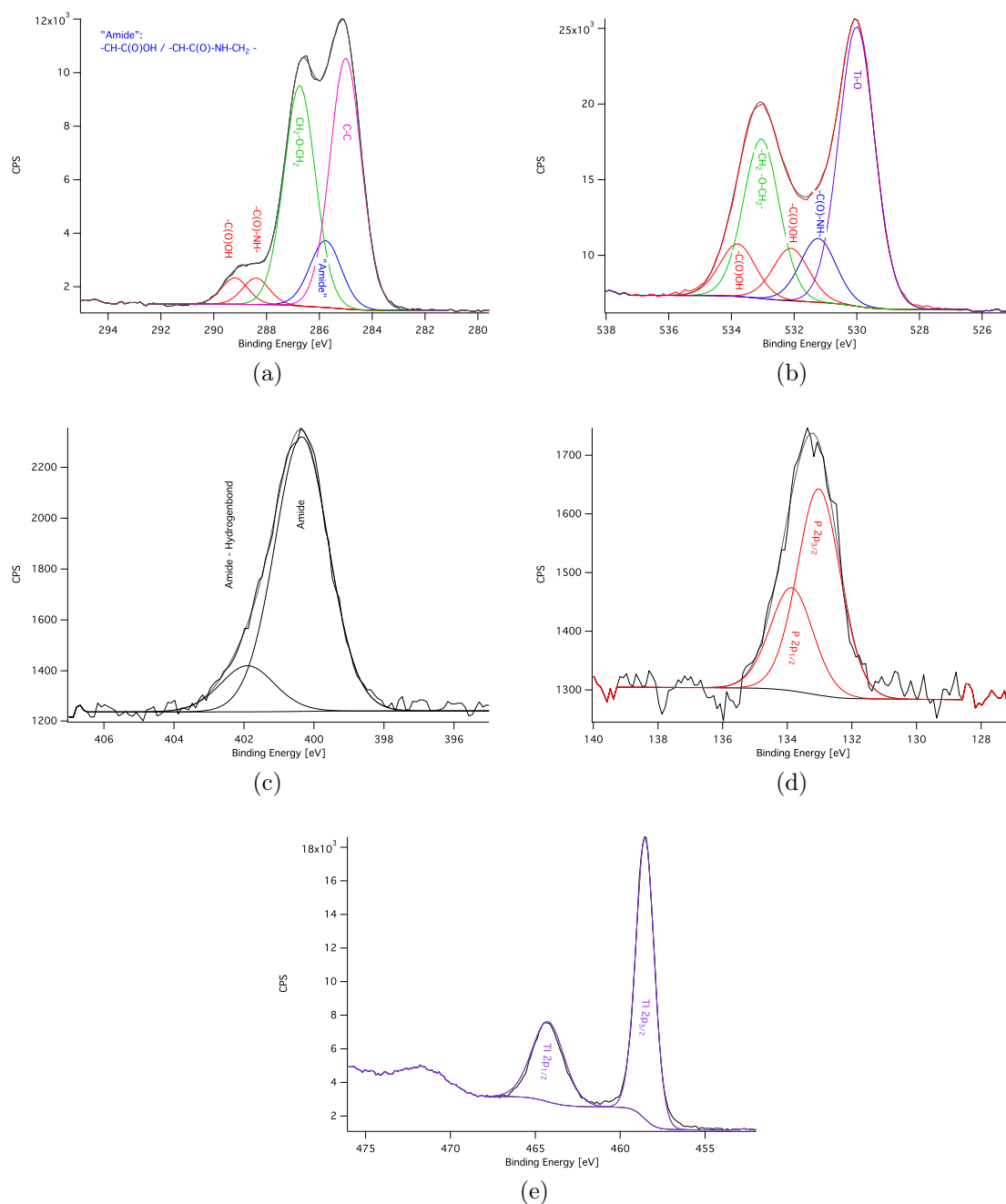


Figure 3.4: Peak modeling of the detail XPS spectra, exemplarily shown for the polymer PIMA(0.30:0.30, EA), measured with the Theta probe instrument. The subfigures show (a) C1s, (b) O1s, (c) N1s, (d) P2p and (e) Ti2p XPS detail spectra

Table 3.4: XPS fitting parameters used to O1s component analysis, using a Gaussian to Lorentzian ratio of 30%.

Component	Position constraints (eV)	Area constraints	fwhm constraints (eV)	Peak position (eV)
Ti-O	529.4 – 530.4	free	free	529.95 ± 0.1
CH ₂ -O-CH ₂	532.6 – 533.2	free	$1 \cdot fwhm_{Ti-O}$	533.1 ± 0.1
-C(O)OH	$BE_{Ti-O} + 2.1$	free	$1 \cdot fwhm_{Ti-O}$	532.1 ± 0.1
-C(O)OH	533.2 – 533.9	$1 \cdot A_{-C(O)OH}$	$1 \cdot fwhm_{Ti-O}$	533.7 ± 0.1
-C(O)-NH-	$BE_{Ti-O} + 1.23$	free	$1 \cdot fwhm_{Ti-O}$	532.1 ± 0.1

that at neutral pH most of the carboxylic acid groups are present in the dehydrogenated, negatively charged state. They are well known to be basic, hydrogen-bond acceptors, whereas the amide groups can act as hydrogen-bond donors. Therefore, a stable hydrogen bonding between the carboxylate and the amide group, additionally stabilized by the formation of a 6-membered ring could well explain the second peak observed at higher binding energies. A partial imide formation of the amide group with the neighboring carboxylic acid group, forming an 5-membered imide ring seems to be not very probable taking into account the high reaction temperatures necessary for the imidation reaction. Another, likely explanation would be a contamination of the surface already present during adsorption, e.g. nitrate salts would result in a peak shifted to even higher B.E. Therefore, the formation of hydrogen bonds between the amide and the carboxylic acid group, forming a stabilized, 6-membered ring will be assumed as the source of the second peak at higher B.E.

The Oxygen peak (O1s) was separated into 4 different chemical contributions deriving from the polymer and one contribution deriving from titanium oxide. The constraints for the peak fitting are shown in Tab. 3.4. As a general constraint, the fwhm of all peaks was fixed to be equal for all contributions. The peak at lowest BE at 529.95 ± 0.1 eV is the oxide peak deriving from titanium dioxide. The peak at 533.1 ± 0.1 eV derives from the grafted poly(ethylene glycol) chains (CH₂ -O-CH₂) and the free carboxylic acids show two characteristic peaks at 532.1 ± 0.1 and 533.7 ± 0.1

Table 3.5: XPS fitting parameters used to C1s component analysis, using a Gaussian to Lorentzian ratio of 30%.

Component	Position constraints (eV)	Area constraints	fwhm constraints (eV)	Peak position (eV)
C-C	285.0 (charge correction)	free	free	285.0
-CH ₂ -O-CH ₂ -	286.4 – 286.9	free	$1 \cdot fwhm_{C-C}$	286.8 ± 0.1
-C(O)-NH-	$BE_{C(O)-OH} - 0.80$	$1 \cdot A_{C(O)-OH}$	free	288.4 ± 0.1
-C(O)OH	288.4 – 289.4	free	$1 \cdot fwhm_{C(O)-NH-}$	289.2 ± 0.1
-CH-C(O)OH / -CH-C(O)-NH-CH ₂ -	$BE_{C-C} + 0.77$	$3 \cdot A_{C(O)-OH}$	$1 \cdot fwhm_{C-C}$	285.8 ± 0.1

eV for the carbonyl oxygen (-C(O)OH) and the hydroxyl group (-C(O)OH), respectively. The areas are constrained to a 1:1 ratio, since both peaks originate from the same functional group. Additionally, the relative position between both peaks was constrained to be 2.1 eV. this value was derived from reference BEs found in literature [226]. The contribution of the carbonyl carbon deriving from the amide groups (-C(O)-NH-) is found at 531.1 ± 0.1 eV and was set to a BE difference from the Ti-O peak of 1.23 eV.

The carbon peak (C1s) was fitted with 5 different chemical contributions, all deriving from the polymeric adlayer. The constraints used for the component analysis are shown in Table 3.5. The full width at half maximum was constrained to be equal for all sp³-hybridized carbons and separately for all sp²-hybridized carbons, resulting in a slightly lower fwhm for sp²-hybridized carbons. The hydrocarbon species (C-C) was used for charge correction and is therefore fixed to 285.0 eV. The contribution of the poly(ethylene glycol) ether chains (-CH₂-O-CH₂-) was found at a position of 286.8 ± 0.1 eV. The peak at 289.2 ± 0.1 derives from the free carboxylic acid (-C(O)OH), the carbonyl peak of the amide functionality (-C(O)-NH-) is constrained to be 0.8 eV below the BE of the free carboxylic acid and both to have the same area. This constraint is derived from the chemical structure of the polymer. All of the anhydride rings generate an equal amount of carboxylic acid and amide groups upon

nucleophilic attack of the amine. Assuming that no hydrolysis of the rings occurred during reaction and that all rings are fully reacted, the ratio of carboxylic acid to amide is expected to be 1:1. The peak fitted with area and position constraints at 285.8 ± 0.1 is a peak derived from different contributions, namely at α -position of the carbonyl groups (from both, free carboxylic acid and amide group) or at γ -position from the carbonyl of the amide group ($\text{C}(\text{O})\text{-NH-}\underline{\text{C}}\text{H}_2\text{-}$), in α -position to the amide nitrogen. The literature values [226] for these three contributions are within a range of 0.5 eV and are therefore not fitted separately but only as one peak with different contributions. This peak is constrained to have an energy difference of 0.77 eV to the hydrocarbon peak. This value was derived in fitting the spectra within a position window and averaging the values obtained. Since even small changes in peak position and peak area may drastically effect the fit of the other peaks, mainly by acting as a moderator between the hydrocarbon and the ether peak, it was necessary to constrain this peak further with another chemical constraint to get a reliable fit: the peak area was constrained to be three times the peak-area derived from the free carboxylic acid. Since one unit of the anhydride produces exactly one carboxylic acid functionality, but three carbons, which are included within this peak, the ratio is fixed to be 1:3. The area constraints introduced for the peaks $\underline{\text{C}}(\text{O})\text{-NH-}$ and peak summarizing the contributions of $\underline{\text{C}}\text{H-C}(\text{O})\text{OH}$ and $\underline{\text{C}}\text{H-C}(\text{O})\text{-NH-}\underline{\text{C}}\text{H}_2\text{-}$ were double-checked for consistency in comparing the results with the corresponding peaks of the resolved oxygen peak. Here no area constraints are used for both carbonyl peaks. The area ratio between both peaks is expected to be approximately 1:1, proving the chemical assumptions taken to fit the carbon peak, but actually the intensity of the peak derived from the amide carbonyl tends to be slightly higher. This is mainly due to contributions of the P-O-Ti and Ti-OH, and P=O, which are not explicitly included in this fit. These contributions are normally found between the Ti oxide peak and the amide carbonyl peak, but are not explicitly included in the curve synthesis. These

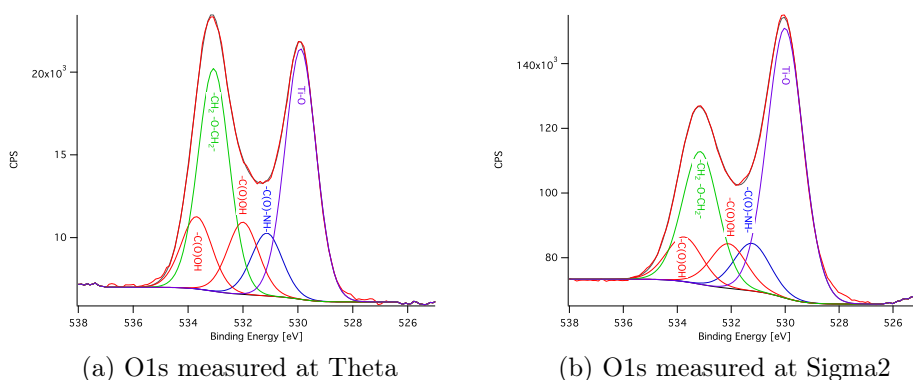


Figure 3.5: Comparison of the O1s peaks of the polymer PIMA(0.30:0.30, DAH) measured with the Theta probe and the Sigma2

contributions are fitted partially into the oxide and the amide carbonyl peak.

The experimental atomic compositions of all detected species are presented in Table 3.6 in order to give an overview over the resulting surface composition as detected with XPS. Here a distinction is needed between the two XPS instruments used. From these contributions, the chemical compositions of the polymer adlayer were calculated, excluding all contributions from the underlying titania layer, namely the Ti2p peak and the separate contribution of titania to the oxygen peak (Ti-O). In using only these contributions, the atomic percentage of every element was calculated in order to be compared with the recalculated bulk composition found by elemental analysis (EA, the data was converted from wt-% to at-%, and additionally the hydrogen contribution was excluded in order to compare the two datasets). The resulting data is summarized in Table 3.7.

Since all XPS measurements are carried out over large areas, the results presented here are averaged values, assuming a lateral homogeneity of the polymers at the surface, which is well confirmed by the low standard deviations. Both values derived from EA and XPS are well correlated, confirming that the average composition at the surface is close to the composition in the assembly solution. The observed de-

Table 3.6: Experimental component compositions derived from peak fitting of the XPS detail spectra. The abbreviation "amide" consists of the contributions -CH-C(O)OH / $\text{-CH-C(O)-NH-CH}_2\text{-}$

XPS	Ttheta				Sigma2			
	(0.30:0.30, EA)	(0.30:0.30, DAH)	(0.30:0.30, EA)	(0.30:0.30, DAH)	(0.40:0.45, EA)	(0.40:0.45, BA)	(0.40:0.45, DAH)	(0.40:0.45, DAH)
Polymer PIMA								
C1s	C-C	23.5 ± 0.5	21.5 ± 0.5	19 ± 2	18 ± 1	21 ± 1	21 ± 1	19 ± 1
	-CH ₂ -O-CH ₂ -	20.3 ± 0.5	25 ± 0.5	18 ± 1	20 ± 2	17 ± 1	18 ± 1	20 ± 1
	-C(O)-NH-	2.1 ± 0.1	2.0 ± 0.2	2.2 ± 0.2	2.2 ± 0.2	2.1 ± 0.1	2.1 ± 0.2	2.0 ± 0.1
	-C(O)OH	2.1 ± 0.1	2.0 ± 0.2	2.2 ± 0.2	2.2 ± 0.2	2.1 ± 0.1	2.1 ± 0.2	2.0 ± 0.1
	"Amide"	6.3 ± 0.2	6.1 ± 0.5	6.7 ± 0.7	6.6 ± 0.4	6.3 ± 0.3	6.3 ± 0.3	6.0 ± 0.4
O1s	Ti-O	15.0 ± 0.7	12.4 ± 0.2	20 ± 1	19 ± 2	20 ± 1	19 ± 1	20 ± 1
	CH ₂ -O-CH ₂	9.7 ± 0.5	10.9 ± 0.3	10 ± 1	9 ± 1	9.5 ± 0.5	9 ± 1	11 ± 1
	-C(O)OH	3.1 ± 0.2	3.5 ± 0.1	3.4 ± 0.2	3.2 ± 0.1	3.1 ± 0.1	3.1 ± 0.2	3.2 ± 0.3
	-C(O)OH	3.1 ± 0.2	3.5 ± 0.1	3.4 ± 0.2	3.2 ± 0.1	3.1 ± 0.1	3.1 ± 0.2	3.2 ± 0.3
	-C(O)-NH-	3.2 ± 0.2	3.4 ± 0.3	3.6 ± 0.5	3.5 ± 0.2	4.1 ± 0.2	3.9 ± 0.2	4.2 ± 0.3
N1s		2.12 ± 0.05	2.1 ± 0.1	1.7 ± 0.1	1.9 ± 0.1	1.7 ± 0.2	1.6 ± 0.1	2.1 ± 0.1
		0.37 ± 0.05	0.6 ± 0.1	0.2 ± 0.1	0.4 ± 0.2	0.1 ± 0.05	0.2 ± 0.1	0.3 ± 0.1
P2p		1.0 ± 0.1	0.9 ± 0.1	1.0 ± 0.1	0.9 ± 0.1	1.20 ± 0.05	1.25 ± 0.05	0.65 ± 0.05
Ti2p		7.1 ± 0.1	6.1 ± 0.1	8.8 ± 0.4	8.7 ± 0.6	9.2 ± 0.2	9.1 ± 0.2	6.3 ± 0.1

Table 3.7: Experimental atomic composition of the polymers as found in bulk (elemental analysis) and at the surface (XPS). The values in brackets for %N are the at-% when only taking into account the main nitrogen peak, without the peak at higher BE. The values in brackets for %P are values calculated with an experimental photoionization cross-section measured in our group (c.f. text for further details)

Polymer PIMA	Method	%C	%O	%N	%P
(0.30:0.30,EA)	EA	67.4	30.5	1.6	0.5
	Theta	70 ± 1	26 ± 1	2.7 ± 0.1	1.0(0.8) ± 0.1
	Sigma	68 ± 2	28 ± 2	2.7 (2.5) ± 0.1	1.4 (1.2) ± 0.1
(0.30:0.30,DAH)	EA	68.0	29.3	2.2	0.5
	Theta	69 ± 1	26.1 ± 0.6	2.9 ± 0.1	0.9(0.7) ± 0.1
	Sigma	69 ± 1	26 ± 1	3.2 (2.8) ± 0.1	1.2 (1.0) ± 0.1
(0.40:0.45,EA)	EA	68.1	29.9	1.4	0.6
	Sigma	68 ± 1	28 ± 1	2.5 (2.4) ± 0.1	1.8 (1.5) ± 0.1
(0.40:0.45,BA)	EA	67.6	30.3	1.4	0.6
	Sigma	69 ± 1	27 ± 1	2.5 (2.3) ± 0.1	1.7 (1.5) ± 0.1
(0.40:0.45,DAH)	EA	67.4	30.2	1.8	0.6
	Sigma	68 ± 1	28 ± 1	2.8 (2.5) ± 0.1	1.7 (0.7) ± 0.1

variations can be partially explained by surface contamination that is already present on the surface during polymer assembly (too high %C) and a degradation of the PEG chains during the XPS measurement (too low %O, too high %C). There are some problems in the interpretation of the %P and %N, which are both too high. Especially for the phosphorus peak, a lower at-% value would have been expected for the XPS measurements, since the phosphorus is expected to bind directly to the titania surface, and thus the electrons emitted from the phosphorus and titanium layer should be attenuated by inelastic scattering in the polymer layer above, leading to a lower apparent concentration. This main problem could be explained with a contamination of the samples with phosphorus.

Another possibility is the application of an experimental photoionization cross-section. The photoionization cross-section calculated first by Scofield [227] is based on quantum-mechanical calculations, assuming a free atom in vacuum. Since the chemical state

of the atom is not included into these calculations, there is a certain error for these Scofield values. Normally this error is assumed to be negligible in comparison to other, experimental and systematic errors of the measurement. Nevertheless, within the PhD thesis of Maura Crobu in our group, an experimental photoionization cross-section was recalculated from measured XPS intensities, in order to better understand the measured stoichiometry of poly(phosphate) glasses. The photoionization cross-section was determined in investigating different reference substances (salts) with a precisely known stoichiometry. The photoionization cross-section was then recalculated from the respective peak areas. This experimental cross-section is 20% higher than the initial factor published by Scofield. Since the phosphonates present at the polymer have quite a lot of structural similarities to phosphates and especially when bound to a metal oxide surfaces, the structure could be well compared to polyphosphates. It was tried to use this modified photoionization cross-section to calculate the atomic concentration of phosphorus. These new values are represented in Table 3.7 in brackets. These calculated values are now in better agreement with the results from elemental analysis. Still, there is a tendency for slightly higher phosphorus percentages. The values measured with the Theta probe are slightly different from the values of the EA, whereas the XPS results measured with the Sigma instrument show a greater deviation. Since the experimental photoionization cross-section was measured with the aid of the Theta probe instrument, there is probably some improvement in investigating this experimental value for the Sigma instrument, too. Since the polymer architecture is based on statistical effects, another probable explanation would be the preferential adsorption of polymers bearing higher phosphonate contents, yielding in a higher phosphate content at the surface.

The problems with the assignment of the peaks fitted into the nitrogen peak have already been discussed briefly on page 89, pointing out that there are two nitrogen species found for all polymers, whereas only one species would be expected for the

polymers not being backfilled with hexanediamine. This effect was already attributed to the hydrogen-bond-induced formation of stable, six-membered rings between adjacent carboxylic acid and amide groups. Still, the nitrogen content seems to be slightly too high, implying that there is most probably some contamination occurring during or before adsorption. In Table 3.7 both contributions are summed to the apparent nitrogen peak, whereas in brackets only the main peak is taken into account. This eliminates the probable hydrogen-bonding, but as well the amine contribution for the polymers backfilled with hexanediamine (since the other values don't change much due to the slight change within 1 at-% in the nitrogen content, the corrected values for the other elements are not named). Even by taking only into account the main nitrogen peak, the atomic composition still remains significantly higher than expected. This effect could be explained by a) a higher nitrogen content in the polymer, b) contamination or c) the need of another experimental photoionization cross-section as described for phosphorus derived from standard materials containing a well-known amount of amide bonds.

Another possibility to be discussed would be the synthesis and assembly mechanism of the polymers, which could explain the deviation of values of both phosphorous and nitrogen: during synthesis, a statistical approach is chosen, meaning that the functionalities are statistically spread over the backbone. This statistical approach implies differences in the chemical composition of different polymer chains: some contain more or less phosphonate chains, some more or less PEG and some more or less backfiller. The result is an averaged value, measured by EA or XPS (large area probing). While EA takes the real, averaged bulk composition into account, XPS takes the averaged composition at the surface, which is not necessarily the same composition as in the assembly solution. Given the fact that the content of phosphonates and PEG varies between different polymer chains, the adsorption kinetics and binding strength could be different depending on the phosphonate content at the polymer.

If polymers with higher phosphonate content are adsorbing faster or stronger, they could adsorb preferentially, either by the kinetics or by replacing the more loosely bound polymer chains at the surface during adsorption or rearrangement. The same argument would be true in looking at the apparent polymer weight. Since the number of grafted PEG chains is constrained by statistics, the polymers are supposed to have a non-negligible polydispersity. Smaller polymers are more mobile in solution, e.g. by diffusion, and additionally could be in a more flexible conformation (due to a lower grafting density of PEG and thus a lower steric barrier between these chains) which can facilitate the adsorption of those smaller chains. Both arguments yield a polymer composition, which is closer to the composition observed by the XPS results. A lower PEG content at the polymer backbone drastically increases the ratio of P (or N) over C (or O) and thus the atomic concentration of phosphorus and nitrogen are higher than expected. Another argument for this hypothesis is the fact that the ratio $[O]/[C]$ is higher for EA (0.43-0.45) than for XPS (0.37-0.41) analysis. Therefore, the grafting density of PEG at the surface is slightly lower than that obtained by EA. These slight differences can be explained by X-ray degradation of the PEG chains during the measurement, too. This could explain partially the slightly higher phosphorus and nitrogen contents measured. A plausible explanation for the higher phosphorus content can be given as above using the experimental photoionization cross-section derived from phosphate reference standards. Assuming that this cross-section could be transferred to the polymeric system, the phosphorus content was shown to be lower than the apparent surface concentration when using the experimental photoionization cross-section. The nitrogen content could not be correlated to a different polymeric structure. Since the amide groups are the connecting bonds between grafted moieties and backbone, a higher nitrogen content would imply a different grafting ratio of these moieties (PEG, phosphonate anchor and backfiller), but this should be then visible in differing carbon and oxygen contents. The nitrogen

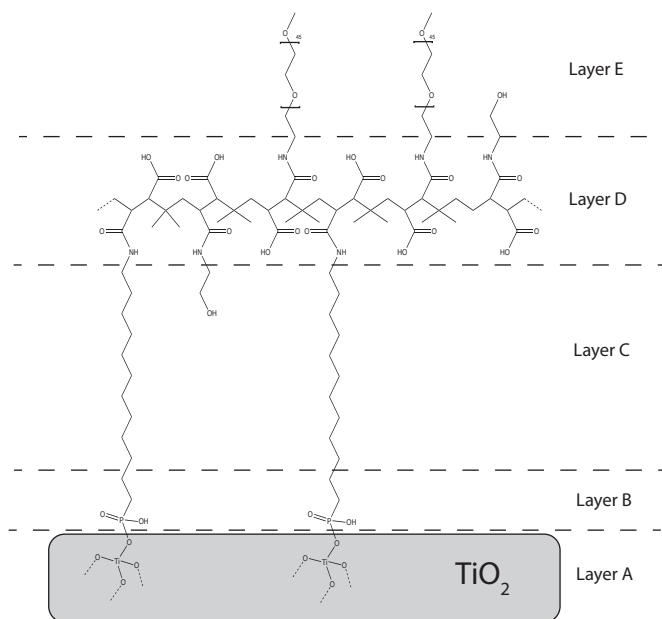


Figure 3.6: Ideal monomolecular polymer adlayer on titania assumed for the interpretation of the AR-XPS studies

content, which is found to be too high, can be explained by a contamination problem during adsorption.

Nevertheless, the atomic concentration at the surface is close to the composition derived from EA (summarized in Table 96) and confirms that the component concentrations on the surface are similar to those in the assembly solution.

3.4.3 Conformation and Structure of the Polymer Adlayer on TiO_2 based on AR-XPS results

In order to obtain preliminary information about the layered structure, namely the distinction between mono- and multilayer) and the lateral architecture of the polymer on TiO_2 , angular-resolved XPS (AR-XPS, c.f. section 7.2.2) measurements were performed. With increasing emission angle, the information depth of the probed sur-

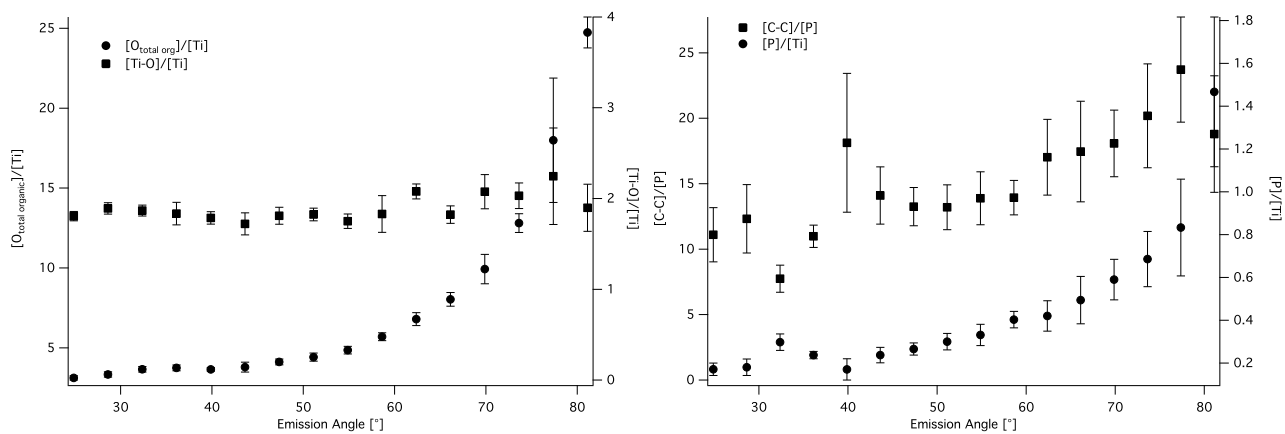
face is lowered, and therefore contributions of the upper part of the polymer layer becomes more significant. It is expected that the polymer binds with the phosphonate surface anchors to the titania surface, the backbone containing the amide and carboxylic acid groups and the top part of the polymer consisting mainly of PEG chains. A scheme and a layered model can be found in Fig. 3.6, where the layers are labeled from the bottom to the top of the polymer chain. Layer A represents the bulk titanium oxide, layer B consists mainly of the phosphonate groups binding directly to the titania surface, followed by layer C, whose main contribution is from the hydrocarbon chains between the phosphonate and the backbone. Layer D consists of the backbone, including all amide and carboxylic acid groups, whereas Layer E is the outermost layer, consisting essentially of the grafted PEG chains.

The spectra were acquired as described in 7.2.2 using the Theta probe instrument. The fitting of the detail spectra for each angle was performed in the same way as described above in Sect. 3.4.2. All atomic concentrations represent averages with standard deviations over 3 independent measurements. Assuming that the peak intensities are not modified by elastic collisions of the photoelectrons with the polymer adlayer, especially at high take-off angles, a simplified model can be derived: with increasing take-off angle θ , rising surface sensitivity and a subsequent decrease of the XPS information depth related to the surface normal is the basis of the angle-dependent phenomena. Thus the influence of the underlying titanium oxide will diminish with rising take-off angles. The contributions of the polymer adlayer are all expected to increase in apparent at% (depending on their localization in their adlayer) with increasing take-off angle. Two different polymers (PIMA(0.30:0.30, EA) and PIMA(0.30:0.30, DAH)) were measured in angle-resolved mode. Since both polymers show similar behavior, only the resulting graphs from one polymer PIMA(0.30:0.30, EA) are shown in the following.

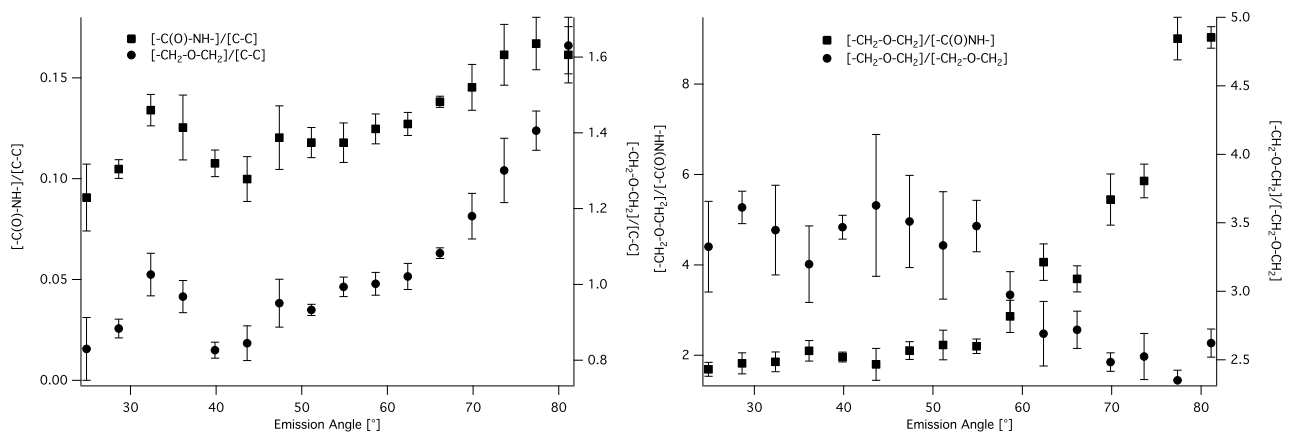
Since both carbon and oxygen have contributions from different layers, the resolved

components have to be taken into account. The layered model presented in Figure 3.6 can be confirmed by calculating ratios of atomic concentrations derived from different components. A constant value is expected when both components originate from the same layer, whereas angle-dependent phenomena are expected when the components taken into account derive from different layers - the more the layers are separated in depth, the more intense the angle-dependent effect. The ratios correspond only to the expected chemical (stoichiometric) ratios, when both components derive from the same layer.

In Fig. 3.7a, the component at% ratio of $[\text{Ti-O}]/[\text{Ti}]$ and $[\text{O}_{\text{total organic}}]/[\text{Ti}]$ are plotted against the take-off angle. It can clearly be seen that the ratio between oxidic oxygen and titanium is constant for all angles (because both contributions to the ratio are originating from the same layer) and correlates very well with the theoretical, stoichiometric ratio of 2. The ratio between all organic oxygen (excluded the contribution of titanium oxide) and titanium is rising with higher take-off angles, indicating that the polymer layer (layer B to layer E) is on top of the Titanium oxide surface (layer A). According to the layer model already described above in Fig. 3.6, the phosphorus layer is supposed to be the layer just on top of the titanium oxide, since the phosphonates are used as surface anchors. The graph in Fig. 3.7b shows the component intensity ratios of $[\text{P}]/[\text{Ti}]$ and $[\text{C-C}]/[\text{P}]$. Both ratios are rising with higher take-off angles, indicating that the layer containing the phosphorus (layer B) is in between the hydrocarbon and titanium oxide layers. Fig. 3.7c provides the information, that both the carbonyl and the ether contributions of the polymer are in a layer further away from the oxide layer than the hydrocarbon layer (component intensity ratios $[\text{C(O)-NH}]/[\text{C-C}]$ and $[\text{CH}_2\text{-O-CH}_2]/[\text{C-C}]$). The ratio $[\text{CH}_2\text{-O-CH}_2]/[\text{CH}_2\text{-O-CH}_2]$ in Fig. 3.7d is indicating that either the carbon fit is overestimating the ether content or that the oxygen fit is underestimating the ether content (the expected stoichiometric ratio between the ether contribution to the car-



(a) Component intensity ratios for $[Ti-O]/[Ti]$ and $[O_{\text{total organic}}]/[Ti]$ (b) Component intensity ratios for $[P]/[Ti]$ and $[C-C]/[P]$



(c) Component intensity ratios for $[CH_2-O-CH_2]/[C-C]$ and $[C(O)-NH]/[C-C]$ (d) Component intensity ratios for $[CH_2-O-CH_2]/[CH_2-O-CH_2]$ and $[CH_2-O-CH_2]/[C(O)-NH]$

Figure 3.7: AR-XPS atomic intensity ratios for polymer PIMA(0.30:0.30, EA).

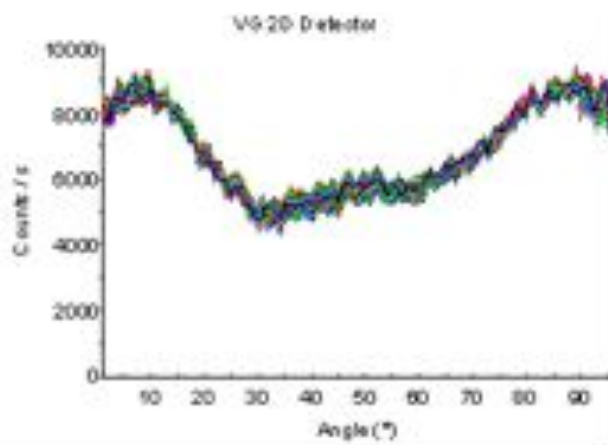


Figure 3.8: Sensitivity of the detector at different angles

bon and oxygen XPS peak is 2). To be sure that all contributions to the ether peak are originating from the same layer, the oxygen fit of the ether content is preferred and the ether over amide ratio ($[\text{CH}_2\text{-}\underline{\text{O}}\text{-CH}_2]/[\text{C}(\underline{\text{O}})\text{-NH}]$) shows that the ether is the uppermost layer (layer E). This proves that the expected layered structure is in agreement with the polymer structure found by AR-XPS.

Generally, a strange bump is visible for some of the at% ratios plotted in Fig. 3.7 in the range of the emission angles 0° and 42°. It has to be stated that this effect is due to a problem in the XPS detector. The response of the detector is shown in Fig. 3.8. For all angles a linear cps should be possible, but actually the detector's sensitivity is differing at a factor of 2, especially between the angles 0° and 42°. This effect is the reason for the unexpected behavior observed at these angles. Nevertheless, the qualitative trends derived above are clearly visible, especially when taking into account the region above 40° and confirm well the lateral architecture of the polymer as presented in Fig. 3.6.

3.4.4 Characterization and Study of Adlayer Thicknesses

Determination of the dry layer thickness

The dry adlayer thickness of the polymers was calculated from VASE, TInAS and XPS measurements. The layer thicknesses were calculated from the XPS spectra in two different ways. In case of AR-XPS data, the information of the Intensity areas of the Ti 2p_{3/2} peaks at two different take-off angles, namely at 42° and 62° was used:

$$\frac{I_{\theta_1}}{I_{\theta_2}} = \exp \left[\frac{d}{\lambda} \left(\frac{1}{\cos \theta_2} - \frac{1}{\cos \theta_1} \right) \right]$$

where d is the layer thickness in nm, λ the inelastic mean free path for Ti calculated by the model of Gries and typically depends on the density of the material through which they are travelling. θ_1 and θ_2 are the two take-off angles (42° and 62°) used to determine the information.

As previously presented in Fig. 3.8, the result of this method is partially affected by the non-linear response of the detector. Indeed, the two angles were chosen from a region, in which the response was as linear as possible (angles 42° and 62°). The layer thickness results to be within the range of 3.2 ± 0.2 nm.

The TInAS layer thicknesses were obtained from the adsorption plateaus of the adsorption kinetics and the dry layer thickness was measured with VASE. Here, two layer thicknesses are given: The layer thickness directly after polymer adsorption and the layer thickness after storage of the samples in HEPES2 solution for several hours. This decrease in layer thickness is due to desorption of polymer chains that are either loosely bound or entangled within the polymer brush, which desorb and diffuse into the buffered solution. The resulting, stable polymer brush is then used as a well-defined surface for protein tests, where no loss of layer thickness or polymer chains could be possible during the protein adsorption process.

Table 3.8: Dry polymer thicknesses evaluated by XPS, AR-XPS and VASE and TInAS. For VASE measurements 2 values are taken, one after adsorption and rinsing and one after a short-time stability test to test the thickness loss due to loosely bound polymer chains.

Polymer	Polymer layer thickness [nm]			
	VASE	VASE after stability	TInAS	AR-XPS
PIMA(0.30:0.30, DAH)	2.99 ± 0.04	2.66 ± 0.09	3.2 ± 0.5	3.2 ± 0.1
PIMA(0.30:0.30, EA)	3.03 ± 0.02	2.60 ± 0.04	3.2 ± 0.5	3.3 ± 0.2
PIMA(0.40:0.45, BA)	2.80 ± 0.02	2.62 ± 0.02	3.5 ± 0.2	-/-
PIMA(0.40:0.45, EA)	2.80 ± 0.04	2.58 ± 0.07	3.5 ± 0.2	-/-
PIMA(0.40:0.45, DAH)	2.90 ± 0.04	2.84 ± 0.05	3.5 ± 0.2	-/-

The layer thicknesses obtained are summarized in Table 3.6

Different layer thicknesses could be found for the different measurement methods. The layer thicknesses are consistent within one measurement method. The *ex-situ* VSAE measurement generally shows lower values than the *in-situ* TInAS method. AR-XPS, however shows layer thicknesses that are slightly higher, perhaps due to a small change in the detector sensitivity, and is thus not further discussed here.

Determination of the swollen layer thickness

Few additional measurements by QCM confirm the quite similar layer thickness achieved with all polymers investigated. The frequency shift ($\Delta f/n$) after polymer adsorption was always 33.0 ± 0.5 Hz on average over all measurements and polymers, resulting in an estimated adsorbed “wet” mass of 570 ± 30 ng/cm², calculated by the Sauerbrey equation (c.f. Sect. 7.2.4 on page 236). The value is much higher than the value derived from TInAS measurements (245-270 ng/cm²), because with this method, the hydration water of the PEG chains is also measured. In case of TInAS, the layer thickness obtained assumes a homogeneous layer of the polymer at the surface, resulting in a “dry” layer thickness, comparable with the results obtained

by VASE. This value can be recalculated, as explained in Sect. 7.2.3. In comparing both values, hydrated (QCM-) and non-hydrated (TInAS-) values, the hydration of the PEG chains x can be calculated as mass percentage by

$$x = \frac{m_{water}}{m_{total}} \cdot 100 = \frac{(m_{QCM} - m_{TInAS})}{m_{QCM}} \cdot 100$$

The calculated hydration is $55 \pm 2\%$ for all polymers. Additionally, in using both masses obtained by TInAS and QCM, an average layer density at the surface could be calculated by

$$\rho_{polymer\ layer} = \frac{m_w \cdot \rho_w + m_p \cdot \rho_p}{m_{total}} = \frac{(m_{QCM} - m_{TInAS}) \cdot \rho_w + m_{TInAS} \cdot \rho_p}{m_{QCM}}$$

This layer density $\rho_{polymer\ layer}$ of 1.03 g/cm^2 lies in between the densities of both, water (ρ_w) and polymer (ρ_p) itself, balanced by the hydration present in the polymer. The value of ρ_p is not known for the polymers investigated, but due to the structural similarities, the value of PLL-g-PEG ($\rho_{PLL-PEG} = 1.08\text{ g/cm}^3$) [166, 228] was taken instead. This layer density is useful to estimate the swollen layer thickness of the polymer adlayer. In using the simplification that the hydration of the PEG chains is constant within the entire polymer layer and that the PEG chains are uniformly stretched, a constant layer density throughout the layer can be assumed. The layer thickness can be estimated by $t \cdot \rho_{polymer\ layer} = m_{QCM}$, resulting in a swollen polymer layer thickness t of $5.5 \pm 0.3\text{ nm}$.

Table 3.9: Summary of the Serum adsorption test, measured with different methods. The adsorbed amount is displayed in terms of protein layer thickness (VSAE, TInAS), in terms of the at% ratio [C]/[N] measured by XPS and with the known [C]/[N] values of the polymer layer, a factor indicating the change towards smaller [C]/[N] after protein adsorption is calculated. The cell density at the surface after cell tests gives an indication as to how well the protein-mediated cell attachment still works at these PEG-ylated surfaces. The row labeled as TiO₂ is the serum test on pure titanium oxide.

Polymer	Serum VASE d[nm]	Serum XPS		Serum TInAS		Cell tests [cells/mm ²]
		[C]/[N]	reduction factor	d [nm]	m [ng/cm ²]	
PIMA(0.30:0.30, DAH)	0.00 ± 0.01	16 ± 1	1.3	0.25	15	600 ± 200
PIMA(0.30:0.30, EA)	0.03 ± 0.04	16 ± 2	1.2	0.35	20	700 ± 200
PIMA(0.40:0.45, BA)	0.09 ± 0.04	19 ± 2	1.03	0.35	20	500 ± 200
PIMA(0.40:0.45, EA)	0.10 ± 0.10	24 ± 1	1.01	0.25	15	500 ± 200
PIMA(0.40:0.45, DAH)	0.00 ± 0.01	20 ± 1	1.02	0.1	5	150 ± 200
TiO ₂	3.2 ± 0.1	4 ± 2	2.5	15.2	880	1200 ± 100.

3.5 Non-fouling properties and biological performance of poly(alkyl-phosphonate) coatings

Protein interactions with the PEG brush were tested after exposure of the samples for several hours to HEPES-2 buffer as described in Sect. 3.4.4, in order to desorb loosely bound or entangled polymer chains from the surface. A second reason is the hydration of the PEG chains before immersion into a protein solution. A dried PEG brush as used for VASE measurements could be more prone to protein adsorption and trapping inside the PEG brush than an already hydrated and stretched PEG brush. Therefore, in all possible cases, the PEG brush was rehydrated at least 15min before the serum test.

The serum adsorption was mainly characterized by VASE, XPS and TInAS. The

protein-layer thickness is directly measured by VASE and TInAS. There, additionally the adsorbed protein mass is calculated according to the formula presented in Sect. 7.2.3. For the XPS measurements, the $[C]/[N]$ at% ratio was taken as indicator for uptake. Since proteins do not have any additional elements that could be used to distinguish between the contributions of the polymer and serum proteins, another approach was chosen here. Since proteins are polyamides, they contain nitrogen in a much higher percentage than the polymers, where it is only used for the coupling of the side-chains. Here a high reduction in serum adsorption is visible, when the surfaces are coated with polymers. The ratio $[C]/[N]$ will get smaller when protein adsorption occurs. A reduction factor was calculated, which is basically $(([C]/[N])_{polymer}/([C]/[N]))_{after\ protein\ test}$.

Cell tests were performed to investigate whether there is a correlation between serum adsorption and cell attachment. A fully protein-resistant surface should not allow cell adhesion, since proteins mediate this process.

The serum-protein adsorption was always drastically decreased when compared to a bare, non-coated TiO_2 surface. Interestingly, the adsorbed layer thickness does not correlate at all for the TInAS and the VASE measurements. Generally, the *in-situ* measurement of TInAS leads to higher values compared with VASE (also for polymer adsorption), which can be the effect of rinsing after the adsorption process. In the *ex-situ* method VASE, the samples can be washed under high shear forces, e.g. by pouring solvent on it. The flow cell of the TInAS only allows more or less laminar flow inside, making the desorption of loosely bound proteins more unlikely. Still, the really high uptake of 15nm protein layer on bare titanium oxide is well above reported values. One possible explanation is the yellow color of the protein solution, which is changing the entire spectrum of the white light, which is recorded. Actually a high positive jump in the signal could be seen observed during the adsorption (when the entire flow cell is filled with the yellow liquid), which disappears after washing with

buffered solution and water. This is mainly attributed to a change in the refractive index n of the polymer solution. One possibility to explain these high values would be agglomerations of proteins, which then deposit on the surface, leading to a higher amount of protein adsorption.

Cell tests are performed by culturing T3T cells for 7 day on the titania surface. After life-dead staining, 8 photos were taken, from which the average cell number per mm² was calculated. Dead cells are shown in red, living cells are shown in green. The areas that are covered with a comparably large number of cells are situated towards the edges of the samples and never in the middle region. Thus it could be assumed, that those areas showing high cell populations, especially at the edges, could be areas where the polymer coating was damaged due to the sample handling using tweezers. Still all representative pictures of the sample surface were taken into account to calculate the average cell density at the surface, but due to this fact, the resulting standard deviations are quite high.

In looking closer to the differences in protein adsorption for the different polymer coatings, some clear tendencies could be seen. Generally, the polymers PIMA(0.40:0.45, BA), PIMA(0.40:0.45, EA) and PIMA(0.40:0.45, DAH) show a much better protein resistance than the polymers PIMA(0.30:0.30, DAH) and PIMA(0.30:0.30, EA). This means that the polymers differing only in backfiller, but with the same grafting ratio in terms of PEG and phosphonate have similar response. The polymers with higher PEG and phosphonate density show better protein resistance. Within the different backfilling agents, there is no real trend visible. It seems that the polymers backfilled with hexanediamine are showing a slightly better response against protein adsorption, whereas the backfilling with ethanolamine and butylamine are not differing visibly, but the protein-resistant effect is slightly worse than for those polymers backfilled with diaminohexane. The influence of the polymer structure and the backfiller is seen throughout all measurement methods, summarized in Table

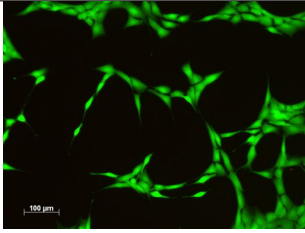
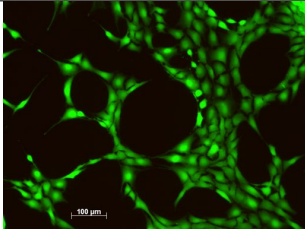
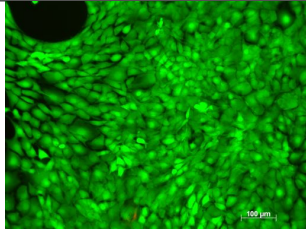
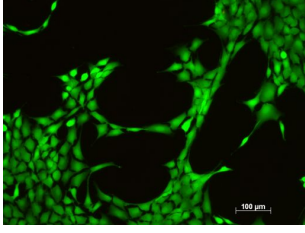
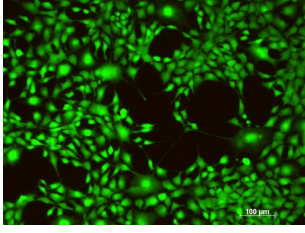
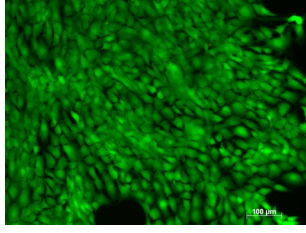
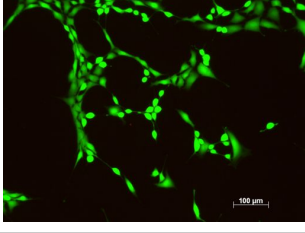
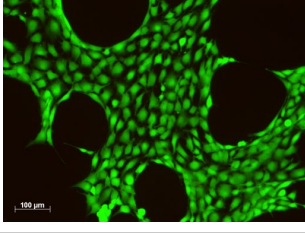
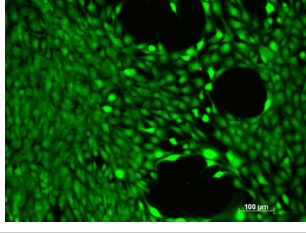
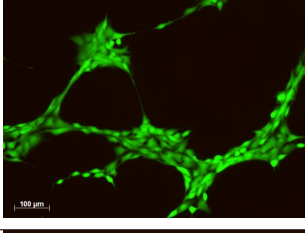
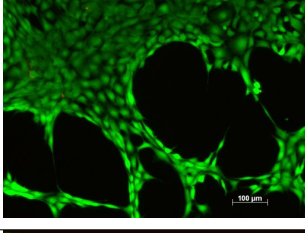
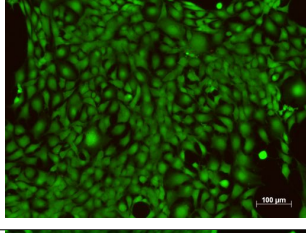

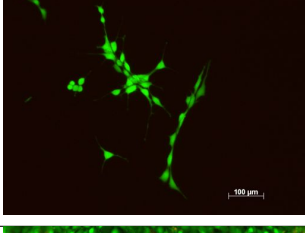
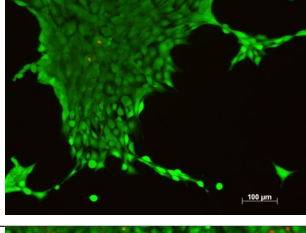
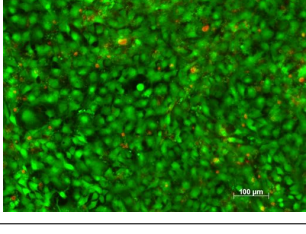
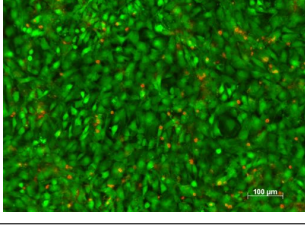
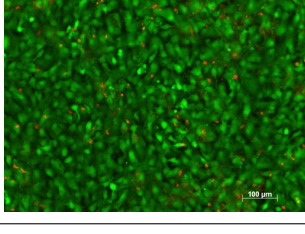
Polymer	minimum cells	average cells	maximum cells
PIMA(0.30:0.30, DAH)			
PIMA(0.30:0.30, EA)			
PIMA(0.40:0.45, BA)			
PIMA(0.40:0.45, EA)			
PIMA(0.40:0.45, DAH)			
Reference			

Figure 3.9: Fluorescence photos of the cell tests (life-dead staining, living cells in green, dead cells in red), the maximum, average and the minimum amount of cells found is shown for each polymer. The averaged number of cells are shown in Tab. 3.9, the average number of cells at the TiO₂ reference is 1200 ± 100.

3.9. There could be an additional, stabilizing effect of the amine groups, yielding a slightly attractive Coulomb attraction with the surface, facilitating the self-assembly process of the polymer.

3.6 Stability of poly(alkyl-phosphonate) coatings in aqueous media

A detailed study of the long and short-term stability of PLL-g-PEG and the poly(phosphonates) developed by Dr. V. Zoulalian can be found in his PhD thesis [133,135,136]. In the present study, the stability parameters of the newly developed polymers are compared to the performance of the polymers described there [133,135,136]. For this reason, an identical stability protocol was used. The stability of the adlayers was investigated in contact to acidic (pH 2, diluted HCl), basic (pH 9, diluted NaOH) and high-ionic-strength neutral, buffered solution (pH 7.2, HEPES2). The substrates were immersed in the test solutions for durations ranging between hours and 3 weeks. After the stability test, the samples were rinsed with ultra-pure water, dried with nitrogen gas and characterized by VASE. As already described in Sect. 3.4.4, a short stability test overnight reduces the layer thickness by a couple of Å, because loosely bound or entangled polymer chains desorb and diffuse away from the bulk surface. This drop in thickness is still included in the stability measurements presented here. In order to compare the polymers, the average of all measured layer thicknesses before the start of the stability test was taken as reference, the remaining adlayer thicknesses after incubation in the test solutions were then used as an indication of the adlayer stability and is presented as the percentage of the initial adlayer thickness.

In Fig. 3.10, the stability of two polymers, PIMA(0.30,0.30, EA) and PIMA(0.40:0.45, DAH) is summarized in the different media including a comparative summary of the findings of Dr. V. Zoulalian for 3 weeks immersion time, adapted from [133]. Since the

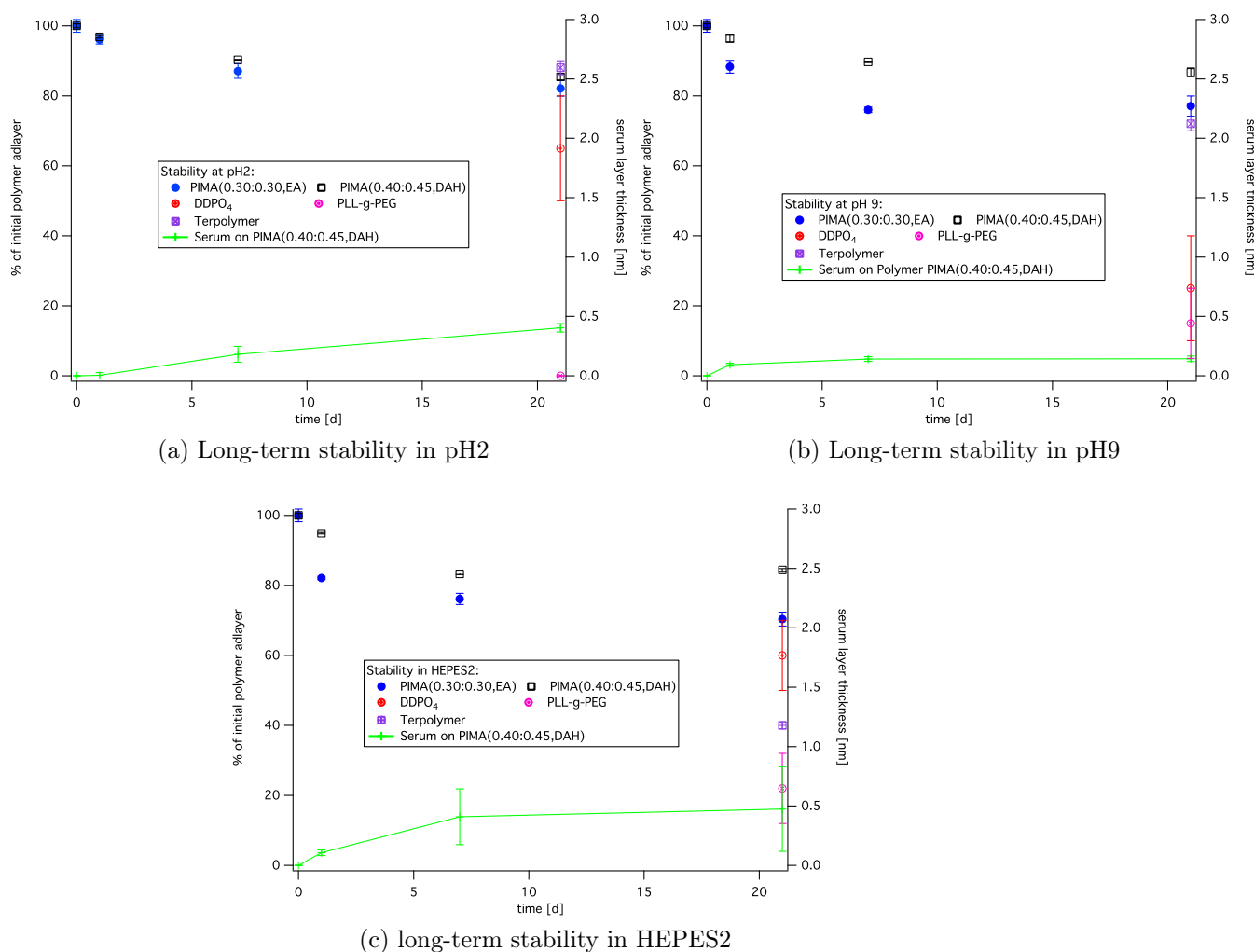


Figure 3.10: Long-term stability of polymers PIMA(0.30:0.30,EA) and PIMA(0.40:0.45,DAH) in different media including reference data for PLL-g-PEG, DDPO₄ and the Terpolymer of Dr. Zoulalian. Additionally, the serum adsorption for polymer PIMA(0.40:0.45,DAH) is plotted. Reference data adapted from [218]

stability is mainly based on the phosphonate content, these polymers with different phosphonate content are chosen to illustrate the difference in phosphonate content.

As expected, the two polymers show comparable stability in the different pH environments. The polymer with the lower phosphonate content shows a slightly reduced

stability at neutral and basic pH values, whereas at pH 2, the polymer stability is comparable for both polymers. After three weeks, the polymer adlayer thickness is reduced to around $85 \pm 2\%$ of the initial layer thickness at pH 2. The Terpolymer of Dr. Zoulalian reaches a stability of $88 \pm 2\%$ of the initial layer thickness after 3 weeks at pH 2. This indicates that at pH 2 the stability against desorption of the polymer is comparable for both polymer architectures. The SAM reference, dodecylphosphate, which contains comparable phosphate binding sites, has already a much lower stability against desorption. The remarkably lower values indicate that the effect of multisite binding, as it is the case for the polymer architectures, is drastically improving the long-term stability at this pH. PLL-g-PEG, however cannot bind in a stable way to Titania at pH2 and completely desorbs. This is mainly due to the electrostatic adsorption mechanism of PLL-g-PEG. It is adsorbed at neutral pH, where the titania surface is charged negatively and the amine adsorption sites are charged positively, resulting in an electrostatic attraction. This attraction is lost due to the low pH, rendering the titania surface positively charged, resulting in a net electrostatic repulsion between PLL-g-PEG and the surface. At neutral and basic pH values, the newly developed polymer seems to have a higher stability than the polymers investigated within the thesis of Dr. Zoulalian [218]. Even though the Terpolymer has a higher amount of phosphonates than the polymers developed within this thesis, the stability of the Terpolymer is decreased in comparison with the polymers PIMA(0.30:0.30, EA) and PIMA(0.40:0.45, DAH). For pH 9, the stability of the Terpolymer after 3 weeks is close to 75% of the initial layer thickness, comparable with the stability of polymer PIMA(0.30:0.30, EA). The polymer PIMA(0.40:0.45, DAH), however leads to an increased stability after 3 weeks at pH9, namely $85 \pm 2\%$ of the initial layer thickness remains. The rather high ionic strength seems to be the most unfavorable environment for the Terpolymer ($\sim 40\%$), whereas the polymers developed in this thesis have a much lower reduction of the remaining layer thickness after 3 weeks,

namely to $70 \pm 2\%$ (PIMA(0.30:0.30, EA)) and $84 \pm 2\%$ (PIMA(0.40:0.45, DAH)), respectively. The stability of PLL-g-PEG is much enhanced in neutral or basic environments compared to the total loss observed at pH 2, but the maximum layer thickness achieved is still only 30% of the initial value. Due to the negative charge of the surface, the electrostatic interaction between polymer and surface remains active, preventing a total polymer loss. Still, electrostatic interactions have much lower binding energies than the reversible, chemical binding that phosphonates are undergoing and thus the resulting adlayer thickness after 3 weeks is in the order of 50% of the initial thickness. Therefore, the phosphate SAMs always show higher resulting layer thicknesses after 3 weeks compared to PLL-g-PEG. The phosphonate SAMs indicate a much higher loss of polymer at basic pH, probably due to a lower stability compared to the polymer, which can be explained by the multisite binding effect of the polymer compared to the single-foot adsorption of the amphiphilic molecules of the SAM. Compared to both reference systems, the polymer system developed within this thesis shows a much higher stability, especially in the basic and neutral, high ionic strength environment. This seems not only an effect of the chosen phosphonate grafting ratio, but due to the interaction of the different functional groups present at the polymer backbone: carboxylic acid, free amine and phosphonate. Given an assumed lower stability of the phosphonates at high ionic strengths or high pH values, apparently the combination of electrostatic attraction of the amines and the phosphonate binding is enhancing the stability against desorption from the surface. The carboxylic acid functionalities seem to be too far away to the surface to contribute to an even more stable binding at acidic pH values. Therefore, the stability at acidic pH is close to the values observed for the Terpolymer. At high ionic strength and at basic pH values, the coating adsorption forces of the electrostatic binding due to the amines and the phosphonate binding render the binding to the surface more stable against environmental changes.

At the same time, serum adsorption on the remaining polymer layers was measured. In Fig. 3.10, the adsorbed protein layer thickness is plotted. After three weeks, no more than 0.5 nm serum are adsorbed in the worst case for the polymer PIMA(0.40:0.45, DAH). Due to the constantly lower remaining polymer thickness, more serum adsorption is observed for polymer PIMA(0.30,0.30, EA), reaching values up to 1 nm after 3 weeks. The maximum serum adsorption, including unusually high standard deviations was observed at high ionic strengths, in HEPES-2. This result is interesting, especially when taking into account the conclusions given in [218], that the low layer thickness of the Terpolymer found after 3 weeks in HEPES-2 was mainly due to a degradation of the PEG chains (autoxidation). Since all the stability tests were performed in the dark, one main degradation source could be excluded, but the biological buffer with ionic strength seems to interact in a different way with the polymer, leading to a loss of polymer thickness in the case of the Terpolymer and leading to high standard deviations in the case of the polymers investigated in this thesis. This could be an indication that within the coated polymer, the PEG chains are starting to degrade and the degradation continues via propagation. This propagation could lead to islands still covered with more or less intact PEG chains and islands with already degraded PEG chains. This hypothesis does not explain the high remaining polymer layer thicknesses we measure after the stability test, which should then have a similar standard deviation, even though the VASE system is averaging the measured value over a certain area.

3.7 Conclusions

In this chapter the polymer adsorption onto titanium oxide coated silicon wafers was presented. Due to the fact that these surfaces have been investigated and characterized already intensively, a rather short substrate characterization was presented. The

adsorption of the polymers onto titanium oxide surfaces was proven to be possible from aqueous solution. The adsorption properties of the polymeric system, i.e. the dependence of the concentration at fixed adsorption times and the dependence of the adsorption time at fixed polymer concentration on the adsorbed layer thickness was studied to find optimum adsorption parameters. In a second step, the adsorption kinetics of the polymers was investigated by TInAS and the kinetics fitted by a Langmuir-type adsorption isotherm. Interestingly, the time-dependence of the adsorption kinetics were found to be even slower than with the diffusion-limited model, which was explained by micelle formation in the adsorption solution and the thereby additional association - dissociation constants that slow down the adsorption kinetics have to be taken into account.

An intensive XPS analysis of the adsorbed polymer layer was conducted. In a first step, the XPS peaks were modeled and the chemical composition of the polymer was extracted. That showed a good agreement with the expected polymer structure, but as well with the elemental analysis of the bulk polymer, indicating, that the polymer is adsorbing at the surface in a comparable composition than it is in bulk. Furthermore, the structure of the polymer at the surface was investigated with AR-XPS, confirming that the adsorption mechanism occurs via the attachment of the phosphonates at the titanium oxide surface and the subsequent ordering of the polymer with the PEG chains pointing away from the surface and thus forming a polymer brush at the surface.

In a further step, the polymer-layer thickness was determined by different *ex-situ* and *in-situ* methods, and comparing the dry layer thickness below 3 nm with an estimation of the swollen layer thickness of approx. 5.5 nm, with an average hydration rate of 55%. The non-fouling properties of the polymers were investigated by different methods, yielding the conclusion that the polymers containing a higher PEG and phosphonate content generally show a better non-fouling performance. In comparing

the different backfillers, it seems that the diaminohexane backfilled polymers show a better performance than the other polymers. Cell tests confirm the findings made by protein-adsorption experiments. The polymer coatings showing the best protein-resistant properties show the best cell resistance, too.

Long-term stability tests were performed to compare the stability against desorption with other polymers. The polymers showed very good performance against desorption, and the polymers with higher phosphonate content were performing especially well, resulting in more than 80% of the initial layer thickness after 3 weeks in buffered, neutral solution, pH2 or pH9. The high stability of phosphonate bonding, combined with the multisite attachment strategy could be demonstrated here.

Poly(phosphonates) on MgO for biomedical applications

The results presented in this chapter are partially based on the master thesis of Henrik Forsgren [229] and Christoph Bruhin [230] and on the master project thesis of Robert Bielecki [231], within the scope of the biodegradable magnesium project, presented below (c.f. 4.1).

4.1 Motivation/Introduction

The present work is linked to the *graft*-copolymers described above (c.f. 1.5) and is part of the interdisciplinary project “Bio-functionalized, bio-degradable, nano-structured magnesium implant for biomedical applications”, a cooperative research project aiming at the development of a completely new stent system, including different interdisciplinary competences ranging from magnesium alloy development (Laboratory of Metal Physics and Technology, ETH Zurich), corrosion science (Laboratory

for Corrosion and Materials Integrity, EMPA), surface biofunctionalization (Laboratory for Surface Science and Technology, ETH Zurich), cell biology and toxicology (Laboratory for Biologically Oriented Materials, ETH Zurich) and stent technology (Biotronik, Berlin).

The main aim of the project is the development of an entirely new stent system, combining the advantages of both the Drug-Eluting Stent (stents coated with a thick polymer layer, which elutes drugs) and Absorbable Metal Stents (metal-based stents, which corrode in contact to water and are thus dissolved with time) [232]. Specially, the aim was

- the development of new Mg alloying systems with controlled dissolution rates and high ductility
- the adaptation of a surface layer consisting mainly of Mg oxides with improved corrosion resistance
- the deposition of a bio-functionalized adlayer that further contributes to a degradation protection as well as tissue regeneration for a specific period after implantation

The synergies of these three elements were determined by means of dedicated corrosion investigations, surface analytical studies and toxicological cell experiments. Part of this PhD thesis deals mainly with the polymer development and the subsequent analysis of such functionalized surfaces.

4.2 Surface Aspects and Applications of Magnesium and Magnesia

Magnesium is a material, which is less noble than other metals and therefore more susceptible to corrosion. Due to its low specific weight it is used especially for lightweight applications, e.g. in alloys combined with aluminum for transportation, such as in planes. Due to the high demand for fuel efficiency, magnesium alloys are entering more and more the automotive sector, especially for motor blocks, but also for wheels and parts of the auto body. The main advantages are [233]:

- lowest density of all metallic construction materials
- high specific strength
- favorable production properties (suitable for high pressure die casting, can be milled at high speeds, good weldability)

However, there is only a limited use of magnesium because of some poor properties, which have to be counteracted in demanding alloy processes or even by non-standard techniques such as fibre reinforcement. These properties are mainly the poor elastic modulus, the limited cold workability and toughness, the limited high strength and creep resistance at elevated temperatures, the high degree of shrinkage on solidification and especially the high chemical reactivity of magnesium. However, the lack of large-scale applications of magnesium alloys in the past has resulted in limited research and development funding. Consequently, there are only few optimized casting alloys and even fewer wrought alloys [233]. Nevertheless, the alloys which have been developed to provide a high range of properties and characteristics to meet the needs of a variety of application can be separated in 2 major classes, one containing aluminum as the principle alloying ingredient, the other containing zirconium.

Table 4.1: Composition of WE43 magnesium alloy [235] according to ASTM designations. RE stands for rare earths and consists of Nd and heavy RE (Yb, Er, Dy, Gd)

Element	Y	RE	Zr	Mg	Ni	Fe	Cu
wt. %	3.7-4.3	2.4-4.4	> 0.4	Balance	< 5 ppm	< 1 ppm	< 20 ppm

Aluminum-based alloys are strong and ductile, and have excellent resistance to atmospheric corrosion, whereas zirconium acts as a potent grain refiner for magnesium alloys.

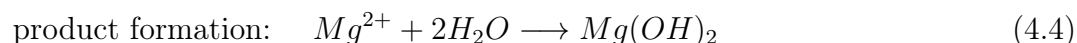
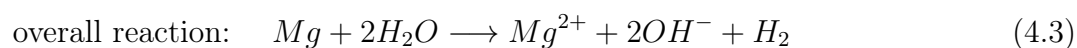
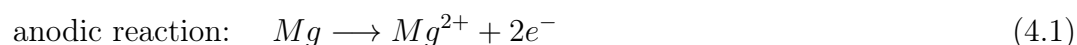
Because of incompatibilities between Al and Zr, zirconium-based alloys contain often other elements, such as rare earths, manganese, zinc or copper [233, 234]. Mg-Zr-alloys containing rare earths or yttrium are especially suited to work at temperatures up to 300°C. Yttrium and rare earths form eutectic systems of limited solubility with magnesium. Therefore, precipitation hardening is possible. The precipitates are very stable, raise thus creep resistance, corrosion resistance and high-temperature strength. Zinc as principle alloying element improves the strongness, ductility and toughness [233]. Due to the high costs, these elements are normally only used for high-tech applications.

The identification of magnesium alloys is standardized worldwide in the ASTM norm. Normally two letters indicate the two main alloy elements, followed by their rounded weight percentages

The alloy WE43, for example, is an alloy with a rated content of 4 wt-% yttrium (W) and 3 wt-% rare earths (E). Further elements can be strictly limited by ASTM, defining maximum upper limits, especially for iron, nickel and copper, which have tremendous negative effects on the corrosion behavior. A table of the full ASTM definition of WE43 can be found in Tab. 4.1

High attention has to be drawn to the ignoble character of magnesium and thus the possible corrosion performance of the bare metal and some of its alloys [233].

Magnesium dissolves in aqueous solution according to the following reactions [236]:



The pH of the solution increases with progression of the corrosion reaction (eq. 4.3), but the increase in pH favors the formation of an at least partially protective $Mg(OH)_2$ film by precipitation, as it is shown in eq. 4.4. This behavior can be shown in the Pourbaix diagram of magnesium in water (Fig. 4.1), which describes the thermodynamic stability of the different magnesium species dependent on the electrochemical potential and pH value. It indicates the stable formation of magnesium oxide and magnesium hydroxide as surface film at elevated pH values. In the presence of water, the oxide is normally hydrated to the corresponding hydroxide due to its higher thermodynamic stability. However, it has been found, that purest magnesium corrodes much more slowly than normal grade magnesium. This is due to the impurities of different other metals inside normal grade alloys, which initiate

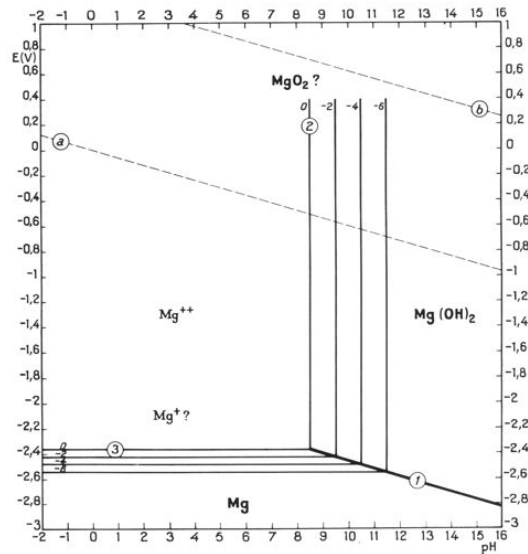


Figure 4.1: Pourbaix diagram of magnesium in water displaying the fields of corrosion (Mg^{++} field, left of line ②), passivation ($\text{Mg}(\text{OH})_2$ field and immunity (Mg field, below lines ① and ③) in dependence on potential and pH value. The position of lines ② and ③ shift in dependence on ion concentration in solution. Between lines ⑥ and ⑨ water is stable.

the corrosion by introducing an electrochemical potential due to their more noble character [237]. That is why there is a limitation for the main impurities found in magnesium within the ASTM definition of magnesium and its alloys, especially for nickel, iron and copper.

The degradation of magnesium leads to hydrogen gas evolution, as indicated in the eq. 4.3. This allows the easy determination of the degradation rate of magnesium as a function of the measured hydrogen evolution over time.

In the field of biodegradable implant materials, magnesium has become an interesting candidate as a bioactive substance. It naturally degrades within the body due to the contact with the body fluids. The main advantage of biodegradable implants is that they don't need to be removed in a second surgical intervention after serving their purpose, rendering them both, more convenient for the patient and more economical

for the whole health care system. Biodegradable materials, however usually yield a lot of degradation products to the body. The great advantage of magnesium is the fact, that magnesium ions, the main degradation product, are an essential element in the human body. Being a metal, its mechanical properties are more advantageous than those of other degradable, organic materials. To be well performing, biodegradable implant materials must possess certain properties [235]:

- in order to offer adequate support to the injured tissue, the mechanical properties of the implant have to be appropriate
- a moderate degradation performance helps to assist the healing process effectively and to prevent from early destabilization
- released degradation products during degradation need to be biocompatible

At a pH below 11.5 magnesium corrodes in aqueous solutions, as described in Fig. 4.1. The formation of OH⁻ ions and hydrogen gas upon the degradation of magnesium may harm injured tissue, as the pH value increases locally and gas bubbles may be formed. That is the main reason a relatively low initial degradation rate of the material is targeted.

4.3 WE43 Substrates

The investigated alloy is part of the Mg-Y-RE alloys family, further denoted as WE43. The exact composition of the WE43 alloy [235], according to ASTM designations is presented in Tab. 4.1. The alloy and the general function of the alloying elements is described in 4.2.

The WE43 was manufactured in 1m extruded bars ($\varnothing = 2.5$ cm). In order to avoid inhomogeneities present in the outermost shell, the bar was dressed to 2.2 cm of

diameter before slicing. Discs with a thickness of 2 mm were cut (Struers Accutom-50) and then all samples were ground three times with shrinking grain sizes up to 4000 SiC-paper and subsequently polished with 3 μm , 1 μm and 1/4 μm diamond particles on both sides, including the edgings. After each step all samples were cleaned by sonication in isopropanol, dried and the grinding/polishing progress controlled by optical microscopy. Heat treatment was conducted in a ventilated oven (Heraeus GmbH, Germany, model 750/1) at 490°C in ambient atmosphere conditions for 48 hours, being supported on tripods in order to minimize surface of contact. Cooling down after heat-treatment was achieved by steady air cooling.

The bare alloy was investigated in several studies, and shown to be a suitable candidate as an implant material [238–240], especially due to its relatively slow and homogeneous corrosion resistance in aqueous solutions. Additionally to the good electrochemical properties, it consists of beneficial mechanical properties, especially including an elastic modulus close to that of human bone [239]. Mainly the element Y in the alloy is responsible for the improved corrosion resistance of WE43. Both the incorporation of oxidized Y in the surface film [241, 242] and the advantageous influence of Y-rich precipitates in the Mg matrix, which slows down the propagation of corrosion [243] were found to be the reason for the enhanced degradation resistance of Mg-Y alloys. The Pourbaix diagram of yttrium is shown in Fig. 4.2. In comparison to magnesium the equilibrium line between the formation of $\text{Y}(\text{OH})_3$ and Y^{3+} is shifted towards lower pH values, close to neutral pH. This is not inhibiting the dissolution of both, yttrium and magnesium, but slowing down the dissolution in buffered medium in forming predominantly yttrium hydroxides at the surface.

A heat-treatment was developed within the PhD thesis of Dr. Hänzi [244]. These results are presented in [235, 244], a short summary will be given in the following paragraphs.

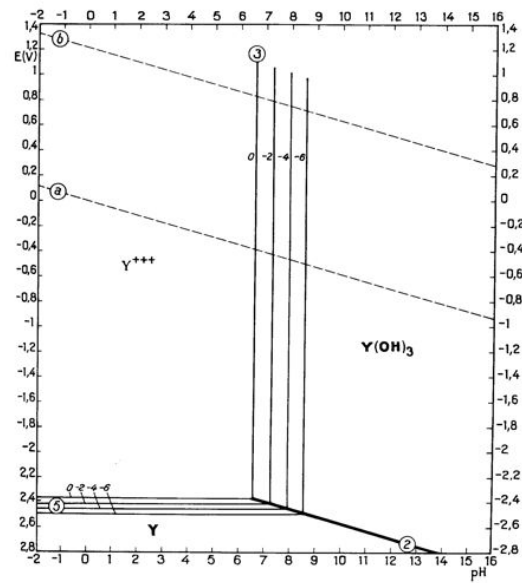


Figure 4.2: Pourbaix diagram of yttrium in water displaying the fields of corrosion (Y^{+++} field, left of line ②), passivation ($Y(OH)_3$ field and immunity (Y field, below lines ① and ③) in dependence on potential and pH value. The position of lines ② and ③ shift in dependence on ion concentration in solution. Between both lines a and b water is stable.

A heat-treatment of the samples was performed in order to further improve the corrosion resistance of the bare, polished WE43 alloy. This heat-treatment in air induced the growth of a thick oxide layer at the surface, comparable to the observations on the oxidation behavior of Mg-Y alloys [245]. It has been shown that the grown oxide layer consisted mainly of Y_2O_3 , in contrast to the thin natural oxide layer (~ 10 nm) consisting of MgO forming at ambient temperature. Auger electron spectroscopy (AES) depth profiles of the heat-treated samples revealed to a quite thick oxide layer ($1.5 \mu\text{m}$), with MgO just present at the surface and yttrium oxide throughout the entire oxide layer. The degradation performance was investigated by hydrogen evolution tests (evolved hydrogen volume vs. degradation time) in a buffered medium (simulated body fluid), where the oxidized species could be compared with non-oxidized, polished samples.

A scheme of these results is shown in Fig. 4.3, where totally different corrosion regimes can be found for the polished and the bare samples. Since degradation of such Mg samples is ascribed to a statistical process, H_2 -evolution regimes rather than defined curves are used to describe the degradation performance of a certain heat-treatment in a qualitative way. The hydrogen evolution of the polished samples can be described as a parabolic law, with a high initial degradation rate due to the large, reactive metallic surface. With time, the corrosion kinetics slows down due to the formation of corrosion products at the surface and their barrier action, which impedes further degradation [246]. This corrosion layer forces a parabolic law over time, since the reaction kinetics is more and more controlled by the diffusion of the reaction species through the surface layer [247]. The degradation performance of the oxidized samples can be approximated in first order by a sigmoidal law.

For the oxidized case, initially a very low degradation rate is observed due to the protective influence of the oxide layer, which covers the whole surface area of the sample. With time, the degradation is impeded at these sites due to the barrier action of deposited corrosion products, while at the same time at other sites new reactive surfaces get exposed to the liquid, featuring accelerated degradation. Now degradation slows, similar to the annealed-polished samples, and tends towards parabolic behavior. Therefore, the oxidation of the sample causes a delay in the onset of acceleration degradation with increasing oxidation time, plus a later switch to the parabolic behavior. Furthermore, since the oxide layer consists mainly of yttrium diffused to the surface, the internal structure close to the surface lacks yttrium precipitates (yttrium depletion), which are known to slow down the propagation of corrosion [243]. Therefore, a tendency towards faster corrosion kinetics at the final state is observed. Furthermore, a thick oxide layer is assumed to have more inhomogeneities than a thin layer because of increasing influence of the different thermal expansion coefficients between the oxide and the metal, rendering it more unpredictable when and

where the first penetration of the surface layer will occur [235, 248, 249].

Since the main application within this research was guided towards implant materials, some attention has to be drawn to the toxicity of the samples during degradation in the body. Due to the fact that the alloy only contains magnesium and yttrium as main alloying elements, a rather non-toxic response of the degradation products was assumed. Magnesium ions are essential ions in the human body and the rather slow corrosion kinetics after implantation avoids high doses. Additionally, the corrosion products are easily diluted in the body fluids. Yttrium has a quite low toxicity, mainly due to the fact that soluble yttrium salts are transformed to colloid materials in the human body and taken up and endocytosed mainly by phagocytosis in the liver and spleen. The long half-life (around 150 days) of Y in that organ is mainly explained by the colloid character of the Y insolubilized in lysosomal inclusions [250]. Since the estimated content of yttrium in this alloy is approx. 4%, the eluted amount of yttrium into the body is rather small. Cytocompatibility studies were performed within the PhD thesis of Dr. A. Haenzi [235, 244] to investigate the performance of the corroding bare alloy in contact to cells. In summary, the viability and metabolic activity of HUVECs cells start to decrease with increasing eluate concentrations. However, the good performance of magnesium alloys in different animal studies [239, 240, 251–253] is confirmed by the fact that in most cases no visual inflammatory reactions, but excellent wound healing was observed. The degradation of the implanted alloy was leading to hydrogen gas formation after implantation, but generally, the kinetics was slowing down after implantation.

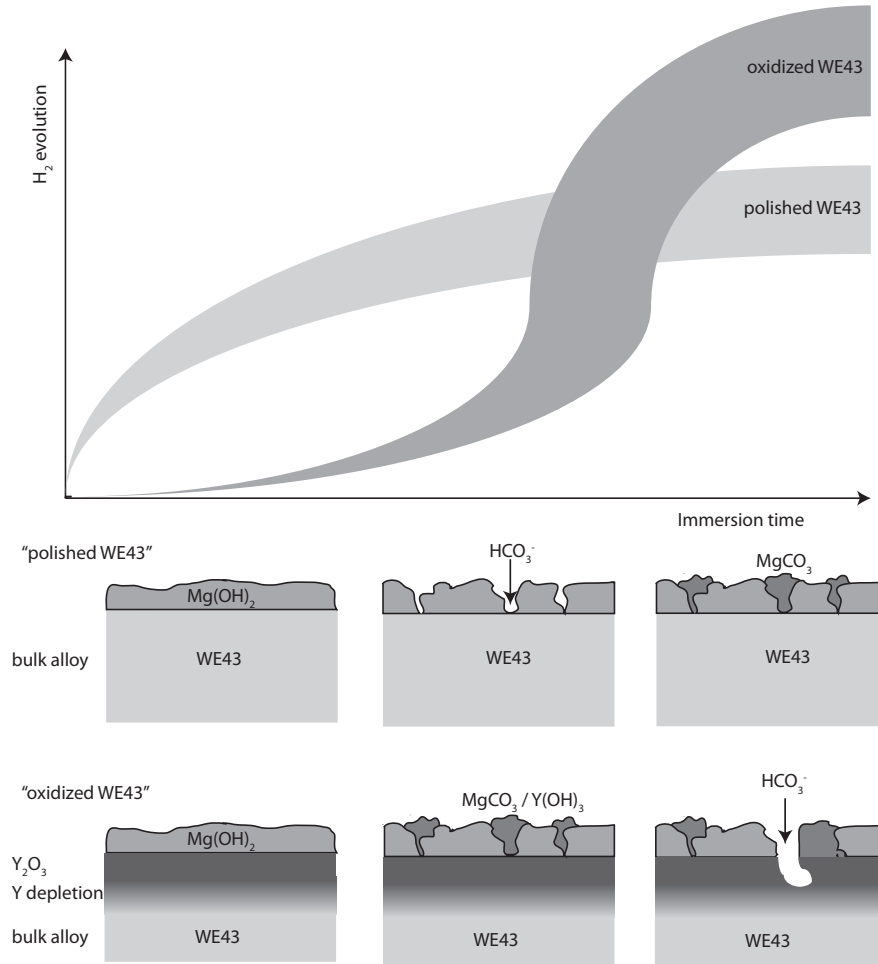


Figure 4.3: Schematic degradation performance of polished and oxidized WE43 samples Simulated body fluid (buffered) and scheme of the corrosion mechanism. Pitting corrosion starts at defects and small cracks present in the protective oxide layer. The oxidized samples have an additional protective yttrium oxide layer, which slows down the degradation rate until the medium passes through the oxide. Since the layer below the oxide has a decreased yttrium content (Y depletion zone), the corrosion rate is thus much enhanced in comparison to the polished sample, which contains more yttrium precipitates, slowing down the corrosion rate. With time, the corrosion spots are inhibited by the precipitation of magnesium carbonate and in both cases the degradation rate is decreasing. [235, 248, 249].

4.4 Characterization of the Magnesium surfaces

4.4.1 Metallurgic characterization

If not otherwise stated, oxidized WE43 was used as standard substrate (48h at 490°C). Due to the quite thick natural oxide layer growing during the heat-treatment, an intense metallurgical investigation and surface characterization of the samples was performed.

A remarkable change in within 10°C of the heat-treatment could have big influence on the results: at temperatures slightly below 500°C, the oxide surface of the samples appears homogeneously grey, whereas at several degrees above 500°C, the oxide surface shows small, black spots, indicating some change in the structure of the sample.

Micrographs

Micrographs of the alloy structure were prepared. The structure close to the surface was investigated in grinding and polishing away the oxide layer, whereas the cross-section reveals the bulk alloy. 0.1M NaH₂PO₄ was used as etching medium and the microstructure imaged using a light microscope.

In Fig. 4.4, a comparison of different micrographs is shown.

The raw WE43 shows grains in the range of 8-12 μm with smaller, darker precipitations. The heat-treatment at samples at 490°C induced a visible growing of the grains to up to 25-50 μm . The smaller, darker precipitations are still visible, but grown to a much lower extend than the other phase. After heat-treatment with temperatures above 500°C, a visible change in the micrograph could be observed. Much higher grain sizes up to 100 μm were observed. Additionally, melted precipitations around the grain boundaries and very small, black precipitations could be found. The

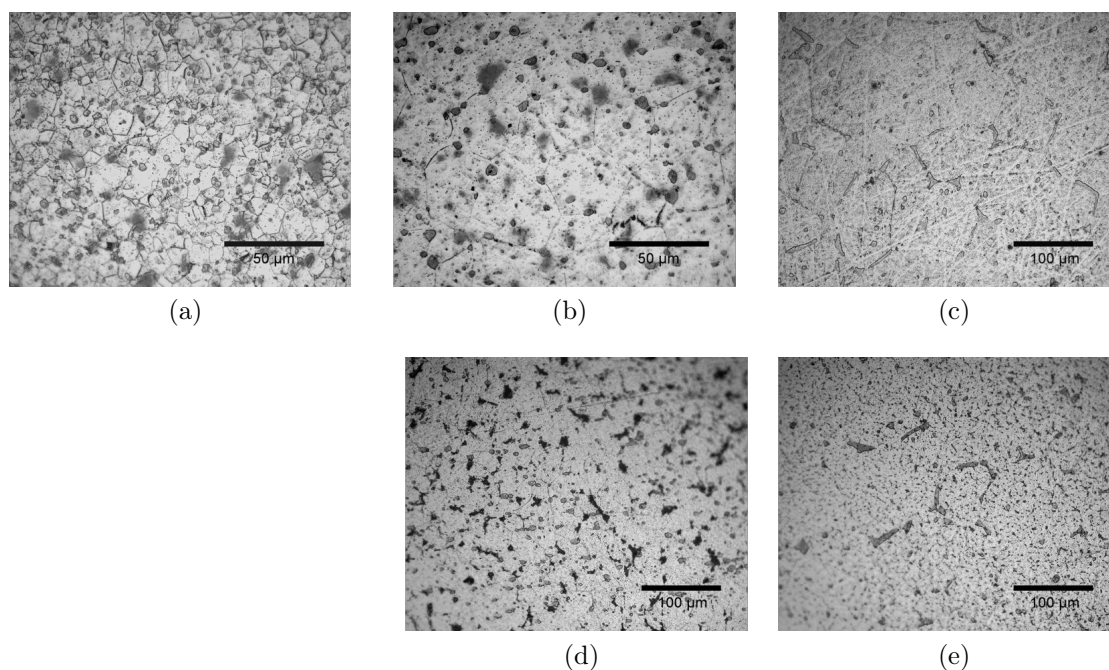


Figure 4.4: Micrographs of different WE43 samples, comparing surface and cross-sections of different heat-treatments. (a) shows the Micrograph of a polished WE43 sample (without heat-treatment), (b) shows the Micrograph of the WE43, heat-treated at 490°C, (c) shows the Micrograph of WE43, heat-treated at $\approx 500^\circ\text{C}$, (d) shows the Micrograph of a cross-section of WE43, heat-treated at 490°C and (e) shows the Micrograph of the cross-section of WE43, heat-treated at $\approx 500^\circ\text{C}$. The Micrograph is taken close to the surface, by removing the surface by grinding and further polishing, whereas the cross-section shows always the state inside the bulk alloy.

micrographs of the cross-sections showed a very similar morphology for the sample heat-treated at 490°. In comparison, the micrograph of the cross-section showed a homogeneous distribution of small, black precipitations, which were not visible in that amount close to the oxide.

In summary, the micrographs shows a visible change in structure towards higher grain sizes and melted precipitations, accumulated around the grain boundaries, starting at temperatures around 500°C. Therefore, in the following, a strict temperature control

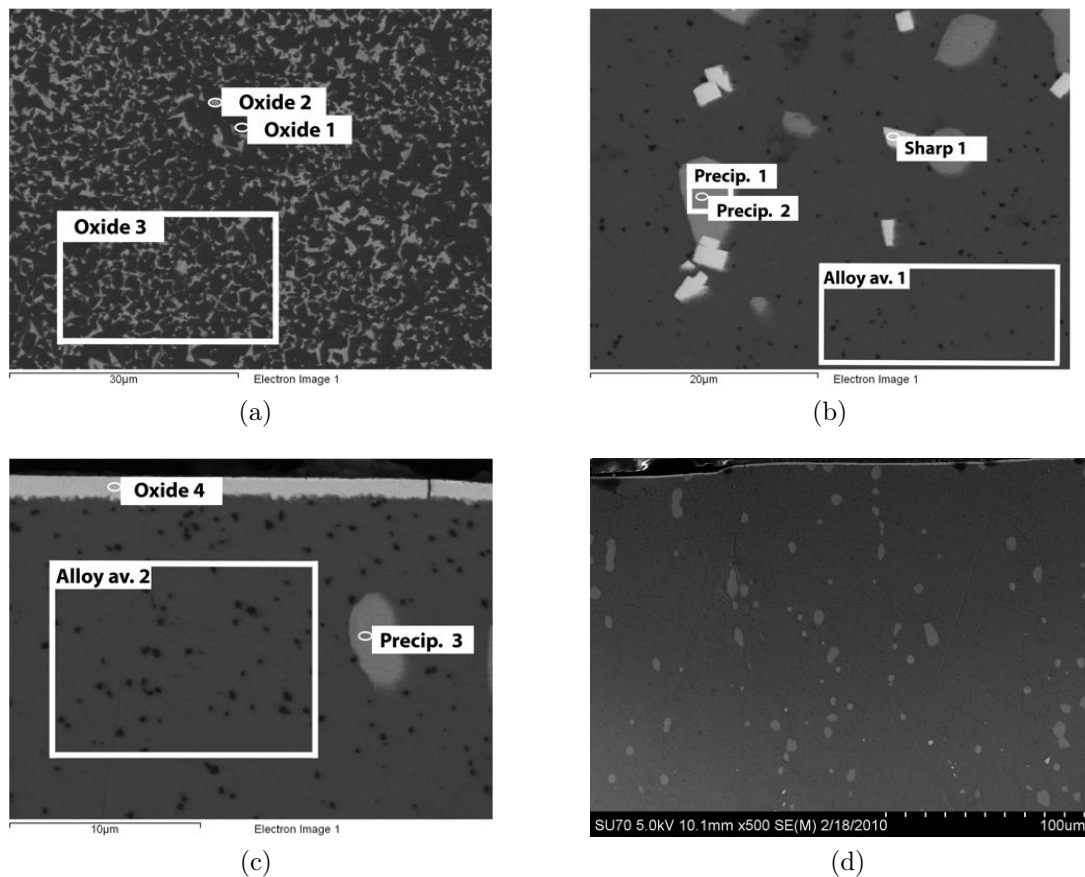


Figure 4.5: Back scattered electron (BSE) pictures on different samples. (a) oxide surface, (b) bulk alloy, (c) cross-section close to oxide layer EDX elemental analysis on these samples is shown in Tab. 4.2

during heat-treatment was set to 490°C in order to avoid that unfavorable temperature regime.

Scanning electron microscope / energy dispersive X-Ray Spectroscopy (SEM-EDX) analysis

The surface of the oxide layer was characterized by means of scanning electron microscope (SEM) and elemental analysis with energy dispersive X-ray spectroscopy

Table 4.2: Elemental analysis with EDX on the the oxide layer, and cross-sections close to the surface and in the bulk alloy. The different samples, including the area of analysis and the respective names used in the table are presented in Fig. 4.5. In some spectra, peaks of low intensity, further assigned to traces of Zn, Ca and Yb were found, which were too weak to be verified and were not counted in the calculation of the surface composition. The spectra labelled with “Oxide” are acquired at different spots at the oxide layer, “Alloy av.” is the label for the base alloy, averaged over a large area. The labels “Precip” and “Sharp” differentiate between 2 different precipitation phases inside the WE43 alloy.

Spectrum	C	O	Mg	Y
Oxide 1	10	66	12	12
Oxide 2	4	64	15	16
Oxide 3	21	71	4	4
Oxide 4	0	25	0	75
Alloy av. 1	0	8	92	1
Alloy av. 2	0	4	95	1
Precip. 1	0	10	88	2
Precip. 2	0	9	88	2
Precip. 3	0	9	90	2
Sharp 1	0	8	2	90

(EDX). Due to its information depth of about $2\mu\text{m}$, EDX is considered to be a bulk analysis method. The main results are summarized in Tab. 4.2 and Fig. 4.5. The composition shows a quite high contamination with hydrocarbons, up to 20 at% and mainly oxygen from the oxide layer. Both metal elements, magnesium and yttrium, are present at the surface. More interesting is the EDX analysis of the bulk micrograph. Here, three main phases can be found, first of all the continuous alloy phase, consisting of mainly magnesium with some small yttrium content. The more roundly shaped, discontinuous phase has approximately a similar composition, with a slightly increased content of oxygen. The sharply edged, discontinuous phase with the brightest color in the backscattered electron images is a highly yttrium-rich phase. The cross-section close to the oxide layer shows clearly the dimensions of the oxide layer in the range of 1-2 micron and consisting only of yttrium and oxygen.

Most interesting on that micrograph is the fact, that no yttrium-rich phase can be observed close to the oxygen layer. In Fig. 4.5 (d) a lower magnification of the alloy below the oxide layer is shown - starting from a depth of around 100 μm first, discrete yttrium-rich phases can be found. This finding is confirming that the growth of the oxide layer is mainly fed by diffusion of yttrium from the yttrium-rich phases situated close to the surface towards the growing oxide layer. This mechanism results in an yttrium depletion layer of the alloy, just below the yttrium oxide layer. Interestingly, in both images of the cross-section, defects in the oxide layer are visible, especially two cracks in Fig. 4.5 (c) are clearly visible (a small one in the middle of the image and a bigger one at the right hand side of the image). These defects and cracks could be possible entrance points and shortcut ways for water, channeling through the resistive oxide layer and leading to localized corrosion effects (pitting corrosion).

4.4.2 XPS surface characterization

oxidized WE43

The surface composition in at-% and XPS detail spectra of the surface's principal components are shown in Fig. 4.6 and the resulting chemical composition is shown in Tab. 4.4. The B.E. of the peaks are calibrated according to the peak position of the hydrocarbon peak. Because of the thick oxide layer, the samples behave like insulators and show high charging of up to 10 eV, which is responsible for the broadening of the peaks, resulting in higher fwhm. Asymmetries in the peaks could not be observed.

The peak fitting is summarized in Tab. 4.3. The main contributions of the C1s peak were found to be one hydrocarbon species (285.0 eV) and one carbonate species (289.7 ± 0.1 eV). The peak at 278-282 eV was first assigned as a satellite peak. There are indications that the peak at 282 eV is deriving from some carbon species at very

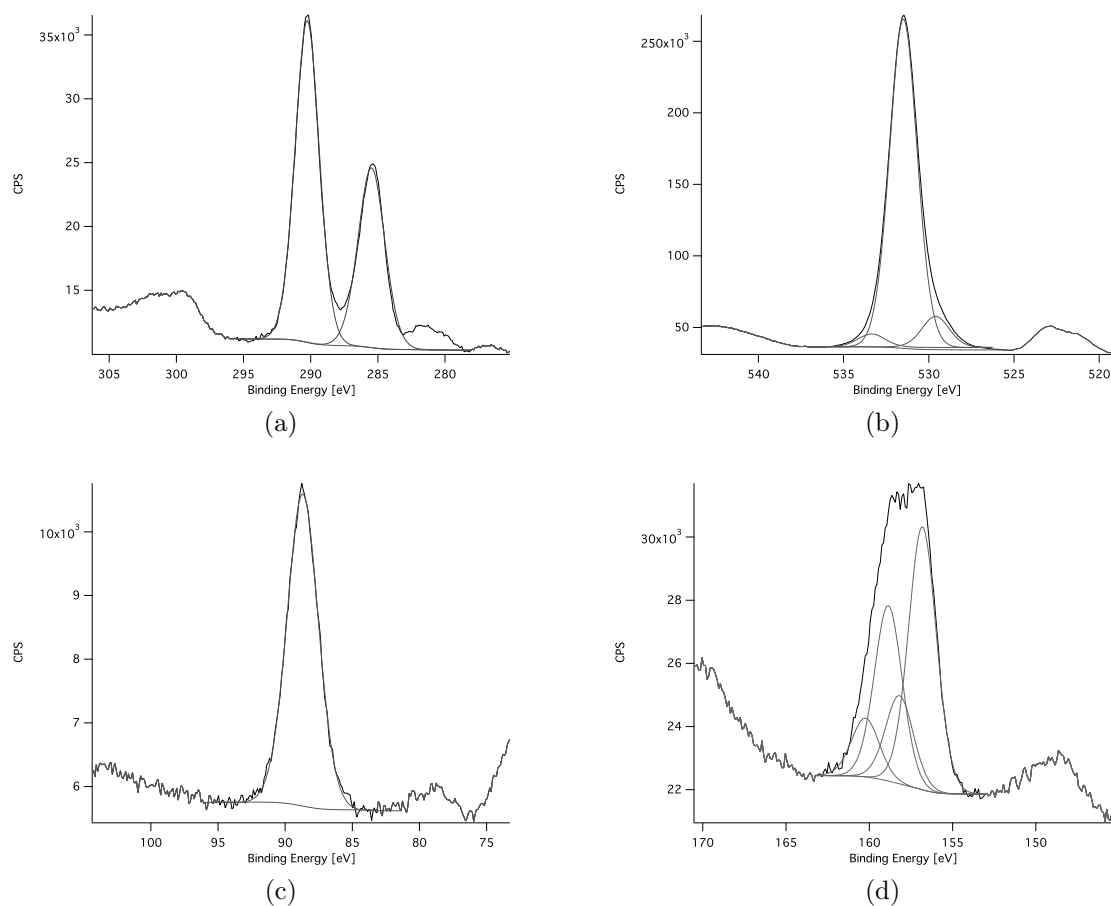


Figure 4.6: XPS detail spectra of oxidized WE43 (a) C1s, (b) O1s, (c) Mg2s (d) Y3d. Calcium, sodium and neodymium peaks are found in small amounts on most of the surfaces

low B.E., which could be assumed to be some carbide species. The peak below 280 eV could be assigned to the Na KLL auger peak, because normally traces of Na were found at the surface.

The O1s peak could be fitted with three contributions, namely the main peak consisting of magnesium oxide (MgO) at 531.5 ± 0.2 eV and one at higher B.E. consisting either of magnesium carbonate or yttrium hydroxide at higher B.E. (533.0 ± 0.3) and yttrium oxide (Y_2O_3) at 529.7 ± 0.3 eV.

Table 4.3: XPS fitting parameters used for component analysis. A Gaussian to Lorentzian ratio of 30% is always used.

Component	Position constraints (eV)	Area constraints	fwhm constraints (eV)	Peak position (eV)
C-C	285.0	free	free	285.0
-CO ₃	288 - 292	free	free	289.7 ± 0.1
MgO	BE _{Ti-O} + 2.1	free	1 · fwhm _{Ti-O}	531.5 ± 0.2
MgOH / MgCO ₃	533.2 - 533.9	free	1 · fwhm _{Ti-O}	533.0 ± 0.3
Y ₂ O ₃	BE _{Ti-O} + 1.23	free	1 · fwhm _{Ti-O}	529.7 ± 0.3
Y ₂ O ₃ (3d _{5/2})	155-157	free	free	156.4 ± 0.2
Y ₂ O ₃ (3d _{3/2})	BE _{3d_{5/2}} + 2.05	0.5 · A _{3d_{5/2}}	1 · fwhm _{3d_{5/2}}	158.4 ± 0.2
Y(OH) ₃ (3d _{5/2})	157-160	free	free	158.6 ± 0.3
Y(OH) ₃ (3d _{5/2})	BE _{3d_{5/2}} + 2.05	0.5 · A _{3d_{5/2}}	1 · fwhm _{3d_{5/2}}	160.7 ± 0.3
Mg2s	87-90	free	free	89.0 ± 0.2
Ca 2p _{3/2}	free	free	free	346.7 ± 0.3
Ca 2p _{1/2}	BE _{2p_{3/2}} + 3.6	0.5 · A _{2p_{3/2}}	1 · fwhm _{2p_{3/2}}	350.3 ± 0.3

The yttrium spectrum was showing either one or two species, depending on the samples. This could be assigned to yttrium oxide (3d_{5/2}, BE~156.4) and yttrium hydroxide (3d_{5/2}, BE~158.7) [254]. For each contribution, two separate peaks with an B.E. difference of 2.05 eV and an intensity ratio of 1:2 were included. The Y 3p_{5/2} was set to 156.4 ± 0.2 eV and 158.6 ± 0.3 eV for the oxide and hydroxide peak, respectively. However, there is no clear indication what is really triggering the transition from full oxide structure as found at some references towards hydroxides. The storage at ambient conditions under exposure of humidity may be the reason for a slow transition of the surface composition away from an oxide structure with predominantly bridging oxygen atoms towards a hydrolyzed, hydroxide-dominated surface.

The Ca2p signal was fitted with 2 peaks with the Ca 2p_{3/2} peak at 346.7 ± 0.3 eV and the Ca 2p_{1/2} at an energy difference of 3.6 eV. The Mg2s peak was fitted with one peak at 89.0 ± 0.2. The Mg KLL peak is visible at lower BE, at 79.5 ± 0.2 eV. The

Table 4.4: Chemical composition (at%) for oxidized WE43, as determined by XPS. Small amounts of calcium, sodium and neodymium are found on most samples.

Element	oxidized WE43 [at-%]	WE43 [at-%]
C1s (Carbonate)	22 ± 8	7 ± 1
C1s (Hydrocarbon)	10 ± 3	11 ± 4
Mg2s	7 ± 3	28 ± 1
O1s	58 ± 7	52 ± 4
Y3d	0.5 ± 0.2	0.5 ± 0.2
Ca2p	$< 0.5 \pm 0.5$	$< 0.5 \pm 0.5$
Na1s	$< 0.1 \pm 0.1$	$< 0.1 \pm 0.1$
Nd3d	$< 0.1 \pm 0.1$	1 ± 0.1

Nd3d peak has a highly rising background. This makes the determination of very small peaks impossible when using the Shirley background subtraction. Therefore, for very small concentrations of neodymium a linear background subtraction was used in order to quantify the peak. An example of the background subtraction of the Nd3d peak and the fitting of the peaks, which are not shown in 4.6 are added in the Appendix A.4.1.

Non-oxidized WE43

Bare WE43 was analyzed to compare the chemical composition at the surface. The resulting concentrations are shown in Tab. 4.4. The peak fitting was performed the same way as described for the oxidized alloy. Only one species of yttrium was found, corresponding to the yttrium oxide peak ($3d_{5/2}$, $BE \sim 156.4$) at lower B.E. A high amount of oxygen can be found, indicating a passivation of the surface after polishing. The magnesium concentration is much higher than for the oxidized sample, whereas the carbonate peak is much reduced. The surface consists mainly of magnesium oxide, additionally a higher neodymium content was observed. It seems that the relatively high carbonate peak observed after heat-treatment is formed during the growth of

the oxide layer and is then dominating the surface composition. Apart from the higher carbonate content for the heat-treated alloy, no big differences can be found. Both surfaces seem to consist of magnesium oxide, with different amounts of carbon contamination.

Unfortunately, due to the rather uncontrolled oxide growth from the magnesium alloy and the different steps necessary for the production of the surface, different batches have a high variation in surface composition, leading to quite high standard deviations. Interestingly, just a small amount of yttrium can be found at the surface of the oxidized sample, whereas it is supposed to be the main element inside the oxide layer. Therefore, the internal composition of the oxide layer was investigated by XPS depth profiling.

4.4.3 XPS depth profiling

The internal composition of the oxide layer was investigated by XPS depth profiling. The maximum depth achieved was measured after the XPS acquisition by profilometry (Nanofocus microsurg explorer) and together with the sputter time a linear sputter rate of $0.15 \mu\text{m}/\text{min}$ was calculated. The depth profile for the elements C, O, Y and Mg is shown in Fig. 4.7.

The depth profile shows different transitions within the sputtered layer. Close to the surface, till a depth of around $0.5 \mu\text{m}$, carbon, mainly in the form of carbonates can be found, as already as already discussed in the surface XP spectra in Fig. 4.6. Due to the high amount of oxygen in carbonates, the oxygen content behaves decreases in parallel with the carbonate content. After the disappearance of the carbonate within the first micrometer of depth, the oxygen concentration levels to a constant value through the entire oxide layer. Yttrium is only found in traces at the surface, but rising strongly within the first micrometer to a constant concentration inside

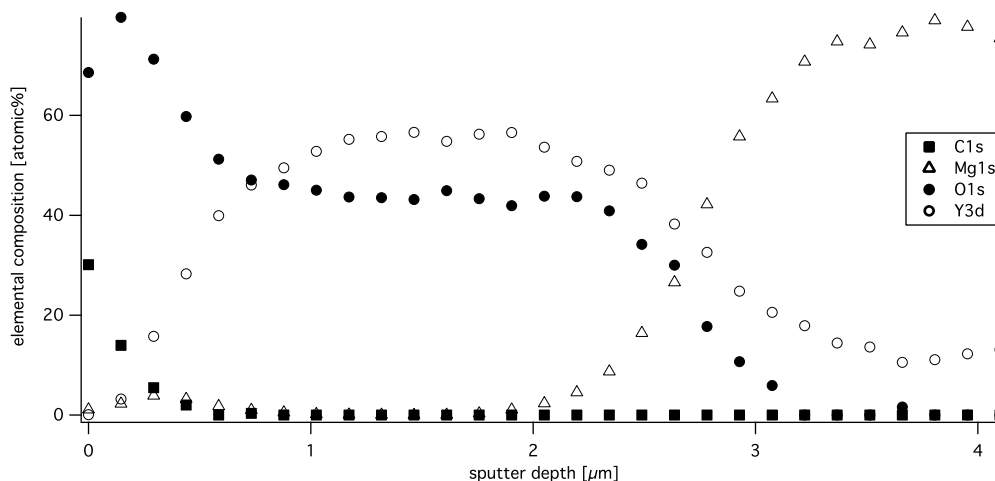


Figure 4.7: XPS depth profile of oxidized WE43 for 48h. The maximum depth achieved was measured after the XPS acquisition by means of profilometry (Nanofocus microsurf explorer) . From the maximum depth achieved and the sputter time, a linear sputter rate was calculated.

the oxygen layer. Magnesium, however is only found at the surface and only traces are visible inside the yttrium oxide layer. Interestingly, the atomic concentrations of oxygen and yttrium don't follow the ratio 2 : 3 as expected from the chemical composition of yttrium oxide, Y_2O_3 . This effect can be explained by preferential sputtering [255] and is related to different surface binding effects or to mass difference effects of the elements [255]. In case of yttria, the mass difference of yttrium and oxygen is relatively high and thus can explain the preferential sputtering, especially when taking into account the quite high sputter rate used for this depth profile, which is potentially amplifying this effect. The border between oxide layer and alloy can be seen as a transition zone of 0.5-1 μm thickness, in which the concentration of oxygen and yttrium get highly reduced and the main alloy element magnesium starts to dominate. From the depth profile, the oxide layer thickness can be assumed to be between 2 and 3 μm , which is in good agreement with the Auger depth profiles shown in [235, 244]. Here, the oxide layer is assumed to be around 2 μm for the same

alloy, heat-treated for 48h.

4.4.4 Development of a cleaning protocol

A new cleaning protocol was developed based on the cleaning protocol for TiO₂ surfaces (c.f. 7.9.2) was developed. The efficiency of different organic solvents was tested for ultrasonication of the samples. The choice of solvents included water, concentrated sodium hydroxide, ethanol, 2-propanol, acetone and pentane. Furthermore, UV-ozone and oxygen plasma were investigated for further surface cleaning. Sonication in an appropriate solvent has the purpose of removing all kinds of loosely bound particles (e.g. dust particles) at the surface, placing them into suspension. Since the compatibility of these solvents with the surface of the sample has to be proven, different solvents were tested.

Investigation of the surface cleaning by XPS

The main focus in this study was assessing the change in the carbon spectra. It was expected that especially the hydrocarbon contaminations and eventually as well the carbonate content is decreased by an efficient cleaning protocol. For each solvent chosen, XPS analysis was performed after (a) ultrasonication for 3x 10min, (b) after ultrasonication and 30min UV-ozone cleaning and (c) after ultrasonication and oxygen-plasma cleaning for 2min. As references bare substrates without, with UV-ozone or with plasma-cleaning were used.

A summary of the atomic concentrations of the main elements observed at the surface after the different cleaning experiments can be found in Fig. A.1 in the Appendix (c.f. A.4.2). In order to compare the data obtained, ratios of the elemental concentration of the hydrocarbon and the carbonate peak referenced to the Mg2s concentration,

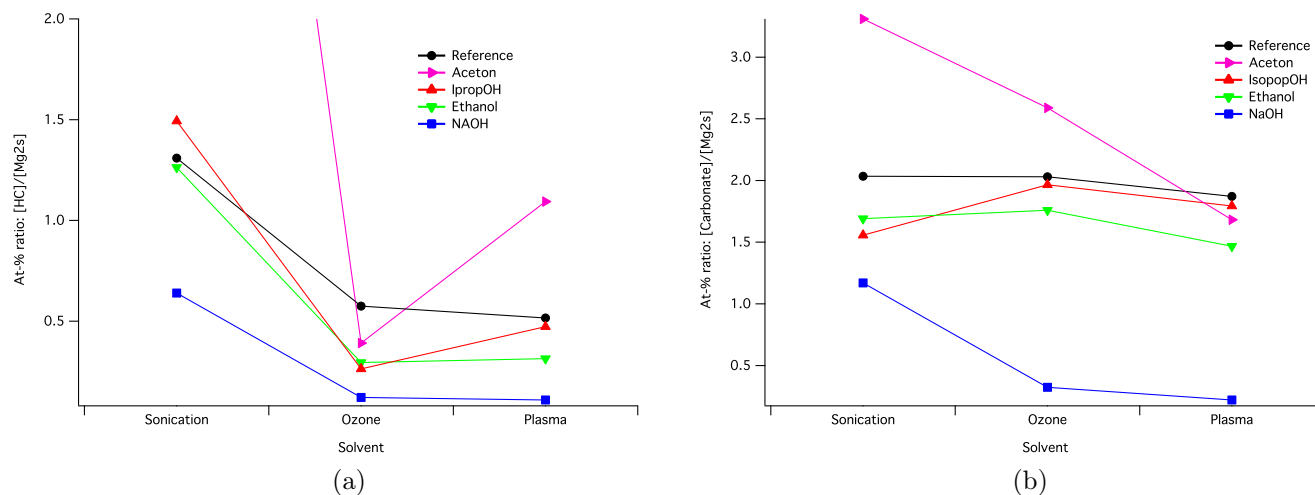


Figure 4.8: Comparison of the cleaning efficiency for (a) the hydrocarbon peak and (b) the carbonate peak presented as the change of the ratio of the elemental concentration with the cleaning protocol. The cleaning protocol consists of just ultrasonication and ultrasonication followed by ozone or plasma cleaning. For the reference sample ultrasonication is skipped, analyzing a non-cleaned sample, which is then cleaned just by means of UV-ozone and plasma.

i.e. $[HC]/[Mg2s]$ and $[Carbonate]/[Mg2s]$ are used. The comparison is shown in Fig. 4.8.

Discussing the organic solvents, it can be seen from Fig. 4.8, that the cleaning efficiency only by ultrasonication is not given. The higher values of the sonicated samples in acetone in comparison with the reference shows that acetone is adsorbing preferentially to the oxide surface and is thus not the solvent of choice. All other solvents show a reduction in the hydrocarbon contamination after UV-Ozone or plasma cleaning, whereas the carbonate contamination stays practically constant. Ethanol seems to work the best of the investigated organic solvents, reducing highly the hydrocarbon contamination after UV-ozone and plasma cleaning. Additionally, it is the only organic solvent that shows a slight trend towards a reduction of the carbonate peak.

The best performance in terms of reduction of both carbon peaks was proven to be by NaOH treatment. Both carbon peaks are highly reduced after the full cleaning protocol. Already after ultrasonication in conc. NaOH, less apparent hydrocarbon contamination is found at the surface and a comparable reduction of the carbonate is shown as it was achieved for the best organic solvent after the entire cleaning protocol, involving ultrasonication and Plasma or UV-ozone treatment.

However, the surface composition changes drastically after the treatment with conc. NaOH, which indicates more significant changes in the surface chemistry after cleaning. Especially the yttrium content is rising at the surface at a factor of 10. The surface composition seems not to change drastically when using organic solvents (c.f. Table A.1 in the Appendix A.4.2).

Investigation of the cleaning protocol by AFM imaging

The influence of the solvents on the oxide structure was investigated by AFM imaging in contact mode. The oxide structure of the uncleaned oxide is comparable to the images obtained by SEM measurements. An exemplary AFM image of the uncleaned surface is shown in Fig. 4.9. The arithmetic surface roughness (R_a) and the RMS roughness (R_q) is highly depending on the different batch, especially depending on the heat-treatment. Whereas within one batch small standard deviations could be measured, the measurements are fluctuating between different batches, producing an overall standard deviation for the surface roughness measurements of ± 20 nm. This indicates a quite high influence of the heat treatment on the surface structure. Unfortunately, the heat-treatment is a rather uncontrolled procedure, which could not be further improved within this study.

Generally, all investigated samples cleaned with organic solvents, showed the same features at the surface: sharp, crystalline-like structures. In direct comparison within

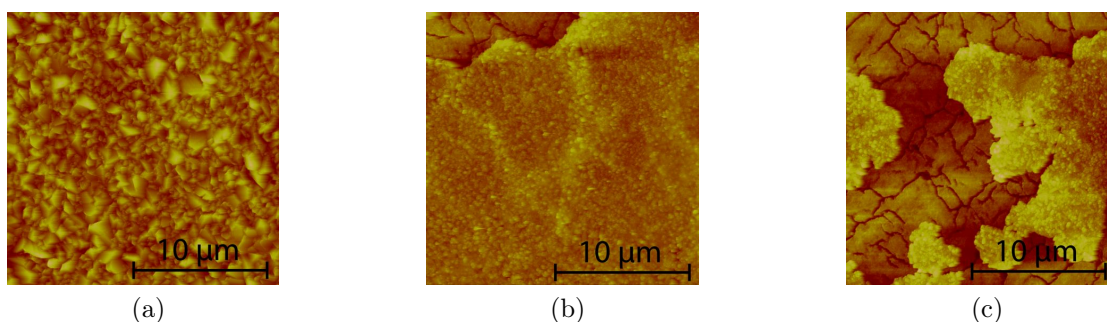


Figure 4.9: Study of oxide structure by AFM imaging (a) exemplary image of the oxide before cleaning (similar to 2-propanol and ethanol cleaning) (b) and (c) of the NaOH cleaned oxide

one batch, the surface roughness of the different cleaning protocols was compared. Similar roughness values of $R_a = 107 \pm 2$ nm and $R_q = 140 \pm 2$ nm were found for the non-cleaned oxide and for the cleaning procedures including ethanol and 2-propanol. The values are found to be slightly smaller for the cleaning involving acetone ($R_a = 95 \pm 1$ nm, $R_q = 125 \pm 1$ nm). Additional UV-ozone or plasma cleaning did not affect the oxide structure and the surface roughness values obtained. As already discussed within the XPS analysis of the cleaning procedure, acetone seems not as efficient as the other organic solvents. Especially after ultrasonication, more hydrocarbon contamination is found at the surface than before. This could indicate already some adsorption mechanism of the acetone molecules to the surface. Either the surfaces cleaned with acetone contained smaller surface features, either by dissolution in acetone, or the adsorption of acetone molecules to the surface is influencing the AFM measurements, showing a smoother surface.

In contrast to the organic cleaning procedures, the NaOH cleaning revealed a drastic change in surface structure as described above. In the AFM image can be seen that the topography of the oxide changed towards a much smaller grain size of the overlying layer. It seems like the concentrated NaOH solution acts as an edging medium

for the oxide layer, lowering the oxide grain size. Since sharp elements and edges are more prone to dissolution than flat or rounded areas, the resulting surface structure has a softening effect on the surface topography. Apparently the sodium hydroxide solution changed towards a partial dissolution or delamination of the oxide layer happening during the sonication process. A highly cracked structure was revealed below the overlying structure, which is supposed to be the initial oxide layer. The brittle upper layer, which is delaminating, seems to be a MgO sublayer, with poor adhesion to the yttrium oxide. The height differences measured from the height profile picture are equal to approx. 100-150 nm, which would correspond well to the Mg-rich oxide layer on top of the thick yttria layer, as shown in the depth-profile in Fig. 4.7. An indication for that assumption is also the elemental composition derived from XPS as shown in Tab. A.1 on page 306, where the highest yttrium content is measured for the samples cleaned with NaOH solution. The RMS values are highly decreased, around $R_q = 60 \pm 10$ nm for the upper layer and $R_q = 100 \pm 10$ nm for the underlying structure. Even when the underlying structure seems to be smoother than the overlying surface, the cracks contribute to the RMS value and thus the overall number is higher compared to the overlying layer. The cracks in the underlying structure seem to be present already inside the natural grown oxide layer. The origin could be the high temperature during the heat-treatment or a too rapid cooling rate. Differences in the thermal expansion coefficient of the metal alloy and the thick and brittle yttrium oxide overlayer could be the main driving forces inducing the cracks. Indications of cracks in the oxide layer have already been observed in Fig. 4.5 on page 133 (c) and (d), when investigating cross-section of heat-treated samples with EDX. These samples were neither sonicated, nor treated with any solvents and thus support the hypothesis that the cracks are formed during heat-treatment or during the cooling phase of the sample.

4.5 Characterization of additional organic adlayers on magnesium substrates

4.5.1 Dodecylphosphate SAMs

The investigation of additional adlayers on magnesium substrates was mainly performed by XPS analysis. Because the rough and inhomogeneous, natural grown oxide layer from the heat-treatment is not reflective, thus VASE could not be used for surface characterization. In a first step, the adsorption of Dodecylphosphate (DDPO4) SAMs as a model adsorption system for the phosphonate polymers was investigated. The SAMs were adsorbed from a 0.5 mM, aqueous solution for 24h, the basic fitting procedure was taken from [84], tested on titania samples and then a modified fit was applied on the heat-treated WE43 samples.

In Fig. 4.10 the main XPS detail spectra of dodecylphosphate on titanium oxide and heat-treated WE43 is shown. The fitting of DDPO4 adsorbed on titanium oxide as reference is described in the Appendix A.4.3 on page 307, based on the fit described in [84]. In comparison to the detail spectra of the bare substrate, as shown in Fig. 4.6, the surface composition changes drastically. Especially the C1s peak changes visibly.

Apparently, the main carbon contamination at the surface, the carbonate peak higher B.E. disappears, due to partial dissolution of the carbonate salts in the aqueous phase and replacement by DDPO4. An intense hydrocarbon peak is detected instead, which could be fitted in the same way than described in [84] and used for the fit of DDPO4 on titanium oxide: basically 2 peaks were fitted - the main contribution originating from aliphatic carbon and a shoulder at higher B.E. of 286.7 ± 0.2 eV originating from the CH₂ group connected to the phosphate. These peaks fit perfectly for both

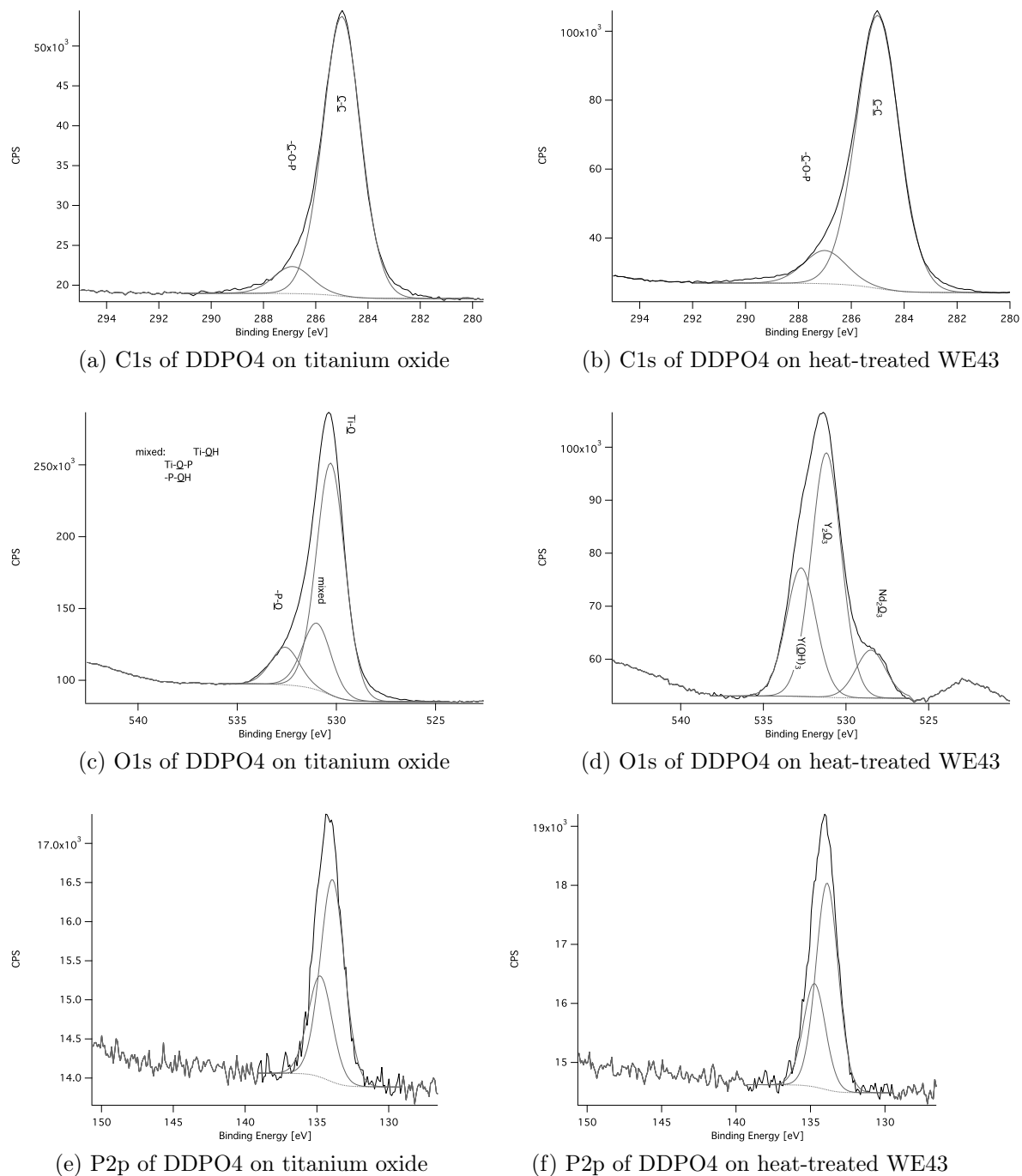


Figure 4.10: XPS detail spectra of Dodecylphosphate SAMs on titania (left column) and heat-treated WE43 (right column)

surfaces used. The P2p peak is present as well in all DDPO4 coated samples and not present in the uncoated reference - a good additional evidence, that the coating works as well on mixed magnesium oxide / yttrium oxide surfaces. This peak was fitted with two peaks and constrained intensity ratio of 1:2. Unfortunately, the WE43 surface changes highly its composition during the adsorption from water, that a more detailed comparison with the bare reference is not possible. Due to the high charging, the oxide peak is rather broad and already two to three different oxide species (yttrium oxide as main peak, magnesium oxide and niobium oxide as smaller contributions) have to be fitted in. Basically the magnesium is almost entirely removed from the surface and yttrium oxide and contributions of neodymium are visible. Another aspect is the high charging obtained for the functionalized samples. Even in comparison with the bare substrates, the charging is by trend higher and the peaks broader. This results in fitted fwhm of 2.2-2.5, especially compared to the much more narrow peaks obtained from the titanium oxide substrates. Since the ratios of these oxides and therefore the surface composition are highly varying between different samples, it is difficult to fit even smaller peaks apart from the three peaks deriving from the oxide layer. The three oxide peaks are fitted as neodymium oxide at 528.6 ± 0.3 eV, yttrium oxide at 531.4 ± 0.3 eV and another peak, assigned to yttrium hydroxide at 533.0 ± 0.4 eV, as already described above for the bare sample. Because the peaks are relatively close to the expected peak positions of the phosphate-derived peaks, these peaks were not fitted into the spectra, since they just balance out the other three components deriving from the substrate and would have to be constrained. The other peaks were fitted as indicated above on page 136 for the XPS analysis of the bare samples. The experimental component composition derived from the peak fitting is shown in Tab. 4.5.

Table 4.5: Experimental component composition derived from peak fitting of the XPS detail spectra. Subtable (a) shows the surface composition on titania, subtable (b) shows the surface composition on oxidized WE43. The abbreviation “mixed” denotes the contributions from Ti-OH, Ti-O-P and P-OH

TiO ₂	at-%	at-%
C-C	24 ± 3	27 ± 3
C-O-P	3.2 ± 1	
TiO ₂	37 ± 3	52 ± 5
“mixed”	8 ± 0.5	
-P=O	7 ± 3	
P	2.5 ± 0.5	2.5 ± 0.5
Ti	19 ± 3	19 ± 3

(a)

ox. WE43	at-%	at-%
C-C	47 ± 6	53 ± 6
C-O-p	5 ± 2	
Y ₂ O ₃	16 ± 3	27.5 ± 5
Y(OH) ₃	8 ± 2	
Nd ₂ O ₃	3.5 ± 2	
P	5 ± 0.5	5 ± 0.5
Y	8.5 ± 4	8.5 ± 4
Mg	3 ± 2	3 ± 2
Nd	2 ± 1	2 ± 1
Ca	1.5 ± 0.5	1.5 ± 0.5

(b)

4.5.2 Surface functionalization by means of poly(alkylphosphonate)s

A study for the adsorption of the PEGylated polymers was performed using XPS analysis and comparison with the polymers adsorbed onto titanium oxide, which have been already described in Sect. 3.1 on page 77. A screen over different solvents was performed in order to find a good condition for adsorption. The main problem observed by adsorption from water was the fast degradation of the sample. This observation was found to be differing from the adsorption of DDPO4 from water. Within the adsorption of DDPO4 the surface chemistry changes remarkably, but apparently the access of water for further corrosion is then hindered by the hydrophobic coating of the DDPO4.

The solvent study for polymer adsorption followed the solvents already used for the

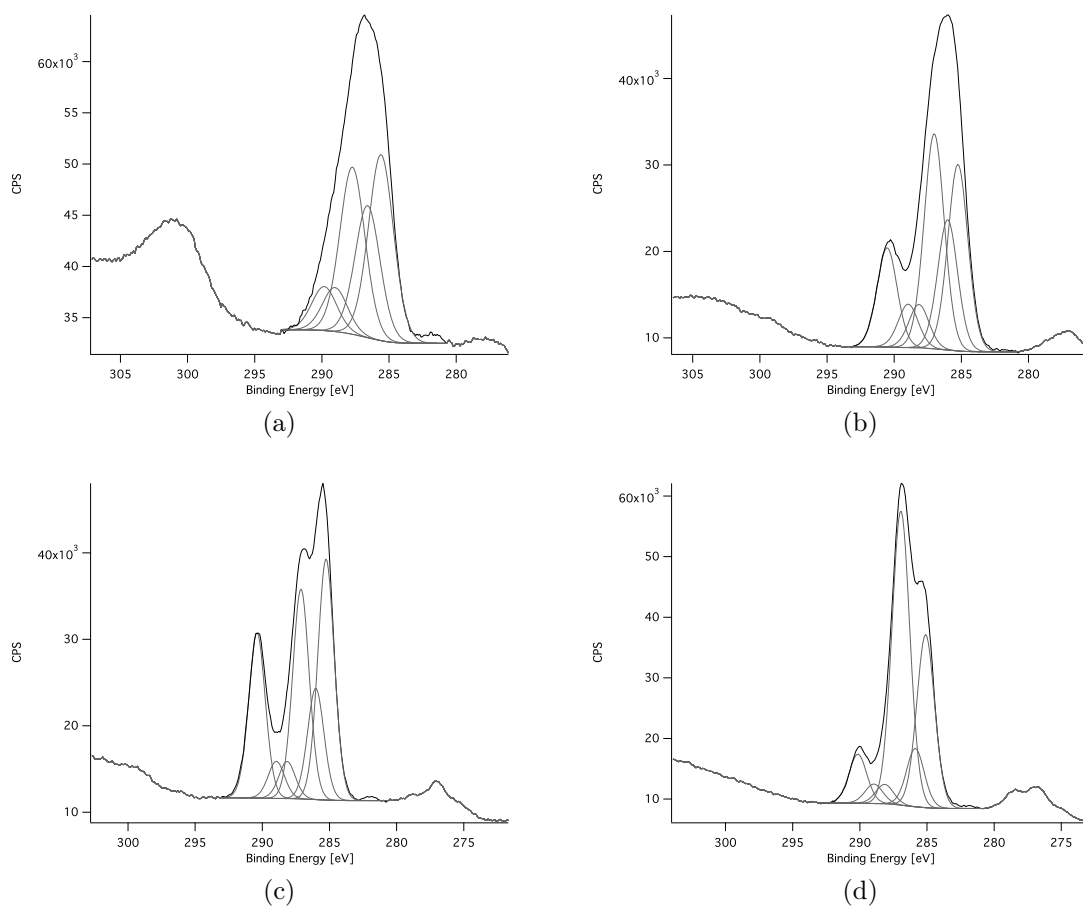


Figure 4.11: XPS detail spectra of the C1s peak after polymer adsorption of PIMA(0.40:0.45, BA) from different solvents (a) from water, (b) from acetone, (c) from ethanol, (d) from 2-propanol.

surface cleaning is summarized in Fig. 4.11. It takes into account the solubility of the polymers in these solvent, resulting in water, acetone, ethanol and 2-propanol as adsorption medium. In water, the degradation of the sample surface was visibly faster than in organic solvents, resulting in a slightly rougher surface, visible by eye, whereas the surfaces after adsorption were visibly not changing during the adsorption process. Nevertheless, big differences between the solvents were observed during XPS analysis. In Fig. 4.11, the different C1s XPS detail peaks are compared after adsorption of a 0.5

mg/ml solution of polymer PIMA(0.40:0.45, BA) from different solvents. Due to the presence of such a high amount of oxygen species deriving from the underlying oxide layer, a detailed fit of the O1s detail spectra was not performed. The other peaks were fitted similarly to the peak fitting performed for the DDPO4 SAMs. A comparable peak fitting for the C1s detail spectrum as described in Sect. 3.1 for the adsorption onto titanium oxide could be used to fit the peaks. The major problem for the fit is the fact that the carbonyl species at 290 eV, assigned to magnesium carbonates at the bare substrate is not disappearing when adsorbing from organic solvents. This results in the necessity to introduce a new carbonate peak at slightly higher B.E. than the carbonyl group deriving from the free carboxylic acid in order to keep all constraints for the C1s peak fitting as developed for the titanium oxide surface. The experimental component composition is summarized in 4.6 and shows clearly the high deviations of the elements deriving from the WE43. It can be stated that the adsorption from water has the most effect on the sample surface. A very high yttrium content is measured, whereas no additional carbonate peak was found. For the other solvents, different influence on the alloy materials was visible, resulting in high values of magnesium (6 at-%) for adsorption from ethanol to no signal deriving from magnesium. The differences observed in the polymer composition, especially the unusual high ether peak for the polymer adsorbed from 2-propanol can only partially explained. First of all a change in solvent is a change in the adsorption conditions, varying adsorption kinetics, surface coverage, conformation of the polymer in solution, and all other adsorption parameters. Therefore, the polymer composition at the surface does not have to be necessarily the same. On the other hand, only one polymer species - apart of possible effects deriving from the polydispersity of the polymers - is present in the adsorption solution, and thus it is supposed to yield in comparable polymer compositions.

Table 4.6: Experimental component composition derived from peak fitting of the XPS detail spectra. The polymer PIMA(0.40:0.45, BA) was adsorbed from different solvents to oxidized WE43. The abbreviation “amide” consists of the contributions $\text{-}\underline{\text{C}}\text{H-C(O)OH}$ / $\text{-}\underline{\text{C}}\text{H-C(O)-NH-}\underline{\text{C}}\text{H}_2\text{-}$. When adsorbed from water, traces of neodymium are found at the surface.

Component	Water	Acetone	Ethanol	2-Propanol
C-C	21 ± 5	22 ± 5	25 ± 3	26 ± 2
$\text{-CH}_2\text{-O-CH}_2\text{-}$	22 ± 1	35 ± 8	22 ± 3	50 ± 4
-C(O)-NH-	7 ± 1	6 ± 0.1	5 ± 1	3.6 ± 1
-C(O)OH	7 ± 1	6 ± 0.1	5 ± 1	3.6 ± 1
“Amide”	20 ± 3	17 ± 0.3	15 ± 4	11 ± 2
Carbonate	0 ± 0	11 ± 4	19 ± 0.5	4 ± 4
P	2.5 ± 0.5	2 ± 0.4	2 ± 0.5	1.5 ± 0.1
Mg	5 ± 4	0.6 ± 0.1	6 ± 2	0.05 ± 0.05
Y	15 ± 3	0.1 ± 0.1	1 ± 0.1	0.2 ± 0.2

4.6 Corrosion Investigation by Electrochemical Impedance Spectroscopy

The corrosion behavior of the polymer coated and bare samples was tested with Electrochemical Impedance Spectroscopy (EIS), which is described in detail in Sect. 7.4. A typical EIS Bode plot is shown in Fig. 4.12. The Bode plot represents the applied frequencies at a logarithmic scale at the x-axis and consists of 2 y-axis: the Bode magnitude plot represents the magnitude in the frequency response gain and/or the frequency response phase shift in case of the Bode phase plot.

The EIS results of the bare substrates are summarized in Fig. 4.13. It is clearly visible that the bare samples have a highly non-reproducible corrosion behavior in the EIS diagrams. The logarithmic scale of the axis of the Bode magnitude plot indicates the high deviations observed between different experiments. For this reason it is difficult to draw conclusions from the data obtained. It has to be emphasized that the observed deviations seem to be a characteristic of that specific system studied, mainly

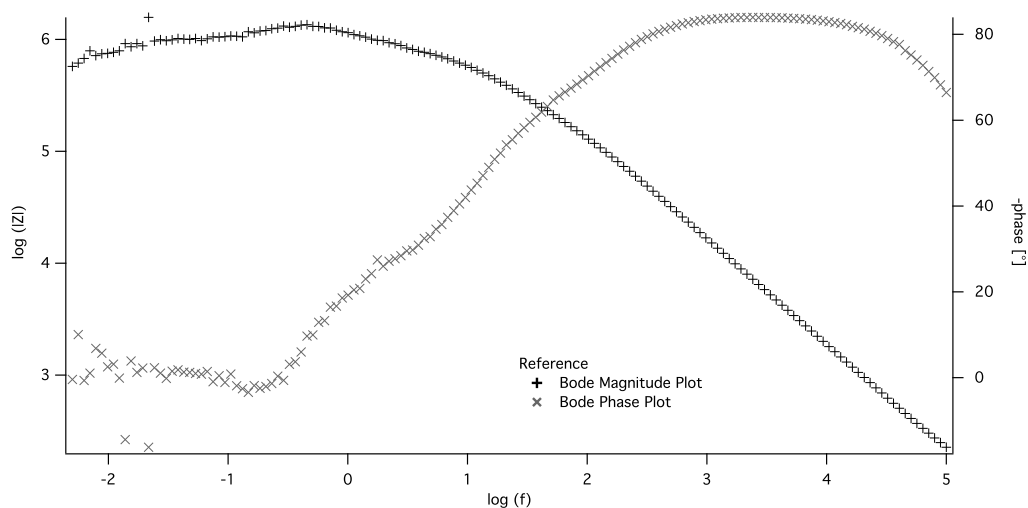


Figure 4.12: Typical Bode plot derived from EIS measurements

induced by the heat-treatment process. Systems with a well defined composition and high control in the sample preparation, such as for titania, normally result in a much better reproducibility than it is the case for the EIS measurements using the oxidized WE43.

Best resistance values were achieved with bare samples, used just after heat-treatment, without further cleaning of the substrate. There is a clear tendency to an aging effect, resulting in less resistant samples after storage for longer than one week. Humidity in ambient air or even light might induce the release of internal stresses, resulting in increased surface cracks, which are then responsible for the earlier occurrence of pitting corrosion and charge-mass transfer to the surface.

It seems that all cleaned references are resulting in lower corrosion resistance than the fresh, non-cleaned samples. However, in the case of the heat-treated WE43 alloys, impedance values vary by factor greater than 100 for the same batch and treatment and up to 4000 times for oxides after various times of storage or after different cleaning programs. The general tendency is that the freshly prepared oxide is characterized by comparably higher impedance values and shows a higher resistance against pitting

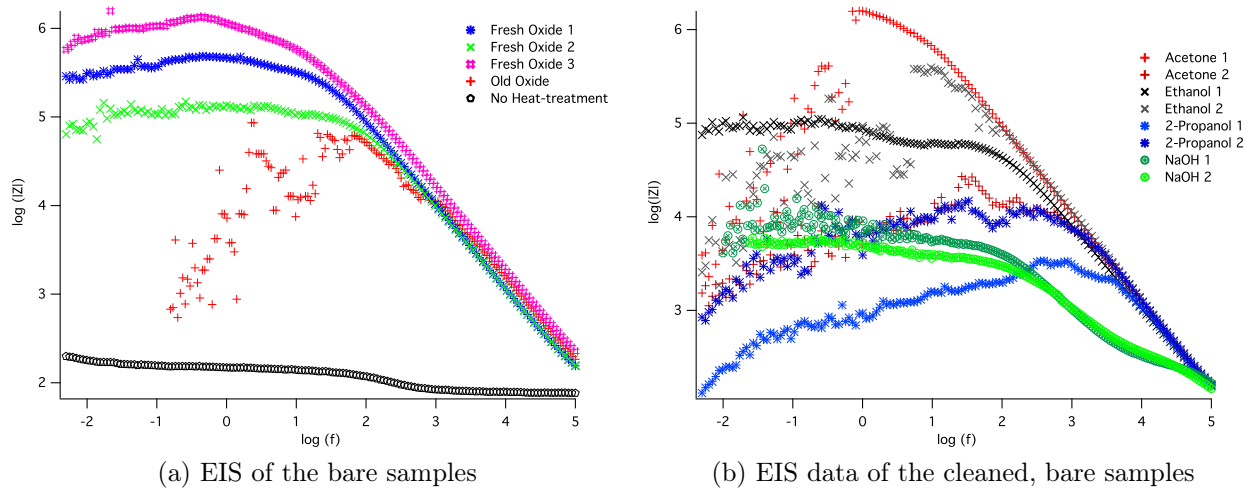


Figure 4.13: Bode Plot of the EIS measurements of the bare samples and cleaned surfaces with different solvents

corrosion. Older samples align towards the lower part of the curves. Therefore, the cleaning strategy has already a quite high effect on the corrosion resistance of the sample

The values between the samples with the same surface cleaning are differing highly and therefore only some tendencies could be derived. As shown in Sect. 4.4, the underlying yttrium oxide structure is highly cracked. Apparently already the solvent itself changes the structure of the overlaying magnesium oxide / magnesium carbonate layer, or the used ultrasonication is inducing a weaker and less corrosion resistant structure in that structure, especially cracks, or the solvent itself is already etching that layer, inducing a less resistant layer structure against corrosion. This is clearly seen for water, which yields in a higher surface concentration of yttrium, indicating the delamination of the outermost oxide layer as seen in the AFM imaging studies.

Assuming that at the start of the measurement a homogeneous surface is present, we see with proceeding experiments (and decreasing frequencies) a straight and smooth line of increasing impedance up to a certain plateau value. Later the impedance either

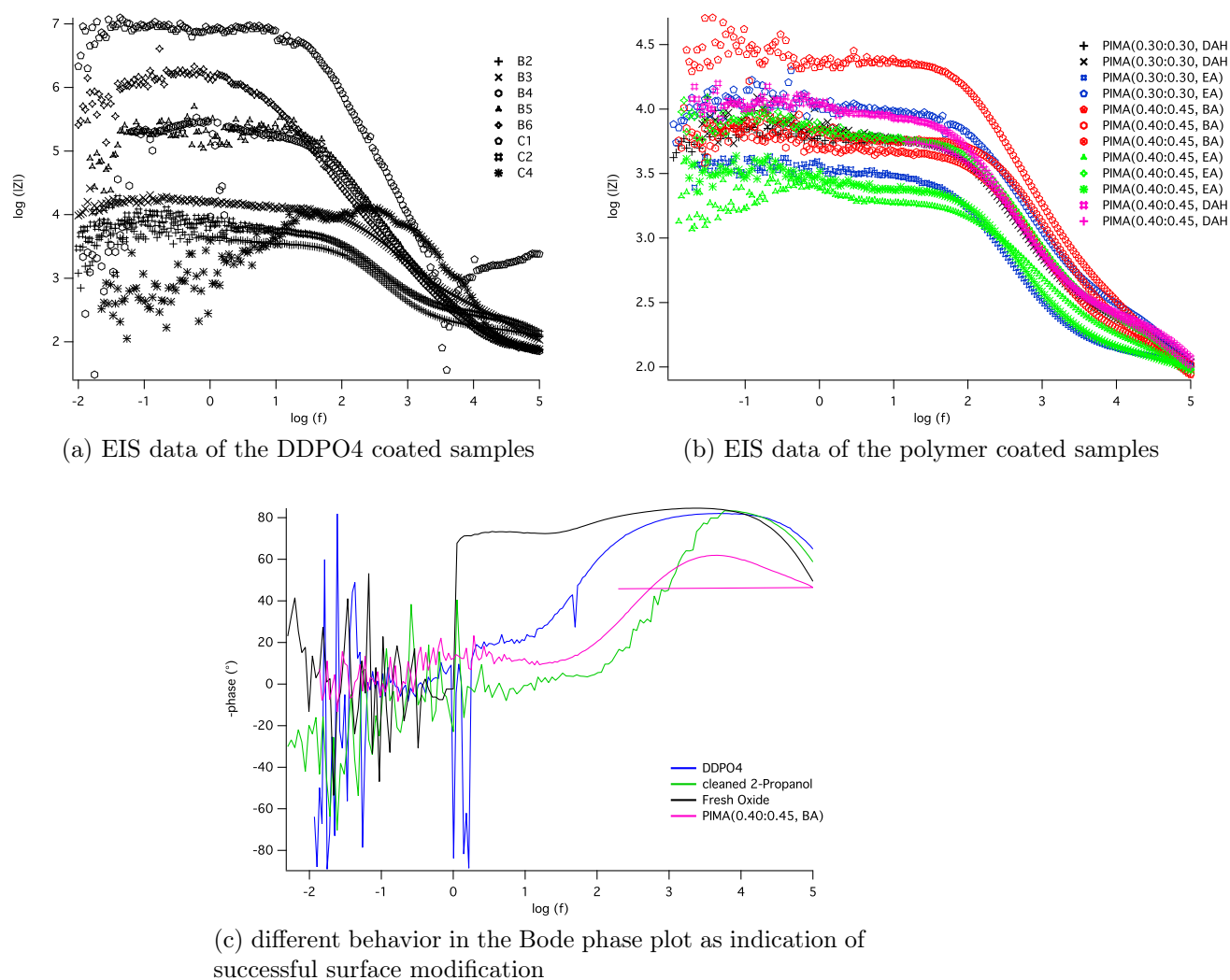


Figure 4.14: EIS investigation of coated samples

stabilizes or breaks down into more or less scattered points. This can be explained by a homogeneous and dense surface and subsequent start of pitting corrosion. The pitting corrosion is a local corrosion attack which then breaks the local impedance and leads to scattered, much lower values of impedance.

In a second step, corrosion resistance of coated samples was investigated. The resulting Bode plots are shown in Fig. 4.14. The impedances measured on the samples

coated with DDPO4 seem to have comparable impedance values with the cleaned, bare substrates. The polymer-coated samples, nevertheless seem to have a lower impedance compared to the bare substrates. The adsorption of the polymers from different solvents did not show big differences within the EIS measurements, except for the polymer coatings in acetone, where pitting corrosion was detected relatively fast. Despite of that solvent effect, both types of samples, coated either with DDPO4 or with the different polymers seem to withstand well the EIS measurement almost down to frequencies of 20 mHz. This indicates a higher resistance against pitting corrosion, meaning both types of surface functionalization render the surface more homogeneous and therefore, the corrosion reaction is performing more consistently. Assessing the performance of the polymer-coated samples, the first apparent difference from the SAM coated samples is the lower dispersity in the samples. This means that polymer coated samples behave more similar than for samples coated with the SAMs. In comparing the polymers, almost all polymers compositions behave the same, only the polymer backfilled with ethanolamine seems to underperform slightly. This is probably the effect of the backfiller, which is supposed to align away from the surface, and direct towards the PEG chains. Therefore, less hydrocarbon chains are present close to the surface, to contribute to both a better ordering and thus a denser packing of the polymers at the surface and to a dense and protecting, hydrophobic surface coating. Still the polymer adlayer is lowering the resistance in comparison with the bare substrate, whereas the SAM adlayer is not influencing the resistance visibly. This could be explained by two different facts related to the polymer built-up. First of all, both systems - SAMs and polymers - are supposed to have a hydrophobic anchoring part. In the case of the DDPO4, due to the dodecyl chain, the surface is rendered hydrophobic. The self-assembly is supposed to take place in the case of the polymer system, too. Due to the much higher molecular weight of the polymers and the less pronounced hydrophobic layer, which is stabilizing the self-

assembly process, the self-assembly is presumably not as well ordered as it is the case for the SAM layer. Therefore, the hydrophobic barrier established by the polymer monolayer is not as high as it is for the SAM coating. Additionally, the presence of PEG chains close to the surface is attracting water and ions close to the surface. Since PEG is a good complexant for alkali metal ions like sodium ions [256–258], chloride ions could be present close to the surface in higher concentrations. Chloride ions are well known to play a predominant role in corrosion mechanisms [236, 259, 260]. Furthermore, there is the presence of the free carboxylic acids at the backbone of the polymer. These carboxylic acids could be responsible for a local change in the pH close to the surface. This slight change towards more acidic environment is destabilizing both yttrium oxide and magnesium oxide, this could be one actuator towards an enhanced corrosion rate. Despite this, the corrosion is still shifted towards more homogeneous corrosion, because less pitting corrosion is observed with both SAMs and polymer coating, which is a basic necessity towards a more controlled corrosion behavior of the samples.

Looking at the phase shift plot (c.f. Fig. 4.14), the maximum phase shift value is for all samples equal to 70-80°. For fresh oxides, the phase shift stays much longer at these high values in comparison to old oxides (due to the lower capacitive effect), which indicates the higher compactness of the fresh oxide layer. At lower frequencies, the phase shift equalizes almost to zero. For the polymer-coated samples, the phase shift does not reach the high values, the plateau is at lower values of around 60°. The phase shift correlates well with the difference in resistance measured in the Bode magnitude plot.

4.6.1 Conclusions

In this chapter, the heat-treated WE43 alloy was investigated. The proposed formation of a thick thermal oxide, mainly composed of yttrium oxide could be confirmed by means of XPS depth profiling. Furthermore, the build-up of the oxide layer has been investigated. The surface of the natural yttrium oxide layer is covered by a approx. 200 nm thick layer rich of magnesium species. Mainly magnesium oxide/hydroxide and magnesium carbonate species could be found. The magnesium carbonates are most probably formed during the heat-treatment at 500 °C from the carbon dioxide in the air. This uppermost layer is supposed to form the main barrier, enhancing the corrosion resistance of the sample. Water and even concentrated sodium hydroxide solutions (where magnesium oxide and hydroxide are supposed to be stable against dissolution) edge away that layer and reveal the yttrium oxide underneath to the solution. This yttrium oxide layer is highly cracked and the corrosion susceptibility inside these cracks is not high enough anymore to avoid pitting corrosion. The proposed mechanism for the edging of the overlaying layer even at the high pH value of concentrated NaOH solution is the fact that magnesium carbonate species are present within this layer, which are most probably more prone to dissolution, in undergoing different hydration states.

This is the main reason why a chemical characterization of the samples is quite difficult - a huge change in the chemical composition of the samples is obtained, varying also between different batches and storage times. In terms of corrosion resistance, ideally, best results were always obtained with freshly prepared samples. Already after one week of storage at ambient conditions, the humidity present in the air weakens the corrosion-inhibiting layer. Still, the bare, oxidized samples showed a huge scattering in the corrosion tests, with a resistivity varying highly, including the tendency to show pitting corrosion towards smaller frequencies. Here one proposed mechanism

is first the more or less homogeneous dissolution of the uppermost magnesium oxide/magnesium carbonate layer by the aqueous buffer used as corrosion medium. From the time that the uppermost layer is penetrated by water and the water finds its way into the underlying cracks inside the yttrium oxide, pitting corrosion is supposed to start. These cracks create tunnels for the water to locally cross the thick yttrium oxide layer rapidly and reaching the bulk, magnesium alloy. Since the oxidized alloy is characterized by an yttrium depletion zone close to the oxide layer and therefore contains much less yttrium than the reference WE43 without heat-treatment, the corrosion reaction starts relatively fast. This leads to the formation of pitting corrosion zones shortly after the first penetration of the overlaying magnesium oxide / carbonate layer and the subsequent penetration of the yttrium oxide layer through the cracks present there.

Surface functionalization with phosphates and phosphonates was proven to be possible from both aqueous and organic solvents. While the adsorption from water dissolves the uppermost magnesium oxide / magnesium carbonate layer, the carbonate layer could be still detected when adsorbing from organic solvents. Therefore, the adsorption on both magnesium oxide and yttrium oxide surfaces is possible. The surface resistance against corrosion was studied after functionalization. The substrates coated with DDPO4 SAMs behave similar to the unfunctionalized substrate. High corrosion resistance is still possible, but due to the high deviations observed, highly dependent on the sample. This is remarkable due to the fact that the uppermost magnesium oxide / carbonate layer is already (partially) dissolved as proven by XPS analysis. The best explanation is that a barrier role against water penetration was performed by the hydrophobic coating, which resists against pitting corrosion, but then subsequently, due to the inhomogeneities in the self-assembly structure, the water is penetrating into the cracks of the yttrium oxide layer, inducing pitting corrosion, comparable to the behavior of the bare substrates. A different corrosion

behavior was found for the samples functionalized with the PEG polymers. The deviations between samples was much less in the EIS measurements, yielding in more comparable results. The resistance was always in between the best and the worst behaving bare substrates, thus the polymer adlayer induces a more homogeneous corrosion property. Additionally, it seems that the pitting corrosion was reduced in favor of a more homogeneous corrosion mechanism - less scattering at smaller frequencies was observed for these samples during corrosion measurements.

Poly(phosphonates) for lubricant applications on Steel

5.1 Introduction to Friction and Tribology

5.1.1 General

Tribology is defined as the science and technology of interacting surfaces in relative motion and focuses on friction, wear and lubrication phenomena [261]. Rolling and sliding applications are central to many technologies in our society. The basics of this technology are very old (e.g. the development of bearings or low-friction surfaces), and have constituted the basis of a vast number of engineering and everyday applications. The fundamental understanding of the interaction between friction, lubrication and wear processes is important to achieve prolonged lifetimes of mechanical devices or for improvements in energy economy [262].

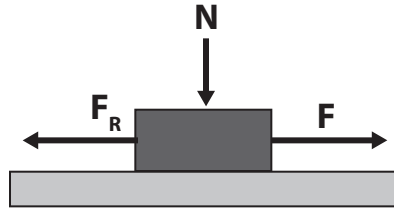


Figure 5.1: The external force F applied to the block which is in contact with a surface, induces an interfacial friction force F_R that counteracts the relative movement between the two bodies [262]

5.1.2 Friction

The friction force F_R is defined as the force occurring at the interface of two bodies that counteracts the relative movement. This is shown in Fig. 5.1, where an external force F is applied to a block that is in contact with a surface. As long as the applied force F is smaller than the static friction force F_{RS} , the block does not move. When the external force F starts to overcome the static friction force ($F > F_{RS}$), the block starts to move in the direction of the applied force. The resulting friction force in relative motion is then called dynamic friction force F_{RD} [262].

The coefficient of friction μ is a characteristic parameter that describes the frictional properties between two sliding bodies. It is defined as the ratio between the friction force F_R and the normal force N . The dynamic friction coefficient is normally lower than the static friction coefficient.

$$\mu = \frac{F_R}{N}$$

This fundamental law was found by Leonardo da Vinci (1452 – 1519) and rediscovered by Guillaume Amontons (1663 – 1705) in 1699 and is therefore usually called Amontons' law. In 1785, Charles Augustin de Coulomb discovered a third law of tri-

bology. All three fundamental laws of tribology are, however, of an empirical nature and can be summarized as:

The friction force is

1. proportional to the normal force
2. independent of the apparent contact area
3. independent of the sliding velocity

These laws are valid for many tribological contacts, lubricated and non-lubricated scenarios, but there exist some cases, in which these laws are no more valid, especially in case of polymers used as tribological contacts.

5.1.3 Wear

Mechanical contact and relative movement of the sliding surfaces generally causes wear, which can be described as a progressive loss of material from a surface. In general, different wear mechanisms can be distinguished [261, 263]:

Adhesive wear occurs mainly in sliding contact of two bodies. Adhesion between asperity contacts, which are sheared by sliding leads to a detachment of fragments from one side of the surface and to a transfer of those fragments to the other surface. In a further stage of wear, these fragments may become loose wear particles.

Abrasive wear occurs mainly in the contact of a hard, rough surface with a softer surface. The harder, rough surface damages the softer surface by plastic deformation, fracture or scratching. Another possibility is the introduction of

abrasive grits sliding between the surfaces, with at least one of the surfaces being softer than the particles.

Fatigue wear is mainly observed for sliding and rolling, where repeated loading and unloading cycles lead to the formation of subsurface or surface cracks, which result after several cycles in the fracture and breakup of larger fragments from the surface.

Others summarizes all wear mechanisms not connected to sliding/rolling and includes impact wear, such as erosion or percussion, chemical wear, reactive wear, electrical-arc induced wear or fretting caused by vibrations.

For sliding (and rolling) mechanisms, the wear volume per sliding distance Q can be related to the normal load N and the hardness of the material H , by using the so called Archard wear equation

$$Q = \frac{K \cdot N}{H}$$

5.1.4 Lubrication

In most engineering applications, lubricants are used in order to reduce friction. The basic principle is the introduction of an additional layer between two sliding surfaces, which has low shear strength. There exist solid, liquid or gaseous lubricants to reduce both friction and wear between surfaces in relative motion. Still, liquids represent the most common materials used for lubrication purposes. Fig. 5.2 shows a generalized Stribeck curve, which is of empirical nature. It shows the variation of the friction coefficient as a function of the quantity $\eta \cdot v/N$, where η is the viscosity of the lubricant, v is the relative sliding velocity and N is the normal load [262].

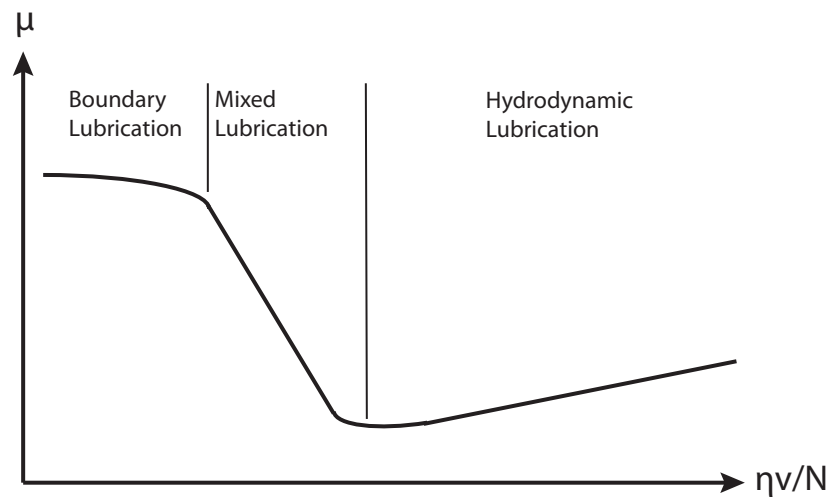


Figure 5.2: The empirical Stribeck curve describes the variation in the coefficient of friction as a function of $\eta v/N$ for lubricated contacts

There are three different, principal lubrication regimes visible in the Stribeck curve:

1. Hydrodynamic lubrication (HL) / Elastohydrodynamic lubrication (EHL), depending on the contact geometry
2. Mixed lubrication (ML)
3. Boundary lubrication (BL)

The basic differentiation between these lubrication regimes is the lubricant film thickness, which separates the sliding surfaces and influences the measured friction forces and the resulting wear.

Hydrodynamic lubrication (HL) In this lubrication regime, the sliding surfaces are separated by a relatively thick lubricant film in comparison to the asperity height. That high lubrication film thickness is supporting the applied normal load by its hydrodynamic pressure. The contact between the two surfaces needs to be (nearly)

Table 5.1: The four elastohydrodynamic lubrication (EHL) regimes

EHL regime	Elastic deformation	Viscosity increase
Isoviscous-rigid	No	No
Piezoviscous-rigid	No	Yes
Isoviscous-elastic	Yes	No
Piezoviscous-elastic	Yes	Yes

parallel over a relatively large area in order that the lubricating effect becomes predominant (conformal system). Additionally, this lubrication regime dominates when sufficiently viscous lubricants are employed under high-sliding-speed conditions. The viscous drag of the lubricant is then largely determining the resulting coefficient of friction. Due to the very thick lubricant film, this regime is sometimes referred to as full-film lubrication. The film thickness is always much higher than the arithmetic surface roughness, R_a . Because of the absence of asperity contacts, wear is assumed to be negligible [262].

Elastohydrodynamic lubrication (EHL) This lubrication regime is found for non-conforming geometries, where a point or line contact between the sliding partners is given. Then, high local pressures are present. Besides the increase in lubricant viscosity with pressure, elastic deformation of the contacts has to be considered in the EHL regime. High local contact pressures and thus considerable elastic deformations are frequently found for non-conforming contacts such as for sphere-on-plane geometries. Depending on the relative role of the two basic parameters in EHL, i.e. elastic deformation of the solids under applied load and increase in lubricant viscosity with pressure, Hamrock and Dowson [264, 265] have defined four different EHL regimes that are presented in Tab. 5.1.

Mixed lubrication (ML) With higher loads and/or slower sliding speeds, the separating lubricant film between the two surfaces gets thinner. When the lubricant film thickness is approaching the value of R_a , first asperities get in first, intermittent contact. It is the intermediate regime between full film lubrication and boundary lubrication.

Boundary lubrication (BL) At high loads and/or low sliding speeds, more and more severe sliding conditions occur, in which it is difficult to maintain even thin lubricant films between the contacting surfaces and more and more asperity contact is predominant. The film thickness is always smaller than the surface roughness R_a . This regime is called the boundary regime and shows high friction and wear.

The first introduction of the phenomena of boundary lubrication was by the term “oiliness” when mineral oils began to replace vegetable oils as lubricants in industry during the late 19th and the beginning of the 20th century. The comparably worse behavior of mineral oils at high loads even at same viscosities led to the introduction of the term “oiliness”. This was a measure for the ability of an oil to reduce friction in boundary lubrication [266] and could be tuned by the addition of long-chain carboxylic acids (fatty acids) [267]. The most accepted explanation is that the carboxylic acids adsorb to the surface, forming a monolayer film, which prevents direct contact of the surfaces and introduces a shear plane between both friction partners. However, there are indications for a change in the structure of the adsorbed monolayer, when water is present at the interface. Then a highly swollen, thick multilayer film is formed, which is destroyed under higher loads, but can be reformed [267].

Today, a more general definition is used, namely molecules that are able to protect the sliding surfaces under boundary lubrication conditions are called boundary lubricants. Boundary lubrication becomes predominant if liquids with a low pressure-coefficient of viscosity are employed as base lubricants or if the contact pressure be-

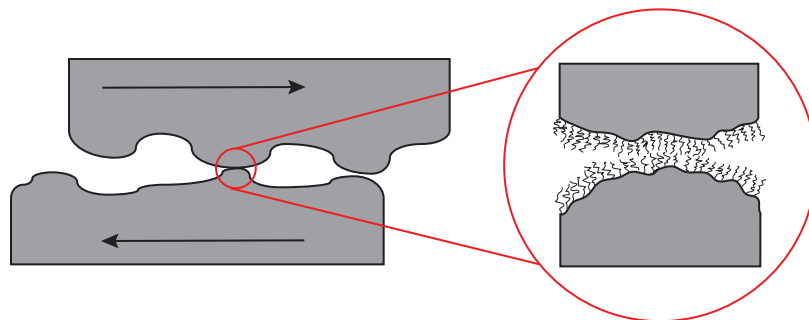


Figure 5.3: Boundary lubricants protect the tribologically stressed surfaces by preventing direct asperity contact in the absence of a fully separating lubricant film

tween both sliding partners becomes very high. The build-up of a separating film between the contacts is circumvented in this case. The lubricating fluid cannot support the external load and is therefore squeezed out of the contact area. Some boundary lubricants, however, can enable the generation of a protecting lubricant film, where the base lubricant is incorporated into the boundary lubricant layer. Under these circumstances, the viscosity of the lubricant becomes secondary, because the low shear-strength interface mainly arises from the adsorbed boundary-lubricant layer on the surfaces. Suitable molecules possess a high surface affinity and ideally form a dense monomolecular layer to protect the surface. This is the case for both SAMs or polymer brushes, as shown in Fig. 5.3. Direct asperity contact can therefore be prevented and ideally is combined with a reduction of the adhesion between asperities compared to that of the “unprotected” surfaces. This lubrication mechanism is generally known as “adsorption lubrication”. The effect increases with lower lubricant film thicknesses and higher number of asperity contacts.

5.2 Surface Properties and Applications of Steel

The most common and widely used metallic material in today's society is steel. Steel is an alloy consisting mainly of iron with a normal carbon content lying between 0.2 - 2%. In a simplified, historical definition, steel can be described as an alloy of iron and carbon, but today, this description is no longer applicable. In some very important steel alloys, e.g. interstitial-free steels and type 409 ferritic stainless steels, carbon is considered as impurity and thus only quantities of a few parts per million are tolerated. Other hardening agents, such as manganese, chromium, vanadium, tungsten, silicon, nickel, molybdenum, niobium and aluminum are used in the wide range of different steel alloys. These elements prevent dislocations in the iron atom crystal lattice from sliding past one another. Furthermore, particular properties such as strength, hardness, corrosion resistance, magnetic permeability and machinability are achieved by these alloying elements. The final properties, such as hardness, ductility and tensile strength are influenced by even small variations of the amount of alloying elements and the form of their presence in the steel, e.g. as solute elements or as a precipitated phase. Steel with increased carbon content becomes harder and stronger than iron, but loses ductility compared to pure iron. By definition, steel always contains at least 50% iron, and must contain one or more alloying elements [268, 269].

An important example for the versatility of steel is in the automobile industry, where it is still the material of choice and accounts for over 60% of the weight of the vehicle. Steel is highly formable and corrosion resistant, especially when coated with zinc-based coatings. That is why it is used for the outer contours of the body, and is strong and therefore used in the body frame, motor brackets, driveshaft and door impact beams of the vehicle and provides exceptional energy absorption in case of a collision. Additionally, steel is comparably inexpensive, especially in contrast to

other competing materials, e.g. aluminum, magnesium or various plastic materials. Another positive effect is its easy recyclability and magnetic separability [268, 269].

These outstanding properties are not only due to the composition of different alloying elements (binary and ternary phase diagrams), but as well heavily influenced by basic metallurgical principles. Especially different processing (rolling, casting, basic oxygen furnace, ...) and the microstructure (heat-treatment, annealing, hardening, quenching, ...) influence the properties [268, 269].

5.3 Motivation

Steel is still the most important surface for lubrication, and oil the most commonly used lubrication fluid. The main motivation of this work was the development of a polymer additives for oil lubrication, which acts in the boundary regime under the formation of a surface brushes. The modular synthesis approach for *graft*-copolymers, together with the phosphonate surface anchor and grafted hydrophobic side-chains was used to explore boundary lubrication. However, the polymer has to face two major challenges, namely the full solubility in apolar oil and surface activity to form polymer brushes at steel surfaces. In order to achieve real oil solubility, the POMA backbone was chosen, because of its higher apolarity due to hexadecane side-chains present at each repetition unit. Oil soluble poly(1,2-butylene glycol) monobutylether was used as polymeric side-chain and the phosphonate surface anchor for chemisorption. The synthesis of the polymer is described in Chapter 2 and the polymer was named POMA(0.40,0.60, Butanol), indicating the grafting densities as used during synthesis. The performance of the polymer additive as boundary lubricant will be investigated mainly by characterizing the coefficient of friction and the wear performance using a pin-on-disk tribometer and a mini traction machine.

Table 5.2: Elemental composition of 100Cr6 steel according to EN ISO 683-1

Element	C	Cr	Mn	S	P	Si
wt. %	0.95–1.100	1.35–1.85	0.25–0.45	< 0.025	< 0.025	< 0.15-0.35

5.4 Steel substrates

The balls (4 and 6 mm diameter, Hydrel GmbH, Romanshorn, Switzerland) and disks were made of common bearing steel 100Cr6 (AISI 52100, DIN 1.3505). This steel, a ferritic Cr alloy, is one of the most widely used materials for bearings. The composition according to EN ISO 683-1 is shown in Tab 5.2. Usual tolerances are within $\pm 0.1\%$.

The steel can be hardened by heating it in to 800-830°C and a subsequent cooling in water or oil. In this work, hardened balls and non-hardened disks were used.

Before each test, the disks were ground with shrinking grain sizes up to 4000 SiC-paper and subsequently polished with 3 μm , 1 μm and 1/4 μm diamond particles on both sides, including the edges. After each step all samples were cleaned by ultrasonication in isopropanol, dried and the progress controlled by optical microscopy. The surface roughness after polishing was measured with optical profilometry to be $R_q = 6 \pm 1.5$ nm (rms roughness) and $R_a = 5 \pm 1.5$ nm (arithmetic roughness).

The hardness of the disks (non-hardened 100Cr6) and the balls used for the pin-on-disk tests (hardened 100Cr6) was tested by Vickers indentation and found to be $195 \pm 10\text{HV}_{10}$ (Brickers 220, Gnehm, Switzerland) and $810 \pm 20\text{HV}_1$ (MTX-CX Microhardness V-Testor 4901, Wolpert AG, Germany), respectively.

The steel surfaces were cleaned as described in Sect. 7.9.2 by ultrasonication in petrol-ether and ethanol and subsequent plasma cleaning. The surface was characterized by means of XPS. The elements C, O, Fe, Si, Cr and Mn could be found at the surface. Especially the alloying components Si, Mn and Cr could be detected as very small

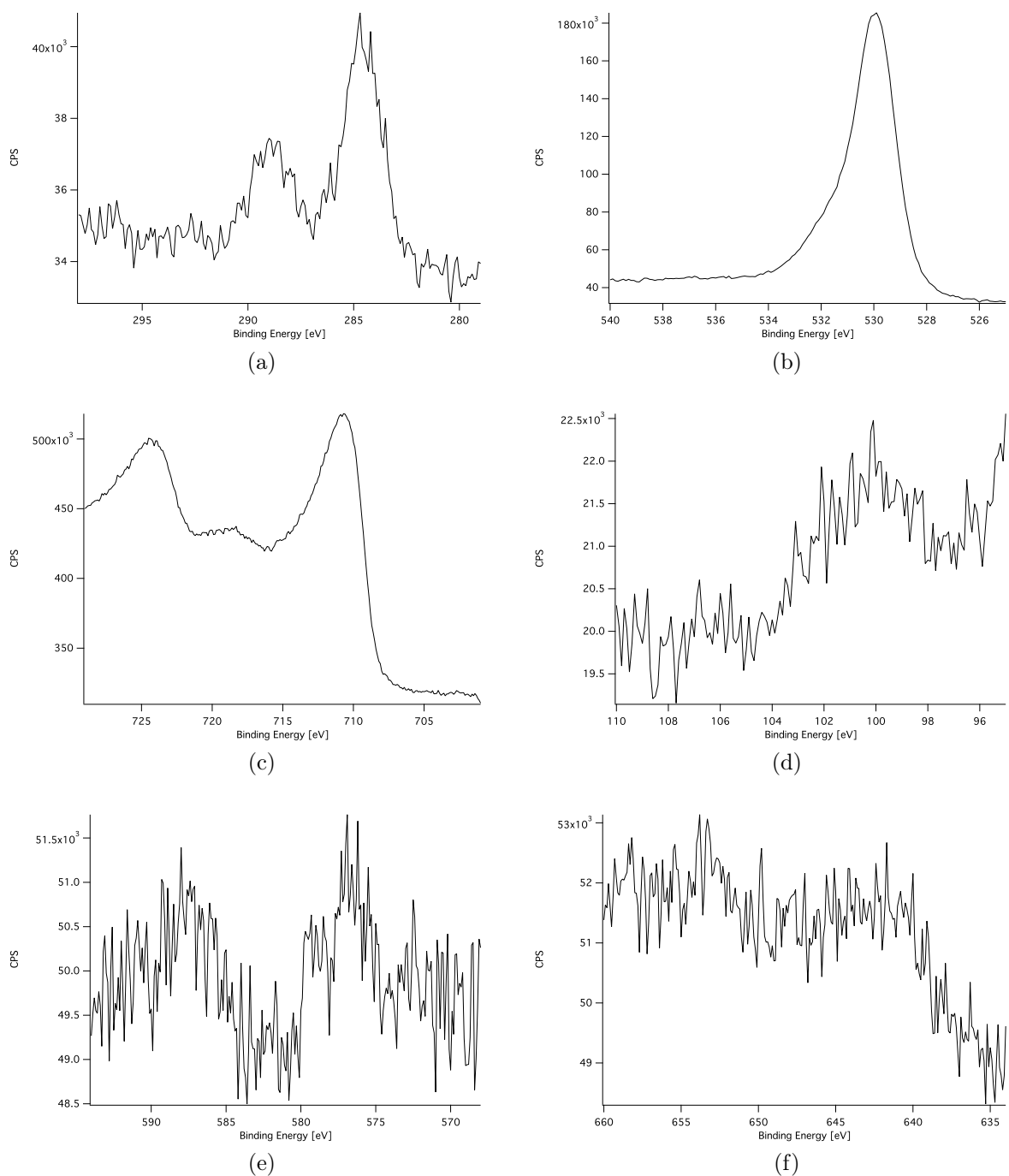


Figure 5.4: XPS (Sigma2) detail spectra of clean steel: (a) C1s spectrum, (b) O1s spectrum, (c) Fe2p spectrum, (d) Si2p spectrum, (e) Cr2p spectrum and (f) Mn2p spectrum. (Sigma 2 instrument)

Table 5.3: Experimental atomic composition of the bare steel surface derived by XPS

Elemental	at-%
C	7.5 ± 1.5
O	67 ± 1
Fe	20 ± 2
Si	3 ± 1
Cr	0.7 ± 0.3
Mn	0.5 ± 0.3

peaks, resulting in very low signal-to-noise ratios. The resulting spectra are shown in Fig. 5.3. For the Fe, Cr and Mn peak, only the respective $2p^{3/2}$ peak was taken into account to determine the surface concentration. The atomic concentrations are summarized in Tab. 5.3

5.5 Polymer Characterization

5.5.1 XPS Characterization of hydrophobic polymer on Titanium oxide

As explained in Sect. 2.8, the characterization of the polymers was hindered by the high amphiphilic behavior of the polymers. That is why the polymers were intended to be characterized after adsorption to the surface. Since the best characterized surface is the titanium oxide surface, where the PEG-ylated, hydrophilic polymers were already proven to adsorb stably, that reference surface was chosen. The polymer was adsorbed from 0.5 mg/ml heptane solution. The peak fitting was performed with identical constraints as explained in 3.4.2. Since for that polymer, ester and amide bonds are present at the polymer, literature values for the differences in the B.E. contribution of amide and ester bonds were compared, resulting in comparable B.E.

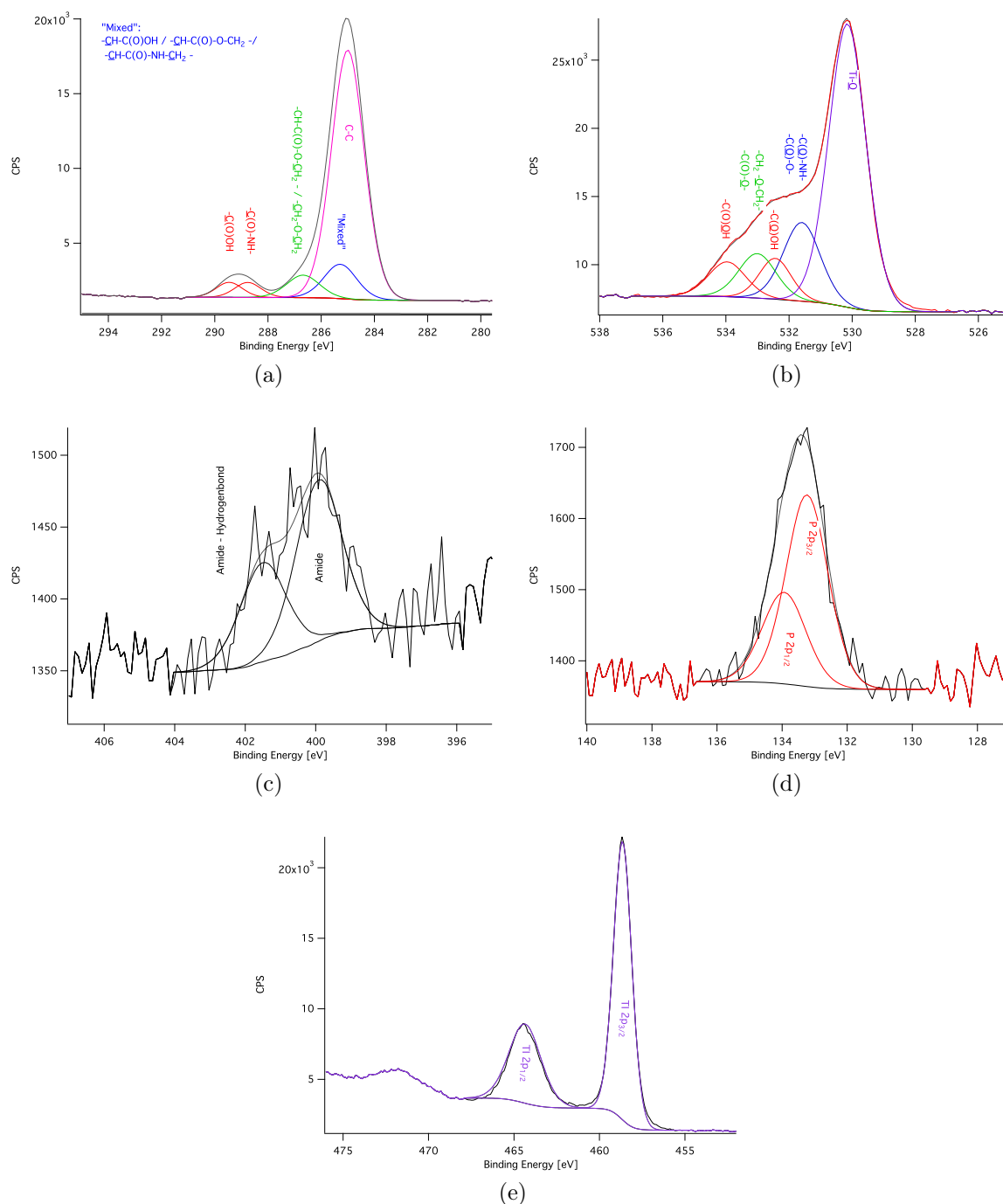


Figure 5.5: Peak modeling of the detail XPS spectra, measured with the Theta probe instrument. The subfigures show (a) C1s, (b) O1s, (c) N1s, (d) P2p and (e) Ti2p XPS detail spectra (Theta instrument)

for the resulting peaks. The chemical contributions, however change slightly. For the C1s spectra, the hydrocarbon peak is still referenced to a B.E. of 285 eV, but is now the predominant species. Two carbonyl contributions could be fitted into the spectrum, resulting in two peaks with a fixed relative area of 1:1, namely the free carboxylic acid and the combined contribution of the respective amide and ester carbonyl contribution. The peak indicating ester groups contains contributions from the carbon directly connected to the oxygen of the ester group. The peak labeled “Mixed” contains the contributions of the neighboring hydrocarbons directly connected at both sides of the amide group. Additionally, the neighboring hydrocarbon to the carbonyl group of the free carboxylic acid and of the ester bond is contributing to that peak. For the oxygen peak, five contributions were fitted. The carbonyl contributions of the amide and the ester are fitted in one peak, whereas the carbonyl contribution of the respective free carboxylic acid is fitted at slightly higher BE. The second contribution of the free carboxylic acid can be found at the highest BE. The signal of the connecting oxygen of the ester bond is fitted together with the contributions of the grafted ether chains. The other peaks are fitted according to the fitting procedures explained above (Sect. 2.8). The resulting fits are illustrated in Fig. 5.5. The grafting with the polyether side-chain resulted in very low grafting densities, as it can be clearly seen in the resulting spectra. Taking into account the contribution of the ester bonds derived from the backfilling with butanol also present in that peak, the contribution of the ether peak is even smaller. Since the ether peak should derive from the poly(1,2-butylene glycol) side chains, the grafting density can be concluded to be close to zero. However, the low grafting density can be calculated from the XPS component composition, as shown in Tab. 5.4.

In Tab. 5.4, the surface concentration of the fits and the total elemental concentration is summarized. The grafting density of the phosphonates can be calculated from the atomic concentration of phosphorus present at the surface. As reference, the free

Table 5.4: Experimental component composition of the polymer adsorbed to titania, derived from peak fitting of the XPS detail spectra. The abbreviation “mixed” consists of the contributions $\text{-}\underline{\text{C}}\text{H-C(O)OH/ -}\underline{\text{C}}\text{H-C(O)-O-CH}_2\text{/ -}\underline{\text{C}}\text{H-C(O)-NH-}\underline{\text{C}}\text{H}_2\text{-}$

Element	Component	at-%	total at-%
C1s	<u>C-C</u>	43 ± 2	58 ± 2
	$\text{-}\underline{\text{C}}\text{H}_2\text{-O-}\underline{\text{C}}\text{H}_2\text{- / -C(O)-O-}\underline{\text{C}}\text{H}_2$	4.4 ± 0.5	
	$\text{-}\underline{\text{C}}\text{(O)-O- / -}\underline{\text{C}}\text{(O)-NH-}$	2.3 ± 0.2	
	-C(O)OH	2.3 ± 0.2	
	“mixed”	5.5 ± 1	
O1s	<u>Ti-O</u>	19.5 ± 0.7	33 ± 3
	$\text{CH}_2\text{-O-}\underline{\text{C}}\text{H}_2\text{- / -C(O)-}\underline{\text{O-}}\underline{\text{C}}\text{H}_2$	3.3 ± 0.5	
	-C(O)OH	2.1 ± 0.3	
	-C(O)OH	2.1 ± 0.3	
	-C(O)-NH-	5.6 ± 0.5	
N1s		0.2 ± 0.1	0.3 ± 0.1
		0.10 ± 0.05	
P2p		0.6 ± 0.05	0.6 ± 0.05
Ti2p		9.0 ± 0.6	9.0 ± 0.6

carboxylic acids are used. The free carboxylic acids are formed quantitatively by the ring-opening process during synthesis, thus the ratio phosphorus to carboxylic acid can be used to determine the grafting density of the surface anchor. The grafting density of the surface anchor is therefore 0.30 ± 0.05 and thus slightly below the expected grafting density of 0.4, assuming quantitative reaction during synthesis. The grafting density of the ether side-chains can be approximated in using the information of the peaks containing the contributions of the ether and the ester. Assuming a full ring-opening of the unreacted anhydride rings by the backfiller, the ester content can be approximated from the grafting density of the surface anchor, thus being 0.70 ± 0.05 . The resulting contribution of the ester to the peak in question is in the order of 1.5 ± 0.1 at-% and has to be subtracted. The resulting at-% resulting from the ether is therefore 1.5-1.8 at-%, normalized to the contribution of one atom per repetition unit of the polyether. Taking into account the number of monomer units

per polymer chains (20 repetition units per chain for a molecular weight of 1.5 kDa), the approximated grafting density of the poly(1,2-butylene glycol) side chains can be calculated to be 0.04 ± 0.01 . Therefore, only 4% of all rings are reacted with the polyether chain, resulting in statistically 2 poly(1,2 butylene glycol) chains grafted onto each polymer backbone.

5.5.2 XPS Characterization of hydrophobic polymer on steel

The polymer was adsorbed on polished 100Cr6 steel from heptane and characterized by XPS. The C1s spectra can be fitted as explained above for the polymer investigated on titania, the resulting fit is shown in Fig. 5.6(a). However, the phosphorus and the nitrogen peak could not be well resolved, resulting in a much lower concentration of phosphorus and nitrogen. A fit of the O1s peak was not performed. Two main peaks are visible, which can be assigned to iron oxide and iron hydroxide at higher BE. A comparison of the O1s peak of bare and polymer coated steel samples are shown in Fig. 5.6(b).

Tab. 5.5 summarizes the atomic percentages obtained for all fits and all elements. Due to the highly reduced phosphorus and nitrogen content, a much lower grafting density of 0.04 was calculated for the surface anchor. It seems that the polymer adsorbing at the surface has a highly reduced amount of phosphonate surface anchor, compared to the XPS analysis on titania surfaces. This indicates a preferential adsorption of polymer chains with a much lower phosphonate content. Since the polymers are statistical polymers, bearing more or less phosphonates, apparently the polymers with less phosphonate content adsorb much better to the surface. This could be due to preferential adsorption, having a higher affinity of the carboxylic acids with the surface. Still with the help of the calculated low grafting density of phosphonate surface anchor, the grafting density of the poly(butylene glycol) side-chains was calculated

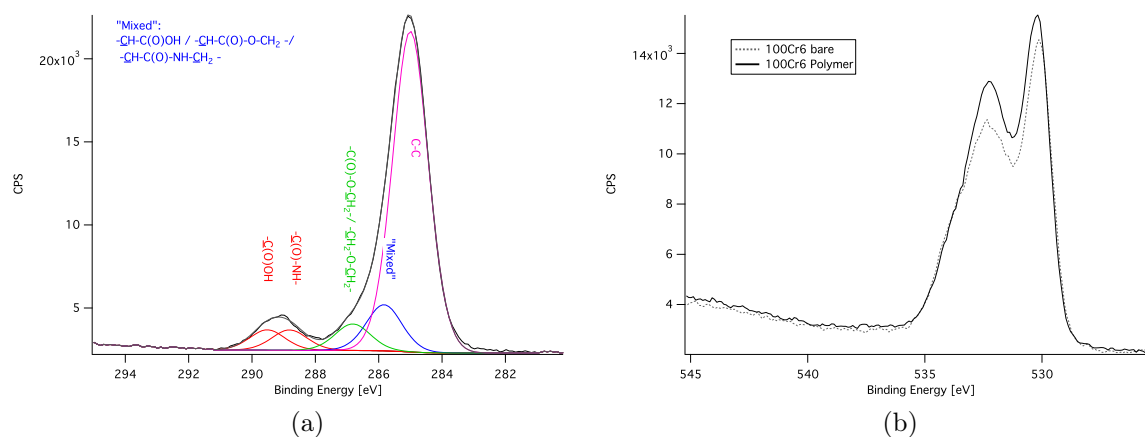


Figure 5.6: XPS spectra of the polymer POMA(30:70, Butanol adsorbed on Steel: (a) C1s peak and (b) O1s peak (of polymer and bare substrate), measured at the Theta instrument

as explained above, resulting in a grafting density of 0.03 ± 0.01 , which is in good agreement with the value obtained at the titanium oxide surface.

5.5.3 Dry and swollen layer thickness

The dry and swollen layer thickness was characterized on titania using VASE (c.f. Sect. 7.2.1) and neutron reflection (c.f. Sect. 7.2.6) measurements, as it was already discussed for the PEG-ylated polymers in Sect. 3.4.4. For both systems, titanium oxide surfaces were used. The dry layer thickness was measured to be 2.2 ± 0.1 nm. The swollen polymer layer thickness was investigated by neutron reflectometry measurements at the “MINE” neutron reflectivity facility at the Japanese Atomic Energy Agency in Tokai village (Ibaraki) in Japan (angle dispersive reflectometer). After fitting of the neutron scattering data (reflectivity profiles), as presented in Sect. 7.2.6, both the swollen thickness and the amount of deuterated hexadecane in the polymer brush could be calculated. The swollen layer thickness was calculated to be 3.0 ± 0.2 nm and a hexadecane content in the polymer layer on the order of

Table 5.5: Experimental component composition of the polymer adsorbed on 100Cr6 steel, derived from peak fitting of the XPS detail spectra. The abbreviation “mixed” consists of the contributions $\underline{\text{C}}\text{H-C(O)OH}$ / $\underline{\text{C}}\text{H-C(O)-O-CH}_2$ / $\underline{\text{C}}\text{H-C(O)-NH-CH}_2$ -

Element	Component	at-%	total at-%
C1s	$\underline{\text{C-C}}$	46 ± 4	66 ± 3
	$\underline{\text{CH}_2\text{-O-CH}_2\text{-}} / \underline{\text{-C(O)-O-CH}_2}$	3.0 ± 0.4	
	$\underline{\text{-C(O)-O-}} / \underline{\text{-C(O)-NH-}}$	3.0 ± 0.4	
	$\underline{\text{-C(O)OH}}$	3.0 ± 0.4	
	“mixed”	9 ± 3	
O1s		26 ± 2	26 ± 2
N1s		0.05 ± 0.01	0.1 ± 0.1
		0.05 ± 0.01	
P2p		0.1 ± 0.05	0.1 ± 0.05
Fe2p		7 ± 3	7 ± 3
Cr2p		0.4 ± 0.1	0.4 ± 0.1

20%. Due to the very low grafting density with poly(1,2-butylene glycol) side chains, a low increase in layer thickness in contact to the solvent was expected. Compared to the PEG-ylated polymers, as discussed in Chapter 3, the relatively low swollen layer thickness is due to the much lower grafting density of the poly(alkylene glycol) chain present here. Additionally, the solvent content inside the layer is much lower than in the case of the PEG-ylated polymers. Due to the low grafting density, the solvent is mainly found between the relatively short hydrocarbon chains originating from the octadecene repetition units and thus the solvation content is much lower than it would be in a much thicker and more flexible polymeric brush. However, the swelling proves the ability of the polymer to form a polymeric layer on top of the surface, capable to integrate and hold the solvent inside the grafted side chains. Due to the swelling the introduction of a probable shear plane outside of the polymeric

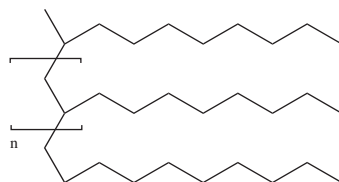


Figure 5.7: Chemical structure of the poly(α -olefin) PAO-166

film can be assumed, which could facilitate the slip between tribostressed surfaces and therefore act as boundary lubricant.

5.6 Polymer additive for lubrication

The polymer POMA(0.3,0.04, butanol) was used as additive for oil lubrication. Poly(α -olefin), PAO-166 (Nexbase 2006, Neste Oil N.V., Beringen, Belgium), a synthetic oil, consisting of branched hydrocarbons was used as base oil. The corresponding structure is shown in Fig. 5.7. The physical properties are a density of 830 kg/m^3 and a viscosity of 43 mPas at 25°C . Due to its apolar character, the solubility of the additives is crucial.

In order to be able to investigate wear effects, hardened 100Cr6 steel balls against non-hardened 100Cr6 steel disks were used, forcing the wear to be mainly at the disk. Additionally, a hardened ball ensures a much more constant contact area during the measurements.

5.6.1 Calculation of the lubrication regime

The lubrication regime can be calculated from the material properties of the contacting solids (Young's Modulus $2.1 \cdot 10^{11} \text{ Pa}$, Poisson's ratio 0.3) and of the lubricant (Pressure-viscosity coefficient $1.45 \cdot 10^{-8} \text{ Pa}^{-1}$, dynamic viscosity 0.025 Pas) and the

experimental conditions, like sliding speed and applied load and the geometry of the contacting surfaces (sphere on disk, ...) using dimensionless parameters, as described in the papers of Hamrock [264, 265]. From these, the film thickness of the lubricant between the contacting surfaces can be calculated. The calculations were performed in using a Matlab Program, developed and maintained by Dr. Jarred Clasohm, based on the formulae presented by Hamrock et al. [264, 265].

The calculations were based on a pin-on-disk experiment with both surfaces consisting of 100Cr6 steel and PAO-166 as lubricant. The calculations were performed for 2 different radii, namely 3mm and 2mm, corresponding to the experimental geometries of the static and oscillating load tribometer. Applied load and sliding speed were varied in a broad range, namely from 0.0001 - 0.01 m/s sliding speed and 1-10 N as applied load. The two calculated dimensionless parameters as defined in [264, 265] were calculated:

- the dimensionless Elasticity parameter g_E has the value of $3.35 \cdot 10^3$
- the dimensionless Viscosity parameter g_V ranges from $4 \cdot 10^8$ to $1 \cdot 10^{17}$

For these values, all experimental conditions investigated are within the piezoviscous-elastic regime (c.f. Sect. 5.1) [264, 265]. These calculations, however simplify the situation present in real experiments. Taking into account the actual, measured RMS surface roughness of the polished disks ($R_q = 6$ nm) as described in Sect. 5.4 and the film thickness that is always calculated to be lower than 2 nm, the separation of the tribopair is much smaller than the height of the asperities. This leads to a predominant hard-hard contact of the asperities, directing the regime towards boundary regime.

The film thicknesses depending on load and sliding speed as obtained from the calculations are summarized in Fig. 5.8. With higher loads and slower speeds, the film

thickness is decreasing. Smaller radii of the ball also decrease the film thickness. It can clearly be observed, that a variation of the applied load is not as efficient as a reduction in speed to decrease the actual film thickness and thus directing the lubrication regime towards boundary lubrication conditions.

5.6.2 Pin-on-disk Measurements

Constant load

First Pin-on-disk Measurements under constant load of 1 N and varying speed, as described in Sect. 7.3.1 were always performed with additive concentrations of 2 mg/g. The planarity of the disk could not be guaranteed during these measurements. The fluctuation of the coefficient of friction that was therefore observed during one turn of the disk was averaged. Towards slower sliding speeds, the amplitude of these fluctuations increased, indicating a change of the friction or wear behavior. Because of the non-stoichiometric reaction reactive polymer backbone with the poly(butylene glycol) side-chain yielding POMA(0.3,0.04, butanol), the latter still contains unreacted, free poly(1,2-butylene glycol). There was a need to compare the effect of the polymer with the effect of just the side-chain itself, both dissolved in PAO. As a reference, pure PAO was used. The results are shown in Fig. 5.9. Towards lower speeds, the coefficient of friction is rising for the pure base-oil, but also for the poly(1,2-butylene glycol) side chain when used as an additive, whereas the polymer additive POMA(0.3,0.04, butanol) influences the coefficient of friction to stay at lower values when approaching lower sliding speeds. Even at higher sliding speeds, the values for the coefficient of friction were slightly lower for both additives in comparison to the pure base-oil. This could be an indication of a viscosity effect, probably mainly induced due to the free poly(1,2-butylene glycol) chains.

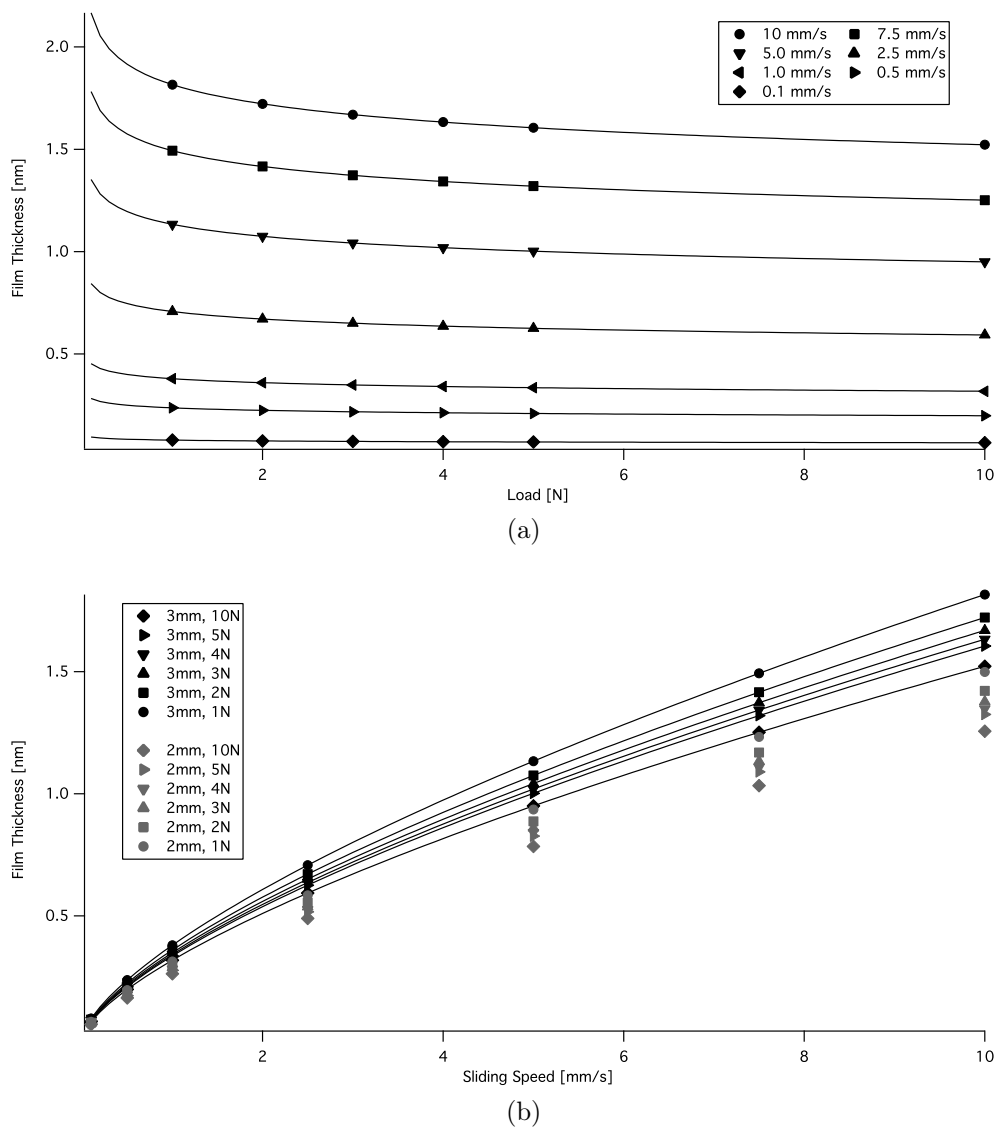


Figure 5.8: Calculated dependence of the film thickness on (a) load (for a ball radius of 3 mm) and (b) sliding speed (for ball radii 2 and 3 mm) for the base oil PAO, based on the formulae of Hamrock et al. [264,265]

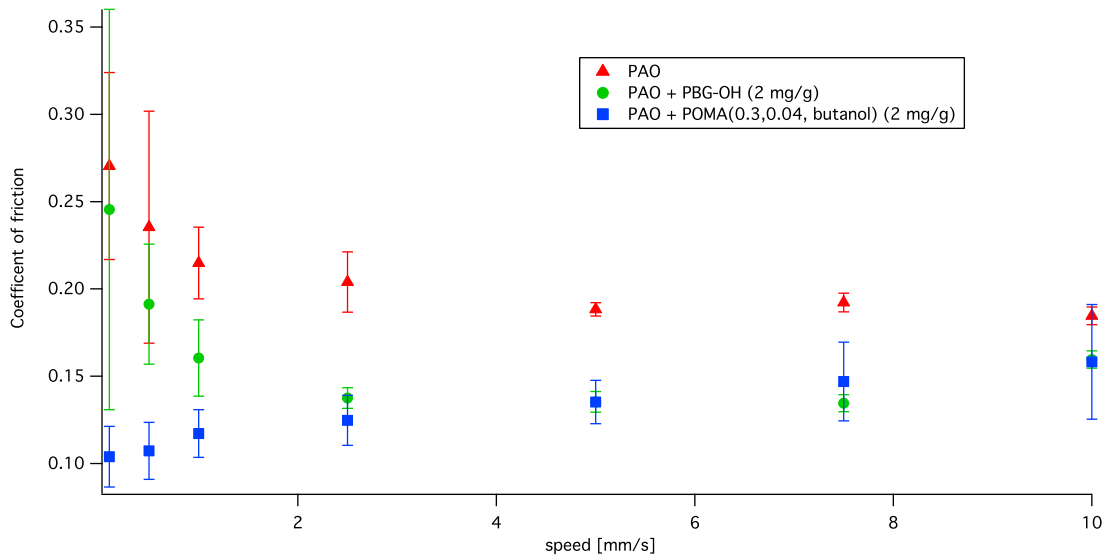


Figure 5.9: Constant load measurements

Cyclic load test

Cyclic load tests as described in Sect. 7.3.1 were performed to investigate the further behavior of the additives (2 mg/g) at higher loads and different sliding speeds. Additionally, wear rates were calculated. The wear rate was calculated as explained in Sect. 7.3.1. Basically, the cross-section area of the wear track was measured by means of optical profilometry and then the wear rate was calculated. The wear rate has the unit $[\text{mm}^3/\text{m}]$ and describes the volume loss by wear per sliding distance. It has to be mentioned, that the wear rate is not normalized by the applied load and thus a correlation with the applied load is possible. The results are shown in Fig. 5.10.

There is no visible influence on the coefficient of friction between the measurements of pure PAO and PAO + Additives. The coefficient of friction seems to be slightly lower with the POMA(0.3,0.04, butanol) additive, but still the decrease is within the experimental deviation. Here, the disk was adapted for planarity, yielding a

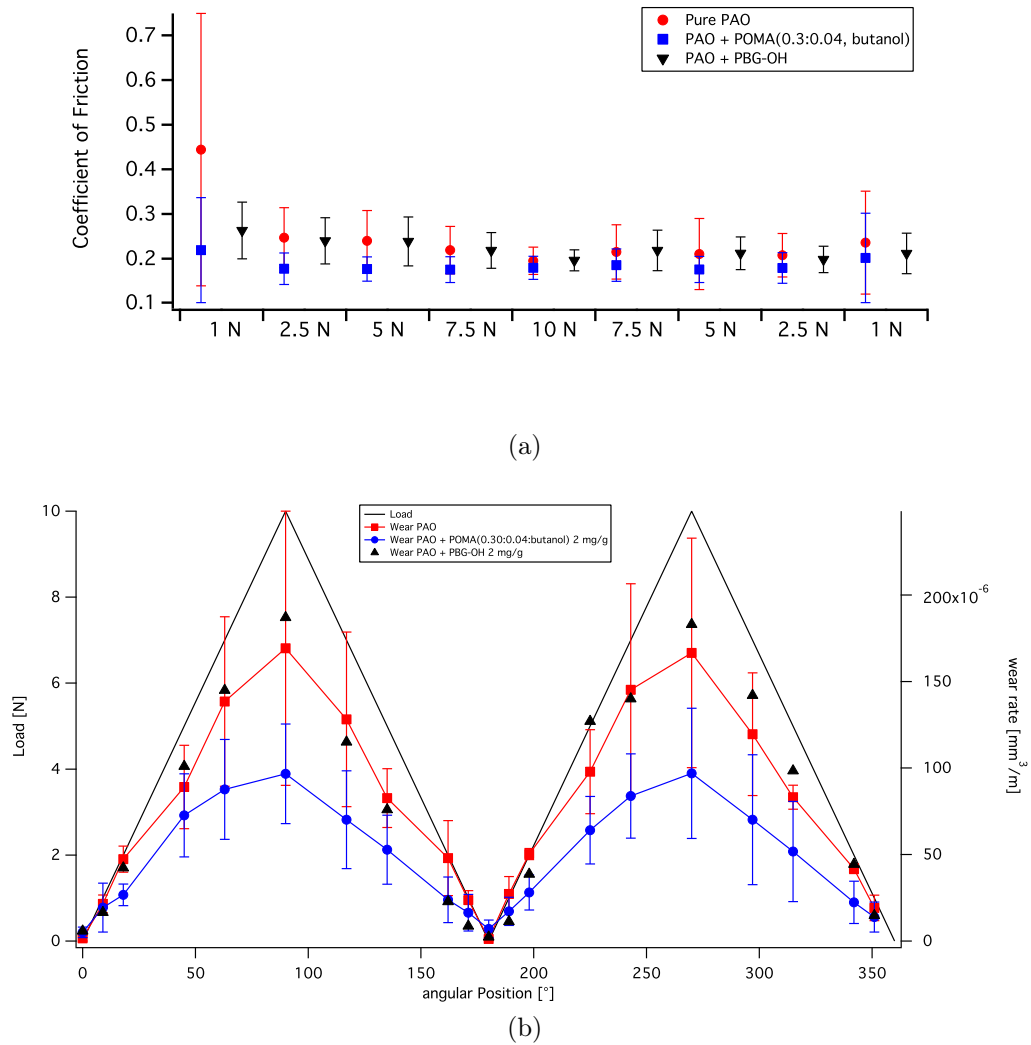


Figure 5.10: Cyclic load tests at 5 mm/s (a) coefficient of friction and (b) wear rate for pure PAO, PAO + PBG-OH and PAO + POMA(0.3,0.04, butanol) polymer

stable coefficient of friction during one turn of the plate. It has to be emphasized here that no shift towards higher COF is visible during these experiments and that a viscosity effect induced by the addition of the small amount of poly(1,2-butylene glycol) as additive is not confirmed by these measurements, which are more accurate. As already discussed based on the calculations shown in Fig. 5.8, a variation in sliding speed is much more efficient than a variation in load, in decreasing the lubricant film thickness. Therefore, much lower lubricant film thicknesses could be achieved in measuring the speed dependence, even at quite low, constant loads of 1N (Fig. 5.9). In looking at the calculated film thicknesses in Fig. 5.8, the cyclic load test performed at a speed of 5 mm/s changes the actual film thickness separating the tribopair between 0.75 and 1 nm. Slowing down the sliding speed for the cyclic load test, stick-slip behavior of the tribopair was observed, especially when increasing load.

There is a clear trend in the wear rate: the POMA(0.3,0.04, butanol) additive reduces the wear under the same conditions of the cyclic load test. Even though the error bars are quite high, the average reduction is on the order of 20-30%. The pure side-chain PBG-OH as additive does not influence the wear rate and thus behaves comparably to the pure PAO. Although the COF is not highly reduced by the polymer additive, there is a clear trend towards lower wear. This could indicate a slower or retarded wear process or even a change in the wear mechanism. Especially apolar oils like PAO or hexadecane have low dielectric constants (refractive index). Due to the resulting, higher Hamaker constants, an enhanced van-der-Waals adhesion is occurring between contacting surfaces. This adhesion phenomenon could easily become the dominant wear mechanism. Wear due to adhesion can be highly reduced by polymer coatings. This change in adhesion with and without polymer coating was investigated by atomic force microscopy using force-distance measurements (c.f. Sect. 7.2.7). However, these were not conducted on steel vs. steel surfaces, but on titania

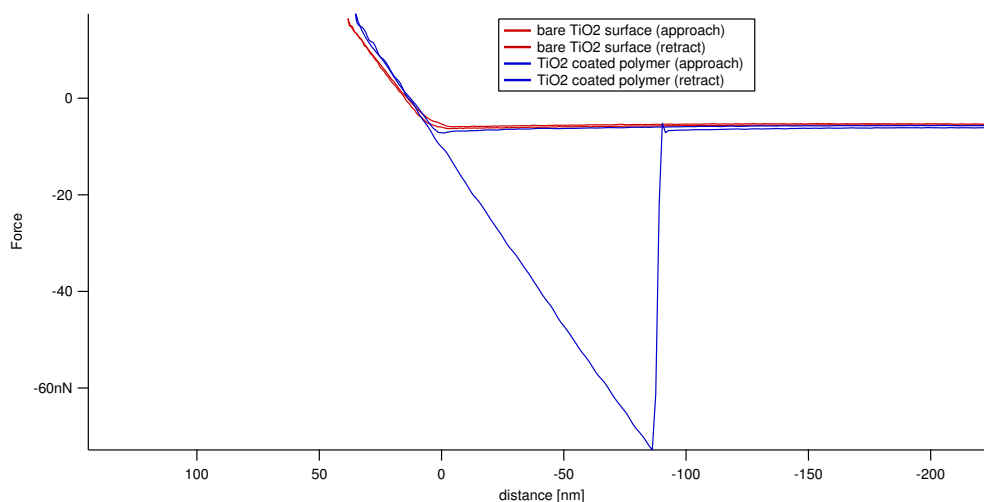


Figure 5.11: AFM force-distance curves of polymer-coated with POMA(0.3,0.04, butanol) and uncoated, bare titania surface for approach and retraction with a silicon oxide colloidal probe of 20 micrometer diameter

surface vs. silicon oxide sphere, using a colloidal probe AFM. In order to decrease viscosity effects of the oil on the measurement, hexadecane was used instead of PAO. Since both are highly comparable in their chemical structure, the effect is supposed to be comparable with that occurring under PAO.

Fig. 5.11 shows the resulting force-distance curves for bare and coated substrate with POMA(0.3,0.04, butanol). The polymer-coated surface was prepared by adsorption from a 0.5 M solution of n-heptane. The difference in adhesion for the retracting path is clearly visible and indicates the high adhesion force present when separating two bare, oxide surfaces. This adhesion is highly reduced after the polymer adsorption. Upon sliding, these adhesion forces induce wear. Due to the lower adhesion forces present at polymer coated surfaces, the resulting wear is highly reduced compared to a bare contact. This effect explains well the different wear rates observed in the cyclic load experiments.

Table 5.6: Experimental summary of the MTM measurements, summarizing the different base oils and additives used

Oil type	
PAO-166	DITA
pure oil	pure oil
oil + 2 mg/g polymer	oil + 2 mg/g polymer
	oil + 2 mg/g stearic acid

5.6.3 Mini Traction Machine

In order to investigate a bit further the influence of the polymer additive at lower sliding speeds, especially without the occurrence of stick-slip phenomena, the mini-traction machine was chosen. Here, the main principle is a combination of rolling and sliding of a ball over a surface with independent turning velocities of the ball and the disk. The ratio of these independent turning velocities leads to the slide-roll ratio (SRR), which is defined in Sect. 7.3.2. Here the harsh conditions of pure sliding and the light conditions of pure rolling can be varied with all intermediate states being possible. The new parameter (SRR) can be varied independently of load and relative speed. Due to the high dynamic range possible in the relative speed, Stribeck curves can be acquired without problems. Due to the combined rolling and sliding, stick-slip phenomena are not present. Tab. 5.6 summarizes the different base oils and additives used within this study.

MTM Investigation of POMA(0.3,0.04, butanol) in PAO

In a first series of measurements, PAO-166 with the polymeric additive was investigated as before. The results are summarized in Fig. 5.12

Different SRR are compared at a load of 7N, and, additionally a higher load of 15N is investigated at a low SRR. At high speeds, a perfect overlap of the MTM

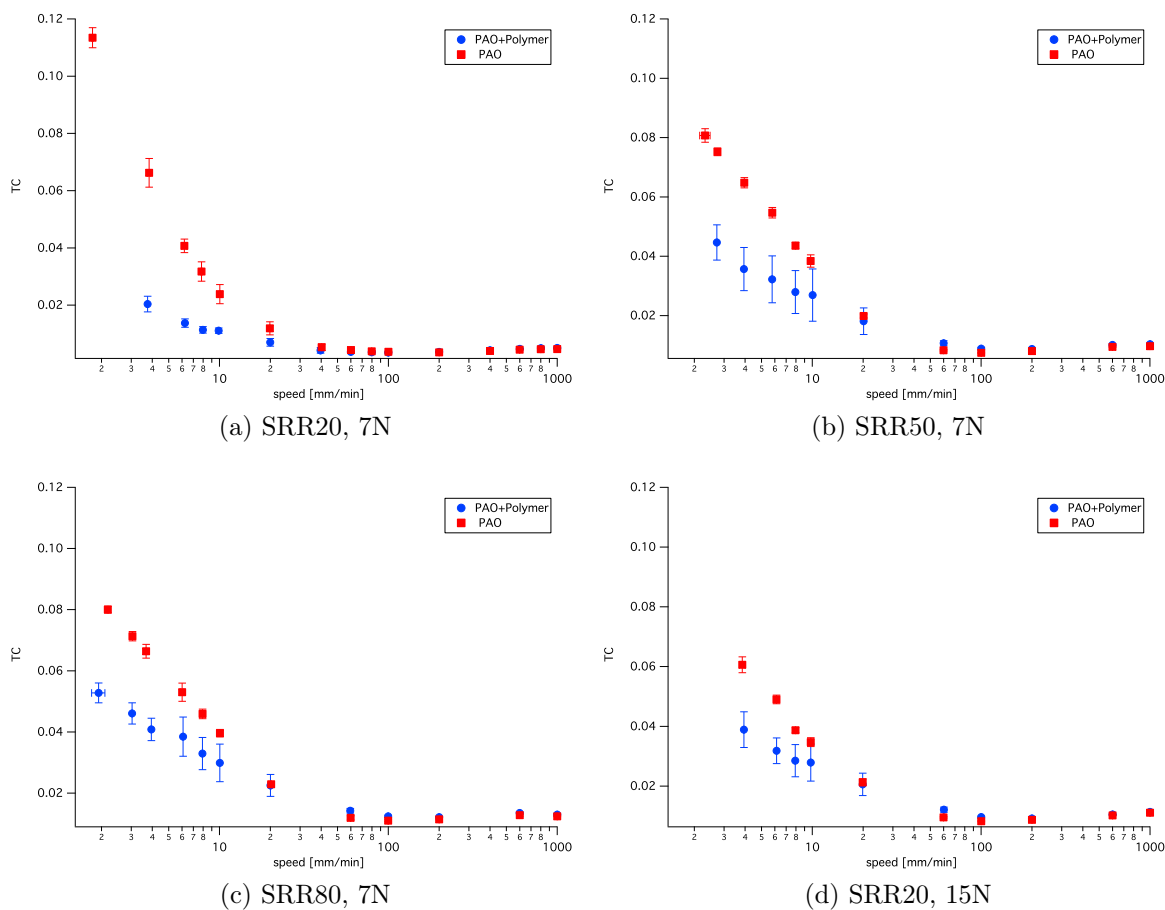


Figure 5.12: MTM Measurements performed in PAO-166

curves with and without additives can be found. This proves that no viscosity effect is introduced by the polymer additive. At lower speeds, the polymer always shows a significant reduction in traction coefficient and proves that it acts as a boundary lubricant. With higher loads, the effective reduction in traction coefficient decreases. At a SRR of 20%, a reduction factor of 3.5 is achieved at lowest speeds, whereas at a SRR of 80% or at higher loads, still a reduction factor of 1.5 is achieved.

MTM investigation of POMA(0.3,0.04, butanol) and stearic acid in DITA

In order to compare the performance of the polymer in another, more polar oil, the same measurements were performed in diisotridecyl adipate (DITA). DITA is the diester of the diacid adipic acid (hexanedioic acid) with isotridecan-1-ol. Due to the ester functionalities inside the oil, it is much more polar than PAO and thus, facilitates dissolution of additives. Stearic acid is one of the oldest and still commonly used boundary lubrication additives. It is, however, not soluble in PAO, but is soluble in DITA and is thus used to compare the performance of the polymer additive.

The MTM measurements in DITA are summarized in Fig. 5.13. No viscosity effect is observed at high speeds. At low SRR of 20%, a reduction in the TC is observed for both stearic acid and the polymer additive. Interestingly, the reduction of the TC is comparable for both additives, resulting in a reduction factor of 1.5. However, for higher SRR or higher loads, the TC of stearic acid overlaps with the TC of pure DITA and no boundary lubrication effect is visible anymore. The polymer additive, however shows a constant reduction of the TC of a factor of 1.3 at higher SRR or higher loads. It seems that the stearic acid is only an active boundary lubricant at very low applied loads or SRR. Under harsher conditions, the additive does not influence the TC. This can be explained by the comparably low adsorption energy of the carboxylic acids, which could get desorbed easily by the applied load and shear stress. Here the monofoot adsorption of stearic acid has to be compared to the much more stable multifoot adsorption of the polymer, explaining the much higher stability of the polymer at the surface.

Comparison of the additives performance

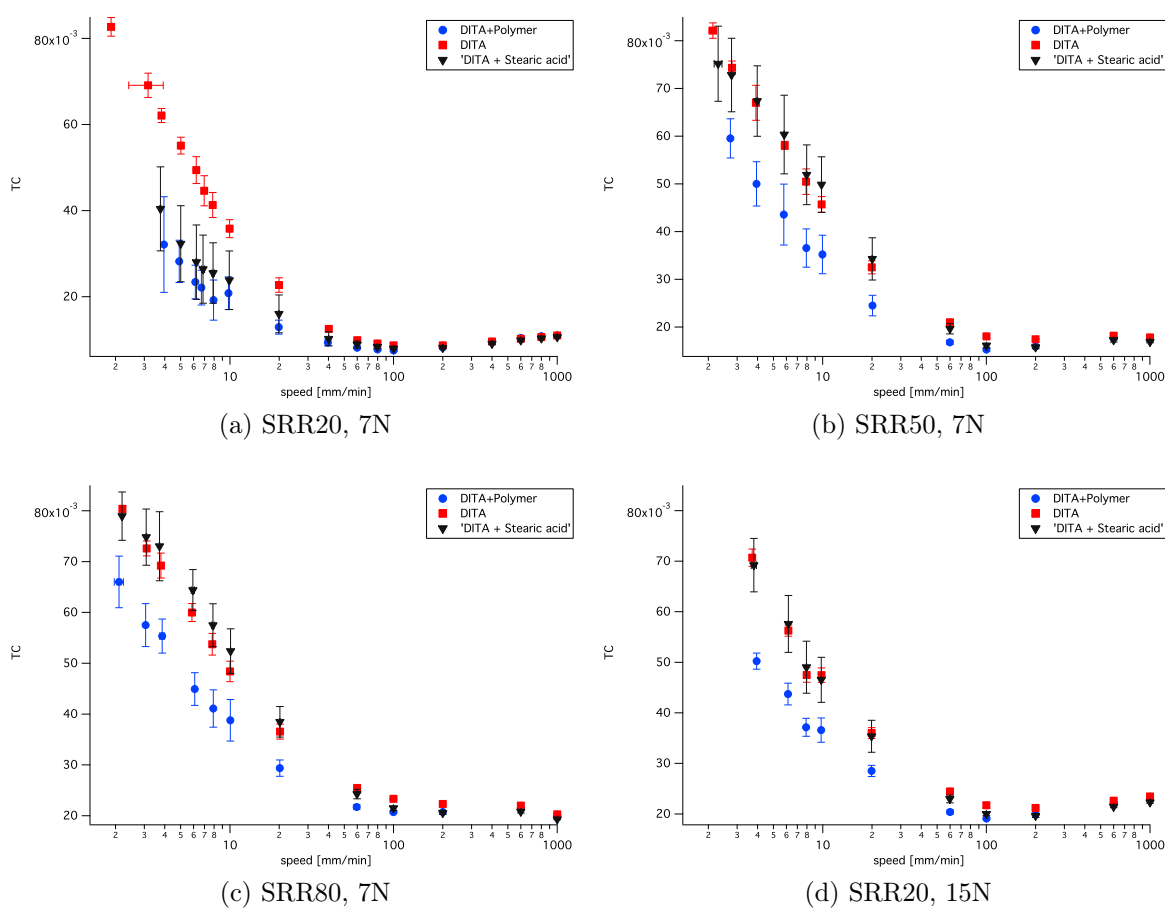


Figure 5.13: MTM Measurements performed in DITA

Performance of the base oils A comparison of the influence of the SRR and the load on the traction coefficient is summarized in Fig. 5.14. For the pure PAO, the observed Stribeck curve is similar for all different SRR and loads applied, resulting in relatively close values of the TC for the same speed but different conditions. However, the DITA base oil shows a different behavior. The Stribeck curve obtained for low SRR is visibly shifted towards lower traction coefficients. This could be explained by a weak interaction of the DITA molecules, especially of the ester functionalities with the oxide surface. Another possible mechanism would be the partial cleavage of some ester bonds due to the harsh conditions, resulting in surface-active carboxylic

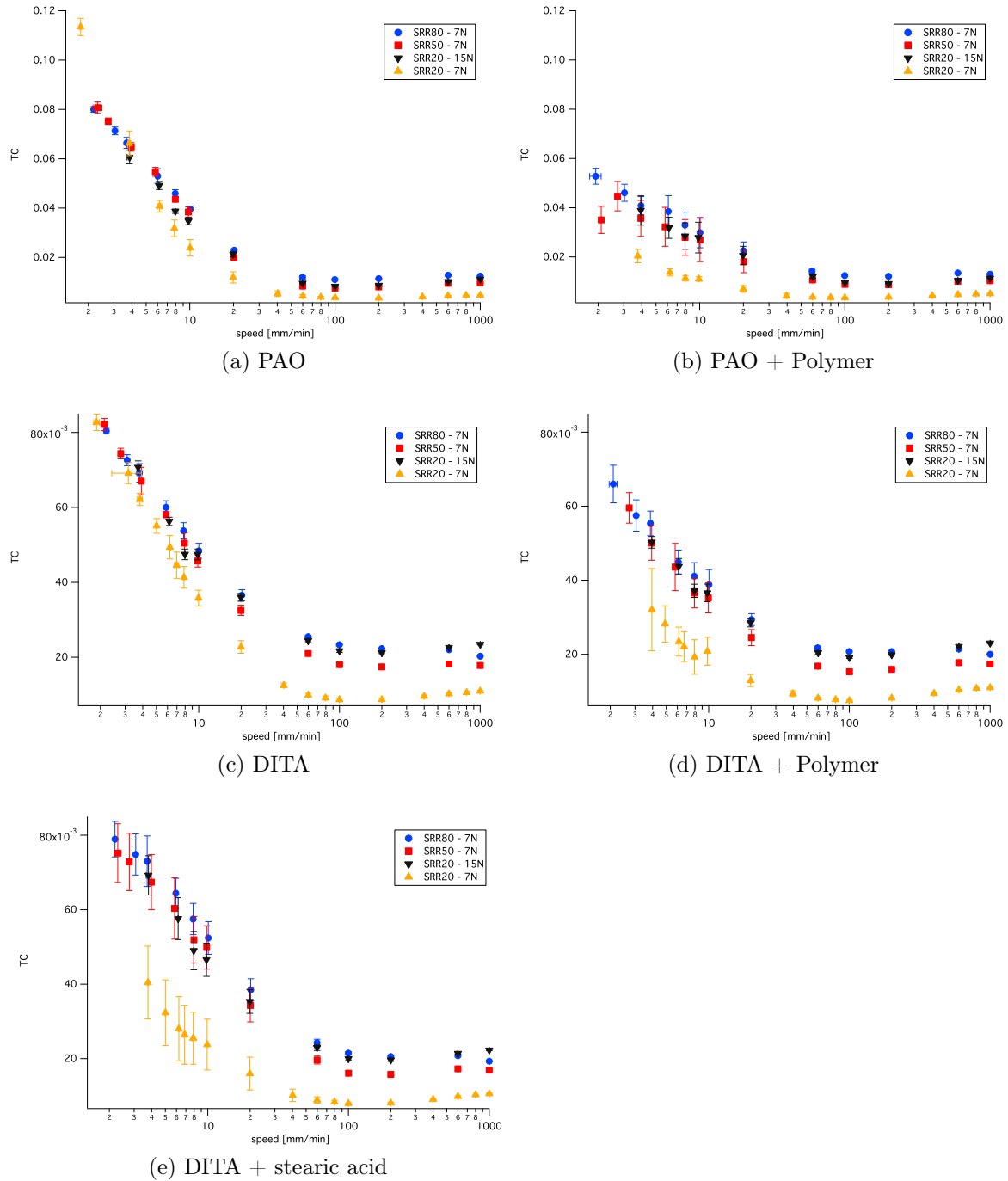


Figure 5.14: Influence of SRR on TC in both oils

acid species. Both possibilities could lower the TC at mild conditions, whereas under harsher conditions, the interaction with the surface seems to be hindered, resulting in a Stribeck curve shifted towards higher SRR.

Performance of the additives The polymer additive shows in both base oils a reduction in the TC depending on the SRR. For a SRR of 20%, the Stribeck curve is shifted towards lower TC in both cases, whereas at higher SRR, the individual Stribeck curves seem to be closer. However, even at higher SRR or higher loads, the reduction in TC at the boundary lubrication regime is much more pronounced in case of the polymer additive in PAO. The stearic acid, however shows a comparable effect, a shifted Stribeck curve to lower TC for the SRR of 20%. However, the Stribeck curves for harsher conditions do not show any favorable effect of the stearic acid.

As already described, it seems that the DITA interacts slightly with the surface, yielding in a Stribeck curve shifted towards lower TC. This interaction could be the reason, why the polymer additive shows a lower efficiency in that oil. If both, oil and additive show a certain affinity to the surface, the adsorption of the additive could be hindered. Especially the high affinity of the polymer to the surface could be counterbalanced by the very low concentration compared to the oil. Therefore, a proposed explanation would be the co-adsorption of oil and polymer additive at the surface, yielding a lower coverage of the surface with polymer. When high loads are applied, the oil molecules are desorbing from the surface and only the lower surface coverage of polymer additive is responsible for the positive effect in TC in the boundary regime. For these very slow speeds, mixed co-adsorption and recovery of the surface composition during each turn is possible. Stearic acid seems not to have a remarkable higher stability at the surface than the DITA itself. It shows only improved boundary lubrication at very low SRR of 20%. For SRR above 20%, the stearic acid does not show any positive effect in boundary lubrication, meaning that

it gets desorbed under harsher conditions and no boundary lubrication film is thus present at the surface.

The polymer additive, however shows a positive effect in boundary lubrication. Even though the effect is much more pronounced in PAO. Due to its hydrocarbon character, PAO is not interacting with the surface as discussed above. The polymer additive acts as boundary lubricant in both oils, reducing the TC under all SRR and applied loads investigated. The lower efficiency in DITA could be due to the co-adsorption of DITA molecules at the surface, resulting in lower surface coverage. Another reason would be the higher polarity of the base oil, resulting in a more stable state of the polymer in solution or a conformational change, rendering the surface adsorption less favorable.

Effect of the binding groups on additive performance The polymer seems to be much more stably bound to the surface in comparison to stearic acid. This is due to the combined interaction of the free carboxylic acid groups present in the polymer backbone and the phosphonate groups grafted onto it. This multisite binding of the polymer has to be taken into account. The additional phosphonate anchor groups present at the surface are assumed to bind more strongly to the surface, yielding an even higher stabilization of the polymer at the surface. However, due to the low content of phosphonates found by XPS surface analysis on steel (contrary to the polymer adsorbed on titanium oxide), the attachment mechanism of the polymer remains unclear and a dominant attachment of the carboxylic acid groups onto steel can be suggested. However, it has to be stated that the adsorption conditions were not optimized for that polymer. An apolar solvent (n-heptane) was used for adsorption, in order to mimic the solvation of the polymer in PAO. Even in considering only the carboxylic acids as active groups, a higher stability is achieved for the polymer because of its high number of carboxylic acids present at the backbone, which are

all capable of binding to the surface in a concerted way. The stearic acid, however, can only bind with one carboxylic acid group, rendering the molecule more prone to desorption under applied load and shear.

Structural comparison of the additives However, comparing the effect visible for the stearic acid at the SRR of 20% with that of the polymer additive at the same SRR, it can be stated that both show approximately the same reduction in TC. As described above, the polymer consists of C_{16} -side chains deriving from the octadecene repetition units and contains a much lower grafting density of only 0.04 of poly(1,2 butylene glycol) side chains, whereas the stearic acid has a C_{17} -hydrocarbon chain. Therefore, the hydrocarbon side-chains are approximately the same length. The comparable reduction in the TC for both stearic acid and polymer at low SRR could be an indication for the lubrication mechanism of the polymer. Apparently, the hydrocarbon chains are dominating the boundary lubrication, which could explain the comparable reduction in TC found for stearic acid and the polymer additive found at low SRR. The much longer, polyether side-chains are probably not packed densely enough to enter the brush regime, which would expand much further away from the surface. However a positive contribution of the polyether side-chains on the lubrication performance could not be excluded. The better performance of the polymer additive at higher loads and SRR is therefore mostly attributed to the more stable adsorption of the polymer to the surface.

An interesting fact is observed when looking at the standard deviations of the measurements. The pure base oils always result in measurements with a lower standard deviation, whereas the polymer additive in both base oils shows remarkably higher standard deviations. This could be an indication that the adsorption kinetics of the additives to the surface is rather slow. Since the application of high loads and shear forces interacts with the adsorbed monolayer of boundary lubricants, partial

desorption and disorder of the self-assembly structure could be the resulting consequence. The consequent necessary readsorption and reorganization of the monolayer film at the surface is a time-dependent phenomenon. The higher standard deviations observed for the boundary lubricant additives indicate that the readsorption and reorganization process at the surface is probably slower than the time between two traction cycles (due to the rotation of the disk and the ball). Therefore, a not perfectly reorganized boundary lubricant is present during the traction cycles and thus resulting in higher local fluctuations in the TC.

5.7 Conclusions

In this chapter the performance of the POMA polymers as oil additive for lubrication was investigated. The polymer structure as adsorbed on titania was investigated by means of XPS and the grafting densities calculated. The polymer adsorbed onto titanium oxide and steel surfaces shows a different phosphorus content. The lower phosphorus content on the steel surfaces was attributed to a preferential adsorption of polymer species containing a lower phosphonate grafting density. The polymer additive was tested in poly(α -olefin) oil in a constant load pin-on-disk tribometer, showing reduced friction in the boundary regime at slow sliding speeds compared to the bare oil. Additional oscillating-load measurements with a pin-on-disk apparatus at 5 mm/s sliding speed resulted in comparable COF for the bare oil and the polymer additive. However a reduction in wear was observed when comparing the polymer additive with the pure base-oil. That reduction in wear is an indication for the formation of a protective layer separating the tribopair and preventing hard asperity contact. Additionally, the difference in adhesion force was shown by AFM force-distance curves and explains the lower wear rate by a lower adhesion force between the contacting asperities.

The polymer additive was further compared using the Mini Traction Machine, where the applied load, the averaged speed and the slide-roll ratio can be varied independently. Here the polymer additive in PAO showed a high reduction in the TC by a factor 1.5-3.5, depending on the conditions applied. The performance of the polymer additive was then further investigated in a more polar oil, diisotridecyl adipate (DITA), which is thus facilitates the solubilization of additives. The performance of the polymer additive in that oil is not as good as with the PAO oil, but still for all conditions investigated, a reduction in the TC of a factor of approximately 1.5 was observed. Furthermore, the performance of the polymer additive in DITA was compared to the additive stearic acid. The polymer additive performed equally for low loads and low traction coefficients, but at higher loads and higher traction coefficients, the polymer still showed a reduction of the TC as compared to pure DITA, whereas the additive stearic acid performed comparable to the pure oil and lost its boundary lubrication properties. The performance of the polymer additive in terms of reduction of the TC compared to the pure oil is not as good as in PAO. As a hypothesis, the surface activity of the DITA oil is discussed briefly, resulting in a mixed adsorption of DITA and the additive at the surface. Therefore, a lower effect of the polymer additive is observed.

Since the polymer contains still contains unreacted side-chains, the performance of the side-chain alone as an oil additive in PAO was checked in order to ensure that the observed boundary lubrication effect is deriving from the side-chain or the polymer. The side-chain as polymer additive showed a performance comparable with pure PAO oil during pin-on-disk measurements and therefore shows no visible effect on lubrication - neither as boundary lubricant nor as viscosity enhancer for the base oil.

Conclusion and Outlook

6.1 Conclusion

6.1.1 Synthesis

A new synthetic route towards graft-copolymers that are capable of chemisorbing onto metal oxide surfaces and forming monomolecular, brush-like adlayers, was developed within this PhD project. The synthetic approach consisted of the coupling of the functionalities onto a reactive polymer backbone. These reactive groups were chosen to be maleic anhydride and the surface-active anchor group to be phosphonate. Grafted PEG chains and poly(1,2-butylene glycol) monobutylether were selected for the formation of hydrophilic and hydrophobic brushes, respectively.

The synthesis was shown to be efficient and stoichiometric for anhydride ring-opening via nucleophilic attack with primary amines on the poly(isobutylene-alt-maleic anhydride) (PIMA) backbone. Exactly the expected grafting density of the polymer was achieved, as used during synthesis. However, with higher steric demands due

to a high grafting density in the polyether chains, a slight reduction in the grafting density was observed, when compared to the ratios used in synthesis.

These highly stoichiometric reactions could not be confirmed using the polymer poly(octadecene-alt-maleic anhydride) (POMA) for the synthesis of hydrophobic polymers with grafted poly(1,2-butylene glycol) side-chains. This was ascribed to the fact that the grafting reaction of the polyether side-chain was not performed using amine chemistry, but using the much less reactive alcohol group that yields in much lower grafting ratios. Additionally, the POMA backbone is more sterically challenging due to the hexadecane side-chains present at each repetition unit. This hinders the nucleophilic attack especially of polymeric reactants, such as the PBG-OH and seems to be unfavorable for the synthesis of *graft*-copolymers.

The ring opening of the anhydride rings results in the formation of free carboxylic acids at the backbone, rendering the polymers highly amphiphilic. This complicates a proper workup, purification and bulk characterization of the polymers. A calculation of the acid-base equilibria of the functionalities for pH 5 in water show that the polymer backbone is mainly negatively charged due to the deprotonated carboxylic acids.

6.1.2 Hydrophilic polymers

The hydrophilic polymers were adsorbed onto surfaces. The surface attachment of the hydrophilic polymers could be proven for titanium oxide and magnesium oxide/yttrium oxide surfaces as model surfaces for different biomedical applications. A full characterization of the PEG adsorption behavior was performed on titanium oxide surfaces. Due to the amphiphilic nature of the polymers synthesized, micellation and aggregation of the hydrophilic polymers was observed. This effect was taken as an explanation for the slower time dependence of the adsorption kinetics, compared

to classic Langmuir adsorption isotherms. Even considering full diffusion limitation during adsorption, the time-dependence was found to be slower and attributed to an additional association-dissociation of the polymer micelles and the consequently slower diffusion constant of the polymeric micelles to the surface.

The composition of the hydrophilic polymers adsorbed onto titanium oxide surfaces was proven to be similar to the bulk value. Angular-resolved XPS measurements confirmed the proposed self-assembly structure of the polymers at the surface, including the phosphonate surface anchor directly attached to the surface and the PEG chains directing away from the surface. The polymer adlayer thickness was characterized using different *in situ* and *ex situ* measurements. The PEG brush showed excellent swelling in water, which is a prerequisite to render a surface non-fouling, as the protein resistance experiments show. The influence of the backfiller on the adlayer formation was investigated. Backfilling with diaminohexane seems to be favorable for the formation of a dense PEG brush. This preferential effect could be explained by changing the character of the backbone from purely polyanionic to polycatanionic. That structural change likely induces conformational changes and more flexibility to the backbone, mainly due to less electrostatic repulsion between the carboxylic acids.

The long-term stability of the polymers at the surface was proven to be better than that of other reference polymers, such as PLL-g-PEG (polyelectrolyte), poly(phosphonate)s developed by Dr. V. Zoulalian (pure phosphonate adsorption) and dodecylphosphate SAMs (single phosphate binding). This improvement was mainly attributed to the combined effect of phosphonate binding and polyelectrolyte backbone, rendering the polymer more stable over a wider range of pH than a polymer carrying only phosphonate functionalities.

6.1.3 Hydrophobic polymers

The hydrophobic polymers were adsorbed onto titanium oxide and steel surfaces. The grafting ratio was calculated from XPS analysis of the polymers at the surface. Apparently, different species adsorb onto these two surfaces—the surface composition on titania is close to the composition of the synthesis, showing a phosphorus and nitrogen peak, whereas on steel no indication of a surface attachment by means of phosphonates was found. This was explained by preferential adsorption of carboxylic acid functionalities onto the surface. In both cases, a very low grafting density for the poly(1,2-butylene glycol) side-chain was calculated from the surface composition. The polymer was used as a boundary lubricant in PAO and DITA oil and showed a reduction of the coefficient of friction in the first oil type. This was attributed to the different polarity of the two base oils and to a possible, slight surface activity of the DITA oil, resulting in a co-adsorption of both species onto the surface. The polymer additives showed a reduction in wear during the tribotests, which was confirmed by force-distance AFM measurements. However, the influence of the low grafting density of the PBG side-chains could not be separated from the influence of the hexadecane side-chains present at each repetition unit.

6.2 Outlook

6.2.1 Synthesis

The use of PIMA as a functionalizable backbone opens several possibilities for generating multi-purpose, thin-film coatings. The advantage of PIMA in respect to POMA resides in its small steric hindrance, rendering the attachment reaction of side chains stoichiometric and reliable. The well-known amine chemistry was here used as an

efficient, stoichiometric and modular reaction towards graft-copolymers, thus allowing the preparation of new polymer generations and the comparison and further investigations of structural and architectural effects.

In particular, the approach chosen could allow the direct comparison of the binding efficiency of different surface anchors, e.g. phosphonate vs. silanes or catechols. Due to the very low reaction temperature (room temperature), the system is a very good potential approach towards biofunctionalized polymers, e.g. bearing antibodies, protein sequences or biocides that would not survive synthetic approaches at elevated temperatures.

One advantage of the polymer system presented within this work is the carboxylic acids formed. Further functionalization with comparably smaller building blocks is assumed possible, for example by grafting short hydrocarbon chains in order to enhance van der Waals forces, which are important for a good self-assembly at the surface. A rising steric hindrance and a loss in polymer flexibility however have to be taken into account. A further possibility is the imidation reaction, where the carboxylic acids are protected within the 5-membered imide ring formed. Here, the adsorption performance of the anchor groups could be decoupled from the polyelectrolyte interaction with the surface. However, the imidation reaction would induce a higher stiffness to the polymer backbone.

6.2.2 Hydrophilic polymers

The adsorption of the hydrophilic polymers was proven on the MgO/Y₂O₃ surfaces. Due to the unstable surface, characterization and quantification of the biological performance of the polymers is difficult. The investigation of the non-fouling properties is always involving aqueous solutions and thus influencing the unstable corroding substrates. The architecture as a polymeric monolayer is probably not sufficient

to achieve one of the principal goals in this project: a better and more controlled corrosion performance. A more promising path towards improved corrosion, including a surface brush of PEG polymers, could be achieved using an adapted surface-functionalization approach including the same chemistry as discussed within this work. Instead of using self-assembly mechanisms to yield polymeric monolayers, the more direct approach of spin-coating could be used. The reactive backbone could be spin-coated as a relatively thick layer onto the surface and would be responsible for both the protection of the surface against water and the functionalization of the surface with anhydride rings. These anhydride rings accessible at the polymer surface could be used to couple PEG chains via the amine chemistry to the surface, thus forming a polymer brush. However, this still involves organic solvents for both processes (spin coating and PEG coupling), and thus still involves changes in the surface chemistry as discussed within the work presented here. Due to the thick film of reactive polymer, the surface should be well protected from water and thus tests using aqueous solutions, e.g. for protein adsorption, would be more easy to perform.

6.2.3 Hydrophobic polymers

The general adsorption capability of the phosphonate chemistry onto MgO surfaces was proven in this work. The knowledge obtained could be used to develop polymers interesting for other applications that use magnesium alloys. Nowadays, lightweight alloys have been introduced into motor construction, especially to achieve fuel economy. Therefore, in addition to the testing of oil additives on steel surfaces for lubrication, it would be very useful and a unique feature to investigate the behavior of those hydrophobic oil additives on magnesium-aluminium alloys, too.

For hydrophobic polymers, a new synthetic route using the less sterically hindered PIMA backbone and PBG with a terminal amine group would lead to much enhanced

grafting densities and thus to a true formation of a dense surface brush of long, polymeric chains. This brush would probably lead to more pronounced reduction of the coefficient of friction, which then could be compared to the surface brush introduced only by the hydrocarbon chains present at the POMA backbone. Using identical grafting densities for the phosphonate surface anchor, a comparative study of the influence of polymer structure and the length of the side-chains on the boundary lubrication would be of further interest.

A further study should be devoted to the different polymer structures observed after adsorption of the polymer onto the steel and titania surfaces. Since almost no phosphonate groups were observed in the polymer structure adsorbed onto steel, this effect was assumed to be preferential adsorption and thus connected to a higher chemical affinity of carboxylic acids to the surface. A comparison of the adsorption strength and kinetics between carboxylic acids and phosphonates would be of interest. This could be performed by investigating different SAM formation, e.g. of lauric acid and dodecyl phosphonate (which could be easily synthesized a slightly modified synthesis protocol of the surface anchor presented in this work). An investigation of the adsorption kinetics either by performing direct measurements with XPS or by using model surfaces (iron/iron oxide coated wafers or biosensors), enabling a broader variety of *in situ* and *ex situ* possibilities. The effect of chemical affinity could be investigated by co-adsorption studies and analysis of the resulting surface composition.

Materials, Methods and General Protocols

In this section, all details regarding experimental techniques, instruments, materials, procedures, protocols and techniques used for this work are described. First, bulk and surface characterization methods are presented, tribotests reviewed and then general protocols are summarized.

7.1 Bulk characterization methods

7.1.1 Nuclear Magnetic Resonance (NMR)

Theory

Nuclear magnetic resonance (NMR) occurs when the nuclei of certain atoms are immersed in a static magnetic field, and exposed to an external oscillating magnetic field at a certain frequency.

A magnetic field \vec{B}_0 can induce within an interacting nucleus an elemental magnetic moment $\vec{\mu}$ rotating at the frequency ν . The main requirement for its magnetization is that the nucleus features an overall non-zero magnetic moment, called spin (I). Normally, all isotopes containing an odd number of protons and/or of neutrons have a non-zero spin.

The electron cloud around the nucleus is exposed also to the magnetic field. It does not stay insensitive to \vec{B}_0 but enters in opposition to it. This opposition depends on a variety of factors, e.g. the proximity of other atoms (coupling effect, shielding, attractor groups/atoms, π -conjugate systems, ...), the solvent, the conformation of the molecule, the temperature, etc. The screen constant (σ) is a corrective parameter that quantifies the general influence of the environment on the electron cloud. Therefore, the nucleus interact with a lower magnetic field:

$$\vec{B} = \vec{B}_0 \cdot (1 - \sigma)$$

The addition of the elemental moment $\vec{\mu}$ of all nuclei having the same environment results in a global magnetization vector \vec{M} , which is collinear with \vec{B} and is rotating at the frequency ν .

\vec{M} is in equilibrium with \vec{B} . The magnitude of \vec{M} depends on the number of nuclei having the same chemical environment and is thus proportional to the concentration of that element in the studied sample.

The NMR measurement consists of disturbing the equilibrium of \vec{M} and recording its relaxation into the initial state. Pulsed NMR uses electromagnetic radiation emitted during a short time at the radio frequency ν_1 . It generates a new precessing magnetic field, perpendicular to \vec{B} that modifies the behavior of \vec{M} . Information on the positions of \vec{M} , recorded as a function of time, are treated by Fourier transformation

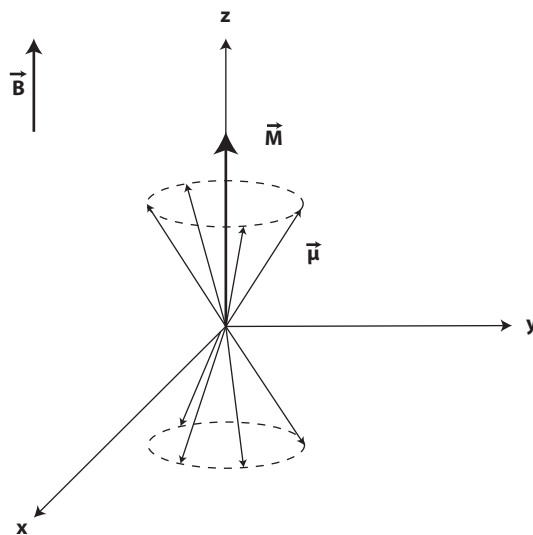


Figure 7.1: Representation of the magnetization vector \vec{M}

in order to get a peak spectrum in frequencies and intensities. One specific frequency is characteristic for a chemical environment and thus related to a defined screening constant σ . The intensities are proportional to the concentration of the detected element in the analyzed sample.

Due to spin-spin-coupling, J (in Hz), resulting from an interaction between the magnetic moments of nonequivalent nuclei in the proximity, several peaks are obtained. An interesting property of J is that its value is independent of B_0 . The consequence is a division of the single peak normally obtained for a family of nuclei without any perturbations. This division is controlled by well-defined rules related to the environment of the nuclei.

The resolution of the measurement is strongly dependent on the magnitude of the magnetic field \vec{B}_0 , whereas the sensitivity is mainly controlled by the isotopic abundance of the nucleus. It is therefore easier to detect 1H and ^{19}F (isotopic abundance respectively 99.98% and 100%) than ^{13}C (1.1%) for example. Moreover, to improve the detection of the elements from the sample, molecules are always dissolved in

deuterated solvents. 1H - NMR is the most commonly used NMR technique, due to the abundance of 1H and the simplicity of its nucleus.

As for all spectroscopic methods, in order to be able to make comparisons, a calibration is required. For 1H -NMR, tetra methyl silane (TMS) is universally used allowing the determination of a chemical shift (δ) related to its H peak:

$$\delta = \frac{\sigma_{TMS} - \sigma_A}{1 - \sigma_{TMS}}$$

δ :chemical shift

σ_{TMS} : screening constant of 1H in $-CH_3$ from TMS

σ_A : screening constant of defined 1H of a molecule A

A small σ indicates a high electron density that shields the 1H nuclei. This screening effect reveals the presence of donor groups or atoms in their vicinity. As δ increases, the electron density decreases, and the nuclei are therefore less shielded from the magnetic field. Consequently, chemical functionalities can be assigned based on chemical shifts and their concentrations determined from the intensities of the corresponding peaks.

Experimental procedure

In this project, nuclear magnetic resonance spectra were recorded with a Bruker (Bruker Co., Billerica, MA, U.S.) 300 or 500 MHz spectrometer with the corresponding solvent signals as internal standards. Chemical shifts are reported in parts per million (ppm). The following abbreviations are used in the experimental section for the description of 1H -NMR spectra: singlet (s), doublet (d), triplet (t) multiplet

(m), doublets of doublet (dd), broad singlet (bs). The chemical shifts of complex multiplets are given by means of the range of their occurrence. The deuterated solvents were purchased from Merck, Fluka or Acros. All spectra were evaluated with iNMR.

7.1.2 Elemental Analysis

Theory

The elemental composition of chemical compounds can be investigated by elemental analysis, which detects the concentration of the elements of interest after decomposition of the initial compound (e.g. combustion) by means of analytical techniques.

C, H and N ratios are determined after dynamic flash combustion of the samples under an oxygen/helium atmosphere. The generated gases (CO_2 , H_2O , NO_2) are then separated by gas chromatography using He as a vector gas and analyzed either by a thermal conductivity or an infrared detector.

O is determined after dynamic flash combustion of the samples using a catalyst. The generated elemental gases (CO and CO_2) are then analyzed via an infrared detector, using a (10% H_2 , 90% N_2) mixture as vector gas.

One possibility to determine P traces is by Inductive Coupled Plasma - Atomic Emission Spectroscopy (ICP-AES). The sample is ionized with a plasma torch and the resulting excited atoms emit radiation upon returning to the ground state at a wavelength characteristic of the particular element. The emission intensity depends on the elemental concentration within the sample and is analyzed using a monochromator or a polychromator grating. Another technique is to transform the phosphorus group to an ionic state using a combination of microwaves, heating, pressure and acid exposures. Thus a complex is formed that can be analyzed quantitatively using photometric titration.

Experimental

In this work, for the determination of C, H and N ratios, the device used was a LECO CHN-900 machine. For O amounts, a LECO RO-478 setup was used. For P traces, an ICP-AES device (Perkin-Elmer and Thermo-Jarrel) was used and additionally quantified photometrically (as a colored complex) after digestion in a pressure-digestion device. All elemental analysis was operated by the chemical analysis service of the chemistry department at ETH.

7.1.3 IR Spectroscopy

Theory

Infrared spectroscopy is a powerful analytical technique. Molecular vibrations and rotations can be excited by absorption of radiation in the infrared region of the electromagnetic spectrum. There are two possibilities to measure those vibrations and rotations of the molecules:

1. directly as absorption bands in the infrared spectrum (IR spectroscopy)
2. indirectly as inelastically (Raman) scattered radiation in the Raman spectrum (Raman spectroscopy)

in the following, the focus will be on infrared spectroscopy.

The position of an absorption band in the IR spectrum can be described in units of the wavelength λ of the absorbed radiation, but the description in reciprocal wavelength, the so called wavenumber ($\tilde{\nu}$ in cm^{-1}) is more commonly used, since it

is proportional to the frequency ν of the absorbed radiation and therefore also to the energy ΔE .

$$\tilde{\nu} = \frac{1}{\lambda}$$

The routinely investigated region of an infrared spectrum is between 4000 and 400 cm^{-1} . A lot of functional groups of organic molecules show characteristic vibrations, which correspond to absorption bands in well-defined regions of the infrared spectrum. These vibrations are mainly localized in one functional group of the molecule. That is why functional groups can be identified by their characteristic absorption band. In analyzing the entire spectrum, more detailed structural informations can be obtained.

Normally a simple model derived from classical mechanics is used to describe the processes that lead to an IR spectrum. The vibrations can be described by considering the atoms as point masses, joined by an elastic spring. If the equilibrium distance r_0 between the masses is increased, a restoring force F ensues. On release of the system, it vibrates about the equilibrium distance. According to Hooke's law the restoring force F is to a first approximation proportional to the extension Δr : $F = -k \cdot \Delta r$ with k being the elastic constant of the spring (the bond strength between the atoms in a molecule).

The vibrational frequency ν is therefore higher, the higher the force constant k and therefore the stronger the molecular bond. Furthermore, smaller masses of the vibrating atoms yield higher frequencies ν . This relationship is useful for spectral interpretations, where qualitative predictions of the absorption frequencies in the IR spectrum can be drawn.

The application of the mechanical model to diatomic molecules fails to explain certain phenomena, e.g. dissociation of the molecule upon irradiation with sufficient energy.

A better description is provided by the anharmonic oscillator with its asymmetric potential energy curve. Additionally, the vibrational levels are no longer equally separated and quantum mechanics must be considered, since at a molecular level energy and its absorption is quantized.

There are only discrete allowable energy levels and therefore vibrational levels. The vibrational state with the quantum number $n = 0$ is called the ground state and has a non-zero energy. The excitation of a vibration corresponds to the absorption of a quantum of light by the molecule, thus raising it from a vibrational level with a quantum number n to a higher level. The energy difference between the two levels must be equal to the energy of the light quantum (resonance condition). The separation between adjacent levels becomes smaller as n becomes larger, until finally a dissociation limit is reached. The lowest transition possible from ground state is called the base transition, excitations from the ground state to higher energy levels yield overtone absorption with higher frequency (double frequency for first overtone, ...), but the probability of these transitions declines very sharply with increasing n . Additionally, the appearance and intensity of absorption bands depend on the dipole moment of the molecule—infrared light is only absorbed when the dipole moment interacts with the electrical vector of the light. Simplified, the dipole moment of the molecule at one extremity of the vibration must be different from that at the other extremity. Due to these selection rules, for a totally symmetric molecule with a center of symmetry, all vibrations which are symmetrical with respect to the centre of symmetry are IR inactive (forbidden), since they produce no change in the dipole moment.

IR spectrometer

Two different spectrometers are currently in use. The traditional grating or prism instruments, operating with a beam splitter on the double-beam principle, have been largely replaced by the more powerful Fourier transform (FT)-IR spectrometers. The basic principle of FT-IR spectrometers is the simultaneous collection of data at all frequencies in the IR spectrum, thus eliminating the time required for scanning through the different frequencies. It is achieved by using an interferometer to convert the intense, multifrequency IR radiation, which is constant with time, into an interferogram, which is not a function of frequency, but of time. Afterwards, the interferogram is converted back from the time domain to the frequency domain via Fourier transformation.

Experimental procedure

The different polymers were analyzed either in the solid state, diluted in dry KBr pellets, or in liquid form confined between two KBr pellets, using Fourier Transformation IR spectroscopy either on a Nicolet 5700 (Thermo Fischer Scientific, Loughborough, GB) FT-IR or on a Bruker IFS 66v (Bruker Co., Billerica, MA, U.S.) FT-IR spectrometer. Data acquisition and treatment was performed with OPUS software in the case of the Bruker spectrometer or with OMNIC software in the case of the Nicolet spectrometer.

7.1.4 Light scattering

From dynamic light scattering (DLS) and static light scattering (SLS) measurements, many useful parameters can be derived, e.g. particle size (radius of gyration R_g and hydrodynamic radius R_h) and size distribution, second virial coefficient determining

the interaction of the polymers with the solvent, the molecular weight (in using dn/dc for the appropriate solvent) and dynamic values, such as the translational and rotational diffusion coefficient. For that reason, light-scattering methods were performed, to investigate the aggregation behavior of the hydrophilic polymers at different concentrations in aqueous solution and different organic solvents. Especially the R_g , R_h , the translational diffusion coefficient D and the molecular weight in M_w were in the focus of interest.

Rayleigh Scattering

Rayleigh scattering is elastic scattering of light by particles. The size of the scattering particle has thus to be much smaller than the wavelength of the light. The scattering depends on the wavelength and on the particle size and can be described by the formula

$$I = I_0 \frac{1 + \cos^2(\theta)}{2L^2} \cdot \left(\frac{2\pi}{\lambda}\right)^4 \left(\frac{n^2 - 1}{n^2 + 2}\right)^2 \left(\frac{d}{2}\right)^6$$

with L the distance to the particle, θ is the scattering angle, n is the refractive index of the particle, and d is the diameter of the particle.

Static light scattering

The light scattering in static light scattering is following the general formula

$$I(q) = Kc \cdot M_w P(q) S(q)$$

with K the optical constant, $K = 4\pi^2 n^2 (dn/dc)^2 / (N_A \lambda_0^4)$, c the concentration of the polymer in g/cm^3 , $P(q)$ the particle form factor, $S(q)$ is the particle structure factor (equals 1 for an ideal sphere) and q is the wave vector $q = (4\pi n / \lambda_0) \cdot \sin(\theta/2)$.

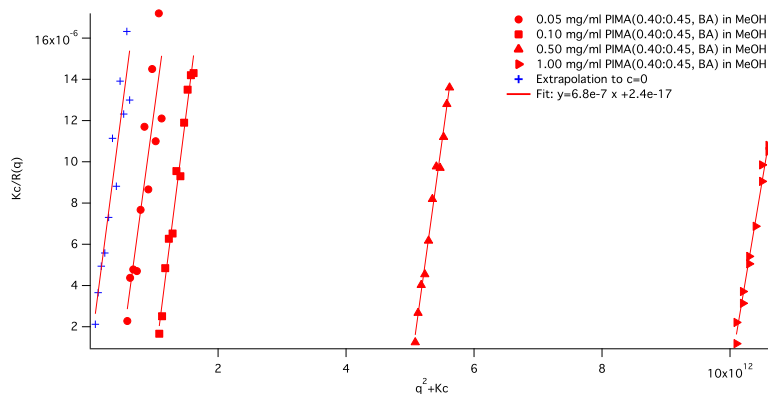


Figure 7.2: Exemplary Zimm plot, from which radius of gyration (R_g) and the molecular mass (M_w) can be derived from static light scattering

The absolute Rayleigh ratio R , the excess intensity of scattered light corrected with the instrument constant is expressed as

$$\frac{Kc}{R(q)} = \frac{1}{M_w \cdot P(q)} + 2 \cdot A_2c$$

with A_2 the second virial coefficient and $P(q)$ the particle form factor. $P(q)$ depends on the dimensions of the particle and is related to the radius of gyration R_g by the Guinier approximation

$$P(q) = 1 - \frac{1}{3}q^2 \langle R_g^2 \rangle + \dots$$

Combining these equations results in a linear function

$$\frac{Kc}{R(q)} = \frac{1}{M_w} \left(1 + \frac{q^2}{3} R_g^2 \right) + 2A_2c$$

while the slope of the curve relates to $R_g^2/3$, the molecular weight can be derived from the axis intercept, with the concentration extrapolated to $c \rightarrow 0$. This plot is then called Zimm plot and one example is shown in Fig. 7.2

Dynamic light scattering

Dynamic light scattering (DLS) gives insight into dynamic properties of the particles by means of single scattering events. Rayleigh scattering occurs in every directions. With a monochromatic laser-light source, time-dependent fluctuations of the laser intensity at a given angle are observed. These fluctuations are based on the Brownian motion of the particles in solution, leading to constructive or destructive interference of the scattered light. The dynamic information of the particles is derived from an autocorrelation of the intensity trace recorded during the experiment.

The second-order autocorrelation function of the scattered light intensity $g^{(2)}(q, \tau)$ can be described as

$$g^{(2)}(q, t) = \frac{\langle I(t)I(t + \tau) \rangle}{\langle I(t) \rangle^2}$$

and is related to the first order, normalized field autocorrelation function $g^{(1)}(q, \tau)$ by

$$g^{(2)}(q, \tau) = B \cdot (1 + \beta \cdot |g^{(1)}(q, \tau)|^2)$$

where B is the base line and β is a constant relating to the coherence of detection and depends on the alignment and geometry of the laser system used. The measured correlation functions can be analyzed using a cumulant method to obtain the average decay rates Γ

$$\ln |g^{(1)}(t, q)| = -\Gamma t + \frac{\mu_2}{2!} t^2 - \frac{\mu_3}{3!} t^3 + \dots$$

with μ_i the i -th cumulant. μ_2/Γ^2 gives the normalized dispersion of the distribution of Γ . If the fluctuation of the scattering light intensity is due to the translational

diffusion of the polymer chains, the decay rate can be calculated in the form

$$\Gamma/q^2 = D_0(1 + k_d c + \dots)$$

with D_0 being the translational diffusion coefficient at infinite dilution and k_d a constant for the effect of polymer concentration. The hydrodynamic radius R_h is related to D_0 by the Stokes-Einstein equation

$$R_h = \frac{k_B T}{6\pi\eta D_0}$$

with k_B the Boltzmann's constant and η the viscosity of the solvent.

Experimental

Light scattering (LS) was performed on a 3D DLS spectrometer (LS instruments, Fribourg, Switzerland) at 25°C with He-Ne Laser emitting a polarized light beam of wavelength of 632.8 nm. The aperture was set before the experiment to obtain the maximum intensity to the detector. Toluene, as a strong and known light scatterer, was used to measure the absolute light scaling reference and the respective pure solvents were used for solvent-intensity calculations. The dynamic light scattering measurements were performed at a fixed angle of 90° for 180s. Static light scattering measurements were performed at angles ranging from 40° to 120°.

1 ml of polymer solutions in the range of 5 mg/l to 0.05 mg/l, thermostated for 15min before the SLS and DLS measurements. The refractive index increments (dn/dc) was measured as shown in Sect. [A.3](#).

7.2 Surface Characterization Techniques

7.2.1 Variable-Angle Spectroscopic Ellipsometry

Theory

Variable-Angle Spectroscopic Ellipsometry (VASE) is an optical analysis technique. Its working principle is based on the polarization change of elliptically polarized light upon reflection from a planar, reflective surface. It is an indirect method, providing information that allows the evaluation of physical properties of the material (i.e. layer thickness) or the determination of the optical properties (refractive indices).

An incident elliptically polarized wave is reflected from a surface with another polarization. The extent of change in polarization depends on the optical properties of the material, namely on the dielectric constant ϵ of a material, which itself relates to the complex refractive index $N = n + ik$. VASE measures two ellipsometric parameters: Δ , which is the phase shift of the reflected light (values range from 0 to 360°) and Ψ , which is the change in amplitude upon reflection (values range from 0 to 90°). Both angles are related to the total reflection coefficients R_p and R_s and the complex ratio ρ

$$\rho = \frac{R_p}{R_s} = \tan \Psi e^{i\Delta}$$

Optical properties and thicknesses of surfaces can be determined by modeling this amplitude (Ψ) and phase change (Δ). If the measurements are performed at one angle of incidence and with a single wavelength, only two unknowns, the real and the imaginary part of the complex refractive index, can be acquired. However often the focus of investigation is on the properties of layered structures with each layer

having a different complex refractive index and a certain thickness. The use of white light allows a multitude of Ψ and Δ values to be obtained as a function of wavelength λ , thus enabling the derivation of many unknowns in multilayered structures by application of regression analysis.

Ψ and Δ also exhibit different sensitivities on the angle of incidence of the light beam. This means that their values may vary substantially for a slight change in thickness at one specific angle, while the same change in thickness would only cause very little change at another angle.

The use of multiple angles increases the sensitivity of the measurement, thus making the fitting procedure more reliable. However, for the theoretical determination and modeling, the refractive indices n must be known. The modeling procedure includes a model of several layers, each having defined refractive index parameters n and k and a certain thickness. The model is then fitted to the measured data with a regression analysis. The parameters n and k may be extracted from a database for standard materials, however for unknown materials these values also need to be modeled.

As an approximation the Cauchy model is often used for the visible wavelength range, especially for insulators, such as oxides or polymeric adlayers.

$$n(\lambda) = A_n + \frac{B_n}{\lambda^2} + \frac{C_n}{\lambda^4}$$

The parameters used in this model are all specific Cauchy coefficients. The thickness is hence determined by fitting of the experimental curves to the model equations.

Instrument

Ellipsometric data was measured in air by a variable-angle spectroscopic ellipsometer (M-2000F, Woollam Co., Inc., Lincoln, Nebraska, USA), whose principle is shown in

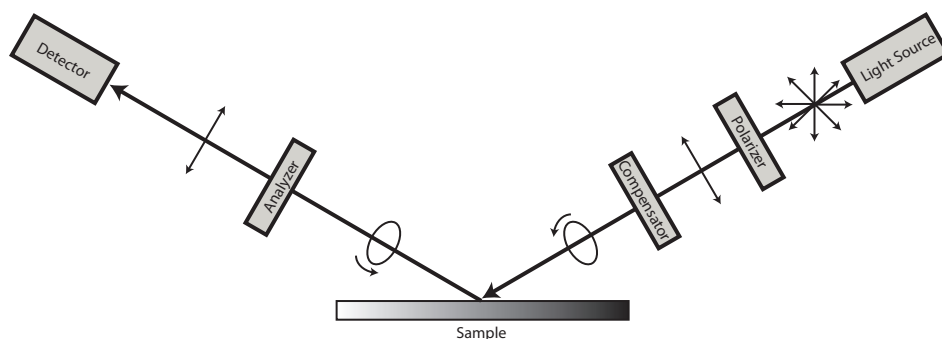


Figure 7.3: Scheme of the M-2000 FTM spectroscopic ellipsometer

Fig. 7.3. Light source is a Xe arc discharge lamp that emits unpolarized light. Polarizer and analyzer are fixed. The rotating compensator (retarder, quarter-wave plate), introduces a phase shift and thus transforms the linearly polarized light into an elliptically polarized one. Upon reflection from the sample, the polarization changes and gets polarized again by an analyzer. The resulting light is a linearly polarized beam of oscillating amplitude. These differences in intensity over time are recorded by the detector and further used to reconstruct the shape of the ellipse. Different angles of incidence can be used. For one wavelength and one incident angle, one polarization is created. As a function of time (depending on the speed of rotation of the compensator), different ellipses are created, modified after their reflection on the surface and polarized by the analyzer.

Experimental procedure

The measurements of amplitude (Ψ) and phase change (Δ) of the polarized light were conducted in the spectral range of 370-1000 nm at three different angles of incidence (65, 70 and 75° relative to the surface normal), averaging 50 measurements at each point and fitting with a multilayer model using the custom SpectraRay analysis software (VWASE32, Version #5728). For each layer, the optical parameters were determined using an appropriate model (Oscillator model for TiO₂ layer and a

Cauchy model for organic layers, the underlying layers of Si (1mm) [270] and SiO₂ (2.1 Å) were assumed to be constant for all wafers). The TiO₂ layer was fitted before adsorption, the Cauchy layer after polymer adsorption and additionally after serum adsorption. For the Cauchy layer, universal values for all polymeric layers were used: $A_n = 1.45$, $B_n = 0.01$, $C_n = 0$. The reported thicknesses represent an average of at least 3 replicate measurements on 3 different samples.

7.2.2 X-Ray Photoelectron Spectroscopy (XPS)

Theory

X-Ray Photoelectron Spectroscopy (XPS) is a surface-sensitive, ultrahigh vacuum technique used to determine the chemical composition of surfaces and thin films. The main principle is based on the collection of specific photoelectrons produced by exposing the surface to X-rays under ultrahigh-vacuum conditions. X-rays are emitted from an anode material, usually Mg or Al due to their narrow Mg-K α and Al-K α - x-ray line width with energies of 1253.6 eV and 1468.6 eV, respectively. The X-ray energy ionizes electrons from the core shells, each with a characteristic binding energy (E_B). If these electrons have acquired sufficient energy to overcome the work function Φ of the material and are created close to the surface (within the first 10 nm), they can therefore pass the surface with a defined kinetic energy (E_{kin}), which can be measured with an electron analyzer and detector. The electron analyzer is responsible for separating electrons with different E_{kin} , whereas the detector counts the electrons emitted per unit time (counts per second) at the certain kinetic energy E_{kin} , which the analyzer selected. (c.f. Fig. 7.4) Not all excited electrons reach the analyzer with their original E_{kin} , because of inelastic scattering within the sample. This inelastic scattering leads to a background, which needs to be subtracted from the spectrum before analysis. The kinetic energy spectrum can be converted into a

binding energy (E_B) spectrum by relating the kinetic energy of the electrons with the initial energy of the X-ray source $h\nu$:

$$E_B = h\nu - E_{kin} - \Phi$$

The work function (Φ) of the instrument can be determined by a calibration with standard reference samples such as gold, silver and copper. In addition to the photoelectron emission peaks that arise in the energy spectrum, there are also Auger emission peaks. These Auger electrons are emitted when ionized atoms, after the occurrence of the emission of a photoelectron, relax: an electron from a higher shell occupies the free electron site and the created energy is high enough to emit an electron from the outer shell of the atom.

Elemental identification is performed by comparing the measured binding energy of the photoelectron emission peak to photoelectron emission peaks from libraries. Moreover, the experimental binding energies allow not only allow the identification of the specific elements present in the surface regions, but due to small deviations in the actual binding energy of electrons deriving from one element (the so called chemical shifts), information about the chemical environment of the corresponding atom can be obtained. The peak area I_A is proportional to the number of emitted electrons. The relative elemental composition N_A can be determined after correction of this area with instrument- and element-related parameters:

$$N_A = \frac{I_A}{\sigma_A T_A \lambda_A \cos \theta}$$

The correction factors are the photoelectric cross-section σ_A (which is the probability that an incident photon will generate a photoelectron from a given sub-shell), the inelastic mean-free path λ_A of an electron, the instrument transmission function T_A (the ratio of the number of electrons at a given energy transmitted through

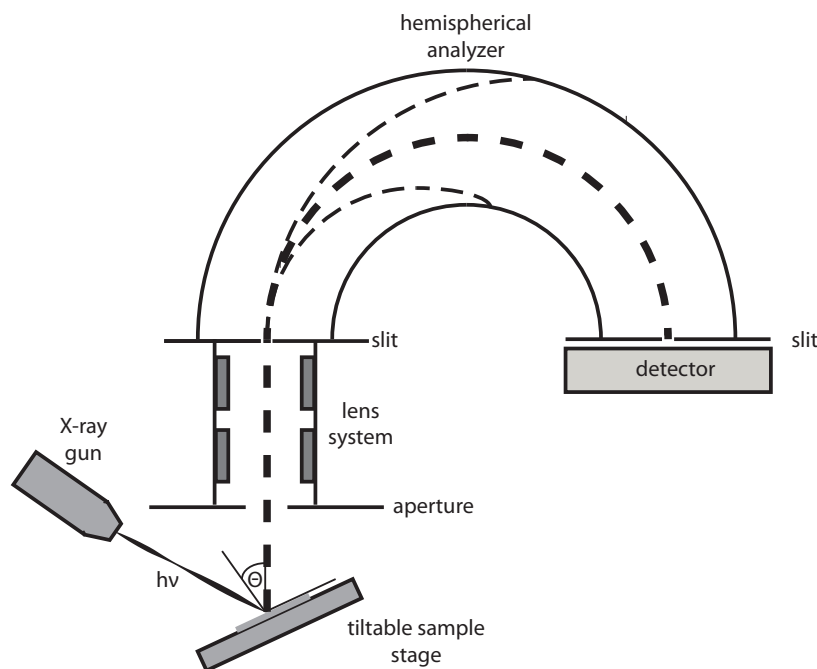


Figure 7.4: Scheme of an XPS setup. X-rays are emitted from an X-ray gun, impinge on the sample and initiate the photoelectric effect. The emitted photoelectrons travel through a lens system and are analyzed with a hemispherical energy analyzer (for example) prior to detection.

the spectrometer to the number entering the aperture of the analyzer at the same energy) and the emission angle θ between surface normal and the detector of the collected electrons. The higher the emission angle, the more surface-sensitive the analysis (typically 10nm information depth at an emission angle of 0°). In order to detect the elemental composition or binding states emitted from different depths of the sample, spectra at different emission angles need to be recorded and compared. This method is called Angle-Resolved-XPS (AR-XPS) and is especially useful when layered structures in the nanometer range above a substrate have to be investigated. With increasing emission angle, the ratio between the signal intensity generated by the photoelectrons of an element in the top layer and by those originating from an element in a lower layer or underlying substrate increases. Variation in the cor-

responding intensity ratio provides information on surfaces with layered structures including thickness determination.

The advantage of the XPS is the possibility to analyze a huge variety of different samples, ranging from conducting to insulating samples, especially its surface sensitivity and the possibility to perform quantitative analysis and to detect almost all elements, except for He and H (which have too low ionization cross-sections to be detected) make it a powerful tool in surface analysis.

Sigma 2

XPS measurements were conducted using a Sigma2 XPS (Thermo Fischer Scientific Inc., Loughborough, GB), equipped with an Al/Mg $K\alpha$ twin source, consisting of a Mg- (1253.6 eV) and a Al- $K\alpha$ (1486.6 eV) source. The emitted electrons are collected by the Alpha 110 hemispherical analyzer, which is mounted at 0° and the X-ray source at 54° to the surface normal (magic source-analyzer angle) and a multichannel detector consisting of seven channeltrons is used.

Acquisitions were performed below a pressure of $1 \cdot 10^{-5}$ Pa using a non-monochromated Mg $K\alpha$ source (1254eV) operated at 200W. The electron-energy pass analyzer was operating at 50 and 25 eV for survey and high-resolution detail scans, respectively. The spot size of the analyzed area is around 400 μm (large-area mode), thus the results represent a laterally averaged chemical composition. Due to the slightly higher resolution when using the Mg- $K\alpha$ source, this source was used preferentially in order to facilitate peak-fitting.

A standard measurement comprised averages over 9 (P, N, O) or 5 (Ti, C) scans for each element plus 3 scans for the survey. The dwell time was left at 50 ms at all times and the energy step-size was set to 0.1 eV/step high resolution detail scans and 1 eV/step for survey scans, resulting in approx. 5min measurement time per spot of

each element, accumulating to about 30-60 min for a complete elemental scan of one spot, depending on the substrate investigated.

Theta Probe

High resolution spectra and angle-resolved measurements were conducted using a Theta Probe (Thermo Fischer Scientific Inc., Loughborough, GB), equipped with an Al/Mg $K\alpha$ twin source and a monochromatic Al- $K\alpha$ source with beam diameters ranging from 15-400 μm . The emitted electrons are collected with a Radian lens with 60° acceptance angle, ranging from 23 to 83° emission angle. The average emission angle is 53°, the source-to-analyzer angle is 67.38°. For the full range of emission angle of 53°, the source-to-analyzer angle ranges from 43.1 to 93.7°. The electrons are detected on a two-dimensional detector with 112 energy channels and 96 angular channels. Further equipment is an ion gun and a combined low-energy electron/ion flood gun for charge compensation and a cooling stage.

All acquisitions were performed in scanned mode below a pressure of $5 \cdot 10^{-6}$ Pa using the monochromated Al $K\alpha$ source operated at 100W and a spot size of 400 μm (large area mode), therefore the results represent a laterally averaged chemical composition. For measurements in standard, scanned mode, the electron-energy pass analyzer was operating at 300 and 100 eV for survey and high-resolution detail scans, respectively. A standard measurement comprised averages over 9 (C, O, Ti, C, O) or 27 (P, N) scans for each element plus the 3 scans for the survey. The dwell time was at 100 ms at all times and the resolution was set to 0.1 eV/step (survey 1 eV/step), resulting in approx. 5-15min measurement time per spot of each element, accumulating to about 60 min for a complete elemental scan of one spot.

A standard AR-XPS acquisition was performed in snapshot mode with a pass energy of 124.224 eV, an energy window (energy width) of 12.5 eV and a 250 (C, O, N, Ti)

or 400 (P) number of frames. The measurement time was set for all spectra to 1s per frame. 112 Channels of the detector were used for energy resolution and 16 channels were used for angle resolution.

Data Processing

Peak fitting All XPS spectra were evaluated using CasaXPS (version 2.3.12 and later, www.casaxps.com). All binding energies are referenced relative to the main hydrocarbon peak, set at a binding energy at 285.0 eV. The signals were fitted using Gaussian-Lorentzian functions fixed to 30% and least-squares-fit routines following Shirley iterative background subtraction. Apparent normalized atomic concentrations were calculated from the respective detail spectra of each element present on the surface (region over all species) or from the fitted species, using a sensitivity factor, including published ionization cross sections σ [227], transmission function of the spectrometer T, inelastic mean free paths (IMFPs) λ calculated using the Gries model and asymmetry function, assuming a homogeneous surface model.

Sensitivity Factor The sensitivity factor in this work is defined as

$$S_{i,M} = \sigma(h\nu) \cdot L_i(\gamma) \cdot T(E_i) \cdot \lambda_{i,M} \cdot \cos(\theta)$$

where $\sigma_A(h, \nu)$ is the photoionization cross-section [227], $L_A(\gamma)$ the angular asymmetry factor, $T(E_i)$ the transmission function, $\lambda_M(E_A)$ the inelastic mean free path (IMFP) of the electrons in the matrix M, θ the emission angle. The sensitivity factors calculated for different elements in different compounds are given in Tab. 7.1 for the XPS instruments used. For the Sigma2, the angular asymmetry factor $L_A(\gamma)$ was not taken into account, because the instrument's source to analyzer angle of 54° is operating at the magic angle.

Instrument	C1s	O1s	N1s	P 2p1/2	P 2p3/2	Ti 2p1/2	Ti 2p3/2
Sigma2	1.410	4.017	2.485	0.591	1.159	3.766	7.376
Theta Probe	1.179	3.318	1.921	0.563	1.103	3.225	6.269

Table 7.1: Calculated sensitivity factors for both XPS machines used within this thesis

Details about the parameters used for calculating the sensitivity factors are described in the following.

Photoionization Cross-section The photoionization cross-section $\sigma_A(h\nu)$ describes the probability that an initial photon traversing the material will produce a specific photoelectron from a defined sub-shell, expressed as an area unit per event. The standard values calculated by Scofield in 1976 [227] were used for this work, given in units of the C1s cross-section and depends on the energy of the X-ray source ($h\nu$) and on the sub-shell of the element A.

Angular Asymmetry Function The intensity of photoelectrons deriving from non-spherical orbitals differs with the angle γ between the source and the analyzer, which is corrected by the asymmetry function [271]

$$L_i(\gamma) = 1 + \frac{1}{2}\beta \cdot \left(\frac{3}{2}\sin^2\gamma - 1\right)$$

The values for the asymmetry value β were calculated based on quantum mechanics and reported for the different energies for the X-ray source and for the various sub-shells by Reilmann et al. [271]. β is 2 for all s-orbitals and ranges between 1 and 2 for p-orbitals. γ is the angle between analyzer and x-ray source. For the Sigma2, γ is 54° and is therefore working at the “magic angle”, where the last term of $L_i(\gamma)$ get zero and thus $L_i(\gamma)$ equals 1. For the Theta Probe operated in standard mode, γ is 67.38° , but it is varying in angle-resolved mode, which is summarized in Tab.

emission angle θ	analyzer-source angle γ
24.875	44.5
28.625	47.3
32.375	50.2
36.125	53.2
39.875	56.3
43.625	59.4
47.375	62.6
51.125	65.8
54.875	69
58.625	72.2
62.375	75.5
66.125	78.8
69.875	82.1
73.625	85.4
77.375	88.7
81.125	92.0

Table 7.2: variation of γ in Angle-resolved mode (Theta Probe)

7.2 and can be calculated by taking into account the geometry of the system at each emission angle θ .

Transmission Function In the constant-energy mode, photoelectrons with a specific kinetic Energy E_i pass a lens system, which focuses and retards the electrons to the applied pass-energy E_p of the hemispherical analyzer. The number of transmitted electrons depends not only on the kinetic energy of the electrons, but is as well a function of the applied settings (lens modes, analyzer operation, X-ray illumination). Since the detectors are able to measure a range of kinetic energies at once or for the Theta probe even dependent on the emission angle, the pass energies can vary slightly and the detector efficiency might be different for the different conditions. Therefore, for the applied settings, the measured intensities have to be corrected by the corresponding transmission function in order to get quantitative

results.

For both XPS instruments the same transmission function was used:

$$\frac{I}{E_p} = \left(\frac{a^2}{a^2 + RR^2} \right)^b$$

$RR = E_i/E_p$ is the retard ratio calculated from the initial kinetic Energy and the Pass Energy, whereas a and b are fitted parameters. These parameters are determined by measuring peaks at different BE at different pass energies. In case of the Transmission function for the Theta Probe sputter-cleaned copper (Cu2p, CuLMM, and Cu3p) at different pass energies (10, 20, 50, 100, 125, 150, 200, 300, 400 eV) was used. For the Sigma2 sputter-cleaned Cu (Cu2p, CuLMM, Cu3p) and Ag (Ag3d) were used at different pass energies (5, 10, 25, 50, 100, 150 eV). The peak areas were corrected for the pass energy and normalized to the maximum intensity for each kinetic energy, as shown exemplary for the Cu2p peak:

$$I_{i,Cu2p}^{corr,normalized} = \frac{I_{i,Cu2p}}{E_{P,i}} / \max_i \left(\frac{I_{i,Cu2p}}{E_{P,i}} \right)$$

This gives a normalized dataset for each peak, which were plotted in a log-log plot against the retard ratio. The curve is then fitted with the parameters a and b .

The values obtained for a and b in standard mode are $a = 11.8 \pm 1.2$ and $b = 0.37 \pm 0.04$ for the Theta probe and $a = 17.9 \pm 2.3$ and $b = 0.49 \pm 0.06$ for the Sigma2.

Inelastic mean-free path The inelastic mean free path (IMFP) describes the average distance measured along the trajectories a photoelectron travels between two

inelastic scattering events in a substance and is an important factor towards quantitative analysis of XPS and Auger spectra [272]. To calculate the IMFP, the Gries model [273] was used and calculated by using the Software NIST Standard Reference Database 71: NIST Electron Inelastic-Mean-Free-Path Database V. 1.1. This model is simpler than that developed by Tanuma, Powell and Penn [274,275], but has shown comparable accuracy in the calculated IMFP values [276]. In comparison to the TPP -model, where the density, band gap and number of valence electrons as additional information is needed to calculate the IMFP, only the density and structural information are needed for the Gries model. Since most of these parameters are not readily available for synthesized polymers, the Gries model is preferred, because the error with an incorrect guess of these parameters would lead to high errors in the resulting, calculated IMFPs for the TPP-model. For all polymers used within this thesis, the density was assumed to be equal to the bulk density of the grafted side chains, i.e. 1.22 for PEG. The predictive formula was taken from the known polymer structure and set to $C_{142}H_{248}N_3P_1O_{58}$. It has been checked that only the simplified, relative stoichiometry of the elements given by the chemical formula is taken into account for the calculations of the IMFP and not the real chemical formula.

Sample charging The binding values reported in this work were corrected for the sample charging, by referring all binding energies to the aliphatic carbon C1s signal at 285 eV.

Angle-resolved XPS Angle-resolved spectra were fitted with the parameter described above to obtain peak intensities in dependence of the emission angle. Assuming a homogeneous compound, the atomic concentrations were calculated in dependence of the emission angle.

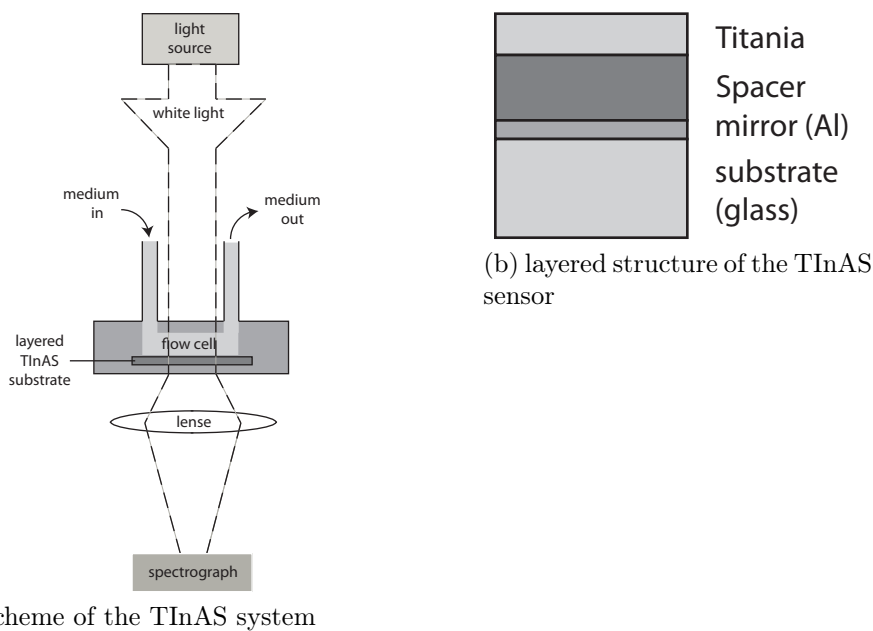


Figure 7.5: principle setup of the TInAS system and the layered structure of the TInAS sensor

7.2.3 Transmission Interference Adsorption Sensor (TInAS)

Theory

The Transmission Interference Adsorption sensor (TInAS) setup is a relatively new optical method for the determination of layer thicknesses on substrates [277, 278]. This includes static measurements, but combined with a flow cell, time-resolved measurements of molecular adsorption onto surfaces are possible, comparable with those obtained from other label-free techniques such as surface plasmon resonance [279], waveguide or evanescent light techniques [280, 281], interferometric systems, ellipsometry, quartz crystal microbalance, field-effect sensing, acoustic wave guiding and a host of molecular labeling techniques.

The underlying theory and physics is described in [278]. A stand-alone TInAS flow cell as described in [277] is used for all investigations. The setup is shown in Fig. 7.5.

White light is shone through the flow cell containing the flat TInAS sensor, which consists of a layered structure and therefore acts as an interferometer. A spectrograph for the readout of the spectrum is placed at the other side of the flow-cell.

The layered structure of the sensor is shown in Fig. 7.5, deposited by Ar-plasma sputter coatings onto a flat glass substrate. In considering a transparent dielectric multilayer structure, each layer exhibits a different refractive index. Partial reflections at these optical interface lead to a superposition of multiple beams, forming an interference spectrum in both reflection and transmission. These interference patterns can be used to determine small changes of film thicknesses, e.g. due to molecular adsorption, given that a sufficiently accurate wavelength calibration and determination of low interference maxima can be obtained. The shift in the peak maxima can be referred to a newly formed adsorption layer or change in the layer thickness. The determination of the adsorbate thickness requires the correct input of the refractive index n_A of the adsorbing material. The resulting effective optical thickness D can readily be transformed into adsorbed Mass M , per unit area, using the relationship $M = \rho \cdot D$, where ρ is the dry density of the adsorbate. Since adsorbates remain partially solvated after adsorption, the density can be expressed in terms of the refractive index difference of the adsorbate, n_A , and the solvent n_C , normalized to the concentration dependence of the refractive index in the mixture, dn/dc [277]:

$$M = \frac{n_A - n_C}{dn/dc} \cdot D$$

A reasonable value for protein adsorbates is $dn/dc = 0.182 \text{ cm}^3\text{g}^{-1}$ with refractive index of 1.44 and a refractive index of the solvent (HEPES2) of 1.33439 [282].

Experimental procedure

In situ investigation of polymer and protein adsorption were conducted with the Transmission Interference Adsorption Sensor (TInAS) [277,278] using a non-thermostated flow cell of around 25 μ l volume. The interference sensors were coated with a 25nm Al mirror layer and 3 μ m SiO₂ spacer layer, and annealed for 2h at 350°C. In a second step a 6nm TiO₂ surface coating was added (all coatings by reactive magnetron sputtering at PSI, Villigen, Switzerland). Adsorption measurements were performed at a sampling rate of \approx 1 Hz. Prior to each experiment the baseline was measured in ultrapure (MiliQ-) water. TInAS yields the optical thickness of the organic adlayer, which can be converted to the thickness D and the adsorbed Mass per unit area M [277, 278].

Since TInAS is an optical method, as is VASE, the refractive index assumed for all organic adlayers was kept constant of $n_A = 1.45$ during data treatment of both methods. The dependence of the refractive index with the concentration of polymer in solution, dn/dc , was determined by a linear fit of the refractive index with varying polymer concentrations. The value of dn/dc is 0.00140 ml/mg and was shown to be independent for all investigated polymers. For more detailed information, c.f. Fig. A.4 in Sect. A.3 on page 303.

For kinetic measurements, 0.5ml of 0.5 mg/ml polymer solution was injected and the kinetics registered for at least 3 hours, until the drift of the saturation curve was in the range of the initial drift of the baseline measured in water. For protein-resistance measurements, a polymer-coated sensor was placed in the flow cell and the initial drift of the baseline measured in contact to water. After changing to HEPES2 in order to be in a buffered environment and the acquisition of another baseline, 1 ml of full human serum was injected. After 20 min incubation it was rinsed thoroughly with HEPES2 and afterwards with water, registering a final baseline for both solvents.

After the measurement the drift during the measurement was adjusted by a linear regression of the drifts measured before and after the measurement and subsequent subtraction.

7.2.4 Quartz Crystal Microbalance with Dissipation Monitoring (QCM-D)

Theory

Quartz crystal microbalance with dissipation monitoring (QCM-D) is a gravimetric based sensing method. The change in resonance frequency and energy dissipation upon adsorption of material on an oscillating piezoelectric quartz crystal resonator is the basic working principle [283–285].

The resonance frequency shift Δf , of a freely oscillating crystal depends strongly on the adsorbed mass and can be calculated for thin and rigid films by using the Sauerbrey equation, where the mass change Δm is directly coupled to the frequency shift Δf , the overtone number n and a constant C , which is dependent on the resonant frequency of the quartz crystal ($C=17.7 \text{ ngHz}^{-1}\text{cm}^{-2}$ for a 5MHz crystal):

$$\Delta m = -\frac{C \cdot \Delta f}{n}$$

In a piezoelectric crystal, only odd harmonics can be excited, therefore $n=1, 3, 5, 7, 9, 11, 13$, etc. When the adsorbed film is viscoelastic, the Sauerbrey relation does not hold anymore and underestimates the mass on the surface. For the characterization of such films, more advanced models, as for instance the Voigt model have to be applied [286]. It is possible to obtain viscosity, elasticity and thickness if the frequency and the dissipation shifts of multiple overtones of the fundamental resonance of the crystal are measured. The dissipation shift can be used as a measure

of the softness of a sample by measuring the damping of the crystal oscillations by energy losses E_{lost} in one period of oscillation and the total energy stored in the oscillator E_{stored} :

$$\Delta D = \frac{E_{lost}}{2\pi E_{stored}}$$

Experimental

For all experiments, a Q-Sense E4 instrument (Q-Sense AB, Västra Frölunda, S) was used. Quasi-simultaneously, the 3rd, 5th, 7th, 9th, 11th and 13th overtones were measured with the software QSoft401 (Q-Sense AB, Västra Frölunda, S) and the 5th was used for comparison. 6nm TiO₂ was magnetron sputter coated (PSI, Villingen, CH) on Au coated, 4.95 MHz QCM-D quartz crystals purchased from Q-Sense. Before the first use, they were cleaned in an ultrasonic bath (Bandelin, D) in toluene and isopropanol for 10 min. Before the measurements, the crystals were cleaned with 2% sodium dodecyl sulfate (SDS, Sigma, Switzerland) and isopropanol in an ultrasonic bath for 10min and treated in a pre-heated UV-Ozone cleaner for 30 min. The solutions were pumped into the cells with a high-precision multichannel dispenser (IPC Ismatec SA, CH) exchanging 0.8 mL (QCM-D cell volume 40 μ L). Measurements were done in batch exchange if not stated otherwise to keep consumption of solutions low. The flow rate for inserting the polymer solutions was set to 579 μ L/min (max. pump speed) and 20 μ L for continuous flow experiments.

7.2.5 Optical Profilometry

Theory

To measure the surface topography of a sample, a profilometer can be used for non-contact optical 3D profiling. There are two main measurement techniques used for

optical profiling: Confocal profiling and Optical Interferometry [261].

Confocal profilers have been developed to measure the surface height of smooth to very rough surfaces and provide high-contrast images by elimination of out-of-focus light. The sample is scanned vertically in steps so that every point on the surface passes through the focus. The height of the surface at each pixel location is found by detecting the peak of the narrow axial response. In order to build up the axial response (i.e. the confocal image) at each vertical step, in-plane raster scanning is required, since the local areas of the surface are illuminated simultaneously. The main advantage is the highest lateral resolution that can be achieved by an optical profilometer.

Interferometric measurements are based on light scattering and reflection at the surface. In an interferometer, a light beam passes through a beam splitter, which directs the light to both the surface of the sample and a built-in reference mirror. The light reflected from the surface and the mirror recombines forming a fringe interference pattern in the detector. There are 2 different profiling modes, namely phase shift interferometric (PSI) profiling and white-light vertical scanning interferometric (VSI) profiling.

PSI profiling has been developed to measure the surface height of very smooth and continuous surfaces with sub-nanometer resolution. The sample placed in focus is scanned vertically in a few steps that are a very precise fraction of the wavelength. A phase map of the surface is then produced, which is then converted into a corresponding height map.

In VSI profiling, the surface height of smooth to moderately rough surfaces can be measured. Maximum fringe contrast occurs at the best focus position for each point on the surface of the sample. The sample is scanned vertically in steps so that every point on the surface passes the focus. The height of the surface at each pixel location

is found by detecting the peak of the narrow fringe envelopes.

Experimental procedure

Surface topographic profiles were measured on a Sensofar PLu neox (Sensofar-Tech, S. L., Terrassa, E) with 50x magnification. For very smooth surface analysis, i.e. surface roughness determination, PSI profiling was used, whereas for structural imaging, i.e. tribological wear tracks, the confocal profiling option was used. The data was acquired with the shipped SensoScan software and processed with the included SensoMap software by preparing the analysis procedure once and using the sample procedure as analysis template (with fixed analysis variables) for subsequent analysis of the same properties of different samples.

Surface roughness determination was performed with PSI profiling. For analysis, the measured topography was leveled with plane defined by three surface points and surface roughness and waviness separated by a Robust Gaussian Filter with 80 μm Cut-off and cut surface edges (by the value of the cut-off length) to avoid end-effects of the topography. From the roughness data, height parameters according to ISO 25178 were calculated. Normally, R_q (root mean square height) and R_a (arithmetic mean height) are stated within this thesis.

Surface profiling was performed by confocal profiling. For analysis, the measured topography was leveled with a plane defined by three surface points. For profile extraction, especially for wear track analysis, a line profile, perpendicular to the tangent of the wear track, was extracted from the middle of the image. From this cross-section, a mean line defined by the outermost, polished parts of the line profile was inserted and the area of the hole below (the cross section of the wear track) and the area above (due to deposition of wear material outside the sliding track) was measured.

7.2.6 Neutron Reflectometry

Neutron reflectometry is a relatively new technique [287,288] for film analysis and has become intensely used for soft-matter research, such as polymer mixing or to determine the structure of liquids at surfaces [288]. Neutrons at thermal energies are used to probe the near-surface structure of materials systems. The two main interactions of neutrons with matter are the strong interaction with the nuclei (scattering) and the magnetic interaction with existing magnetic moments (magnetic scattering). Neutrons are incident on a surface at a grazing angle of less than 3° . At these small angles, the potential for scattering can be approximated by a continuous value and this value is called the scattering length density (SLD) usually denoted in equations as ρ . It is a product of the scattering length b of each isotope and that isotope's number density N . The key property of neutrons for polymer studies is their large contrast between ^1H and ^2H which allows selective labeling by deuteration.

There are three main scattering geometries at grazing incidence shown in Fig. 7.6, which allow the study of a very wide range of length scales ξ :

- specular reflection ($3 \text{ nm} < \xi < 100 \text{ nm}$): it probes the structure along the depth in the film
- scattering in the incidence plane or off-specular scattering ($600 \text{ nm} < \xi < 60 \mu\text{m}$): it probes surface features at a micrometer scale
- scattering perpendicular to the incidence plane or grazing-incidence small-angle neutron scattering ($3 \text{ nm} < \xi < 100 \text{ nm}$): it probes surface features in the nm-range.

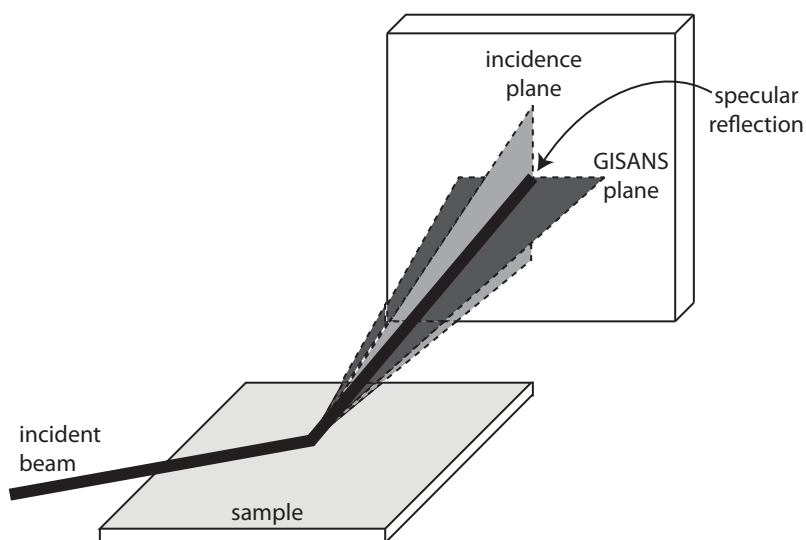


Figure 7.6: Scheme of an neutron reflectometry experiment and the different surface-scattering geometries: specular reflectivity geometry (black line), off-specular scattering plane, corresponding to the incidence plane (light gray) and grazing-incidence small-angle neutron scattering plane, perpendicular to the incidence plane (dark gray).

Experimental procedure

The neutron reflectometry measurements were performed at the Japanese Atomic Energy Agency in Tokai Village (Ibaraki) in Japan at the “MINE” neutron reflectometry facility. A nuclear reactor was used as a beam source, with a beam size of 10 mm width and 30 mm height. The wavelength was set to 8.8 \AA^{-1} with an accuracy of 3%. The optical alignment used in the experiments is presented in Scheme 7.7. The neutron beam cut by two upstream slits enters the target surface through the silicon block and is reflected at the surface. In the low-angle range ($0.2^\circ \leq \theta \leq 0.45^\circ$), the width of the slits 1 and 2 were set to 0.224 mm and 0.064 mm and in the high-angle range ($0.45^\circ \leq \theta \leq 0.9^\circ$) to be 0.312 mm and 0.156 mm, respectively. The slit of the neutron detector, which analyzes the reflected beam, was set to 10 mm in order to capture all reflected beam regardless of the surface roughness present at the sample.

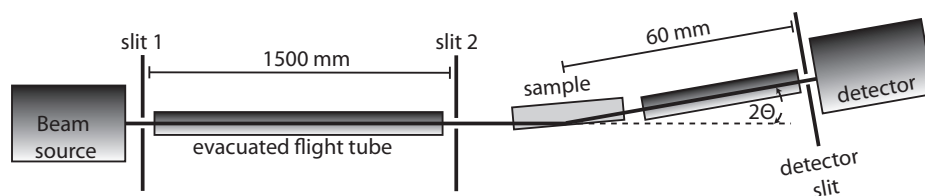


Figure 7.7: Optical alignment of the experimental setup used for the experiments at “MINE”

In the analysis, the steps in θ moved by precision stepping motors was set to 0.01. The sample was fixed in vertical position.

The target samples were ultra-flat Si blocks with 60nm magnetron sputter coated TiO_2 (PSI, Villingen, CH). Polymers were adsorbed according to the appropriate protocols stated below (c.f. 7.9.3). The analysis was done in a flow cell with deuterated hexadecane- d_{34} as solvent.

For analysis and modeling, a simplified polymer model, similar to that of De Gennes [289] was used, consisting of a homogeneous layer composed of a mixture of polymer and solvent. For all fitting procedures, the software Parratt32 v1.52 Build 211 (Gnu General Public License v2; developed at the Hahn-Meitner-Institut, Berlin, Germany) fitting software for neutron reflectometry was used.

For the measurements performed at “MINE”, the following procedure was chosen:

In a first step, the bare, titanium oxide sample was measured against air and the scatter length density ρ , the layer thickness d and the surface roughness of the titanium oxide layer was calculated by fitting the reflection data with a simple 3-layer model consisting of a semi-infinite layer of silicon with one layer of titanium oxide on top, which is in contact to a semi-infinite layer of air.

The polymer-coated samples were measured in contact with the deuterated solvent. Since the polymer has a scattering length density close to zero, because of the negative scattering values of ^1H , mainly the change in the density of the deuterated

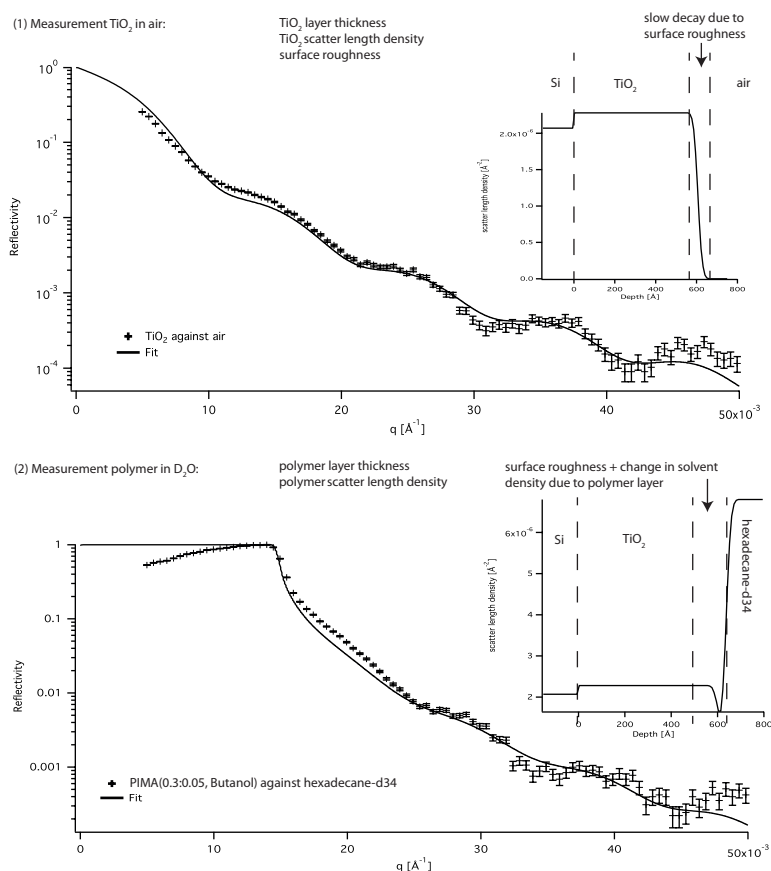


Figure 7.8: Explanation of the fit performed for the data acquired at “MINE” on titanium oxide, coated with POMA(0.3:0.04, Butanol). The larger graphs show the experimental reflectivity profile and the best fit. The small graphs show the vertical structure estimated by the best fitting and describes the layers fitted. In a first step TiO_2 in contact to air was measured and the layer thickness, scatter length density and the surface roughness was obtained. In the second step, the reflectivity profile of the polymer-coated sample in contact with deuterated hexadecane was fitted. Taking into account the parameters derived from the first fitting of the titanium oxide layer, the polymer layer thickness and the scattering length density of the polymer layer can be derived.

solvent is measured at the interface. This effect is overlaid by the roughness profile of the titanium oxide layer and thus the appropriate roughness value is important for the fit. The polymer-coated samples were fitted with an appropriate 4 layer model, consisting of a semi-infinite layer of silicon with a layer of titanium oxide on top, which is in contact to the deuterated solvent. The polymer thickness was calculated from the broad transition zone between the titanium oxide layer and the bulk solvent state, which contains the information about the change in the solvent density and the information about the surface roughness. This transition zone was defined as one separate layer, having a discrete and constant ρ , meaning a homogeneous layer consisting of a mixture of deuterated solvent and polymer. Since for all other layers, the surface roughness and scattering parameters were already known, for that polymer layer a one-layer model was used, taking the same surface roughness value as it was determined for the pure titanium oxide layer. This assumes a homogeneous layer of polymer on top of the titanium oxide, following smoothly the surface roughness as specified by the titanium oxide surface. Therefore, the polymer-layer thickness was assumed to be uniformly constant. The ratio between polymer and solvent in the polymer layer was calculated in using the fitted scatter length density ρ and comparing it to the pure scatter length density of the pure solvent (deuterated hexadecane: $6.8 \cdot 10^{-6} \text{ \AA}$). The fit procedure is summarized in Fig. 7.8

7.2.7 Atomic force microscopy (AFM)

Theory

Atomic force microscopy (AFM) is a high resolution surface topography probing instrument that provides a nanoscale 3D profile of a conducting or non-conducting surface [290,291]. It takes advantage of the interaction of a surface with a sharpened tip. It measures the forces exerted by a probe (radius $<10 \text{ nm}$) attached to a can-

tilever when the probe is a short distance away (0-10 nm probe-sample separation). It is a scanning technique where the image (x, y) is built up line by line with a slow and a fast scanning axis. The deflection of the cantilever is determined by means of a laser, which illuminates the back of the cantilever when it is measuring the surface. The tip or the sample is mounted on a piezoelectric scanner, which keeps the deflection or oscillation (depending on the measurement mode applied) constant using a feedback loop.

There are three primary modes of AFM imaging:

- contact mode: the probe is brought in contact with the surface and the cantilever is kept at a constant deflection (sensing of repulsive contact force)
- non-contact mode: the tip interacts only by attractive forces (Van der Waals forces, capillary forces, chemical bonding, electrostatic forces) with the surface. During the measurement, the cantilever is kept at a constant deflection (according to Hooke's law $F = -k \cdot x$). For higher accuracy, the cantilever is normally oscillated constantly at its resonant frequency with a certain free amplitude, which changes due to the attractive forces when the tip is approaching the surface. During the Measurement, the oscillation of the cantilever is kept constant.
- intermittent contact or tapping mode: the cantilever is vibrated in oscillating mode closer to the surface, that the oscillating cantilever at the bottom of its travel just barely hits ("taps") the surface of the sample.

A schematic diagram of an AFM is shown in Fig. 7.9. Quantitative information can be obtained when the scanner and the tip are properly calibrated. The tip geometry plays an important role when interpreting images, because some artifacts, such as double peaks or blurred images, may be caused by a blunt, broken or contaminated

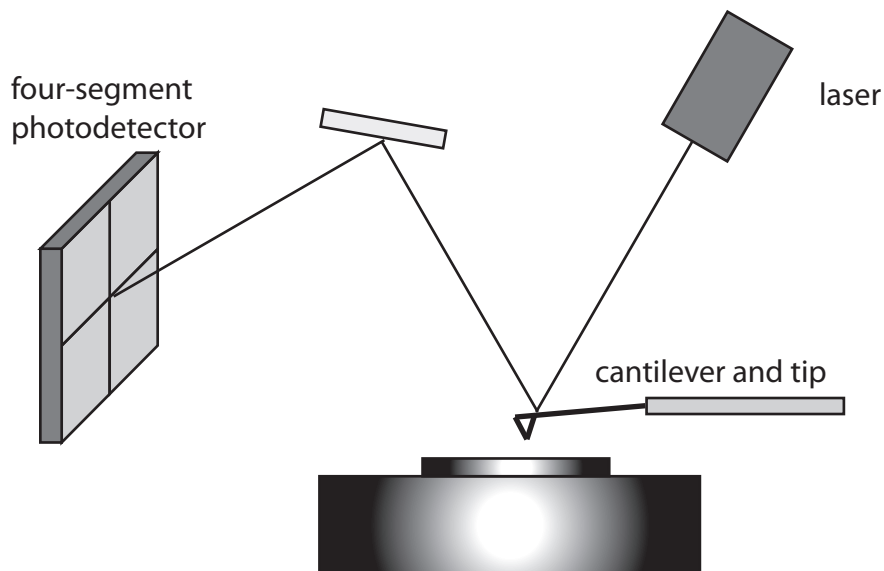


Figure 7.9: Schematic diagram of an AFM

tip. A colloidal probe with a spherical particle attached to the cantilever can be used when a well-defined and stable contact geometry is needed during the measurement. Interactions between the tip and the surface can be determined by performing force-distance measurements. In this mode, the deflection of the cantilever in relation to the traveled distance is measured. Because it is not possible to measure absolute separations with the AFM, an appropriate calibration has to be found for the transformation of raw deflection-distance curves in force-separation curves. For the transformation the algorithm reported by Senden [292] is used to transform deflection versus displacement curves with known cantilever spring constant into force-versus-separation curves. These transformed curves are referred to as force-distance curves in the following.

Experimental procedure

For imaging and force-distance measurements, an Asylum MFP-3D (Asylum Research, Santa Barbara, CA, USA) was used. The cantilevers were cleaned by incubation in Cobas cleaner (Roche, Basel, CH), water and isopropanol and treated in a pre-heated UV-Ozone cleaner for 30min. The spring constants k of individual cantilevers were calibrated based on the thermal noise spectrum using the Asylum software [293]. For experiments conducted in air, the samples were directly imaged either using contact mode or tapping mode. For experiments conducted in liquid, after addition of the liquid to the Petri dish, the AFM head was lowered into the liquid and allowed to thermally equilibrate for 30min before scanning.

Force measurement were carried out using the Atomic force microscope (Asylum research, MFP-D). Silica microsphere (EKA chemicals AB, Kromasil®) were glued to a tipless cantilever (Micromasch, Tallinn, Estonia) with Norland optical glue using a home-built micromanipulator and used as a colloidal probe AFM. The diameter of the sphere used in this study was 20 μm . The normal calibration of the cantilevers was carried out by the thermal-noise method before attachment of the colloidal sphere and the spring constants was found to be $k = 0.58\text{N/m}$.

7.3 Tribological tests

7.3.1 Pin-on-disk Tribometer

Constant load tribometer

The pin-on-disk tribometer (CSM Instruments SA, Peseux, CH) employed in this thesis represents a macroscopic technique to measure the sliding friction for sphere-on-plane configurations. The characteristic parts of the instrumental setup are illus-

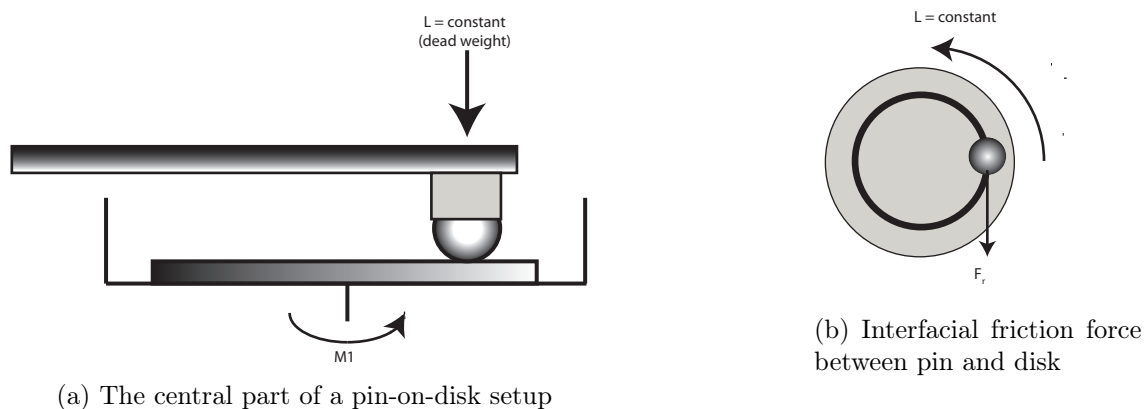


Figure 7.10: The central parts of a pin-on-disk setup (left) and the top view of the rotating disk with the relevant forces indicated (right). Interfacial friction forces between pin and disk are detected by the lateral deflection of a strain gauge in the measuring arm. [294]

trated in Fig. 7.10. The measurement arm bearing the pin is loaded by dead weights in order to apply a normal force (N) and is brought into contact to the disk, which is fixed inside a cup holder. The holder is driven by a motor and the disk inside the cup holder is rotated at a certain velocity. The interfacial friction forces generated upon contact between the pin and the rotating disk are determined via the lateral deflection of the measuring arm, which is equipped with a strain gauge [294].

The available sliding speed ranges typically from 10 mm/s to 0.01 mm/s and therefore allows the investigation of different lubrication regimes ranging from fluid film to boundary lubrication [294].

Experimental procedure

Before the experiment, both the polished steel surface as described in 5.4 and the steel ball were cleaned by ultrasonication for 3 x 10 min in isopropanol and plasma-treated for 2min. All parts used for the experiment were first cleaned with Cobas cleaner (Roche, Basel, CH) under tap water and then rinsed with deionized water.

Later they were ultrasonicated in petrolether (technical grade) and ethanol (p.a.) and finally dried under a nitrogen stream. At the end of the experiment, the oil present on disks and ball surfaces was removed by ultrasonication with petrolether and ethanol (p.a.). The reference oil used for lubrication was poly(α -olefin), PAO-166 (Nexbase 2006, Neste Oil N.V., Beringen, Belgium).

Before the start of the measurements, the ball was run in at 5 N load. For the tribological experiments, the load applied was always 1N and for each sliding speed a new track on the disk was used, with a minimum distance between the tracks of 0.5mm. The speeds applied were 1, 0.75, 0.5, 0.25, 0.1, 0.05, 0.025 and 0.01 cm/s. To investigate the effect of a probable hysteresis, the speed was first reduced from high speeds towards low speeds, subsequently followed by a second measurement with increasing speeds.

Oscillating Load Tribometer

All oscillating load tribotests were performed in a ball-on-disk arrangement using the CETR UMT-2 tribometer (Center for Tribology, Campbell CA, USA) as shown in Fig. 7.11.

The contact was always pure sliding without any rolling of the ball. The disk is mounted on a sample holder inside a cup that is filled with 6 mL of oil, so that both the ball and the disc are fully immersed in the lubricant oil during the test. The carriage of the tribometer can be moved up and down in the z-direction, while a horizontal slider allows movement along the x-axis. A rotational drive turns the disk. All motors are under computer control and the positions are determined with an encoder and sent back to the computer. The ball is pressed on the disk via a spring and the y/z-load cell measures the resulting friction force and load. The computer

compares the measured load with the nominal load and corrects the applied load by moving the carriage up or down.

There are two load cells with different force ranges, one for forces up to 5 N and another for forces up to 20 N. Only the 20N load cell was used for the tribological tests. The load cell was regularly calibrated using a dead weight.

The tribotests are programmed in test procedures. In such a procedure, a sequence of experiments can be programmed by setting the load, speed, radius and time for each experiment. In addition, the load can be cycled several times over one turn (linear increase and decrease of the load in dependence on the encoders (x, z and rotation) and the time is recorded during an experiment.

Prior to an experiment, the planarity of the disk was checked in order to have constant conditions all over the disk to avoid varying frictional behavior depending on the angular position on the disk. A stylus was pressed down on the sample with 100 mN load for one lap of the turning disk. The z-values of the carriage during this turn determine the planarity of the sample. By placing aluminum foil between the sample holder and the rotational drive, the planarity was adjusted until it was better than 15 μm on a radius of 7 mm.

Experimental procedure

Before the experiment, both, the polished steel surface as described in 5.4 and the steel ball were cleaned by ultrasonication for 3 x 10 min in isopropanol and plasma-treated for 2min. All parts used for the experiment were first cleaned with Cobas cleaner (Roche, Basel, CH) under tap water and then rinsed with deionized water. Later they were ultrasonically cleaned in petrolether (technical grade) and ethanol (p.a.) and finally dried under a nitrogen stream. At the end of the experiment, the oil present on disks and ball surfaces was removed by ultrasonication with petrolether

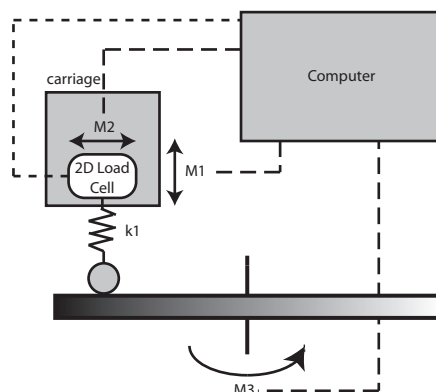


Figure 7.11: Schematic of a CETR tribometer. The tribometer consists of the carriage, on which the upper sample holder is mounted and the sample table bearing the lower sample holder. The carriage can be moved up and down with the motor 1 (M1) and has a two dimensional load cell mounted on the vertical slider, driven by motor 2 (M2). The upper sample holder is connected to the load cell by a spring with a spring constant k_1 . The lower sample holder is mounted on the sample table, which is driven by the rotational drive (M3). All three motors are equipped with encoders, which monitor the position of the respective direction of movement. The load cell is capable of measuring the load in two dimensions (x- and z-axis). The z-axis is perpendicular to the sample plate and the x-axis is tangential to the rotational direction. During a tribotest, the normal load can be programmed and is maintained by a feedback loop. The normal load is measured continuously and is adjusted by moving the carriage up or down with motor M1. [294]

an ethanol (p.a.). The reference oil used for lubrication was poly(α -olefin), PAO-166 (Nexbase 2006, Neste Oil N.V., Beringen, Belgium).

The oscillating test was performed to test both, the coefficient of friction and the wear behavior at different loads. Prior to the actual test, a running-in of the ball in PAO was performed with a load of 10N at an outer radius for half an hour, in order to achieve a well-defined flat-flat contact. During the actual test, the load was cycled two times per turn from 1 to 10 N according to the scheme of Fig. 7.12. In order to produce measurable wear during the applied turns, non-hardened disks (100Cr6) were used together with a hardened 100Cr6 steel ball of 4 mm diameter. Normally, 2 cycles were acquired per disk, one with the PAO reference, one with PBG and

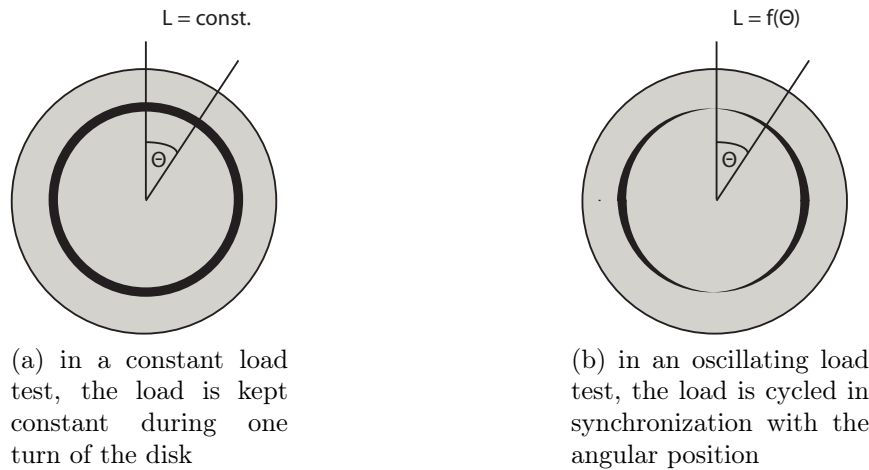


Figure 7.12: Wear track in dependence of the angular position on the disc

additive at a speed of 5 mm/s [294].

During a tribological experiment, the friction force, the load, the position of the encoders (x , z and rotation) and the time were written into a data file, which was converted into an ASCII file by the Viewer.exe program (Center of Tribology, Campbell CA, USA). The ASCII file was read and processed with Matlab 2010a software (The MathWorks, Inc, Natick, MA, USA). The procedure was developed by Dr. R. Heuberger [294]. From the tribological data, the average friction coefficient of all data points, the friction coefficients for several loads in dependence of the number of turns, and the friction coefficients for a certain number of turns in dependence on the applied load were calculated, including the standard deviations [294].

In order to investigate the wear tracks on the tribostressed disks, the surface topography was measured by optical profilometry (c.f. 7.2.5) at certain points with a predefined angular position from which the applied load could be derived. The wear rate r was calculated by using the crosssection area of the wear track by the following formula:

$$r = \frac{V_{total}}{l_{total}} = \frac{A \cdot l_i}{n \cdot l_i} = \frac{A}{n}$$

with V_{total} the total volume of the wear track and l_{total} the total sliding length of the tribotest, l_i the circumference of the wear track, n the number of cycles and A the cross section of the wear track.

In oscillating load tests, the load is cycled two times from the minimum value to the maximum value. For each load, corresponding values were averaged to get the wear.

7.3.2 Mini Traction Machine

Instrument

The Mini Traction Machine (MTM, PCS Instruments, London, UK) is a ball-on-disc test rig, where a ball and a disc were independently driven by motors so that the overall entrainment speed $U = (U_1 + U_2)/2$ and the slide-roll ratio (SRR) can be controlled. The SRR is defined as

$$SRR = \frac{2 \cdot |U_2 - U_1|}{U_2 + U_1} \cdot 100$$

A scheme of an MTM is shown in Fig. 7.13. The test specimens used are a 19.05mm (3/4 inch) steel ball and a 46 mm diameter steel disc, which were received from the manufacturer in a highly polished condition. The ball is loaded against the face of the disc and the ball and disc are driven independently to create a mixed rolling/sliding contact. The frictional force between the ball and disc is measured by a stiff force transducer mounted perpendicular to, and in contact with the ball shaft. These were translated to traction coefficient (TC) values by $\mu = F_L/L$, where F_L is the friction force and L is the applied load. Additional sensors measure the applied load and the lubricant temperature.

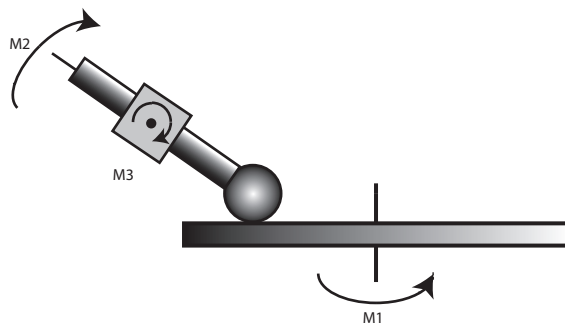


Figure 7.13: Scheme of a Mini Traction Machine (MTM). To vary the slide roll ratio (SRR), Motor M1 rotates the disk with a different speed than M2 drives the rotation of the ball. M3 varies the normal load. The Traction Force (TC) is measured normal to the shaft.

Experimental procedure

Before the experiments, the polished steel surface and the steel ball were cleaned by ultrasonication in toluene, acetone and ethanol. The reference oil used for lubrication was PAO-166 (Nexbase 2006, Neste Oil N.V., Beringen, Belgium) or diisotridecyladipate (DITA). A standard experiment consisted of the variation of different speeds (e.g. 1000, 800, 600, 400, 200, 100, 80, 60, 40, 20, 10, 8, 6, 4, 2 mm/s) at one fixed SRR (20, 40 or 80%). The applied load was 7N or 14N. To investigate the effect of a probable hysteresis, the speed was first reduced from high speeds towards low speeds subsequently followed by a second measurement with increasing speeds.

7.4 Corrosion tests

7.4.1 Electrochemical Impedance Spectroscopy (EIS)

Theory

Electrochemical impedance spectroscopy (EIS) is an electrochemical technique used for studying corrosion phenomena and measures the dielectric properties of a medium as a function of frequency. It is based on the interaction of an external field with the electric dipole moment of the sample, often expressed by permittivity [295, 296].

It is commonly agreed that corrosion measurements can be conducted in a steady state, but also in a non-steady manner. The underlying principle of EIS is based on the corroding interface placed in a steady state, in this case with a small voltage applied. The induced current response is rather linear. Current response to the voltage perturbations is often measured over a range of frequencies, which allow a differentiation between the corrosion processes characterized by different reaction rates. Contrary to polarization techniques, little interference and shadowing of the corrosion parameters occurs normally, leading to a more reliable image of the occurring processes.

Since the EIS method applies perturbations with a well-defined frequency, the electrochemical circuit can be analyzed by amplified circuit analysis. In contrast to the direct current methods, the respective relation between current and voltage is described by the impedance in AC circuits. When the input signal is the voltage, then the current response is measured. Impedance takes under account the possible phase shifts between voltage and current and therefore, input and output signals differ in phase. An important feature of electrochemical impedance spectroscopy is that the excitations of the system are rather small (in the range of 10mV), so that the cell's response is considered pseudo-linear. Linearity in this case means that the frequency

of the response does not change, only the phase shift ϕ may occur. Such shift can be represented as

$$E_t = E_0 \cdot \sin(\omega t)$$

$$I_t = I_0 \cdot \sin(\omega t + \phi)$$

In amplified current circuits an analogous expression to the Ohm's law exists, that defines the impedance as:

$$Z = \frac{E_t}{I_t} = Z_0 \cdot \frac{\sin(\omega t)}{\sin(\omega t + \phi)}$$

The impedance can thus be expressed in terms of its magnitude Z_0 and a phase shift ϕ . Analysis of the amplified circuits can be started on the circuit composed of the pure resistance R only Ohm's law always holds true and the phase shift is equal to zero for the entire frequency domain. It is convenient to represent the voltage as a rotating vector, called a phasor, which actual value can be read out as a projection on the x-axis. Relation between the phasors is given as $E = I \cdot R$.

When a pure capacitance is analyzed starting from the simple relation of the voltage with charge, it is possible to calculate the expected phase shift as showed below:

$$q = C \cdot E$$

$$I = \frac{dq}{dt} = C \cdot \frac{dE}{dt} = C \cdot \frac{E \cdot \sin(\omega t)}{dt}$$

$$I = \omega \cdot C \cdot E \cdot \cos(\omega t)$$

$$I = \frac{E}{X_C} \cdot \sin(\omega t + \pi/2)$$

with $X_C = \frac{1}{\omega C}$ the capacitive resistance, here the relation between the AC resistance is dependent on the frequency. Moreover, the phase shift is defined as $\pi/2$ with the current leading the voltage. In this case a phasor representation is convenient to be expanded to a plane, what is even easier with complex number notation. Components at the x-axis are real (*Re*) and components on the y-axis are considered to be imaginary (*Im*) and values of the latter must be multiplied by $j = \sqrt{-1}$. Therefore, the phasor is defined as

$$E = -jX_C I$$

Circuits composed of capacitance and resistance circuits in series are described by the following relation

$$E = E_R + E_C$$

$$E = I \cdot (R - j \cdot X_C)$$

$$E = I \cdot Z$$

This defines the impedance as dependent on the frequency as:

$$Z(\omega) = R - \frac{j}{\omega C} = Z_{Re} - j \cdot R$$

Bode and Nyquist Plots are the most popular ways of representing the EIS data. The Bode Plot is a representation of the impedance modulus on the ordinate axis versus

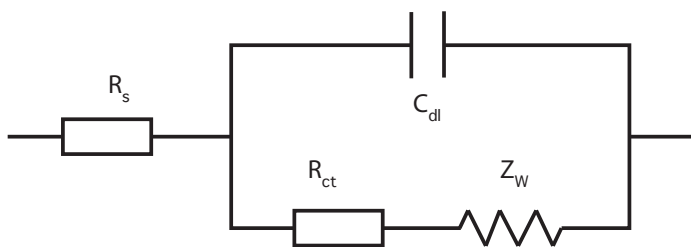


Figure 7.14: Randles circuit representing the standard electrochemical cell. C_{dl} is the double layer capacitance, R_{ct} the charge-transfer impedance, R_s the solution resistance and Z_W the Warburg impedance.

frequency on the abscissa axis. The plot is usually in form of a double logarithmic representation, $\log(|Z|)$ vs. $\log(\omega)$. The Nyquist Plot is a representation of a real part and imaginary part of the impedance on the x- and y-axis, respectively.

For the resistance and capacitance in series, a Nyquist Plot is a straight line, perpendicular to the Z_{Re} -axis at a fixed value, since the real part is independent of ω . In the case of capacitance and resistance coupled parallel, the curve of such RC circuit shows a semi-circular shape.

The model equivalent of an electrochemical circuit is represented in Fig. 7.14, which is called the Randles circuit, where the resistance of an electrolyte is inserted in series with a parallel RC segment, consisting of the double-layer capacitance and the general impedance of the charge-transfer resistance and the Warburg Impedance, which is a measure of mass transfer, i.e. ionic dissolution of a material.

For surfaces, degrading in a corrosive environment, different mechanisms can be detected with the EIS measurements:

- Active dissolution: a well-behaved semi-circular arc on the Z vs. Z plot with $Z=0$ at $\omega = 0$. Sometimes both real and imaginary parts may attain positive values while inductive behavior occurs. Inductance is sometimes referred to as negative capacitance, either due to the action of adsorbed intermediates or due

to passivation phenomena.

- Pitting corrosion: pitting corrosion of equivalent circuits developed to describe a pitting corrosion at a passive surface.
- Mass-transport-controlled situations: energy is dissipated by the moving charged species by a periodic perturbation giving a rise to the resistance and reactance measured by EIS.

Experimental

EIS experiments were performed at the corrosion department at EMPA Dübendorf. For the experiments, a three-electrode set-up was used. The Pt reference electrode was placed in a Lugin capillary with a ceramic filter diminishing the ion exchange and providing a stable environment in the vicinity of the reference electrode. The tip of the Lugin capillary was facing the working electrode (test sample) from a distance of approx. 1.5 cm. In order to extinguish the artifact effects related to capacitive character of ceramic filter present, additional Pt. wire was coupled at the outside in the vicinity of the end of the capillary. This is an important element, when reliable results in the high frequency domain are needed.

In order to investigate the phenomena present at the sample-solution interface, the working electrode (investigated surface) was outside a chamber filled with solution. Contact was achieved through a defined, 1 cm^2 area defined by the circular window in the chamber, sealed with an o-ring. The backside of the tested sample was polished on 200 and 600 SiC-grinding paper in order to remove the oxide layer and to provide a good metal-metal contact with the attached wires. A saturated calomel electrode present in the chamber was spaced roughly 4-5 cm away from the analyzed surface. The first step of the experiment is the programming of the applied voltage and frequencies over time in form of a procedure for the connected computer. This allows

the sample to be kept in the solution as short a time as possible before the start of the experiment. FRA AutoDesk software was used to control the experimental cell. The frequency range was always set from 10^5 kHz to 10^{-2} kHz. The perturbation introduced into the system was equal to 1 mV.

When filling the measurement chamber with solution, it was always checked that the whole sample surface is covered with solution without any bubbles sitting at the surface and that all electrodes are immersed in the solution. In case of bubbles at the working electrode, these were removed by liquid perturbations introduced with a clean glass pipette.

When the electrochemical cell is enabled, the open circuit potential (OCP) is always measured before the start of an experiment. An OCP below of -2.5V indicates some systematic errors in the system.

7.5 Cell tests

Cell cultures were performed with 3T3 mouse fibroblasts. Cells were taken out of liquid nitrogen and cultured in α -MEM supplemented with 10% FCS (fetal calf serum). All cultures were kept at 37° in a humidified atmosphere of 5% CO₂ and 95% air. When the bottom of the culture flask was covered with a monolayer of cells, enzymes were used to detach them. After centrifugation, viable cells were counted in a hemacytometer and inoculated at $3 \cdot 10^3$ cells/ml in a 24-well plate containing the TiO₂ samples. After 7 days in the incubator, live-dead staining was performed. Live cells have intracellular esterases that convert nonfluorescent, cell-permeable calcein acetoxymethyl (calcein AM). Cleaved calcein is retained within cells and shows a green fluorescence. Dead cells have damaged membranes. The ethidium homodimer-1 (EthD-1) enters damaged cells and is fluorescent when bound

to nucleic acids. EthD-1 produces a bright red fluorescence.

The cells were washed with PBS, fixed in 4% paraformaldehyde in PBS for ten minutes and subsequently washed with PBS. The number of cells on the sample was counted on random pictures taken with a Zeiss Observer D1 microscope with illumination X-Cite 120 XL.

7.6 Chemicals and Solvents for Surface Modification

All commercially available chemicals were purchased from Fluka (Fluka Chemie AG, CH), Sigma-Aldrich (Sigma-Aldrich, Buchs, CH), Merck (Merck, Darmstadt, D) or Acros (Acros Organics, VWR International, Inc, West Chester, PA, US) and used without further purification. Ultra pure water (MQ-water: Milli-Q Gradient A 10, Millipore, CH), equipped with a an Elix 3 (three step purification process) and a ultraviolet lamp for photo-oxidation was always used. The resistivity and total organic carbon (TOC) were in the range of 18.2 M Ω cm and <5 ppb, respectively. Nitrogen gas (N 5, purity >99.999%) was purchased from PanGas, Dagmarsellen, CH.

7.7 Buffers

Buffers are crucial for biological applications, where the pH of the system has to be fixed to biological environment. Buffers are differing widely in their composition, starting from totally inorganic buffers such as phosphonate buffers to fully organic buffers, such as HEPES (N-2-Hydroxyethylpiperazine-N'-2-Ethanesulfonic Acid). The advantage of some organic buffers is that there are no components in in

Table 7.3: Ion concentrations of PBS, SBF and HEPES-2 [mmol/l]

Ions	PBS	SBF-27	HEPES-2
Na ⁺	153	127	152
K ⁺	3	4	-/-
Mg ²⁺	-/-	1	-/-
Ca ²⁺	-/-	2.5	-/-
Cl ⁻	140	105	150
HCO ₃ ⁻	-/-	27	-/-
HPO ₄ ²⁻	8	-/-	-/-
H ₂ PO ₄ ⁻	2	1	-/-
SO ₄ ²⁻	-/-	1	-/-
HEPES	-/-	-/-	10
TRIS	-/-	77	-/-

the buffer solution that could adsorb or react with an oxide surface, unlike e.g. phosphates. In this thesis, different buffers were used for different applications: HEPES-2 was used for testing the non-fouling properties of the polymers as described in 7.9.4, SBF (simulated body fluid) and PBS (phosphate buffered solution) were used for corrosion testing of magnesium alloy surfaces, as described in Sect.4.2. All buffers are prepared without the addition of the toxic biocide NaN₃. For that reason the solutions were prepared freshly on a regular basis as indicated in the protocols.

Table shows the ion concentrations of PBS, SBF and HEPES-2 as described in the following Tab. 7.3.

7.7.1 PBS

There are many possible recipes that can be used to prepare PBS buffer, depending mainly on the molarity of phosphate and total ionic strength needed. In this work, a phosphate concentration of 10 mM and a total ionic strength of 150 mM was used, prepared by addition of 8 mmol sodium hydrogen phosphate (Na₂HPO₄ x 7H₂O,

A.C.S., Aldrich, Milwaukee, WI, USA), 2 mmol potassium dihydrogen phosphate (KH_2PO_4 , puriss. p.a., Fluka, CH), 3 mmol potassium chloride (KCl, puriss. p.a., Fluka, CH) and 137 mmol sodium chloride (NaCl , puriss. p.a., Fluka, CH) to 1l of MQ-water. The buffers were adjusted to pH 7.4 with 0.1M NaOH or HCl and filtered through a 0.2 micron filter. For in vitro assays the buffer was autoclaved in water steam at 120°C for 2 h.

7.7.2 SBF-27

SBF simulates the ion composition of human blood, but does not contain any proteins or blood cells. The calculated amounts (ml) of concentrated solutions listed in Tab. 7.4 were added in the sequence KCl, NaCl, NaHCO_3 , $\text{MgSO}_4 \times 7 \text{H}_2\text{O}$, CaCl_2 , (TRIS + HCl) and KH_2PO_4 into 700ml of MiliQ water to prevent precipitation of calcium phosphates or other salts by minimization of the changes in pH during preparation.

All stock solutions were prepared in dissolving the appropriate salt in MilliQ-water. TRIS+HCl solution was prepared by dissolving 121.16 g of TRIS (tris-hydroxymethyl aminomethan) in 650ml MilliQ water. During stirring the pH was adjusted to 7.6-7.7 at 25°C by adding conc. HCl. The clear solution of TRIS and HCl was quantitatively transferred into a 1000ml-flask and filled up with MilliQ-water.

The SBF buffer was freshly prepared from stock solution and used for no longer than 1 week. The stock solutions were stored for several months, the TRIS+HCl stock solution was prepared freshly each time.

7.7.3 HEPES-2

HEPES-2 buffer was prepared by dissolution of 8.766g NaCl and 2.383g 4-(2-hydroxyethyl) piperazine-1-ethane sulfonic acid (HEPES, Fluka Chemie AG, CH), 0.688 ml NaOH (6M) in

Table 7.4: Preparation of 1 l SBF buffer from stock solutions

Substance	concentration of stock solution [g/l]	Volume of stock solution for 1 liter of SBF [ml]
KCl	59.64	5
NaCl	116.88	50
NaHCO ₃	45.37	50
MgSO ₄ x 7 H ₂ O	49.30	5
CaCl ₂ x 2 H ₂ O	9.81	25
TRIS+HCl	see text	50
KH ₂ PO ₄	27.22	5

1L MilliQ-water. The resulting, stirred solution is then adjusted to a pH of 7.4 using aqueous HCl or NaOH solution. The solution contains a salt concentration of 160mM, whereas 150mM are derived from the NaCl addition. The solutions were stored in a fridge and kept no longer than 1 month.

7.8 Substrates

Different types of substrates were used within this thesis. The choice depended mainly on the application and on the instrumental setup of the planned investigations:

Titanium dioxide is a widely used implant material. Furthermore, due to its optical properties this material is used for further characterization and comparison of the polymers adsorbed to the surface with ellipsometry.

WE43 magnesium alloy is a newly developed implant alloy, which degrades within months after implantation.

100Cr6 Steel is a model alloy for all applications using steel as a construction material. In this thesis the main focus for this materials is mainly for tribological

applications, such as in motors.

These substrates are explained in the appropriate chapters, namely chapter 3 for titania surfaces, chapter 4 for magnesia surfaces and chapter 5 for steel surfaces.

All surfaces were cleaned as described in the section 7.9.2 before any further use.

7.9 General Protocols

7.9.1 Glassware and tools cleaning

All glassware used for surface functionalization and surface cleaning were first cleaned with Piranha solution (3:7 (v/v) 30% H₂O₂ : 96% H₂SO₄) and subsequently rinsing to neutral pH of the rinsing MQ-water and dried in an ventilated oven at 130°C. To ensure the cleanliness of the glassware, the dried glassware was wrapped in aluminum foil for storage.

7.9.2 Substrate cleaning before adsorption

Before adsorption of the surface-active compounds, the surfaces were cleaned by means of ultrasonication in a highly clean (Piranha cleaned) PTFE container. The samples were fixed to a vertical position to remove all kind of small (dust) particles by suspension and thus avoiding redeposition by gravitational forces. For further cleaning, Oxygen plasma (Harrick Scientific Corp., model PDC-002) treatment for 3min or UV-Ozone (Boekel Industries, Inc, model 135500) treatment for 30min were used to remove all kind of organic contaminations from the surfaces [211]. To minimize the recontamination of the surface after the last cleaning step (UV-Ozone cleaning or Oxygen Plasma Cleaning), the samples were placed and handled afterwards under a laminar flow-box (Skan USA-180). The protocol is highly dependent on the

substrate and on the experiment performed. If nothing else is stated, the following standard cleaning methods were used.

Titanium oxide

For already pre-cleaned TiO₂ samples (3x10 min ultrasonication in Toluene and isopropanol after sputter-coating, as described in 3.3), the final cleaning procedure before adsorption was fixed for all experiments to 3x10min ultrasonication in isopropanol and subsequent UV-Ozone cleaning for 30min. This protocol was used for all kind of TiO₂ cleaning, including the cleaning of TiO₂ coated biosensors, e.g. TInAS (c.f. 7.2.3).

Magnesium oxide

For magnesium oxide samples, a similar approach is used, but due to the less investigated substrate, no standard protocol can be given for the cleaning procedure. Typically the cleaning steps are comparable with the cleaning steps used for TiO₂ substrates, but neither the solvent for ultrasonication (3x10min) nor the use of which type of surface cleaning (UV-ozone for 30min vs. Oxygen plasma for 2min) were fixed within this research and were varied depending on the experiment. Further details on the solvent used and the cleaning process will always be stated in the results part in chapter 4.

Steel

The polished samples were ultrasonicated in isopropanol to suspend probably still remaining diamond polishing particles, dried with nitrogen gas and treated for 3min in oxygen plasma.

Table 7.5: Standard adsorption parameters for the different polymers and SAMs molecules used

Surface active compound	solvent	conc. [mg/ml]	adsorption time [h]
dodecyl phosphate	water / org. solvent	0.15	48
12-hydroxy dodecyl phosphate	water / org. solvent	0.15	48
hydrophilic poly(alkylphosphonate)s	water / org. solvent	0.5	20
hydrophobic poly(alkylphosphonate)s	org. solvent	0.5 - 2	20

7.9.3 Adsorption of amphiphilic adlayers

The cleaned substrates were directly immersed into a solution of the appropriate surface-active compound for 20h at room temperature. Concentration and solvent are depending on the polymer, SAM molecule and the experiment. Table 7.5 summarizes the standard adsorption parameters for the different surface-active molecules used.

Preparation of solutions

The solutions containing the surface-active compound were always prepared by weighing a rough amount of polymer and addition of a recalculated volume of the used solvent (water or organic solvent). In order to assure a good dissolution, the solution was sonicated. In case of subsequent experiments in aqueous solution, a bigger initial volume was prepared and aliquots of the samples were taken and stored in the freezer.

Adsorption protocol

All adsorption steps were prepared and performed in a laminar flow-box (Skan USA-180) . The samples were placed tilted in glass vials with the surface of interest directing towards the bottom of the vial to avoid gravitational effects by deposition

of possibly precipitated polymer onto the surface. The immersed samples were stored covered and wrapped in aluminum foil in the dark. The adsorption time and the solvents used for each polymer are summarized in 7.5. After adsorption, the samples were immersed for 15 min in the appropriate solvent used for adsorption, rinsed thoroughly with the same solvent and dried with nitrogen gas (N 5).

7.9.4 Adsorption of serum to metal oxide surfaces

Before exposure to reconstituted lyophilized human serum (150 μ l Precinorm U Control Serum dissolved in MQ water, Roche Diagnostics, Switzerland), the polymer-coated samples were immersed for 5min in 1 mL HEPES 2 buffer for rehydration of PEG chains under physiological conditions. After 20min exposure to 200 μ L serum (filtered with a 20 μ m filter), 1 mL HEPES 2 was added to the serum solution to dilute the concentration. The substrates were removed from the well and extensively rinsed with MQ water and subsequently dried under a stream of nitrogen and analyzed by surface characterization methods, mostly by VASE or XPS. The ability of the polymer coating to render the surfaces protein resistant was calculated from ellipsometry data, using the increase of adlayer thickness after serum adsorption. For certain cases these results were compared to values calculated from XPS data using the difference of nitrogen atomic percentage before and after the serum test.

Bibliography

Bibliography

- [1] HG Elias. *Macromolecules: Physical Structures and Properties*. Wiley-VCH, 2007. 1.1
- [2] L H. Sperling and George Odian. *Introduction to Physical Polymer Science, Fifth Edition*. Wiley-VCH, 2005. 1.1
- [3] W Brittain and S Minko. A structural definition of polymer brushes. *Journal of Polymer Science Part A: Polymer Chemistry*, 45(16):3505–3512, 2007. 1.1, 1.1
- [4] RC Advincula, editor. *Polymer brushes: synthesis, characterization, applications*. Wiley-VCH, 2004. 1.1, 1.1
- [5] EPK Currie, W Norde, and MAC Stuart. Tethered polymer chains: surface chemistry and their impact on colloidal and surface properties. *Advances in Colloid and Interface Science*, 100:205–265, 2003. 1.1, 1.1
- [6] A Halperin, M Tirrell, and TP Lodge. Tethered chains in polymer microstructures. *Adv Polym Sci*, 100:31–71, 1992. 1.1
- [7] YC Wang, XZ Du, WG Miao, and YQ Liang. Molecular recognition of cytosine- and guanine-functionalized nucleolipids in the mixed monolayers at the air-water interface and langmuir-blodgett films. *Journal of Physical Chemistry B*, 110(10):4914–4923, 2006. 1.1, 1.3.2
- [8] B Zhao and W Brittain. Polymer brushes: surface-immobilized macromolecules. *Prog Polym Sci*, 25(5):677–710, 2000. 1.1
- [9] RR Netz and D Andelman. Neutral and charged polymers at interfaces. *Phys Rep*, 380(1-2):1–95, 2003. 1.1
- [10] GS Grest. Normal and shear forces between polymer brushes. *Polymers in Confined Environments*, 138:149–183, 1999. 1.1

- [11] L Leger, E Raphael, and H Hervet. Surface-anchored polymer chains: Their role in adhesion and friction. *Polymers in Confined Environments*, 138:185–225, 1999. 1.1
- [12] JE Raynor, JR Capadona, DM Collard, TA Petrie, and A J Garcia. Polymer brushes and self-assembled monolayers: Versatile platforms to control cell adhesion to biomaterials (review). *Biointerphases*, 4(2):FA3–FA16, 2009. 1.1
- [13] BD Ratner. The engineering of biomaterials exhibiting recognition and specificity. *J Mol Recognit*, 9(5-6):617–625, 1996. 1.1
- [14] JA Hubbell. Synthetic biodegradable polymers for tissue engineering and drug delivery. *Curr Opin Solid St M*, 3(3):246–251, 1998. 1.1
- [15] R Tadmor, J Janik, J Klein, and L Fetters. Sliding friction with polymer brushes. *Physical review letters*, 91(11), 2003. 1.1
- [16] J Klein. Shear, friction, and lubrication forces between polymer-bearing surfaces. *Annual Review of Materials Science*, 26:581–612, 1996. 1.1
- [17] P Jain, GL Baker, and ML Bruening. Applications of polymer brushes in protein analysis and purification. *Annu Rev Anal Chem*, 2:387–408, 2009. 1.1
- [18] M Chiari, M Cretich, F Damin, G Di Carlo, and C Oldani. Advanced polymers for molecular recognition and sensing at the interface. *J Chromatogr B*, 866(1-2):89–103, 2008. 1.1
- [19] S Santer and J R uhe. Motion of nano-objects on polymer brushes. *Polymer*, 45:8279–8297, 2004. 1.1
- [20] F Zhou and W Huck. Surface grafted polymer brushes as ideal building blocks for “smart” surfaces. *Physical Chemistry Chemical Physics*, 8:3815–3823, 2006. 1.1
- [21] R Toomey and M Tirrell. Functional polymer brushes in aqueous media from self-assembled and surface-initiated polymers. *Annu Rev Phys Chem*, 59:493–517, 2008. 1.1
- [22] MAC Stuart, WTS Huck, J Genzer, M Mueller, C Ober, M Stamm, GB Sukhorukov, I Szleifer, VV Tsukruk, M Urban, F Winnik, S Zauscher, I Luzinov, and S Minko. Emerging applications of stimuli-responsive polymer materials. *Nat Mater*, 9(2):101–113, 2010. 1.1
- [23] H Nandivada, AM Ross, and J Lahann. Stimuli-responsive monolayers for biotechnology. *Prog Polym Sci*, 35(1-2):141–154, 2010. 1.1

- [24] S Dai, P Ravi, and KC Tam. Thermo- and photo-responsive polymeric systems. *Soft Matter*, 5(13):2513–2533, 2009. 1.1
- [25] PM Mendes. Stimuli-responsive surfaces for bio-applications. *Chem Soc Rev*, 37(11):2512–2529, 2008. 1.1
- [26] Y Ito, YS Park, and Y Imanishi. Visualization of critical pH-controlled gating of a porous membrane grafted with polyelectrolyte brushes. *Journal of the American Chemical Society*, 119(11):2739–2740, 1997. 1.1
- [27] Y Ito, S Nishi, YS Park, and Y Imanishi. Oxidoreduction-sensitive control of water permeation through a polymer brushes-grafted porous membrane. *Macromolecules*, 30(19):5856–5859, 1997. 1.1
- [28] SE Burke and CJ Barrett. pH-responsive properties of multilayered poly(l-lysine)/hyaluronic acid surfaces. *Biomacromolecules*, 4(6):1773–1783, 2003. 1.1, 3.3
- [29] C Padeste, P Farquet, C Potzner, and HH Solak. Nanostructured bio-functional polymer brushes. *J Biomat Sci-Polym E*, 17(11):1285–1300, 2006. 1.1
- [30] M Husemann, M Morrison, and D Benoit. Manipulation of surface properties by patterning of covalently bound polymer brushes. *J. Am. Chem. Soc.*, 122:1844–1845, 2000. 1.1
- [31] M Husseman, EE Malmstrom, M McNamara, M Mate, D Mecerreyes, DG Benoit, JL Hedrick, P Mansky, E Huang, TP Russell, and CJ Hawker. Controlled synthesis of polymer brushes by "living" free radical polymerization techniques. *Macromolecules*, 32(5):1424–1431, 1999. 1.3.1
- [32] S Edmondson, VL Osborne, and WTS Huck. Polymer brushes via surface-initiated polymerizations. *Chem Soc Rev*, 33(1):14–22, 2004. 1.3.1
- [33] F Bretagnol, M Lejeune, A Papadopoulou-Bouraoui, M Hasiwa, H Rauscher, G Ceccone, P Colpo, and F Rossi. Fouling and non-fouling surfaces produced by plasma polymerization of ethylene oxide monomer. *Acta Biomaterialia*, 2(2):165–172, 2006. 1.3.1
- [34] YLJ Wu, RB Timmons, JS Jen, and FE Molock. Non-fouling surfaces produced by gas phase pulsed plasma polymerization of an ultra low molecular weight ethylene oxide containing monomer. *Colloid Surface B*, 18(3-4):235–248, 2000. 1.3.1
- [35] N Hadjichristidis, S Pispas, and G Floudas. *Block copolymers: synthetic strategies, physical properties, and applications*. Wiley-VCH, 2003. 1.3.2

- [36] JH Lee, J Kopecek, and JD Andrade. Protein-resistant surfaces prepared by peo-containing block copolymer surfactants. *J Biomed Mater Res*, 23(3):351–68, 1989. [1.3.2](#)
- [37] A Ulman. *An Introduction to Ultrathin Organic Films: from Langmuir Blodgett to Self-assembly*. Academic Press, 1991. [1.3.2](#)
- [38] H Byrd, JK Pike, and DR Talham. Inorganic monolayers formed at an organic template - a langmuir-blodgett route to monolayer and multilayer films of zirconium octadecylphosphonate. *Chem Mater*, 5(5):709–715, 1993. [1.3.2](#)
- [39] WG Miao, XZ Du, and YQ Liang. Molecular recognition of nucleolipid monolayers of 1-(2-octadecyloxycarbonyl)ethyl)cytosine to guanosine at the air-water interface and langmuir-blodgett films. *Langmuir*, 19(13):5389–5396, 2003. [1.3.2](#)
- [40] H Dautzenber, W Jaeger, J Kötz, B Philipp, Ch Seidel, and D Stscherbina. *Polyelectrolytes - Formation, Characterization and Application*. Hanser Publishers, 1994. [1.3.2](#), [1.3.2](#), [1.3.2](#), [1.3.2](#)
- [41] EB Zhulina, OV Borisov, J van Male, and FAM Leermakers. Adsorption of tethered polyelectrolytes onto oppositely charged solid-liquid interfaces. *Langmuir*, 17(4):1277–1293, 2001. [1.3.2](#), [1.3.2](#)
- [42] NG Hoogeveen, MAC Stuart, and GJ Flier. Polyelectrolyte adsorption on oxides .2. reversibility and exchange. *Journal of Colloid and Interface Science*, 182(1):146–157, 1996. [1.3.2](#), [1.3.2](#), [1.3.2](#)
- [43] NG Hoogeveen, MAC Stuart, and GJ Flier. Polyelectrolyte adsorption on oxides .1. kinetics and adsorbed amounts. *Journal of Colloid and Interface Science*, 182(1):133–145, 1996. [1.3.2](#), [1.3.2](#), [1.3.2](#)
- [44] KE Bremmell, GJ Jameson, and S Biggs. Polyelectrolyte adsorption at the solid/liquid interface - interaction forces and stability. *Colloid Surface A*, 139(2):199–211, 1998. [1.3.2](#), [1.3.2](#)
- [45] A Shafir and D Andelman. Polyelectrolytes adsorption: Chemical and electrostatic interactions. *Phys. Rev. E*, 70:061804, 2003. [1.3.2](#), [1.3.2](#), [1.3.2](#)
- [46] G Decher. Fuzzy nanoassemblies: Toward layered polymeric multicomposites. *Science*, 277(5330):1232–1237, 1997. [1.3.2](#)
- [47] SE Burke and CJ Barrett. Acid-base equilibria of weak polyelectrolytes in multilayer thin films. *Langmuir*, 19(8):3297–3303, 2003. [1.3.2](#)

- [48] SE Burke and CJ Barrett. Controlling the physicochemical properties of weak polyelectrolyte multilayer films through acid/base equilibria. *Pure Appl Chem*, 76(7-8):1387–1398, 2004. [1.3.2](#)
- [49] M Erol, H Du, and S Sukhishvili. Control of specific attachment of proteins by adsorption of polymer layers. *Langmuir*, 22(26):11329–11336, 2006. [1.3.2](#)
- [50] JL Menchaca, B Jachimska, F Cuisinier, and E Perez. In situ surface structure study of polyelectrolyte multilayers by liquid-cell afm. *Colloid Surface A*, 222(1-3):185–194, 2003. [1.3.2](#)
- [51] SS Shiratori and MF Rubner. ph-dependent thickness behavior of sequentially adsorbed layers of weak polyelectrolytes. *Macromolecules*, 33(11):4213–4219, 2000. [1.3.2](#)
- [52] G Romet-Lemonne, J Daillant, P Guenoun, J Yang, and JW Mays. Thickness and density profiles of polyelectrolyte brushes: Dependence on grafting density and salt concentration. *Physical review letters*, 93(14):148301, 2004. [1.3.2](#)
- [53] ST Dubas and JB Schlenoff. Factors controlling the growth of polyelectrolyte multilayers. *Macromolecules*, 32(24):8153–8160, 1999. [1.3.2](#), [3.3](#)
- [54] A Fery, B Scholer, T Cassagneau, and F Caruso. Nanoporous thin films formed by salt-induced structural changes in multilayers of poly(acrylic acid) and poly(allylamine). *Langmuir*, 17(13):3779–3783, 2001. [1.3.2](#)
- [55] NA Kumar and C Seidel. Polyelectrolyte brushes with added salt. *Macromolecules*, 38(22):9341–9350, 2005. [1.3.2](#)
- [56] R Steitz, V Leiner, R Siebrecht, and R von Klitzing. Influence of the ionic strength on the structure of polyelectrolyte films at the solid/liquid interface. *Colloid Surface A*, 163(1):63–70, 2000. [1.3.2](#)
- [57] HL Tan, MJ McMurdo, GQ Pan, and PG Van Patten. Temperature dependence of polyelectrolyte multilayer assembly. *Langmuir*, 19(22):9311–9314, 2003. [1.3.2](#), [1.3.2](#)
- [58] I Borukhov, D Andelman, and H Orland. Scaling laws of polyelectrolyte adsorption. *Macromolecules*, 31(5):1665–1671, 1998. [1.3.2](#)
- [59] M Salomaki, IA Vinokurov, and J Kankare. Effect of temperature on the buildup of polyelectrolyte multilayers. *Langmuir*, 21(24):11232–11240, 2005. [1.3.2](#), [1.3.2](#)

- [60] J W Bullard and MJ Cima. Orientation dependence of the isoelectric point of tio₂ (rutile) surfaces. *Langmuir*, 22(24):10264–10271, 2006. 1.3.2
- [61] A Baumgartner and M Muthukumar. Effects of surface-roughness on adsorbed polymers. *J Chem Phys*, 94(5):4062–4070, 1991. 1.3.2
- [62] K Lowack and CA Helm. Molecular mechanisms controlling the self-assembly process of polyelectrolyte multilayers. *Macromolecules*, 31(3):823–833, 1998. 1.3.2, 1.3.2
- [63] GL Kenausis, J Voros, DL Elbert, NP Huang, R Hofer, L Ruiz-Taylor, M Textor, JA Hubbell, and ND Spencer. Poly(l-lysine)-g-poly(ethylene glycol) layers on metal oxide surfaces: Attachment mechanism and effects of polymer architecture on resistance to protein adsorption. *Journal of Physical Chemistry B*, 104(14):3298–3309, 2000. 1.3.2, 3.1, 3.3, 3.3
- [64] MS Wagner, S Pasche, DG Castner, and M Textor. Characterization of poly(l-lysine)-graft-poly(ethylene glycol) assembled monolayers on niobium pentoxide substrates using time-of-flight secondary ion mass spectrometry and multivariate analysis. *Analytical Chemistry*, 76(5):1483–1492, 2004. 1.3.2
- [65] WR Fawcett and TG Smagala. New developments in the theory of the diffuse double layer. *Langmuir*, 22(25):10635–10642, 2006. 1.3.2
- [66] D Chen and J Li. Interfacial design and functionization on metal electrodes through self-assembled monolayers. *Surface Science Reports*, 61:445–463, 2006. 1.3.2
- [67] JJ Gooding and DB Hibbert. The application of alkanethiol self-assembled monolayers to enzyme electrodes. *Trends in Analytical Chemistry*, 18:525–533, 1999. 1.3.2
- [68] D Mandler and I Turyan. Applications of self-assembled monolayers in electroanalytical chemistry. *Electroanalysis*, 8:207–13, 1996. 1.3.2
- [69] D Roy and J Fendler. Reflection and absorption techniques for optical characterization of chemically assembled nanomaterials. *Advanced Materials*, 16:479–508, 2004. 1.3.2
- [70] B Dordi, H Schonherr, and GJ Vancso. Reactivity in the confinement of self-assembled monolayers: Chain length effects on the hydrolysis of n-hydroxysuccinimide ester disulfides on gold. *Langmuir*, 19(14):5780–5786, 2003. 1.3.2

- [71] W Gao, L Dickinson, C Grozinger, FG Morin, and L Reven. Self-assembled monolayers of alkylphosphonic acids on metal oxides. *Langmuir*, 12(26):6429–6435, 1996. [1.3.2](#), [1.3.2](#), [3.3](#)
- [72] ES Gawalt, MJ Avaltroni, N Koch, and J Schwartz. Self-assembly and bonding of alkanephosphonic acids on the native oxide surface of titanium. *Langmuir*, 17(19):5736–5738, 2001. [1.3.2](#), [3.3](#)
- [73] JP Folkers, CB Gorman, PE Laibinis, S Buchholz, GM Whitesides, and RG Nuzzo. Self-assembled monolayers of long-chain hydroxamic acids on the native oxides of metals. *Langmuir*, 11(3):813–824, 1995. [1.3.2](#), [1.3.2](#)
- [74] S Ferretti, S Paynter, DA Russell, KE Sapsford, and DJ Richardson. Self-assembled monolayers: a versatile tool for the formulation of bio-surfaces. *TrAC-Trend Anal Chem*, 19(9):530–540, 2000. [1.3.2](#)
- [75] F Schreiber. Structure and growth of self-assembling monolayers. *Progress in Surface Science*, 65(5-8):151–257, 2000. [1.3.2](#), [1.3.2](#)
- [76] DH Lee, D Kim, T Oh, and M Cho. Phase state effect on adhesion behavior of self-assembled monolayers. *Langmuir*, 20(19):8124–8130, 2004. [1.3.2](#), [1.3.2](#)
- [77] DH Lee, T Oh, and K Cho. Combined effect of chain length and phase state on adhesion/friction behavior of self-assembled monolayers. *Journal of Physical Chemistry B*, 109(22):11301–11306, 2005. [1.3.2](#)
- [78] DK Schwartz. Mechanisms and kinetics of self-assembled monolayer formation. *Annual Review of Physical Chemistry*, 52:107–137, 2001. [1.3.2](#), [1.3.2](#)
- [79] CD Bain, EB Troughton, YT Tao, J Evall, GM Whitesides, and RG Nuzzo. Formation of monolayer films by the spontaneous assembly of organic thiols from solution onto gold. *Journal of the American Chemical Society*, 111(1):321–335, 1989. [1.3.2](#)
- [80] S Marcinko and AY Fadeev. Hydrolytic stability of organic monolayers supported on tio₂ and zro₂. *Langmuir*, 20(6):2270–2273, 2004. [1.3.2](#)
- [81] F Schreiber. Organic molecular beam deposition: Growth studies beyond the first monolayer. *Phys Status Solidi A*, 201(6):1037–1054, 2004. [1.3.2](#)
- [82] F Tao and SL Bernasek. Understanding odd-even effects in organic self-assembled monolayers. *Chemical Reviews*, 107(5):1408–1453, 2007. [1.3.2](#)

- [83] Frank Schreiber. Self-assembled monolayers: from simple model systems to bio-functionalized interfaces. *Journal of Physics: Condensed Matter*, 16(28):R881–R900, 2004. [1.3.2](#), [1.3.2](#)
- [84] DM Spori, NV Venkataraman, SGP Tosatti, F Durmaz, ND Spencer, and S Zuercher. Influence of alkyl chain length on phosphate self-assembled monolayers. *Langmuir*, 23(15):8053–8060, 2007. [1.3.2](#), [3.3](#), [3.3](#), [3.3](#), [4.5.1](#), [4.5.1](#), [A.4.3](#)
- [85] KV Wolf, DA Cole, and SL Bernasek. High-resolution tof-sims study of varying chain length self-assembled monolayer surfaces. *Analytical Chemistry*, 74(19):5009–5016, 2002. [1.3.2](#)
- [86] O Dannenberger, K Weiss, HJ Himmel, B Jager, M Buck, and C Woll. An orientation analysis of differently endgroup-functionalised alkanethiols adsorbed on au substrates. *Thin solid films*, 307(1-2):183–191, 1997. [1.3.2](#)
- [87] N Faucheux, R Schweiss, K Lutzow, C Werner, and T Groth. Self-assembled monolayers with different terminating groups as model substrates for cell adhesion studies. *Biomaterials*, 25(14):2721–2730, 2004. [1.3.2](#)
- [88] L Ruiz, JG Hilborn, D Leonard, and HJ Mathieu. Synthesis, structure and surface dynamics of phosphorylcholine functional biomimicking polymers. *Biomaterials*, 19(11-12):987–998, 1998. [1.3.2](#)
- [89] M Franco, PF Nealey, S Campbell, AI Teixeira, and CJ Murphy. Adhesion and proliferation of corneal epithelial cells on self-assembled monolayers. *J Biomed Mater Res*, 52(2):261–269, 2000. [1.3.2](#)
- [90] N Adden, LJ Gamble, DG Castner, A Hoffmann, G Gross, and H Menzel. Phosphonic acid monolayers for binding of bioactive molecules to titanium surfaces. *Langmuir*, 22(19):8197–8204, 2006. [1.3.2](#)
- [91] RG Chapman, E Ostuni, L Yan, and GM Whitesides. Preparation of mixed self-assembled monolayers (sams) that resist adsorption of proteins using the reaction of amines with a sam that presents interchain carboxylic anhydride groups. *Langmuir*, 16(17):6927–6936, 2000. [1.3.2](#)
- [92] L Vyklicky, A Afzali-Ardakani, and CR Kagan. Self-assembly and oligomerization of alkyne-terminated molecules on metal and oxide surfaces. *Langmuir*, 21(25):11574–11577, 2005. [1.3.2](#)
- [93] V Kitaev, M Seo, ME McGovern, Y Huang, and E Kumacheva. Mixed monolayers self-assembled on mica surface. *Langmuir*, 17(14):4274–4281, 2001. [1.3.2](#)

- [94] PE Laibinis, MA Fox, JP Folkers, and GM Whitesides. Comparisons of self-assembled monolayers on silver and gold - mixed monolayers derived from $\text{hs}(\text{ch}_2)_{21}\text{x}$ and $\text{hs}(\text{ch}_2)_{10}\text{y}$ ($\text{x}, \text{y} = \text{ch}_3, \text{ch}_2\text{oh}$) have similar properties. *Langmuir*, 7(12):3167–3173, 1991. [1.3.2](#)
- [95] J Sagiv. Organized monolayers by adsorption .1. formation and structure of oleophobic mixed monolayers on solid-surfaces. *Journal of the American Chemical Society*, 102(1):92–98, 1980. [1.3.2](#)
- [96] S Morgenthaler, SW Lee, S Zuercher, and ND Spencer. A simple, reproducible approach to the preparation of surface-chemical gradients. *Langmuir*, 19(25):10459–10462, 2003. [1.3.2](#), [1.5.1](#)
- [97] E Beurer, NV Venkataraman, ARossi, F Bachmann, R Engeli, and ND Spencer. Orthogonal, three-component, alkanethiol-based surface-chemical gradients on gold. *Langmuir*, 26(11):8392–8399, 2010. [1.3.2](#)
- [98] ML Sushko and AL Shluger. Dipole-dipole interactions and the structure of self-assembled monolayers. *Journal of Physical Chemistry B*, 111(16):4019–4025, 2007. [1.3.2](#)
- [99] M Zwahlen, S Tosatti, M Textor, and G Hahner. Orientation in methyl- and hydroxyl-terminated self-assembled alkanephosphate monolayers on titanium oxide surfaces investigated with soft x-ray absorption. *Langmuir*, 18(10):3957–3962, 2002. [1.3.2](#), [3.3](#), [3.3](#)
- [100] NT Flynn, TNT Tran, MJ Cima, and R LANGER. Long-term stability of self-assembled monolayers in biological media. *Langmuir*, 19(26):10909–10915, 2003. [1.3.2](#)
- [101] L Feuz, P Strunz, T Geue, M Textor, and O Borisov. Conformation of poly(l-lysine)-graft-poly(ethylene glycol) molecular brushes in aqueous solution studied by small-angle neutron scattering. *Eur Phys J E*, 23(3):237–245, Jan 2007. [1.5.1](#)
- [102] L Feuz, FAM Leermakers, M Textor, and O Borisov. Adsorption of molecular brushes with polyelectrolyte backbones onto oppositely charged surfaces: A self-consistent field theory. *Langmuir*, 24(14):7232–7244, 2008. [1.5.1](#)
- [103] S Lee and ND Spencer. Adsorption properties of poly(l-lysine)-graft-poly(ethylene glycol) (pll-g-peg) at a hydrophobic interface: Influence of tribological stress, ph, salt concentration, and polymer molecular weight. *Langmuir*, 24(17):9479–9488, 2008. [1.5.1](#)

- [104] R Heuberger, G Sukhorukov, J Voros, M Textor, and H Mohwald. Biofunctional polyelectrolyte multilayers and microcapsules: Control of non-specific and bio-specific protein adsorption. *Adv Funct Mater*, 15(3):357–366, 2005. [1.5.1](#)
- [105] S Pasche, M Textor, L Meagher, ND Spencer, and HJ Griesser. Relationship between interfacial forces measured by colloid-probe atomic force microscopy and protein resistance of poly(ethylene glycol)-grafted poly(l-lysine) adlayers on niobia surfaces. *Langmuir*, 21(14):6508–6520, 2005. [1.5.1](#), [3.3](#)
- [106] S Pasche, J Voros, HJ Griesser, ND Spencer, and M Textor. Effects of ionic strength and surface charge on protein adsorption at pegylated surfaces. *Journal of Physical Chemistry B*, 109(37):17545–17552, 2005. [1.5.1](#), [3.3](#)
- [107] TM Blattler, S Pasche, M Textor, and HJ Griesser. High salt stability and protein resistance of poly(l-lysine)-g-poly(ethylene glycol) copolymers covalently immobilized via aldehyde plasma polymer interlayers on inorganic and polymeric substrates. *Langmuir*, 22(13):5760–5769, 2006. [1.5.1](#)
- [108] R Michel, S Pasche, M Textor, and DG Castner. Influence of peg architecture on protein adsorption and conformation. *Langmuir*, 21(26):12327–12332, 2005. [1.5.1](#)
- [109] M Kosmulski. *Chemical Properties of Material Surfaces*. Marcel Dekker, 2001. [1.5.1](#), [3.2](#)
- [110] NP Huang, J Voros, SM De Paul, M Textor, and ND Spencer. Biotin-derivatized poly(l-lysine)-g-poly(ethylene glycol): A novel polymeric interface for bioaffinity sensing. *Langmuir*, 18(1):220–230, 2002. [1.5.1](#)
- [111] M Schuler, DW Hamilton, TP Kunzler, CM Sprecher, M de Wild, DM Brunette, M Textor, and SGP Tosatti. Comparison of the response of cultured osteoblasts and osteoblasts outgrown from rat calvarial bone chips to nonfouling krsr and fhrrika-peptide modified rough titanium surfaces. *J Biomed Mater Res B*, 91B(2):517–527, 2009. [1.5.1](#)
- [112] M Schuler, G Owen, D Hamilton, M Dewild, M Textor, D Brunette, and S Tosatti. Biomimetic modification of titanium dental implant model surfaces using the rgdsp-peptide sequence: A cell morphology study. *Biomaterials*, 27(21):4003–4015, 2006. [1.5.1](#)
- [113] RR Maddikeri, S Tosatti, M Schuler, S Chessari, M Textor, R. G Richards, and LG Harris. Reduced medical infection related bacterial strains adhesion

- on bioactive rgd modified titanium surfaces: A first step toward cell selective surfaces. *J Biomed Mater Res A*, 84A(2):425–435, 2008. [1.5.1](#)
- [114] MR Dusseiller, D Schlaepfer, M Koch, R Kroschewski, and M Textor. An inverted microcontact printing method on topographically structured polystyrene chips for arrayed micro-3-d culturing of single cells. *Biomaterials*, 26(29):5917–5925, 2005. [1.5.1](#)
- [115] M Ochsner, MR Dusseiller, HM Grandin, S Luna-Morris, M Textor, V Vogel, and M L Smith. Micro-well arrays for 3d shape control and high resolution analysis of single cells. *Lab Chip*, 7(8):1074–1077, 2007. [1.5.1](#)
- [116] S Morgenthaler, C Zink, B Staedler, J Voeroes, S Lee, ND Spencer, and S G. P Tosatti. Poly(l-lysine)-grafted-poly(ethylene glycol)-based surface-chemical gradients. preparation, characterization, and first applications. *Biointerphases*, 1(4):156–165, 2006. [1.5.1](#)
- [117] S Morgenthaler, C Zink, and ND Spencer. Surface-chemical and -morphological gradients. *Soft Matter*, 4(3):419–434, 2008. [1.5.1](#)
- [118] D Falconnet, D Pasqui, S Park, R Eckert, H Schiff, J Gobrecht, R Barbucci, and M Textor. A novel approach to produce protein nanopatterns by combining nanoimprint lithography and molecular self-assembly. *Nano Lett*, 4(10):1909–1914, 2004. [1.5.1](#)
- [119] W Franks, S Tosatti, F Heer, P Seif, M Textor, and A Hierlemann. Patterned cell adhesion by self-assembled structures for use with a cmos cell-based biosensor. *Biosens Bioelectron*, 22(7):1426–1433, 2007. [1.5.1](#)
- [120] JW Lussi, D Falconnet, JA Hubbell, M Textor, and G Csucs. Pattern stability under cell culture conditions - a comparative study of patterning methods based on pll-g-peg background passivation. *Biomaterials*, 27(12):2534–2541, 2006. [1.5.1](#)
- [121] V Saravia, S Kupcu, M Nolte, C Huber, D Pum, A Fery, U. B Sleytr, and J. L Toca-Herrera. Bacterial protein patterning by micro-contact printing of pll-g-peg. *J Biotechnol*, 130(3):247–252, 2007. [1.5.1](#)
- [122] CS Tang, P Schmutz, S Petronis, M Textor, B Keller, and J Voros. Locally addressable electrochemical patterning technique (laept) applied to poly (l-lysine)-graft-poly(ethylene glycol) adlayers on titanium and silicon oxide surfaces. *Biotechnol Bioeng*, 91(3):285–295, 2005. [1.5.1](#)

- [123] R Marie, JP Beech, J Voeroes, JO Tegenfeldt, and F Hook. Use of pll-g-peg in micro-fluidic devices for localizing selective and specific protein binding. *Langmuir*, 22(24):10103–10108, 2006. [1.5.1](#)
- [124] C Perrino, S Lee, SW Choi, A Maruyama, and ND Spencer. A biomimetic alternative to poly(ethylene glycol) as an antifouling coating: Resistance to nonspecific protein adsorption of poly(l-lysine)-graft-dextran. *Langmuir*, 24(16):8850–8856, 2008. [1.5.1](#), [3.1](#)
- [125] R Konradi, B Pidhatika, A Muehlebach, and M Textor. Poly-2-methyl-2-oxazoline: A peptide-like polymer for protein-repellent surfaces. *Langmuir*, 24(3):613–616, 2008. [1.5.1](#), [3.1](#)
- [126] B Pidhatika, J Moeller, V Vogel, and R Konradi. Nonfouling surface coatings based on poly(2-methyl-2-oxazoline). *Chimia*, 62(4):264–269, 2008. [1.5.1](#), [3.1](#)
- [127] S Lee, M Mueller, R Heeb, S Zuercher, S Tosatti, M Heinrich, F Amstad, S Pechmann, and N. D Spencer. Self-healing behavior of a polyelectrolyte-based lubricant additive for aqueous lubrication of oxide materials. *Tribol Lett*, 24(3):217–223, 2006. [1.5.1](#)
- [128] S Lee and ND Spencer. Poly(l-lysine)-graft-poly(ethylene glycol): a versatile aqueous lubricant additive for tribosystems involving thermoplastics. *Lubr Sci*, 20(1):21–34, 2008. [1.5.1](#)
- [129] S Lee, S Zuercher, A Dorcier, GS Luengo, and ND Spencer. Adsorption and lubricating properties of poly(l-lysine)-graft-poly(ethylene glycol) on human-hair surfaces. *Acs Appl Mater Inter*, 1(9):1938–1945, 2009. [1.5.1](#)
- [130] SS Perry, X Yan, FT Limpoco, S Lee, M Mueller, and ND Spencer. Tribological properties of poly(l-lysine)-graft-poly(ethylene glycol) films: Influence of polymer architecture and adsorbed conformation. *Acs Appl Mater Inter*, 1(6):1224–1230, 2009. [1.5.1](#)
- [131] XP Yan, SS Perry, ND Spencer, S Pasche, SM De Paul, M Textor, and MS Lim. Reduction of friction at oxide interfaces upon polymer adsorption from aqueous solutions. *Langmuir*, 20(2):423–428, 2004. [1.5.1](#)
- [132] S Saxer, C Portmann, S Tosatti, K Gademann, S Zuercher, and M Textor. Surface assembly of catechol-functionalized poly(l-lysine)-graft-poly(ethylene glycol) copolymer on titanium exploiting combined electrostatically driven self-organization and biomimetic strong adhesion. *Macromolecules*, 43(2):1050–1060, 2010. [1.5.1](#), [1.5.2](#)

- [133] V Zoulalian. *Functionalization of titanium oxide surfaces by means of poly(alkyl-phosphonate) polymers*. PhD thesis, ETH Zurich No 17618, 2008. [1.5.2](#), [3.3](#), [3.6](#)
- [134] Firat Durmaz. *A Modular Approach to Functional Self-Assembled Monolayers*. PhD thesis, ETH Zurich No 16942, 2006. [1.5.2](#), [2.9.1](#)
- [135] V Zoulalian, S Monge, S Zuercher, M Textor, J. J Robin, and S Tosatti. Functionalization of titanium oxide surfaces by means of poly(alkyl-phosphonates). *Journal of Physical Chemistry B*, 110(51):25603–25605, 2006. [1.5.2](#), [3.3](#), [3.6](#)
- [136] V Zoulalian, S Zuercher, S Tosatti, M Textor, S Monge, and JJ Robin. Self-assembly of poly(ethylene glycol)-poly(alkyl phosphonate) terpolymers on titanium oxide surfaces: Synthesis, interface characterization, investigation of nonfouling properties, and long-term stability. *Langmuir*, 26(1):74–82, 2010. [1.5.2](#), [3.3](#), [3.6](#)
- [137] S Lord, S Sheiko, I LaRue, and H Lee. Tadpole conformation of gradient polymer brushes. *Macromolecules*, 37:4235–4240, 2004. [1.5.2](#)
- [138] N Liu and WE Baker. Reactive polymers for blend compatibilization. *Advances in Polymer Technology*, 11(4):249–262, 1992. [2.1](#), [2.1](#)
- [139] JMJ Frechet, GD Darling, S Ituno, PZ Lu, MV Demeftahi, and WA Rolls. Reactive polymers - design considerations, novel preparations and selected applications in organic-chemistry. *Pure Appl Chem*, 60(3):353–364, 1988. [2.1](#), [2.1](#)
- [140] G Manecke. Reactive polymers and their use for the preparation of antibody and enzyme resins. *Pure Appl. Chem*, 2–4:507–520, 1962. [2.1](#)
- [141] J Lahann, M Balcells, H Lu, and T Rodon. . . . Reactive polymer coatings: a first step toward surface engineering of microfluidic devices. *Analytical Chemistry*, 75(9):2117–2122, 2003. [2.1](#)
- [142] J Lahann, M Balcells, T Rodon, J Lee, I Choi, KF Jensen, and R Langer. Reactive polymer coatings: A platform for patterning proteins and mammalian cells onto a broad range of materials. *Langmuir*, 18(9):3632–3638, 2002. [2.1](#), [2.1](#)
- [143] MN Tahir, M Eberhardt, P Theato, S Faiss, A Janshoff, T Gorelik, U Kolb, and W Tremel. Reactive polymers: A versatile toolbox for the immobilization of functional molecules on tio2 nanoparticles. *Angew Chem Int Edit*, 45(6):908–912, 2006. [2.1](#), [2.1](#)

- [144] D Kessler, PJ Roth, and P Theato. Reactive surface coatings based on polysilsesquioxanes: controlled functionalization for specific protein immobilization. *Langmuir*, 25(17):10068–10076, 2009. [2.1](#), [2.1](#)
- [145] D Beyer, TM Bohanon, W Knoll, H Ringsdorf, G Elender, and E Sackmann. Surface modification via reactive polymer interlayers. *Langmuir*, 12(10):2514–2518, 1996. [2.1](#), [2.1](#)
- [146] D Kessler and P Theato. Reactive surface coatings based on polysilsesquioxanes: Defined adjustment of surface wettability. *Langmuir*, 25(24):14200–14206, 2009. [2.1](#), [2.2](#), [2.1](#)
- [147] B O’Shaughnessy and D Vavylonis. Reactive polymer interfaces: How reaction kinetics depend on reactivity and density of chemical groups. *Macromolecules*, 32(6):1785–1796, 1999. [2.1](#)
- [148] GCM Steffens, L Nothdurft, G Buse, H Thissen, H Hocker, and D Klee. High density binding of proteins and peptides to poly(d,l-lactide) grafted with polyacrylic acid. *Biomaterials*, 23(16):3523–3531, 2002. [2.1](#)
- [149] P Theato, J Kim, and JC Le. Controlled radical polymerization of active ester monomers: Precursor polymers for highly functionalized materialsk. *Macromolecules*, 37(15):5475–5478, 2004. [2.2](#), [2.1](#)
- [150] M. Eberhardth and P Théato. Raft polymerization of pentafluorophenyl methacrylate: Preparation of reactive linear diblock copolymers. *Macromolecular rapid Communications*, 26(18):1488–1493, 2005. [2.2](#), [2.1](#)
- [151] P Theato. Synthesis of well-defined polymeric activated esters. *Journal of Polymer Science Part A: Polymer Chemistry*, 46(20):6677–6687, 2008. [2.2](#), [2.1](#)
- [152] ER Kenawy, FI Abdel-Hay, AERR El-Shanshoury, and MH El-Newehy. Biologically active polymers.v. synthesis and antimicrobial activity of modified poly(glycidyl methacrylate-co-2-hydroxyethyl methacrylate) derivatives with quaternary ammonium and phosphonium salts. *J Polym Sci Pol Chem*, 40(14):2384–2393, 2002. [2.1](#)
- [153] S Lee and OO Park. Preparation of poly(butylene terephthalate)/oxazoline containing polystyrene graft copolymer through melt-blending and their application as a compatibilizer in polycarbonate/polystyrene blend. *Polymer*, 42(15):6661–6668, 2001. [2.1](#)
- [154] LD Taylor, HS Kolesinski, AC Mehta, L Locatell, and PS Larson. Synthesis of poly(4,4-dimethyl-2-vinyl-5-oxazolone) an interesting material for preparing polymeric agents. *Makromol Chem-Rapid*, 3(11):779–782, 1982. [2.1](#)

- [155] Lee G Stanek, Steven M Heilmann, and William B Gleason. Synthesis and characterization of copolymers containing n,n-dimethylacrylamide and 2-vinyl-4,4'-dimethylazlactone. *Polym. Bull.*, 55(6):393–402, 2005. [2.1](#)
- [156] D Fournier, S Pascual, V Montembault, D M Haddleton, and L Fontaine. Well-defined azlactone-functionalized (co)polymers on a solid support: Synthesis via supported living radical polymerization and application as nucleophile scavengers. *J Comb Chem*, 8(4):522–530, 2006. [2.1](#)
- [157] A conix and G Smets. Ring opening in lactam polymers. *J Polym Sci*, 15(79):221–229, 1955. [2.1](#)
- [158] Wolfgang H Binder and Robert Sachsenhofer. 'click' chemistry in polymer and materials science. *Macromol Rapid Comm*, 28(1):15–54, 2007. [2.1](#)
- [159] Wolfgang H Binder and Robert Sachsenhofer. 'click' chemistry in polymer and material science: An update. *Macromol Rapid Comm*, 29(12-13):952–981, 2008. [2.1](#)
- [160] M Davies, J Dawkins, and D Hourston. Radical copolymerization of maleic anhydride and substituted styrenes by reversible addition-fragmentation chain transfer (raft) polymerization. *Polymer*, 46(6):1739–1753, 2005. [2.2](#)
- [161] E Chernikova, P Terpugova, C Bui, and B Charleux. Effect of comonomer composition on the controlled free-radical copolymerization of styrene and maleic anhydride by reversible addition-fragmentation chain transfer (raft). *Polymer*, 44(15):4101–4107, 2003. [2.2](#)
- [162] MS Montaudo. Determination of the compositional distribution and compositional drift in styrene/maleic anhydride copolymers. *Macromolecules*, 34(9):2792–2797, 2001. [2.2](#)
- [163] ES Park, MN Kim, IM Lee, HS Lee, and JS Yoon. Living radical copolymerization of styrene/maleic anhydride. *J Polym Sci Pol Chem*, 38(12):2239–2244, 2000. [2.2](#)
- [164] U Schmidt, S Zschoche, and C Werner. Modification of poly(octadecene-alt-maleic anhydride) films by reaction with functional amines. *Journal of Applied Polymer Science*, 87(8):1255–1266, 2003. [2.2](#)
- [165] M Hesse, H Meier, and B Zeeh. *Spektroskopische Methoden in der organischen Chemie*. Thieme, 1987. [2.2](#), [2.3](#)
- [166] S Pasche. *Mechanisms of protein resistance of adsorbed PEG-graft copolymers*. PhD thesis, ETH Zurich No 15712, 2004. [2.6.1](#), [3.4.3](#)

- [167] A Michaelis and R Kaehne. Ueber das verhalten der jodalkyle gegen die sogen. phosphorigsäureester oder o-phosphine. *Berichte der deutschen chemischen Gesellschaft*, 31(1):1048–1055, 1898. [2.9.1](#)
- [168] B A Arbusow. Michaelis-arbusow- und perkow-reaktionen. *Pure and Applied Chemistry*, 9(2):307–336, 1964. [2.9.1](#)
- [169] HSP Rao and P Siva. Facile reduction of azides with sodium borohydride / copper (ii) sulphate system. *Synthetic Comm.*, 24(4):549–555, 1994. [2.9.1](#)
- [170] CE McKenna, MT Higa, NH Cheung, and MC McKenna. Facile dealkylation of phosphonic acid dialkyl esters by bromotrimethylsilane. *Tetrahedron Letters*, (2):155–158, 1977. [2.9.2](#), [2.9.3](#)
- [171] BD Ratner, AS Hoffman, FJ Schoen, and JE Lemons, editors. *Biomaterials Science*. Academic Press, 2004. [3.1.1](#), [3.1.2](#), [3.2](#)
- [172] O Goktekin N Peeters J Verbist M Bosiers K Deloose B Heublein R Rohde V Kasese Cs Ilsley R Erbel C DiMario, H Griffiths. Drug-eluting bioabsorbable magnesium stent. *Journal of Interventional Cardiology*, 17(6):391–395, 2004. [3.1.1](#)
- [173] DG Castner and BD Ratner. Biomedical surface science: Foundations to frontiers. *Surface Science*, 500(1-3):28–60, 2002. [3.1.1](#), [3.1](#)
- [174] AK Dillow and LM Lowman, editors. *Biomimetic Materials and Design: Biointerfacial Strategies, Tissue Engineering and Targeted Drug Delivery*. Marcel Dekker, 2004. [3.1.1](#)
- [175] JM Harris, editor. *Poly(ethylene glycol) Chemistry - Biotechnical and biomedical applications*. Plenum Press, 1992. [3.1.1](#), [3.1.2](#), [3.1.2](#)
- [176] JM Harris. *Poly(ethylene glycol) : chemistry and biological applications*. Plenum Press, 1997. [3.1](#), [3.1.2](#)
- [177] KL Prime and GM Whitesides. Adsorption of proteins onto surfaces containing end-attached oligo(ethylene oxide): a model system using self-assembled monolayers. *Journal of the American Chemical Society*, 115:10714, 1993. [3.1](#)
- [178] JT Li and KD Caldwell. Plasma protein interactions with pluronic(tm)-treated colloids. *Colloid Surface B*, 7(1-2):9–22, 1996. [3.1](#)
- [179] M Morra and C Cassinelli. Surface studies on a model cell-resistant system. *Langmuir*, 15(13):4658–4663, 1999. [3.1](#)

- [180] LM Dai, HAW StJohn, JJ Bi, P Zientek, RC Chatelier, and HJ Griesser. Biomedical coatings by the covalent immobilization of polysaccharides onto gas-plasma-activated polymer surfaces. *Surface and Interface Analysis*, 29(1):46–55, 2000. [3.1](#)
- [181] Y Iwasaki, S Sawada, N Nakabayashi, G Khang, HB Lee, and K Ishihara. The effect of the chemical structure of the phospholipid polymer on fibronectin adsorption and fibroblast adhesion on the gradient phospholipid surface. *Biomaterials*, 20(22):2185–2191, 1999. [3.1](#)
- [182] LA Cantarero, JE Butler, and JW Osborne. The adsorptive characteristics of proteins for polystyrene and their significance in solid-phase immunoassays. *Analytical Biochemistry*, 105(2):375–382, 1980. [3.1](#)
- [183] GP Lopez, BD Ratner, RJ Rapoza, and TA Horbett. Plasma deposition of ultrathin films of poly(2-hydroxyethyl methacrylate) - surface-analysis and protein adsorption measurements. *Macromolecules*, 26(13):3247–3253, 1993. [3.1](#), [3.1.2](#)
- [184] WR Gombotz, W Guanghai, TA Horbett, and AS Hoffman. Protein adsorption to poly(ethylene oxide) surfaces. *Journal of Biomedical Materials Research*, 25:1547 – 1562, 2004. [3.1.2](#)
- [185] B Herren, J Van Alstine, R Snyder, S Shafer, and J Harris. Control of electroosmosis in coated quartz capillaries. *Journal of Colloid and Interface Science*, 115:46–55, 1987. [3.1.2](#)
- [186] JM J.M. Harris. Laboratory synthesis of polyethylene glycol derivatives. *Journal of macromolecular science. C, Reviews in macromolecular chemistry and physics*, C25:325, 1985. [3.1.2](#)
- [187] D Leckband, S Sheth, and A Halperin. Grafted poly(ethylene oxide) brushes as nonfouling surface coatings. *Journal of Biomaterials Science Polymer Edition*, 10(10):1125–1147, 1999. [3.1.2](#)
- [188] A Kidane, GC Lant, S Jo, and K Park. Surface modification with pectin-containing triblock copolymer for improved biocompatibility: in vitro and ex vitro studies. *Journal of Biomaterials Science Polymer Edition*, 10(10):1089–1105, 1999. [3.1.2](#)
- [189] V Panchalingam, B Poon, HH Huo, CR Savage, RB Timmons, and RC Eberhart. Molecular surface tailoring of biomaterials via pulsed rf plasma discharges. *Journal of Biomaterial Science Polymer Edition*, 5:131–45., 1993. [3.1.2](#)

- [190] NA Alcantar, ES Aydil, and JN Israelachvili. Polyethylene glycol-coated biocompatible surfaces. *Journal of Biomedical Materials Research*, 51(3), 2000. [3.1.2](#)
- [191] SJ Sofia, V Premnath, and EW Merrill. Poly(ethylene oxide) grafted to silicon surfaces: Grafting density and protein adsorption. *Macromolecules*, 31(15):5059–5070, 1998. [3.1.2](#)
- [192] J Israelachvili. The different faces of poly(ethylene glycol). *Proceedings of the National Academy of Sciences*, 94(16):8378–8379, 1997. [3.1.2](#)
- [193] SI Jeon, JH Lee, JD Andrade, and PG De Gennes. Protein-surface interactions in the presence of polyethylene oxide i. *Journal of Colloid and Interface Science*, 142:149–158, 1991. [3.1.2](#)
- [194] M Malmsten, K Emoto, and JM Van Alstine. Effect of chain density on inhibition of protein adsorption by poly(ethylene glycol) based coatings. *Journal of Colloid and Interface Science*, 202:507–515, 1998. [3.1.2](#)
- [195] WR Gombotz, W Guanghai, TA Horbett, and AS Hoffman. Protein adsorption to poly(ethylene oxide) surfaces. *Journal of Biomedical Materials Research*, 25(12):1547–1562, 1991. [3.1.2](#)
- [196] RS Kane, P Deschatelets, and GM Whitesides. Kosmotropes form the basis of protein-resistant surfaces. *Langmuir*, 19(6):2388–2391, 2003. [3.1.2](#)
- [197] SI Jeon and JD Andrade. Protein-surface interactions in the presence of polyethylene oxide ii. *Journal of Colloid and Interface Science*, 1:159–166, 1991. [3.1.2](#)
- [198] DM Brunette. *Titanium in medicine: material science, surface science, engineering, biological responses, and medical applications*. Springer, 2001. [3.2](#)
- [199] GLütjering and JC Williams. *Titanium*. Springer, 2007. [3.2](#)
- [200] P Tengvall and Ingemar Lundström. Physico-chemical considerations of titanium as a biomaterial. *Clinical materials*, 9(2):115–134, 1992. [3.2](#)
- [201] SG Steinemann. Titanium - the material of choice? *Periodontol 2000*, 17:7–21, 1998. [3.2](#)
- [202] A Ashrafizadeh and F Ashrafizadeh. Structural features and corrosion analysis of thermally oxidized titanium. *J Alloy Compd*, 480(2):849–852, 2009. [3.2](#)

- [203] M Browne and PJ Gregson. Surface modification of titanium-alloy implants. *Biomaterials*, 15(11):894–898, 1994. 3.2
- [204] HP Boehm. Acidic and basic properties of hydroxylated metal-oxide surfaces. *Discuss Faraday Soc*, (52):264, 1971. 3.2
- [205] Andrey A Levchenko, Guangshe Li, Juliana Boerio-Goates, Brian F Woodfield, and Alexandra Navrotsky. Tio2 stability landscape: Polymorphism, surface energy, and bound water energetics. *Chem Mater*, 18(26):6324–6332, 2006. 3.2
- [206] EL Bullock, L Patthey, and SG Steinemann. Clean and hydroxylated rutile tio2(110) surfaces studied by x-ray photoelectron spectroscopy. *Surf Sci*, 352:504–510, 1996. 3.2
- [207] A Fujishima and XT Zhang. Titanium dioxide photocatalysis: present situation and future approaches. *Cr Chim*, 9(5-6):750–760, 2006. 3.2
- [208] A Fujishima, X Zhang, and DA Tryk. Tio2 photocatalysis and related surface phenomena. *Surf Sci Rep*, 63(12):515–582, 2008. 3.2
- [209] A Mills and S LeHunte. An overview of semiconductor photocatalysis. *J Photoch Photobio A*, 108(1):1–35, 1997. 3.2
- [210] N Sakai, R Wang, A Fujishima, T Watanabe, and K Hashimoto. Effect of ultrasonic treatment on highly hydrophilic tio2 surfaces. *Langmuir*, 14(20):5918–5920, 1998. 3.2
- [211] C Scheuerlein and M Taborelli. The assessment of metal surface cleanliness by xps. *Appl Surf Sci*, 252(12):4279–4288, Jan 2006. 3.2, 7.9.2
- [212] M Rodenstein. *Surface-chemical gradients and patterns on metal oxide substrates*. PhD thesis, ETH Zurich, No 19224, 2010. 3.3, 3.3
- [213] S Tosatti. *Functionalized titanium surfaces for biomedical applications*. PhD thesis, ETH Zurich, No 15095, 2003. 3.3, 3.3
- [214] W Hartung. *Aqueous lubrication of ceramics by means of brush-forming graft copolymers*. PhD thesis, ETH Zurich, No 18428, 2009. 3.3
- [215] S Tosatti, R Michel, M Textor, and ND Spencer. Self-assembled monolayers of dodecyl and hydroxy-dodecyl phosphates on both smooth and rough titanium and titanium oxide surfaces. *Langmuir*, 18(9):3537–3548, 2002. 3.3, 3.3
- [216] D Andelman and J Joanny. Polyelectrolyte adsorption. *Comptes Rendus de l’Academie des Sciences Series IV Physics*, 2000. 3.3

- [217] A Pina, E Nakache, B Feret, and P Depraetere. Copolymer polyelectrolyte adsorption onto titanium dioxide. *Colloid Surface A*, 158(3):375–384, 1999. [3.3](#)
- [218] V Zoulalian. *Functionalization of titanium oxide surfaces by means of poly(alkyl-phosphonate) polymers*. PhD thesis, ETH Zurich No 17618, 2008. [3.3](#), [3.10](#), [3.6](#)
- [219] W Gao, L Dickinson, C Grozinger, FG Morin, and L Reven. Self-assembled monolayers of alkylphosphonic acids on metal oxides. *Langmuir*, 12(26):6429–6435, 1996. [3.3](#)
- [220] KA Peterlinz and R Georgiadis. In situ kinetics of self-assembly by surface plasmon resonance spectroscopy. *Langmuir*, 12(20):4731–4740, 1996. [3.3](#)
- [221] O Dannenberger, M Buck, and M Grunze. Self-assembly of n-alkanethiols: A kinetic study by second harmonic generation. *J Phys Chem B*, 103(12):2202–2213, 1999. [3.3](#)
- [222] Alexandros G Koutsioubas, Nikolaos Spiliopoulos, Dimitris L Anastassopoulos, Alexandros A Vradis, and George D Priftis. Formation of alkane-phosphonic acid self-assembled monolayers on alumina: an in situ spr study. *Surf Interface Anal*, 41(11):897–903, 2009. [3.3](#)
- [223] ES Gawalt, K Brault-Rios, MS Dixon, DC Tang, and J Schwartz. Enhanced bonding of organometallics to titanium via a titanium(iii) phosphate interface. *Langmuir*, 17(21):6743–6745, 2001. [3.3](#)
- [224] ES Gawalt, MJ Avaltroni, MP Danahy, BM Silverman, EL Hanson, KS Midwood, JE Schwarzbauer, and J Schwartz. Bonding organics to ti alloys: Facilitating human osteoblast attachment and spreading on surgical implant materials. *Langmuir*, 19(1):200–204, 2003. [3.3](#)
- [225] PH Mutin, V Lafond, AF Popa, M Granier, L Markey, and A Dereux. Selective surface modification of sio2-tio2 supports with phosphonic acids. *Chem Mater*, 16(26):5670–5675, 2004. [3.3](#)
- [226] G Beamson and D Briggs. *High Resolution XPS of organic Polymers - The Scienta ESCA300 Database*. Wiley, 1992. [3.4.2](#), [3.4.2](#), [3.4.2](#)
- [227] J Scofield. Hartree-slater subshell photoionization cross-sections at 1254 and 1487 ev. *Journal of Electron Spectroscopy and Related*, 8(2):129–137, 1976. [3.4.2](#), [7.1.4](#), [7.1.4](#), [7.1.4](#)

- [228] L Feuz. *On the conformation of graft-copolymers with polyelectrolyte backbone in solution and adsorbed on surfaces*. PhD thesis, ETH Zurich, No 16644, Jan 2006. [3.4.3](#)
- [229] H Forsgren. Surface modification and physicochemical and biological characterization of monomolecular polymeric coatings on magnesium alloys. Master's thesis, ETH Zurich, D-MATL, LSST, 2008. [4](#)
- [230] C Bruhin. Surface modification and electrochemical characterization of we43 magnesium alloys. Master's thesis, ETH Zurich, D-MATL, LSST, 2009. [4](#)
- [231] R Bielecki. Surface modification of we43 magnesium alloy with novel organic coatings in the context of biodegradable vascular stent applications. Semester thesis, ETH Zurich, D-MATL, LSST, 2009. [4](#)
- [232] C DiMario, H Griffiths, O Goktekin, N Peeters, J Verbist, M Bosiers, K De-loose, B Heublein, R Rohde, V Kasese, C Ilsley, and R Erbel. Drug-eluting bioabsorbable magnesium stent. *Journal of Interventional Cardiology*, 17:391–395, 2004. [4.1](#)
- [233] BL Mordike and T Ebert. Magnesium - properties - applications - potential. *Mat Sci Eng A-Struct*, 302(1):37–45, 2001. [4.2](#), [4.2](#)
- [234] R Busk and H Head. Magnesium and its alloys. *Handbook of materials selection*, Jan 2002. [4.2](#)
- [235] A Hänzi, P Gunde, and M Schinhammer. On the biodegradation performance of an mg–y–re alloy with various surface conditions in simulated body fluid. *Acta Biomaterialia*, 5(1):162–171, 2009. [4.1](#), [4.2](#), [4.3](#), [4.3](#), [4.3](#), [4.4.3](#)
- [236] GL Song and A Atrens. Corrosion mechanisms of magnesium alloys. *Adv Eng Mater*, 1(1):11–33, 1999. [4.2](#), [4.6](#)
- [237] GL Song and A Atrens. Understanding magnesium corrosion - a framework for improved alloy performance. *Adv Eng Mater*, 5(12):837–858, 2003. [4.2](#)
- [238] F Witte, V Kaese, H Haferkamp, E Switzer, A Meyer-Lindenberg, CJ Wirth, and H Windhagen. In vivo corrosion of four magnesium alloys and the associated bone response. *Biomaterials*, 26(17):3557–3563, 2005. [4.3](#)
- [239] MP Staiger, AM Pietak, J Huadmai, and G Dias. Magnesium and its alloys as orthopedic biomaterials: A review. *Biomaterials*, 27(9):1728–1734, 2006. [4.3](#), [4.3](#)

- [240] G Mani, MD Feldman, D Patel, and CM Agrawal. Coronary stents: A materials perspective. *Biomaterials*, 28(9):1689–1710, 2007. 4.3, 4.3
- [241] PL Miller, BA Shaw, RG Wendt, and WC Moshier. Assessing the corrosion-resistance of nonequilibrium magnesium-yttrium alloys. *Corrosion*, 51(12):922–931, 1995. 4.3
- [242] HB Yao, Y Li, and ATS Wee. Passivity behavior of melt-spun mg-y alloys. *Electrochim Acta*, 48(28):4197–4204, 2003. 4.3
- [243] AJ Davenport, C Padovani, BJ Connolly, NPC Stevens, TAW Beale, A Groso, and M Stampanoni. Synchrotron x-ray microtomography study of the role of y in corrosion of magnesium alloy we43. *Electrochem Solid State*, 10(2):C5–C8, 2007. 4.3, 4.3
- [244] A Hänni. *Development of biodegradable magnesium alloys for cardiovascular stent applications*. PhD thesis, ETH Zurich No 18547, 2009. 4.3, 4.3, 4.4.3
- [245] X. M Wang, X. Q Zeng, Y Zhou, G. S Wu, S. S Yao, and Y. J Lai. Early oxidation behaviors of mg-y alloys at high temperatures. *J Alloy Compd*, 460(1-2):368–374, 2008. 4.3
- [246] R Rettig and S Virtanen. Composition of corrosion layers on a magnesium rare-earth alloy in simulated body fluids. *J Biomed Mater Res A*, 88A(2):359–369, 2009. 4.3
- [247] VK Pareek, TA Ramanarayanan, JD Mumford, A Ozekcin, and JC Scanlon. The role of morphology and structure in the kinetic evolution of iron-sulfide films on fe-base alloys. *Oxid Met*, 41(5-6):323–341, 1994. 4.3
- [248] Ngoc-Chang Quach, Peter J Uggowitzer, and Patrik Schmutz. Corrosion behaviour of an mg-y-re alloy used in biomedical applications studied by electrochemical techniques. *Comptes rendus Chimie*, 11(9):1043–1054, 2008. 4.3, 4.3
- [249] Anja C Haenzi, Isabel Gerber, Michael Schinhammer, Joerg F Loeffler, and Peter J Uggowitzer. On the in vitro and in vivo degradation performance and biological response of new biodegradable mg-y-zn alloys. *Acta Biomaterialia*, 6(5):1824–1833, 2010. 4.3, 4.3
- [250] S Hirano, N Kodama, K Shibata, and KT Suzuki. Metabolism and toxicity of intravenously injected yttrium chloride in rats. *Toxicol Appl Pharm*, 121(2):224–232, 1993. 4.3

- [251] B Heublein. Biocorrosion of magnesium alloys: a new principle in cardiovascular implant technology? *Heart*, 89(6):651–656, 2003. 4.3
- [252] Carlo Di Mario, Huw Griffiths, Omer Goktekin, Nicolas Peeters, Jan Verbist, Marc Bosiers, Koen Deloose, Bernhard Heublein, Roland Rohde, Victor Kasese, Charles Ilesley, and Raimund Erbel. Drug-eluting bioabsorbable magnesium stent. *Journal of Interventional Cardiology*, 17(6):391–5, 2004. 4.3
- [253] Patrick W Serruys, Michael J B Kutryk, and Andrew T L Ong. Coronary-artery stents. *The New England Journal of Medicine*, 354(5):483–95, 2006. 4.3
- [254] TL Barr. Esca study of termination of passivation of elemental metals. *J Phys Chem-Us*, 82(16):1801–1810, 1978. 4.4.2
- [255] JB Malherbe, S Hofmann, and JM Sanz. Preferential sputtering of oxides - a comparison of model predictions with experimental-data. *Appl Surf Sci*, 27(3):355–365, 1986. 4.4.3
- [256] RD Rogers, AH Bond, CB Bauer, JH Zhang, and ST Griffin. Metal ion separations in polyethylene glycol-based aqueous biphasic systems: Correlation of partitioning behavior with available thermodynamic hydration data. *J Chromatogr B*, 680(1-2):221–229, 1996. 4.6
- [257] MJ Hey, DP Jackson, and H Yan. The salting-out effect and phase separation in aqueous solutions of electrolytes and poly(ethylene glycol). *Polymer*, 46(8):2567–2572, 2005. 4.6
- [258] H Schott. Effect of electrolytes and protein denaturants on nonionic surfactants - a survey of the effect of electrolytes and protein denaturants on cloud points and krafft points of nonionic surfactants. *Tenside Surfact Det*, 33(6):457–463, 1996. 4.6
- [259] R Ambat, NN Aung, and W Zhou. Studies on the influence of chloride ion and ph on the corrosion and electrochemical behaviour of az91d magnesium alloy. *J Appl Electrochem*, 30(7):865–874, 2000. 4.6
- [260] R Tunold, H Holtan, MB Haggberge, A Lasson, and R Steenhansen. Corrosion of magnesium in aqueous-solution containing chloride-ions. *Corros Sci*, 17(4):353–365, 1977. 4.6
- [261] Bharat Bhushan. Introduction to tribology. *Wiley*, page 732, Jan 2002. 5.1.1, 5.1.3, 7.2.5

- [262] R Heeb. Surface modifications for improved aqueous lubrication under low-contact-pressure conditions. [5.1.1](#), [5.1](#), [5.1.2](#), [5.1.4](#), [5.1.4](#)
- [263] Gwidon W. Stachowiak and Andrew W. Batchelor. Engineering tribology. page 801, Jan 2005. [5.1.3](#)
- [264] B J Hamrock and D Dowson. Minimum film thickness in elliptical contacts for different regimes of fluid-film lubrication. *Proc. Fifth Leeds-Lyon Symp. on Tribology on "Elastohydrodynamics and Related Topics"*, Mech. Eng. Publ. Bury St. Edmunds, pages 22–27, Jan 1979. [5.1.4](#), [5.6.1](#), [5.8](#)
- [265] M ESFAHANIAN and BJ HAMROCK. Fluid-film lubrication regimes revisited. *Tribol T*, 34(4):628–632, Jan 1991. [5.1.4](#), [5.6.1](#), [5.8](#)
- [266] R Deeley. Discussion on lubrication. *Proceedings of the Physical Society of London*, Jan 1919. [5.1.4](#)
- [267] M Ratoi, V Anghel, C Bovington, and HA Spikes. Mechanisms of oiliness additives, Jan 2000. [5.1.4](#)
- [268] Jonathan Beddoes and James Gordon Parr. Introduction to stainless steels. page 315, Jan 1999. [5.2](#)
- [269] Myer Kutz. Handbook of materials selection. page 1497, Jan 2002. [5.2](#)
- [270] G Jellison. Optical functions of silicon determined by two-channel polarization modulation ellipsometry. *Optical Materials*, 1(1):41–47, 1992. [7.1.4](#)
- [271] R F Reilman, A Msezane, and S T Manson. Relative intensities in photoelectron spectroscopy of atoms and molecules. *Journal of Electron Spectroscopy And Related Phenomena*, 8:389, 1976. [7.1.4](#)
- [272] CJ Powell, A Jablonski, S Tanuma, and DR Penn. Effects of elastic and inelastic electron-scattering on quantitative surface-analyses by aes and xps. *J Electron Spectrosc*, 68:605–616, 1994. [7.1.4](#)
- [273] WH Gries. A universal predictive equation for the inelastic mean free path-lengths of x-ray photoelectrons and auger electrons. *Surf Interface Anal*, 24(1):38–50, 1996. [7.1.4](#)
- [274] S Tanuma, CJ Powell, and DR Penn. Proposed formula for electron inelastic mean free paths based on calculations for 31 materials. *Surf Sci*, 192(1):L849–L857, 1987. [7.1.4](#)

- [275] S Tanuma, CJ Powell, and DR Penn. Calculations of electron inelastic mean free paths for 31 materials. *Surf Interface Anal*, 11(11):577–589, 1988. [7.1.4](#)
- [276] S Tanuma, CJ Powell, and DR Penn. Calculations of electron inelastic mean free paths (imfps) .6. analysis of the gries inelastic scattering model and predictive imfp equation. *Surf Interface Anal*, 25(1):25–35, 1997. [7.1.4](#)
- [277] T. E Balmer and M Heuberger. Precision thickness and refractive index imaging of molecular films. *Rev. Sci. Instrum.*, 78(9):093105, Jan 2007. [7.1.4](#), [7.1.4](#), [7.1.4](#)
- [278] M Heuberger and T E Balmer. The transmission interferometric adsorption sensor. *J. Phys. D: Appl. Phys.*, 40(23):7245–7254, Nov 2007. [7.1.4](#), [7.1.4](#), [7.1.4](#)
- [279] D Shankaran, K Gobi, and N Miura. Recent advancements in surface plasmon resonance immunosensors for detection of small molecules of biomedical, food and environmental interest. *Sensors & Actuators: B. Chemical*, 121(1):158–177, 2007. [7.1.4](#)
- [280] J Vörös, R Graf, G Kenausis, and A Bruinink. Feasibility study of an online toxicological sensor based on the optical waveguide technique. *Biosensors and Bioelectronics*, 15(9–10):423–429, 2000. [7.1.4](#)
- [281] M Wiki, H Gao, M Juvet, and R Kunz. Compact integrated optical sensor system. *Biosensors and Bioelectronics*, 16(1–2):37–45, 2001. [7.1.4](#)
- [282] J Vörös. The density and refractive index of adsorbing protein layers. *Biophysical journal*, 87(1):553–561, 2004. [7.1.4](#)
- [283] G Sauerbrey. Verwendung von schwingquarzen zur wägung dünner schichten und zur mikrowägung. *Zeitschrift für Physik A Hadrons and Nuclei*, 155(2):206–222, 1959. [7.2.4](#)
- [284] B Kasemo. On the measurement of thin liquid overlayers with the quartz-crystal microbalance. *Sensors and Actuators A: Physical*, 54(1–3):448–456, 1996. [7.2.4](#)
- [285] B Kasemo. A simple setup to simultaneously measure the resonant frequency and the absolute dissipation factor of a quartz crystal microbalance. *Review of scientific instruments*, 67(9):3238–3241, 2009. [7.2.4](#)
- [286] M Rodahl, F Hook, C Fredriksson, and C Keller. . . . Simultaneous frequency and dissipation factor qcm measurements of biomolecular adsorption and cell adhesion. *Faraday Discussions*, 107:229–246, Jan 1997. [7.2.4](#)

- [287] G Felcher, R Hilleke, and R Crawford. . . . Polarized neutron reflectometer: A new instrument to measure magnetic depth profiles. *Review of Scientific Instruments*, 58(4):609, 1987. [7.2.6](#)
- [288] J Daillant and A Gibaud. X-ray and neutron reflectivity: principles and applications. *Springer*, page 348, 2009. [7.2.6](#)
- [289] P De Gennes. Polymers at an interface; a simplified view. *Advances in Colloid and Interface Science*, 27:189, Jan 1987. [7.2.6](#)
- [290] MW Rutland AA Feiler J Ralston, I Larson and M Kleijn. Atomic force microscopy and direct surface force measurements. *Pure Appl. Chem*, 77(12):2149–2170, 2005. [7.2.7](#)
- [291] G Binnig and C Quate. Atomic force microscope. *Physical review letters*, 56(9):930–933, 1986. [7.2.7](#)
- [292] T Senden. Force microscopy and surface interactions. *Curr Opin Colloid In*, 6:95–101, 2001. [7.2.7](#)
- [293] J Hutter and J Bechhoefer. Calibration of atomic force microscope tips. *Review of scientific instruments*, 64(7):1868, 1993. [7.2.7](#)
- [294] R Heuberger. *Combinatorial study of the tribochemistry of anti-wear lubricant additives*. PhD thesis, ETH Zurich No 17207, Jan 2007. [7.10](#), [7.3.1](#), [7.3.1](#), [7.11](#), [7.3.1](#), [7.3.1](#)
- [295] Evgenij Barsoukov and James Ross Macdonald. *Impedance spectroscopy: theory, experiment and applications*. Wiley, 2005. [7.4.1](#)
- [296] ME Orazem and B Tribollet. *Electrochemical impedance spectroscopy*. Wiley, Jan 2008. [7.4.1](#)

Appendix

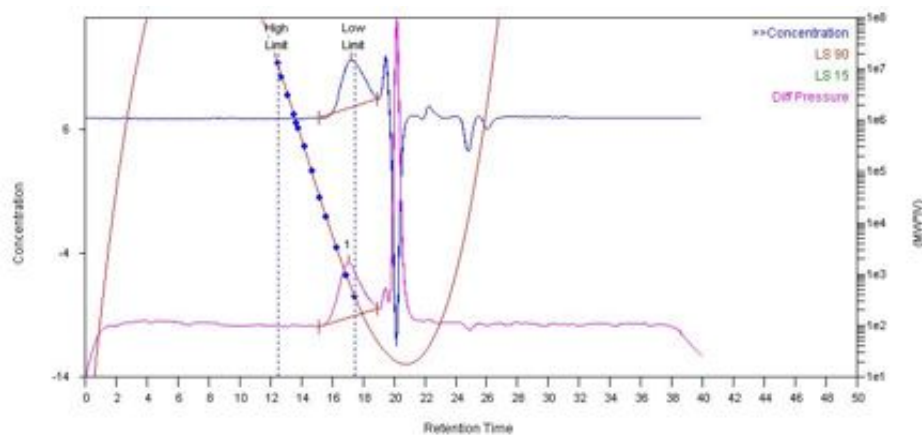
Appendix**A.1 GPC spectrum of the polymer backbone
PIMA**

Figure A.1: GPC spectrum of the polymer backbone poly(isobutylene-alt-maleic anhydride) (PIMA) resulting in a polydispersity of 2.38 with values for $M_n=11500$ and $M_w=27500$

A.2 NMR spectra of the polymers synthesized

Here, the ^1H - and ^{31}P -NMR spectra of the polymers synthesized and used are summarized. The polymers of the Family PIMA(0.3:0.3, XX) are summarized in Fig.

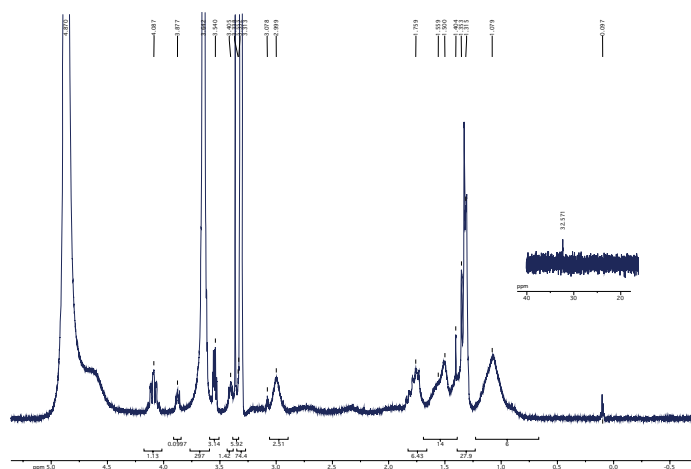
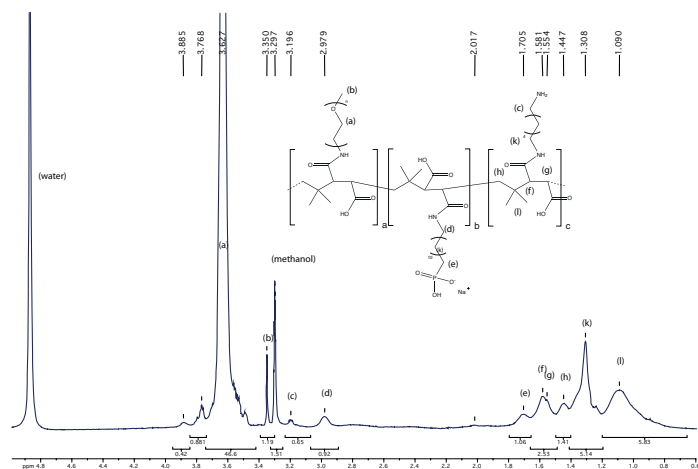
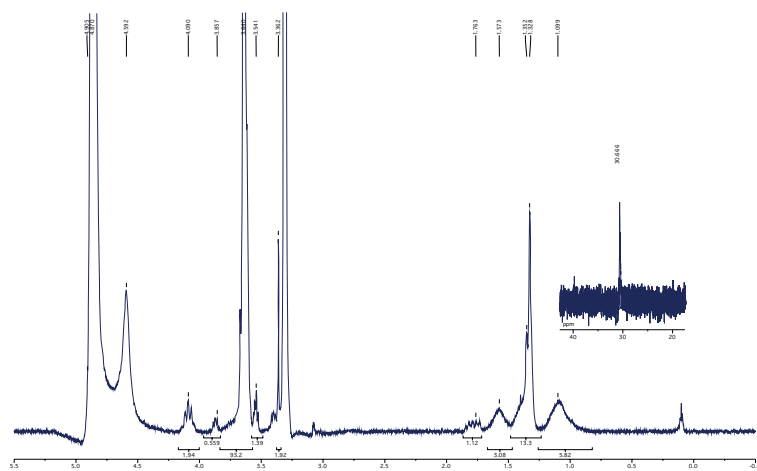
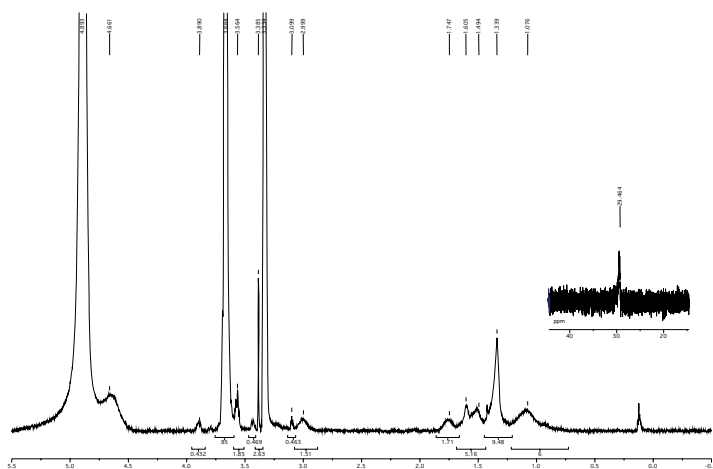


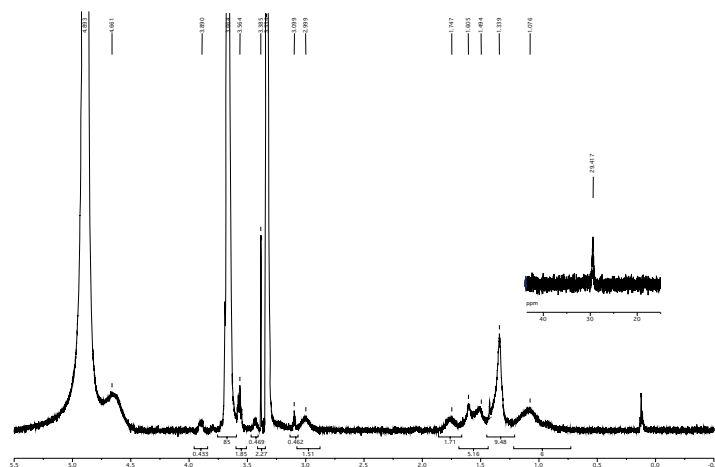
Figure A.2: NMR spectra of the polymers (a) PIMA(0.3:0.3, DAH) and (b) PIMA(0.3,0.3, EA)



(a)



(b)



(c)

Figure A.3: NMR spectra of the polymers (a) PIMA(0.40:0.45,BA), (b) PIMA(0.40:0.45,EA), (c) PIMA(0.40:0.45,DAH)

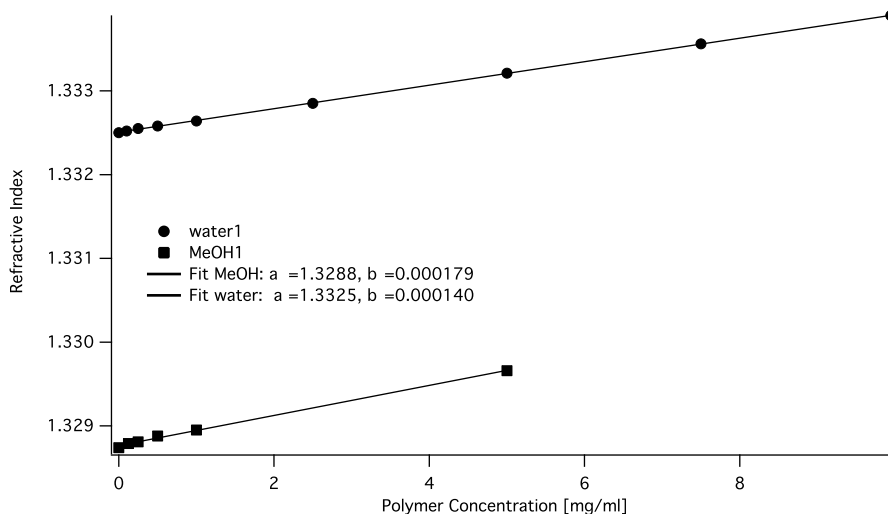


Figure A.4: Exemplary concentration dependence of the PEG-ylated polymers in water and methanol. For different polymers similar dn/dc values are obtained and is mainly dependent on the solvent, the slope b of the curve is the value dn/dc .

A.3 Concentration dependence of refractive index of the polymer

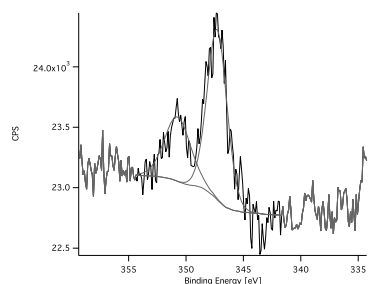
The concentration dependence of the refractive index of the polymer was measured with an Atago RX-5000CX (ATAGO CO. LTD, Tokyo) refractometer. A dilution series of the polymer in the solvent of interest was measured. Attention was drawn to the point that a good cleaning of the refractometer cell was assured after each concentration, i.e. in measuring from pure solvent to higher concentrations. After each data point the pure solvent was measured again in order to double-check a consistent value for the refractive index of the solvent, indicating a good rinsing procedure.

The concentration dependence of the polymer was investigated in water and methanol. These values are further used for the modeling of the TInAS data explained in Sect. 7.2.3 and for some calculations deriving from the SLS and DLS measurements as explained in Sect. 7.1.4.

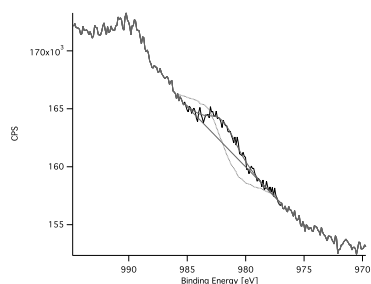
The concentration dependence was obtained by a linear fit of the data points obtained at different concentrations, exemplary fits for water and methanol are shown in Fig. A.4.

The slope of the fit, is the value of dn/dc , it is found to be $1.40 \cdot 10^{-4} \pm 1 \cdot 10^{-6}$ ml/mg for water and $1.79 \cdot 10^{-4} \pm 1 \cdot 10^{-6}$ ml/mg for methanol. The differences between

different polymers were within the error of the fit and therefore only one average value is taken for all PEG-ylated polymers.



(a) Ca2p XPS peak



(b) small Nd3d XPS peak, fitted with one peak and two different background subtractions shown. black line indicates a linear background subtraction which fits well the rising background, whereas the dashed line indicates background subtraction with the Shirley algorithm, which is not usable for these small peaks.

Figure A.5: Minor XPS peaks of bare, heat-treated WE43. The main peaks are shown in Fig. on page 136

A.4 XPS peak analysis of heat-treated WE43

A.4.1 Bare WE43

In Fig. on the current page all XPS detail spectra of the bare WE43 with the appropriate peak fitting are shown. The main contributions are shown in the main discussion in Fig. on page 136, here the trace element and smaller peaks are shown additionally. Furthermore, the different background subtractions (linear vs. Shirley algorithm) are shown.

A.4.2 WE43 Surface Cleaning

In Tag. A.1, The surface composition of the heat-treated WE43 samples is shown after different cleaning procedures. A more detailed discussion of the cleaning protocol development is given on page ??.

Table A.1: Summary of the main composition (at-%) of the different cleaning tests (excluded elements in traces: Nd, Ca, Na)

Cleaning	C1s (Carbonate)	C1s (Hydro- carbon)	Mg2s	Y3d (total)	O1s
Reference	22 ± 8	10 ± 3	7 ± 3	0.5 ± 0.2	58 ± 7
Ozone	18	5	9	0.5	65
Plasma	15	4	8	0.5	72
Acetone	15	32	5	0.3	47
Acetone + UV	20	3	8	0.5	67
Acetone + Plasma	14	9	8	0.6	67
Ethanol	17	13	10	0.8	56
Ethanol + UV	18	3	10	0.7	63
Ethanol + Plasma	13	3	9	0.7	71
2-Propanol	16	15	10	0.8	56
2-Propanol + UV	19	3	9	0.6	69
2-Propanol + Plasma	16	3	7	0.6	71
conc. NaOH	19	10	17	1.5	52
NaOH + UV	5.5	2	16	11	64
NaOH + Plasma	5	4	17	11	63

A.4.3 DDPO4 Surface Functionalization

XPS analysis of DDPO4 on titanium oxide was used as reference system in order to reproduce the fitting used in [84]. The P2p peak was fitted as a single doublet with P 2p_{3/2} at 133.9 ± 0.1 eV and a binding-energy difference of 0.85 eV with the P 2p_{1/2} peak and a fixed-area ratio of 2:1. Only one chemical species was fitted into the Ti2p peak at a B.E. of 458.6 ± 0.1 eV for the Ti 2p_{3/2} peak. The main contribution of the C1s signal is the aliphatic signal with a B.E. of 285 eV. A shoulder at higher B.E. of 286.8 ± 0.1 eV originates from the CH₂-group directly connected to the phosphate. The oxygen peak was fitted with a main contribution of the titanium oxide at 530.2 ± 0.1 eV and two minor species deriving from the SAMs overlayer: the contributions of Ti-OH, Ti-O-P and P-OH, which are assumed to have very similar B.E. are fitted in one peak at B.E. difference of 2.3 eV to the oxide peak. The contributions deriving from the P=O are fitted relative to the to the oxide peak at a B.E. difference of 0.7 eV.

The appropriate spectra are shown and discussed in Fig. 4.10 on page 147.

APPENDIX

B

Curriculum Vitae

Christoph Karl Kilian Mayer
Department of Materials Science
Swiss Federal Institute of Technology (ETH) Zurich
Zurich, Switzerland

Personal

Birth September 27th, 1980 in Ochsenfurt, Germany

Nationality German

Address Wolfskeelstr. 2
 D-97294 Unterpleichfeld
 Germany

Education

2006–11 SWISS FEDERAL INSTITUTE OF TECHNOLOGY (ETH)
 Dpt. of Materials Science, Laboratory of Surface Science and Technology,
 Zurich, Switzerland
 Prof. Dr. N. Spencer

- 2006 CEA SACLAY, SACLAY, FRANCE
Atomic Research Center, Service de Chimie Moléculaire, Laboratoire Interdisciplinaire sur l'Organisation Nanométrique et Supramoléculaire
Master/Degree thesis: "Cation Adsorption at Solid-Liquid Interphase on Mesoporous Materials (SBA)"
Dr. F. Testard
Foreign Exchange Scholarship of German Academic Exchange Service (DAAD)
- 2004–06 ECOLE NATIONAL SUPERIOR DE CHIMIE DE LILLE (ENSCL), Lille France
Master Recherche "Master Chimie et Ingénierie de la Formulation", October 2006
Prof. Dr. J.-M. Aubry
- 2001–06 UNIVERSITY OF REGENSBURG, GERMANY
Degree in Chemistry (Diplom), October 2006
Specialization "Condensed Complex Materials and Soft Matter" (COSOM/EMASCO)
Prof. Dr. W. Kunz
- 2000 ABITUR, WÜRZBURG, GERMANY
Intensive courses in Chemistry and Physics

Affiliations

German Chemical Society (GDCh)

Swiss Chemical Society (SCG)